



UNIVERSITÀ DEGLI STUDI DI MILANO  
FACOLTÀ DI SCIENZE E TECNOLOGIE

Dipartimento di Chimica

TESI DI DOTTORATO IN  
CHIMICA INDUSTRIALE

**Photocatalytic processes  
for the valorization of waste  
and renewable substrates**

**Relatrice:**

Prof.ssa Ilenia Rossetti

**Candidato:**

Francesco Conte

Anno accademico 2022-2023



# INDEX

<b>1.</b>	<b>Foreword</b>	<b>1</b>
1.1.	General introduction	1
1.2.	Overview about photocatalysis	5
1.3.	Photocatalysis principles	7
1.4.	Titanium dioxide	10
1.5.	Graphitic carbon nitride	16
	References	18
<b>2.</b>	<b>Experimental</b>	<b>25</b>
2.1.	Photocatalyst in form of powder	25
2.2.	Immobilized photocatalysts	30
2.3.	Materials characterization	33
2.4.	Experimental setup for activity testing	35
2.4.1.	Photoreduction of CO <sub>2</sub>	35
2.4.2.	Photoreforming of carbohydrate	37
2.4.3.	Photocatalytic test with immobilized photocatalyst	40
2.4.4.	Photo abatement of pollutants	41
2.4.5.	Toxicity test	43
	References	44
<b>3.</b>	<b>Material characterization</b>	<b>47</b>
3.1.	BET	47
3.2.	XRD	53
3.3.	DRS UV-Vis	62
3.4.	Photoluminescence	69
3.5.	TGA	70
3.6.	XPS	71
3.7.	SEM-EDX	74
3.8.	FT-IR	75
3.9.	References	78
	Appendix A	83

<b>4.</b>	<b>CO<sub>2</sub> photo-reduction</b>	<b>91</b>
4.1.	Introduction	91
4.2.	Results and discussion	96
4.2.1.	CO <sub>2</sub> photoreduction tests with TiO <sub>2</sub> , g-C <sub>3</sub> N <sub>4</sub> -TE and composites	96
4.2.1.1.	Effect of pH	96
4.2.1.2.	Effect of pressure	97
4.2.1.3.	Effect of HS concentration	100
4.2.1.4.	Effect of reaction time	101
4.2.1.5.	Economic assessment of photocatalytic process	103
4.2.2.	CO <sub>2</sub> photoreduction tests with g-C <sub>3</sub> N <sub>4</sub> and WO <sub>3</sub> composites	104
4.2.2.1.	Tests with exfoliated g-C <sub>3</sub> N <sub>4</sub>	105
4.2.2.2.	Tests with C <sub>3</sub> N <sub>4</sub> /WO <sub>3</sub> composites	109
4.2.3.	CO <sub>2</sub> photoreduction tests with catalysts synthesized via FSP	111
4.2.4.	Comparison with other photocatalysts	113
4.2.5.	Test with different hole scavenger	115
4.3.	Conclusion	126
	References	127
	Appendix B	136
<b>5.</b>	<b>Carbohydrate photoreforming</b>	<b>141</b>
5.1.	Introduction	141
5.2.	Result and discussion	143
5.2.1.	Effect of composition and metal loading	143
5.2.2.	Effect of pH	145
5.2.3.	Photoreforming of wastewater from pulp industry	146
5.3.	Conclusions	155
	References	156
<b>6.</b>	<b>Photo abatement of pollutants</b>	<b>159</b>
6.1.	Introduction	159
6.2.	Results and discussion	163
6.2.1.	Photocatalytic test	163
6.2.2.	Diclofenac	164
6.2.2.1.	Direct photolysis	164
6.2.2.2.	Effect of DCF concentration	165

6.2.2.3.	Effect of $\text{Fe}^{2+}$ concentration	167
6.2.2.4.	Effect of hydrogen peroxide concentration	167
6.2.2.5.	Effect of pH	167
6.2.2.6.	Effect of illumination system	169
6.2.2.7.	Photocatalysis with $\text{TiO}_2$ and M/ $\text{TiO}_2$	170
6.2.2.8.	Comparison between heterogeneous and homogeneous treatments	174
6.2.3.	Erythromycin	175
6.2.3.1.	Toxicity test	176
6.2.4.	Acid Orange, Bromophenol Blue, Amoxicillin	178
6.2.4.1.	Catalysts comparison	179
6.2.4.2.	Effect of pollutant irradiation system	182
6.2.4.3.	Effect of pollutant concentration	183
6.2.4.4.	Effect of pollutant nature	184
6.2.4.5.	Effect of exfoliation power	186
6.2.4.6.	Effect of photocatalyst concentration	187
6.2.4.7.	Photo-Fenton	188
6.2.5.	Test and acute toxicity with Amoxicillin	190
6.3.	Conclusion	193
	References	195
	Appendix C	203
<b>7.</b>	<b>Photocatalyst deposition</b>	<b>207</b>
7.1.	Introduction	207
7.2.	Results and discussion	208
7.2.1.	Optimization of the deposition process	208
7.2.2.	Supported photocatalysts functionalization	216
7.2.3.	Design of reactor supports	218
7.1.1.	Photocatalytic tests using the deposited glasses	225
7.3.	Conclusions	230
	References	231
<b>8.</b>	<b>Final conclusion and future developments</b>	<b>233</b>
	<b>Appendix D</b>	<b>235</b>



## Abstract

In this work, innovative photocatalysts based on titanium dioxide and graphitic carbon nitride have been synthesized and tested in an innovative pilot photoreactor which is unique for several reasons, including its high volume (more than one liter), the ability to sustain pressure up to 20 bar and the irradiation system located inside the photoreactor (that allows a homogeneous and efficient distribution of the light).

This setup allowed to achieve interesting results in the photoreduction of carbon dioxide in the liquid phase to small organic molecules (e.g. formic acid, methanol and formaldehyde), in particular, previously seen productivities have been obtained with exfoliated carbon nitride photocatalysts. Moreover, the same photoreactor was also used to perform the photo reforming of sugars and acid to hydrogen, which represent a benchmark for more complex mixtures derived from biomass treatment.

On the other hand, the photocatalyst proved to be active even for other processes, such as the photo abatement of pollutants (e.g.  $\text{NO}_3^-$ ,  $\text{NO}_2^-$ ,  $\text{NH}_3$ , dyes, pharmaceuticals, etc.) from wastewaters, which most of the time led to a decreases of the toxicity of the solution according to *in vitro* toxicity tests performed after the process.

Lastly, a small step toward the scale up of the photocatalytic processes was represented by the development of a robust and reliable procedure for the immobilization and functionalization of the photocatalytic materials over a solid support, (i.e. glass), which simplify the treatments and theoretically allows the recovery and reuse of photocatalysts.





# 1. Foreword

## 1.1. General introduction

The year 2020 has been characterized by one of the most difficult challenges ever faced by humankind. Suddenly, every aspect of our lives which was taken for granted was upset and many of us begun to be more aware of the life we are living and the environment around us. Few months of hard lockdown were enough to observe a remission of the harmful effects that our concept of "economic growth" was causing to the planet. Eventually, we breathe the same air, drink the same water, and eat the same food so every damage that we cause to the ecosystem Earth will come back by starting a vicious circle that can only get worse. Some boundaries have already been exceeded, for example, biodiversity and the nitrogen cycle, while others like climate change are dangerously approaching [1]. In order to prevent irreversible changes, it is necessary to adopt new behaviors that are more respectful towards the nature and characterized by a sustainable development. The latter is becoming the driving force of our research activity as chemist as well as the one of the chemical industry sectors, since the idea of a sustainable processes or products is not linked anymore to something that you are forced to develop but it rather identifies an opportunity of economic growth due to the increased awareness of the market toward these solutions. The way forward is certainly that one traced by the principles of green chemistry, that with its twelve points reminds us that we should always try to make more with less (*i.e.* atom economy) while using the minimum amount of energy and renewable sources [2]. Although the meaning of "sustainable" cannot be summarized in few words, it usually refers to something that can be exploited virtually "forever". However, resources on our planet are finite, especially the most important one, which is the energy, and we are not yet close to sustain the current growth of the

population, with the few alternatives that emerged in the last 20 years (*e.g.* solar, wind, etc...) [3]. Despite the abundance of ore and raw materials in the Earth's crust, the exploitability of a resource is strictly correlated with the amount of energy necessary for its extraction and processing. Our society is based primarily on the usage of the oil as energy vector, indeed, only 5 to 20% of its total production is directed to the chemical industry, depending on the type of plant [4]. Back in 1995, the average Standard Energy Return On Investment (EROI<sub>st</sub>) for the production of oil and gas was 30:1, which means that a thirtieth of the energy content extracted from the wells was used in the extraction process itself. Nowadays, this value dropped to 18:1 in 2008, while locally, for example in the United States, can be as low as 10:1 (2010) [5]. It is out of question that there are enough hydrocarbons reservoir for the centuries to come, but will it economically sustainable to exploit?

Renewable energy sources offer a partial solution to this problem, as nuclear energy has a mean EROI of 14:1, while hydroelectric can reach the outstanding value of 84:1 [5]. Unfortunately, the availability of the latter is mainly dependent on the hydrography of the territory, while the former is strongly hampered by public opinion [6]. It does not get better for alternative fuels such as bioethanol, which is actually wasting energy when it comes from fermentation of woody biomass (EROI 0.64:1) rather than molasses or sugar cane [7]. On the other hand, solar and wind, which have gained a lot of attraction lately, compete directly with fossil fuels, with performance of respectively 10:1 and 18:1. It has to be said that, without considering the problem of the disposal of the outdated systems, the energy output of both these two renewables are quite unpredictable due to the uncertainty of the weather conditions. For instance, in 2021 the total Germany's PV installations grew by 5.4% and still the energy produced during the period considered

was the same of 2020, due to a cloudy summer. Fraunhofer Institute offers a nice overview about that topic [8].

Ultimately, the only true and virtually infinite (at least for our conception of the time) energy source is the light that every day is delivered on our planet by the Sun. Indeed, it comes for free, almost equally distributed all over the world, and its consumption does not harm the environment (the process in which the energy is involved might be polluting, but there are not products of the consumption, like the CO<sub>2</sub> in case of fossil fuels). The photosynthesis has worked for hundreds of millions of years, converting in a relatively efficient way the noxious carbon dioxide into sugar-based biomass. This harvesting process has been barely imitated by humans through the development of photovoltaic systems, whose efficiency is as high as 30% in the best case [9]. Moreover, the so produced electricity needs to be consumed immediately, since commercial batteries and accumulators add inefficiency and costs to the process and are not applicable on a large scale. If we take into account that the global annual consumption of energy is over 162'000 TWh [10] and that the energy from the sunlight is 2.9-6.6 kWh/m<sup>2</sup> each day, e.g. in the USA depending on the season [11], it is clear that even the smallest improvement in its energy storage could free the humanity from the dependence on fossil fuels. As already mentioned, the excess energy can be stored through a conventional electrochemical cell, and, in that case, the typical Li-ion battery has an energy density up to 0.95 MJ/kg, which is way lower than the energy content of gasoline (46 MJ/kg) [12]. Other commercially available solutions include the power-to-gas technology, in which the excess energy is used to perform water electrolysis and the so formed hydrogen combines with carbon dioxide in order to obtain methane, which is then injected into the gas grid [13]. It must be pointed out that even this approach is characterized by low

efficiency, since most commercial plants rely on alkaline electrolysis [14], and the performance of PV system must be added to obtain the overall efficiency. Thus, it is crucial to develop a different approach, like chemists have done with photochemistry starting from the 19<sup>th</sup> century and photo-catalysis one century later [15].

Photoactive molecules and materials are able to absorb the light and use that energy to break bonds and perform reactions. Instead of converting the radiation into electricity, that potential energy is stored into the chemicals, mainly organics, which can be then used into the well-established petrochemical industrial processes (*e.g.* catalytic cracking, hydrocracking, reforming and so on) or directly employed as fuels for power plant and transportation. Countless articles about the benefit of the photo-catalysis in that field have been published and the research is still going on, from the classic titanium dioxide-based semiconductors to the more innovative molecular machine [16].

In this manuscript, three different green chemistry processes that are based on photo-catalysis will be presented and discussed, and they are:

- CO<sub>2</sub> photo-reduction to liquid fuels
- Carbohydrate photo-reforming to hydrogen
- Photo-degradation of pollutants from wastewater

All these treatments may share the same materials and equipment, however, each one focus on one aspect of the photo-catalytic process, which is then optimized for the specific application.

In this regard, photocatalysis may be the key that unlocks the revolution. It is no secret that the annual energy demand is actually only a tiny fraction of the energy delivered on our planet by the sun, and generally speaking, we are surrounded by the results of millions of years of natural photosynthesis [17]. Green plants use pigments to

absorb photons and excite electrons, whose energy is then stored into carbohydrates, and in a similar fashion, scientists are exploiting the sunlight using photoactive materials that accept the incoming energy and use the latter to perform chemical reactions. Yet, the term photocatalysis is used in a misleading way. Indeed, it can refer to an uphill reaction that will not be feasible thermodynamically without an external energy source, even with a conventional catalyst, for which the term photosynthesis may be more appropriate, but it can also describe a spontaneous reaction in which the activation energy hinders the formation of the products [17]. In any case, the reaction is not the consequence of the direct interaction between the light and the reactants, nor the results of the thermal heating induced by light, and a photocatalyst is required to obtain the desired products.

## **1.2. Overview about photocatalysis**

The very first experiments where the light was used to promote reactions were carried out by the Italian chemist Giacomo Ciamician, at the beginning of the 20<sup>th</sup> century, however, only a decade later a photocatalyst, in particular ZnO, was exploited to oxidize Prussian Blue under illumination [17]. Since then, countless semiconductors have been employed to promote reactions, from the basic water splitting of Fujishima and Honda in 1972 to artificial photosynthesis [18,19]. Regardless of the reaction, a semiconductor is involved, with the catch that its band potentials should match the redox potential of the reactions that one is trying to carry out. The band gap ( $E_g$ ) expresses the difference in energy between the valence band ( $E_v$ ) and the conduction band ( $E_c$ ) of a semiconductor. As the name suggests, in a semiconductor it is necessary to provide energy in order to break free an electron and promote it to the conduction band, whereas in conductors the  $E_v$  and  $E_c$  are overlapped, so the  $e^-$  are free to flow at ambient temperature and without external

input. Conversely, insulators are characterized by a very high resistivity and the charge carriers cannot move until a breakdown voltage is applied. When one thinks of a semiconductor, it usually refers to a metal oxide or doped silicon, like the one used for PV systems. Figure 1.1 illustrates the band gap values of many well studied semiconductors and their band-edge, both compared with the standard reduction potential of common chemicals, like molecular oxygen, water and CO<sub>2</sub>. From a thermodynamical point of view, a semiconductor must have a conduction band that is more negative than the reduction potential of the couple considered [20]. For instance, TiO<sub>2</sub> should be theoretically able to reduce carbon dioxide to formic acid, while this is not expected when using iron oxide. Similarly, the valence band needs to be more positive than the potential of the oxidation semi-reaction, thus, most of the semiconductors reported in Figure 1.1 are able to perform the oxidation of water.

Anyhow, once the semiconductor bands match with the selected reaction, the focus shifts on its  $E_g$  value since it will ultimately tell if that material will be able to operate under sunlight. The natural light is mostly composed of visible wavelengths (400–760 nm) and infrared radiation (IR, >760 nm), which account respectively for 45% and 50%, while the UV radiation (mostly UVA, 300-400 nm) represents only a minor fraction (5%) [21]. Therefore, if we consider the 400 nm threshold, then the maximum value of BG allowed for a photocatalyst that is supposed to work efficiently under sunlight is calculated according to equation 1.1:

$$(Eq. 1.1) \quad \text{Energy of photon (eV)} = h \cdot c / \lambda \text{ (nm)}$$

Where  $h$  is the Plank's constant whose value is  $4.14 \times 10^{-15} \text{ eV} \cdot \text{s}$  and  $c$  is the speed of the light expressed in nanometer. The  $hc$  term is equal to  $1240 \text{ eV} \cdot \text{nm}$ . If we use a wavelength of 400 nm the result of that formula is 3.1 eV, and it turns out that several photocatalysts

such as  $\text{TiO}_2$  and  $\text{ZnO}$  could not operate under sunlight just as they are and without surface modification or doping, which will be discussed later in this section. On the other hand, most of the other materials whose  $E_g$  is lower than 3.1 eV have their conduction bands more positive than the  $\text{CO}_2$  reduction potential and water splitting. In conclusion, it is not trivial to develop a photocatalyst that can be employed for the conversion of this noxious molecule.

But why is a photocatalyst able to carry out such a reaction in the first place?

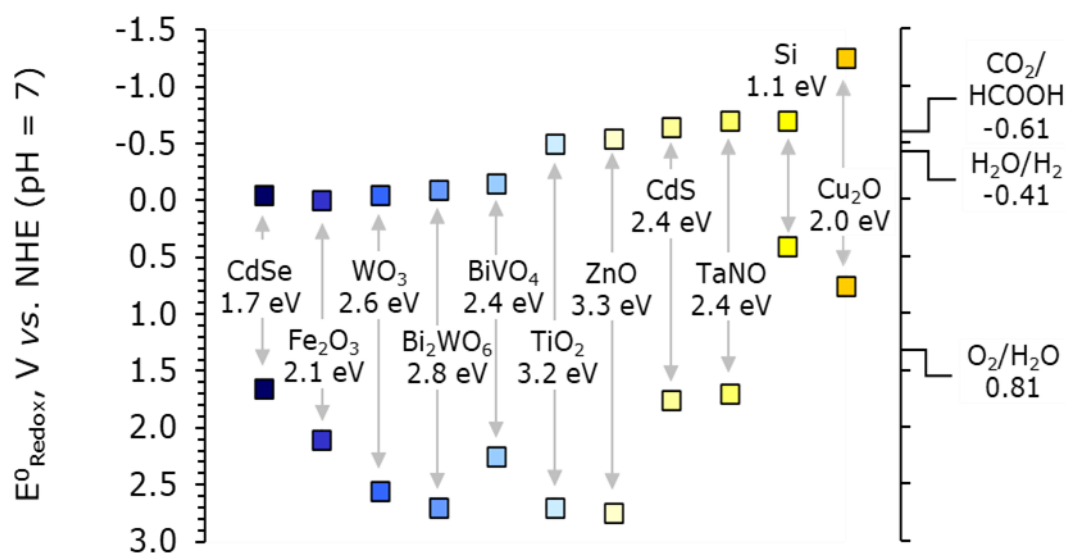


**Figure 1.1.** Band gaps and Band-edge position of common semiconductors and reaction potential of selected chemical species. Reproduced and adapted from [20]

### 1.3. Photocatalysis principles

As already mentioned, the first step is actually the illumination of the photocatalyst with an appropriate source of photons, whose energy needs at least to match the gap between the valence and conduction bands (Figure 1.2). When this criterion is fulfilled, one electron is excited and promoted from the highest occupied level of  $E_v$  to the lowest unoccupied energy level of  $E_c$ , leaving an hole behind [22]. After the photoexcitation, the

promoted electron could take various decay pathways, which are in general (i) radiative emission (*i.e.* emission of light, also known as photoluminescence) and (ii) non-radiative transition. The second case is the one that matter the most to chemists since it not only includes the thermal dissipation but also the migration and combination of the electron with a chemical adsorbed over the photocatalyst surface. In addition, when the  $e^-$  is used in the reduction semi-reaction, the hole ( $h^+$ ) should react as well (with an electron donor) in order to maintain the electric neutrality and prevent its accumulation. Indeed, the longer the charges are separated, the higher will be the efficiency of the photocatalyst. In materials such as titanium dioxide, the expected lifetime of photogenerated electrons is roughly tens of nanoseconds [23,24], which allows for a moderate activity. However, the efficiency of a photoactive material is often evaluated through the Quantum Yield ( $\Phi$ ), that is the rate at which the target molecules undergo a certain reaction compared to the photons absorbed per unit of time by the photocatalyst, or rather the Quantum Efficiency ( $\eta$ ) when a polychromatic source is used [25]. Although this is the canonical definition, that statement is only valid for homogeneous systems and in case of heterogeneous one, like catalysts in form of powder and dispersed in a liquid medium, it should be used the term Photonic Efficiency ( $\zeta$ ), which defines the number of chemical transformations that occurs divided by the number of incident photons at a given wavelength and that pass through a unit of area. This is worth to highlight, since in heterogeneous system the scattering effect is not negligible and reaction medium always absorbs a portion of the radiation. In addition, all the characteristic of the photocatalyst surface should be included (*e.g.* BET area, number of superficial groups, etc.), because there is not a clear definition of “active site” for a solid material and there are also several steps that are not catalyzed by light, like adsorption and desorption of chemicals.



After the illumination, if the photogenerated electron-hole couple does not recombine, the charges migrate to the surface or get trapped by the lattice (Figure 1.2). In fact, the  $E_g$  of a given material that can be found in literature refers to the wavelength of the light absorbed but does not fully describe its behavior when employed for photocatalysis. Surface modification, defects in the crystalline structure, doping and coupling of different materials are techniques also aimed to increase the lifespan of the photogenerated charges [26]. If that is successfully applied, then the holes and the electrons can react with the molecules present at the photocatalyst surface (as already mentioned, that is still a kind of non-radiative emission), hopefully carrying out the desired reaction (Figure 1.2)

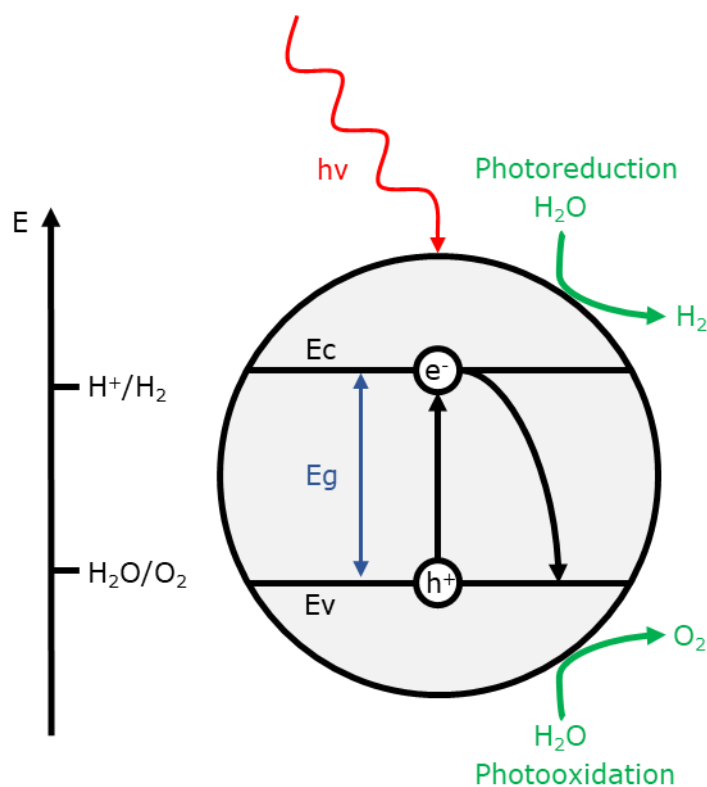


**Figure 1.2.** Simplified mechanism of the photocatalyzed reactions

#### 1.4. Titanium dioxide

This thesis focuses mainly on the performance of two of the most adopted photocatalysts worldwide, that are titanium dioxide and graphitic carbon nitride.

Titanium dioxide is a transition metal oxide which is obtained from the processing of Ilmenite ore [27]. That kind of mineral is well distributed within the Earth crust and the concentration of titanium results to be one hundred times higher than that of copper, thus, unlikely other industrial metal like vanadium (which has been classified as a critical raw material), there are not concerns about the depletion of its reserve, at least in the foreseeable future [27]. The  $\text{TiO}_2$  is mostly employed in the production of paints and as a filler for polymers (80% overall), while metallic titanium substitutes the steel in those application in which durability, lightness and resistance toward corrosion are seek, such as aerospace and naval industry.

$\text{TiO}_2$  naturally occurs in the rutile and anatase forms, with small percentages of brookite, and the first two forms are based on a tetragonal structure while the latter shows an orthorhombic one [28]. Rutile is the most stable polymorph, in which the other structures convert after thermal treatment [29]. What makes that oxide so attractive to scientists is that the nanostructured titanium dioxide, especially anatase, exhibits photocatalytic properties when illuminated with ultraviolet radiation [28,30]. Indeed, it is currently used for self-cleaning tiles and paints, particularly useful in the healthcare sector as it not only decomposes pollutants but also bacteria [31]. Back in the sixties, Fujishima and Honda were among the first to discover that an electrochemical cell in which the anode is coated with a thin layer of titanium dioxide was able to evolve oxygen when irradiated with a xenon lamp [32]. That was a game changer discovery, since the water itself is transparent to visible light and therefore it is impossible to perform the water splitting directly, though

the standard reduction potential of  $\text{H}_2\text{O}$  (1.23 V at 25°C and 1 atm) could be theoretically overcome by using radiations below 1000 nm [30,32].

In 2018, more than 13'000 published papers included the keyword “photocatalysis” [33], and  $\text{TiO}_2$  related publications are amongst the most published. As a photocatalyst, titanium dioxide almost perfectly fits that role, since it is massively produced at a low cost [34], it is not particularly toxic to humans or hazardous toward the environment (it has to be said that the WHO recently affirmed that potential carcinogenicity of the titanium dioxide used as food additive cannot be excluded [35]) and it is inert in most conditions. In addition, it does not suffer of photo-corrosion when used in water solution, such as in case of CdS, which is a phenomenon that involves the oxidation of the photocatalyst carried out by the holes entrapped on its surface [36]. However, all that glitters is not gold. Titanium dioxide has one major limitation, which is its wide band gap. The  $E_g$  of anatase is one of the lowest among the polymorphs and it is equal to 3.2 eV, with an absorption threshold of 387 nm [37]. As already discussed, the UV portion of the sunlight is less than 5%, thus it is difficult to imagine a revolution in the energy sector based solely on titanium dioxide as it is. In order to harvest the virtually unlimited amount of energy that comes in the form of visible light, it is necessary to extend its response range. The band structure of anatase is reported in Figure 1.3. To narrow the  $E_g$  and improve the performance under sunlight, there are three main approaches, that are (i) a downward shift of the conduction band, (ii) an upward shift of the valence band and also (iii) both those solutions combined [38].

That modifications take place in different ways, such as doping with either metallic or non-metallic ions, phase mixing (*e.g.* anatase/rutile with controlled ratio), metallization

of the surface with noble metal NPs, coupling with other semiconductors or sensitizers and many more [26,33,39–42].

A kind of titania often employed for photocatalytic purposes is found on the market under the commercial name P25, which is supplied by Evonik, former Degussa. It is a standard when it comes to assess the photocatalytic activity of any kind of active material, and it is prepared via flame hydrolysis of an aerosol obtained by using a volatile titania precursor (*e.g.*  $\text{TiCl}_4$ ) [43]. The so formed photocatalyst is nanosized and highly crystalline, with a 70% to 80% of anatase phase while the rest is rutile. The relatively high photocatalytic activity is attributed to the presence of both the polymorphs, which are electrically connected, and the consequent formation of defects on the NPs surface that contribute to entrap and stabilize the photogenerated charges [44]. In addition, when a photocatalyst is nanosized, the number of atoms that compose the bulk and the surface of the material are comparable, so there are less chances for charges recombination in the former [44].

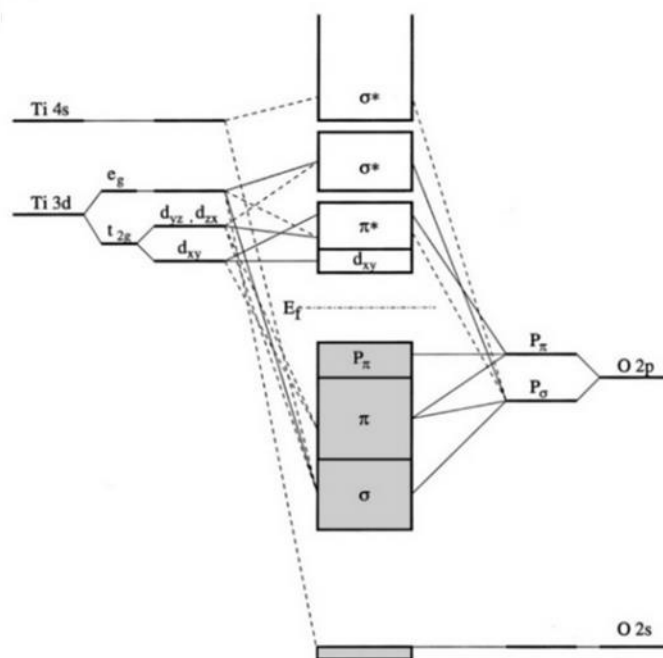
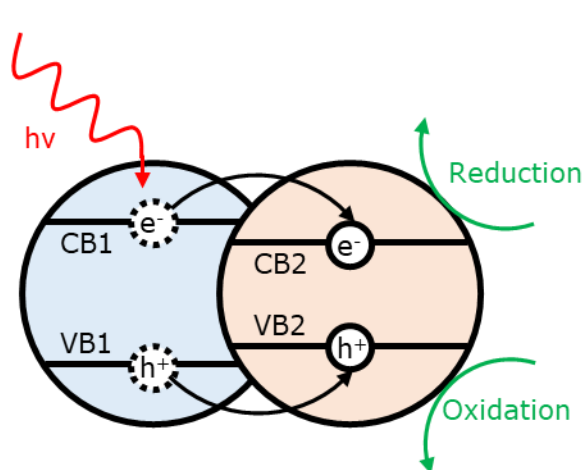
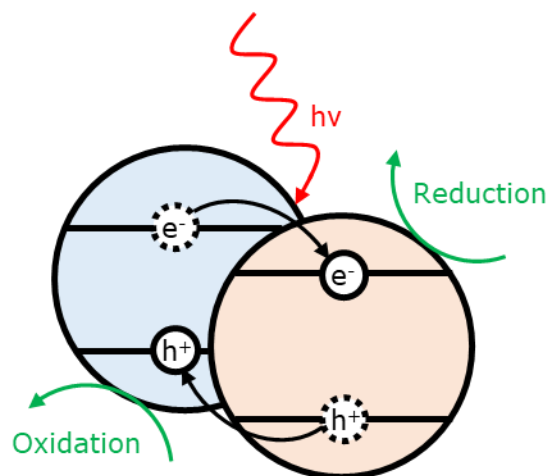


**Figure 1.3.** Molecular-orbital structure of anatase. Reproduced from [40]

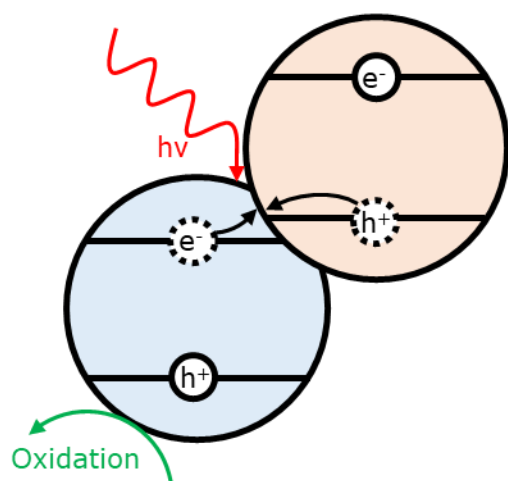
On the other hand, heterojunction with other oxides and metallization are an effective and scalable ways to lower the BG of titania and reduce its charge recombination rate. When  $\text{TiO}_2$  is compounded with another material, there are several outcomes possible and based on the relative position of both the VBs and CBs, as reported in Figure 1.4 and 1.5 [45]. In type I heterojunction (Figure 1.4.a) the photoexcited charges are generated on the first semiconductor and then collected by the second one, which has a CB more positive and a VB more negative than the other material. That behaviour is similar for type II junction (Figure 1.4.b), however, due to the relative position of the bands, the two half-reactions occur on one semiconductor each. In type III heterojunction (Figure 1.4.c), the VB on one photocatalyst is higher than the CB of the other, so the charges are quenched. More in details, the type II heterojunction can also lead to the formation of the so-called Z-scheme, which is usually adopted when the goal is to obtain a photocatalyst with both strong photooxidation and photoreduction capabilities [46]. That category can be further divided into more schemes, as the two semiconductors can be electrically connected directly (Figure 1.5.e), put in contact by an inert semiconductor (Figure 1.5.f) or quench the respective charges via a redox couples present in the reaction medium (Figure 1.5.g). The direct Z-scheme is the one formed in P25, since the anatase and rutile phases have different BGs, but it is even seen in  $\text{g-C}_3\text{N}_4/\text{TiO}_2$  composites. More interesting for our purposes is the electrical connection formed when metallic nanoparticles are deposited over the photocatalyst surface (Figure 1.4.d).



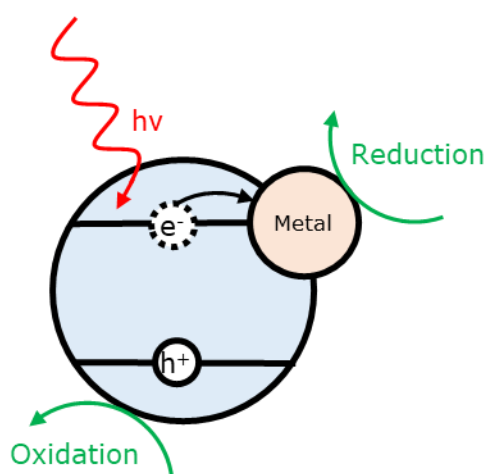
**(a)** Type I heterojunction



**(b)** Type II heterojunction



**(c)** Type III heterojunction



**(d)** Schottky heterojunction

**Figure 1.4.** Type of heterojunctions formed when two compounds are mixed together

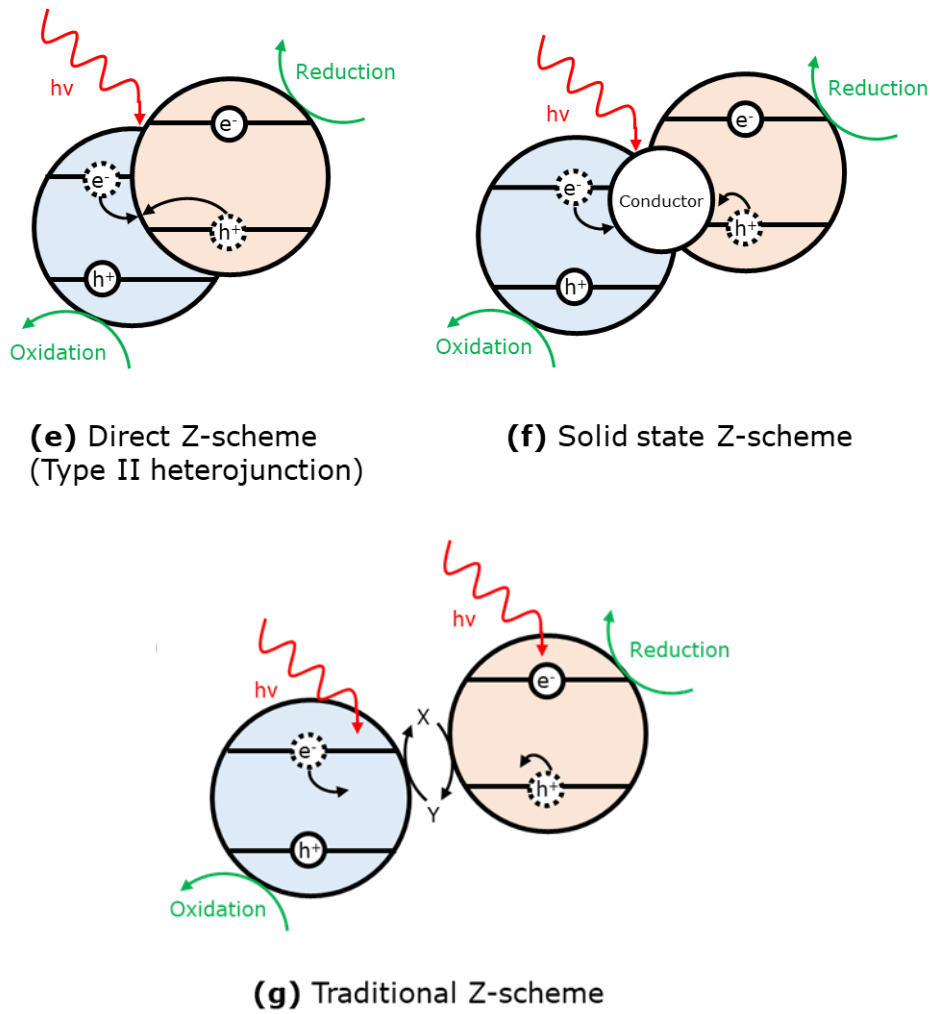


**Figure 1.5.** Three kinds of Z-scheme

In such system, the metal acts as electron sink which helps to stabilize the photogenerated charges via the formation of a Schottky barrier [47,48]. Briefly, when the metal is put in contact with the semiconductor, the electrons will flow freely from the latter to the former, which in general has a lower Fermi level (*i.e.* the highest energy level that an electron can occupy at 0K). At the equilibrium, there will be only one Fermi level for the whole system and the semiconductor will be depleted of electrons, while the metal NPs will see a surplus, therefore positive and negative charges will accumulate at the interface in order

to maintain a net neutrality. This results in the upward bending of the semiconductor CB, since the positive charges repels each other [48,49].

### **1.5. Graphitic carbon nitride**

The same technique described for the modification of titanium dioxide are valid when applied to graphitic carbon nitride (g-C<sub>3</sub>N<sub>4</sub>). The C<sub>3</sub>N<sub>4</sub> is a polymeric material in which the C and N atoms are connected with an alternating arrangement. It is based mainly on s-tri-triazine (also known as heptazine) building blocks and it is named differently depending on the degree of polymerization, such as “melam” for its dimer, “melem” when three units condensate and “melon” for polymeric chains of heptazine [50], as illustrated in Figure 1.6. That material is commonly prepared via thermal condensation of various nitrogen-containing organic precursors, including melamine, urea, dicyandiamide and many others, which are heated under air and above 525°C for several hours. The so-formed polymeric carbon nitride (PCN) shows a diffraction pattern similar to that of graphitic carbon nitride and it is converted in the latter upon a second treatment at high temperature, or rather via chemical and ultrasonic exfoliation. Doing so, an extensive 2D structure similar to graphite is obtained, though the monolayer is quite difficult to obtain and employ. Indeed, the staked layers are only partially detached from each other by the treatments and then used as they are.



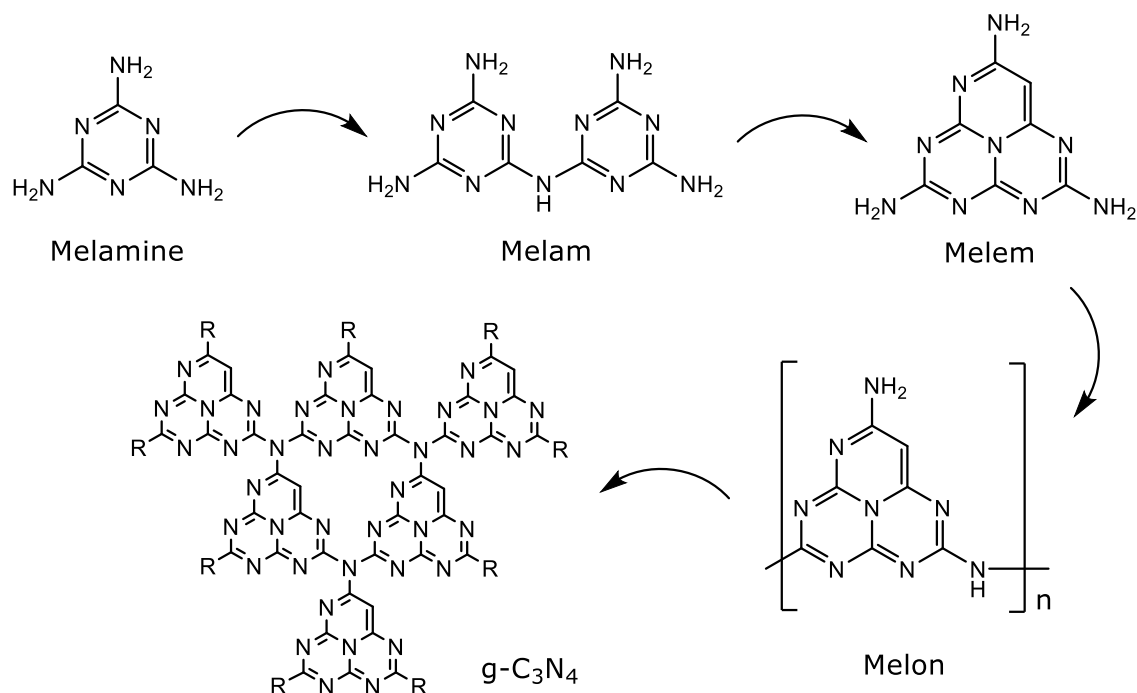


**Figure 1.6** Intermediates encountered during the thermal decomposition of melamine or other kind of precursor [51]

The main advantage of C<sub>3</sub>N<sub>4</sub> over TiO<sub>2</sub> is that the bulk material has a band gap between 2.7 and 2.9 eV, with a relative position that allows to perform the water splitting reaction [50,52]. Thanks to this narrow band gap and thermal and chemical stability, the carbon nitride was recognized as a good candidate for the development of photocatalytic processes under sunlight [50]. However, the low surface area of the bulk material, combined with the fast recombination of the charge carriers, limit its applicability as photocatalyst [50,53].

## References

1. Rockström, J.; Steffen, W.; Noone, K.; Persson, Å.; Chapin, F.S.; Lambin, E.F.; Lenton, T.M.; Scheffer, M.; Folke, C.; Schellnhuber, H.J.; et al. A safe operating space for humanity. *Nature* **2009**, *461*, 472–475, doi:10.1038/461472a.
2. Sheldon, R.A. Fundamentals of green chemistry: Efficiency in reaction design. *Chem. Soc. Rev.* **2012**, *41*, 1437–1451, doi:10.1039/c1cs15219j.
3. Apergis, N.; Payne, J.E. Renewable energy consumption and economic growth: Evidence from a panel of OECD countries. *Energy Policy* **2010**, *38*, 656–660, doi:10.1016/j.enpol.2009.09.002.
4. Tullo, A. Why the future of oil is in chemicals, not fuels. *Chem. Eng. News* **2019**, 97.
5. Hall, C.A.S.; Lambert, J.G.; Balogh, S.B. EROI of different fuels and the implications for society. *Energy Policy* **2014**, *64*, 141–152, doi:10.1016/j.enpol.2013.05.049.
6. Sonnberger, M.; Ruddat, M.; Arnold, A.; Scheer, D.; Poortinga, W.; Böhm, G.; Bertoldo, R.; Mays, C.; Pidgeon, N.; Poumadère, M.; et al. Climate concerned but anti-nuclear: Exploring (dis)approval of nuclear energy in four European countries. *Energy Res. Soc. Sci.* **2021**, *75*, 102008, doi:10.1016/j.erss.2021.102008.
7. Pimentel, D.; Patzek, T.W. Ethanol production using corn, switchgrass, and wood; Biodiesel production using soybean and sunflower. *Nat. Resour. Res.* **2005**, *14*, 65–76, doi:10.1007/s11053-005-4679-8.
8. <https://energy-charts.info/?l=en&c=DE>.
9. Green, M.A.; Emery, K. Solar cell efficiency tables (version 3). *Prog.*

- Photovoltaics Res. Appl.* **1994**, 2, 27–34, doi:10.1002/pip.4670020105.
10. Ritchie, H.; Roser, M. Energy. *Our World Data* **2020**, Accessed on 19/07/2022, Available at <https://ourworldindata.org/energy>.
  11. Bhatia, S.C. Solar radiations. In *Advanced Renewable Energy Systems*; Elsevier, 2014; pp. 32–67.
  12. Winter, M.; Brodd, R.J. What Are Batteries, Fuel Cells, and Supercapacitors? *Chem. Rev.* **2004**, 104, 4245–4270, doi:10.1021/cr020730k.
  13. Götz, M.; Lefebvre, J.; Mörs, F.; McDaniel Koch, A.; Graf, F.; Bajohr, S.; Reimert, R.; Kolb, T. Renewable Power-to-Gas: A technological and economic review. *Renew. Energy* **2016**, 85, 1371–1390, doi:10.1016/j.renene.2015.07.066.
  14. Ursua, A.; Gandia, L.M.; Sanchis, P. Hydrogen Production From Water Electrolysis: Current Status and Future Trends. *Proc. IEEE* **2012**, 100, 410–426, doi:10.1109/JPROC.2011.2156750.
  15. Roth, H.D. The Beginnings of Organic Photochemistry. *Angew. Chemie Int. Ed. English* **1989**, 28, 1193–1207, doi:10.1002/anie.198911931.
  16. Melchionna, M.; Fornasiero, P. Updates on the Roadmap for Photocatalysis. *ACS Catal.* **2020**, 10, 5493–5501, doi:10.1021/acscatal.0c01204.
  17. Zhu, S.; Wang, D. Photocatalysis: Basic principles, diverse forms of implementations and emerging scientific opportunities. *Adv. Energy Mater.* **2017**, 7, 1700841, doi:10.1002/aenm.201700841.
  18. Nguyen, V.H.; Nguyen, B.S.; Jin, Z.; Shokouhimehr, M.; Jang, H.W.; Hu, C.; Singh, P.; Raizada, P.; Peng, W.; Shiung Lam, S.; et al. Towards artificial photosynthesis: Sustainable hydrogen utilization for photocatalytic reduction of CO<sub>2</sub> to high-value renewable fuels. *Chem. Eng. J.* **2020**, 402, 126184,

doi:10.1016/j.cej.2020.126184.

19. Saravanan, R.; Gracia, F.; Stephen, A. Basic Principles, Mechanism, and Challenges of Photocatalysis. In; 2017; pp. 19–40.
20. Xie, S.; Zhang, Q.; Liu, G.; Wang, Y. Photocatalytic and photoelectrocatalytic reduction of CO<sub>2</sub> using heterogeneous catalysts with controlled nanostructures. *Chem. Commun.* **2016**, 52, 35–59, doi:10.1039/c5cc07613g.
21. Malato-Rodríguez, S. Solar Detoxification and Disinfection. *Encycl. Energy* 2004, 587–596.
22. Tan, H.L.; Abdi, F.F.; Ng, Y.H. Heterogeneous photocatalysts: An overview of classic and modern approaches for optical, electronic, and charge dynamics evaluation. *Chem. Soc. Rev.* **2019**, 48, 1255–1271, doi:10.1039/c8cs00882e.
23. Yamada, Y.; Kanemitsu, Y. Determination of electron and hole lifetimes of rutile and anatase TiO<sub>2</sub> single crystals. *Appl. Phys. Lett.* **2012**, 101, 133907, doi:10.1063/1.4754831.
24. Vequizo, J.J.M.; Matsunaga, H.; Ishiku, T.; Kamimura, S.; Ohno, T.; Yamakata, A. Trapping-Induced Enhancement of Photocatalytic Activity on Brookite TiO<sub>2</sub> Powders: Comparison with Anatase and Rutile TiO<sub>2</sub> Powders. *ACS Catal.* **2017**, 7, 2644–2651, doi:10.1021/acscatal.7b00131.
25. Serpone, N. Relative photonic efficiencies and quantum yields in heterogeneous photocatalysis. *J. Photochem. Photobiol. A Chem.* **1997**, 104, 1–12, doi:10.1016/S1010-6030(96)04538-8.
26. Humayun, M.; Raziq, F.; Khan, A.; Luo, W. Modification strategies of TiO<sub>2</sub> for potential applications in photocatalysis: A critical review. *Green Chem. Lett. Rev.* **2018**, 11, 86–102, doi:10.1080/17518253.2018.1440324.

27. Rachman, T. *Mineral Commodity Summaries 2022. Diatomite*; 2022;
28. Zhang, J.; Zhou, P.; Liu, J.; Yu, J. New understanding of the difference of photocatalytic activity among anatase, rutile and brookite TiO<sub>2</sub>. *Phys. Chem. Chem. Phys.* **2014**, *16*, 20382–20386, doi:10.1039/c4cp02201g.
29. Allen, N.S.; Mahdjoub, N.; Vishnyakov, V.; Kelly, P.J.; Kriek, R.J. The effect of crystalline phase (anatase, brookite and rutile) and size on the photocatalytic activity of calcined polymorphic titanium dioxide (TiO<sub>2</sub>). *Polym. Degrad. Stab.* **2018**, *150*, 31–36, doi:10.1016/j.polymdegradstab.2018.02.008.
30. Fujishima, A.; Rao, T.N.; Tryk, D.A. Titanium dioxide photocatalysis. *J. Photochem. Photobiol. C Photochem. Rev.* **2000**, *1*, 1–21, doi:10.1016/S1389-5567(00)00002-2.
31. Fujishima, A.; Zhang, X. Titanium dioxide photocatalysis: present situation and future approaches. *Comptes Rendus Chim.* **2006**, *9*, 750–760, doi:10.1016/j.crci.2005.02.055.
32. Fujishima, A.; Honda, K. Electrochemical photolysis of water at a semiconductor electrode. *Nature* **1972**, *238*, 37–38, doi:10.1038/238037a0.
33. Zhang, Z.; Bai, L.; Li, Z.; Qu, Y.; Jing, L. Review of strategies for the fabrication of heterojunctional nanocomposites as efficient visible-light catalysts by modulating excited electrons with appropriate thermodynamic energy. *J. Mater. Chem. A* **2019**, *7*, 10879–10897, doi:10.1039/c9ta02373a.
34. Donald, V.B. Titanium Dioxide: Commodity Or Speciality? *Pigment Resin Technol.* **1994**, *23*, 10–15, doi:10.1108/eb043098.
35. Grande, F.; Tucci, P. Titanium Dioxide Nanoparticles: a Risk for Human Health? *Mini-Reviews Med. Chem.* **2016**, *16*, 762–769,

doi:10.2174/1389557516666160321114341.

36. Weng, B.; Qi, M.Y.; Han, C.; Tang, Z.R.; Xu, Y.J. Photocorrosion Inhibition of Semiconductor-Based Photocatalysts: Basic Principle, Current Development, and Future Perspective. *ACS Catal.* **2019**, *9*, 4642–4687, doi:10.1021/acscatal.9b00313.
37. Yan, H.; Wang, X.; Yao, M.; Yao, X. Band structure design of semiconductors for enhanced photocatalytic activity: The case of TiO<sub>2</sub>. *Prog. Nat. Sci. Mater. Int.* **2013**, *23*, 402–407, doi:10.1016/j.pnsc.2013.06.002.
38. Kang, X.; Liu, S.; Dai, Z.; He, Y.; Song, X.; Tan, Z. Titanium dioxide: From engineering to applications. *Catalysts* **2019**, *9*, 191, doi:10.3390/catal9020191.
39. Sandulescu, A.; Anastasescu, C.; Papa, F.; Raciulete, M.; Vasile, A.; Spataru, T.; Scarisoreanu, M.; Fleaca, C.; Mihailescu, C.N.; Teodorescu, V.; et al. Advancements on basic working principles of photo-driven oxidative degradation of organic substrates over pristine and noble metal-modified TiO<sub>2</sub>. Model case of phenol photo oxidation. *Catalysts* **2021**, *11*, 487, doi:10.3390/catal11040487.
40. Zielińska-Jurek, A. Progress, challenge, and perspective of bimetallic TiO<sub>2</sub>-based photocatalysts. *J. Nanomater.* **2014**, *2014*, 1–17, doi:10.1155/2014/208920.
41. Kavitha, R.; Kumar, S.G. Review on bimetallic-deposited TiO<sub>2</sub>: preparation methods, charge carrier transfer pathways and photocatalytic applications. *Chem. Pap.* **2020**, *74*, 717–756, doi:10.1007/s11696-019-00995-4.
42. Bagheri, S.; Muhd Julkapli, N.; Bee Abd Hamid, S. Titanium dioxide as a catalyst support in heterogeneous catalysis. *Sci. World J.* **2014**, *2014*, 1–21, doi:10.1155/2014/727496.

43. Si, Z.; Zhang, X.; Liu, Y.; Zhou, H.; Chen, X.; Yang, X.; Chen, H.; Zhan, J. Revisiting the preparation of titanium dioxide: aerosol-assisted production of photocatalyst with higher catalytic activity than P25. *J. Mater. Sci.* **2020**, *55*, 565–576, doi:10.1007/s10853-019-03950-6.
44. Ohtani, B.; Prieto-Mahaney, O.O.; Li, D.; Abe, R. What is Degussa (Evonic) P25? Crystalline composition analysis, reconstruction from isolated pure particles and photocatalytic activity test. *J. Photochem. Photobiol. A Chem.* **2010**, *216*, 179–182, doi:10.1016/j.jphotochem.2010.07.024.
45. Low, J.; Yu, J.; Jaroniec, M.; Wageh, S.; Al-Ghamdi, A.A. Heterojunction Photocatalysts. *Adv. Mater.* **2017**, *29*, 1601694, doi:10.1002/adma.201601694.
46. Xu, Q.; Zhang, L.; Yu, J.; Wageh, S.; Al-Ghamdi, A.A.; Jaroniec, M. Direct Z-scheme photocatalysts: Principles, synthesis, and applications. *Mater. Today* **2018**, *21*, 1042–1063, doi:10.1016/j.mattod.2018.04.008.
47. Khan, M.R.; Chuan, T.W.; Yousuf, A.; Chowdhury, M.N.K.; Cheng, C.K. Schottky barrier and surface plasmonic resonance phenomena towards the photocatalytic reaction: Study of their mechanisms to enhance photocatalytic activity. *Catal. Sci. Technol.* **2015**, *5*, 2522–2531, doi:10.1039/c4cy01545b.
48. Schukraft, G.E.M.; Moss, B.; Kafizas, A.G.; Petit, C. Effect of Band Bending in Photoactive MOF-Based Heterojunctions. *ACS Appl. Mater. Interfaces* **2022**, *14*, 19342–19352, doi:10.1021/acsami.2c00335.
49. Ren, K.; Zheng, R.; Yu, J.; Sun, Q.; Li, J. Band Bending Mechanism in CdO/Arsenene Heterostructure: A Potential Direct Z-scheme Photocatalyst. *Front. Chem.* **2021**, *9*, doi:10.3389/fchem.2021.788813.
50. Kessler, F.K.; Zheng, Y.; Schwarz, D.; Merschjann, C.; Schnick, W.; Wang, X.;

- Bojdys, M.J. Functional carbon nitride materials-design strategies for electrochemical devices. *Nat. Rev. Mater.* **2017**, *2*, 17030, doi:10.1038/natrevmats.2017.30.
51. Mamba, G.; Mishra, A.K. Graphitic carbon nitride (g-C<sub>3</sub>N<sub>4</sub>) nanocomposites: A new and exciting generation of visible light driven photocatalysts for environmental pollution remediation. *Appl. Catal. B Environ.* **2016**, *198*, 347–377, doi:10.1016/j.apcatb.2016.05.052.
52. Wang, X.; Maeda, K.; Thomas, A.; Takanabe, K.; Xin, G.; Carlsson, J.M.; Domen, K.; Antonietti, M. A metal-free polymeric photocatalyst for hydrogen production from water under visible light. *Nat. Mater.* **2009**, *8*, 76–80, doi:10.1038/nmat2317.
53. Wang, L.; Wang, K.; He, T.; Zhao, Y.; Song, H.; Wang, H. Graphitic carbon nitride-based photocatalytic materials: Preparation strategy and application. *ACS Sustain. Chem. Eng.* **2020**, *8*, 16048–16085, doi:10.1021/acssuschemeng.0c05246.



## 2. Experimental

### 2.1. Photocatalyst in form of powder

P25 is a commercial  $\text{TiO}_2$  photocatalysts composed of anatase and rutile phases and it is produced by Evonik, former Degussa, and supplied by EIGENMANN & VERONELLI S.p.A. It was used as a benchmark in our photocatalytic processes.

FSP- $\text{TiO}_2$  and FSP- $\text{WO}_3$  were prepared via flame spray pyrolysis (FSP) by using a home-made apparatus described elsewhere [1]. It is composed of a burner with a central hole surrounded by several flamelets fed with methane (0.5 L/min) and oxygen (1 L/min). In case of FSP- $\text{TiO}_2$ , the precursor solution is prepared dissolving titanium isopropoxide (Sigma Aldrich, 97%) in propionic acid (Sigma Aldrich, 99.5%) to obtain a 0.2 M solution. Then, it is pumped at 2.7 mL/min through a needle fixed in the central hole, where a co-current flow of oxygen (5 L/min) disperses the solution at the nozzle and creates small droplets which are rapidly vaporized and burned by the flame. The resulting powder deposits over the wall of a glass bell that is set over the burner plate, with an average yield of solid particles of 35%, with respect to the theoretical value. In order to obtain nanoparticles of the proper size, the pressure drop at the nozzle was set at 1.5 bar. FSP- $\text{WO}_3$  and the composite with  $\text{TiO}_2$  were obtained from ammonium metatungstate hydrate (Sigma Aldrich, 99.99%) and  $\text{Ti}(\text{iPrO})_4$  dissolved into dimethylformamide (DMF), as reported in Table 2.1. DMF was used as the only solvent even in case of the composite.

FSP- $\text{TiO}_2$ -PAL was prepared by using the same titanium isopropoxide dissolved into a 1:1 mixture of o-xylene (Sigma Aldrich, 97%) and propionic acid until reaching a 0.7M concentration.

**Table 2.1.** Composition of the precursor solution injected into the burner

Catalyst	Precursor	$\frac{W_{\text{precursor}}}{W_{\text{solvent}}}$ %	Solvent	W:Ti molar ratio	Yield (%)
FSP-WO <sub>3</sub>	(NH <sub>4</sub> ) <sub>6</sub> H <sub>2</sub> W <sub>12</sub> O <sub>40</sub>	3.0	DMF	/	≈35%
FSP-TiO <sub>2</sub> /WO <sub>3</sub> -60/40	(NH <sub>4</sub> ) <sub>6</sub> H <sub>2</sub> W <sub>12</sub> O <sub>40</sub> + Ti(iPrO) <sub>4</sub>	3.0 + 4.7	DMF	1:16.3	≈35%
FSP-TiO <sub>2</sub>	Ti(iPrO) <sub>4</sub>	5.7	Propionic acid	/	≈40%
FSP-TiO <sub>2</sub> -PAL	Ti(iPrO) <sub>4</sub>		(1:1) o-Xylene: Propionic acid	/	≈40%

TiO<sub>2</sub>-exCl was prepared at University of Palermo (Prof. Marci) via the hydrolysis of TiCl<sub>4</sub> as described previously [2]. In brief, titanium tetrachloride (Fluka, 98%) was added to distilled water (TiCl<sub>4</sub>/H<sub>2</sub>O 1:10 vol/vol) at room temperature. After 12 h of stirring, the solution was boiled for 0.5 h under vigorous stirring obtaining a milky white TiO<sub>2</sub> dispersion that was dried under vacuum at 50 °C to recover the solid.

Monometallic photocatalysts (0.36%wt. Au, 0.36%wt. Pt, 0.1%mol Ag, 0.1%mol Pd) were prepared by wet impregnation. Briefly, the desired amount of metal precursor is dissolved in distilled water. Then, in a round flask, it is added under stirring to a water dispersion of titania P25 (Table 2.2). The suspension was stirred for 2h and then the solvent was removed via evaporation under reduced pressure. The resulting powder was collected and dried overnight into an oven (105 °C) and then either reduced to metallic form or activated in a tubular oven at the selected temperature (Table 2.2), according to preliminary Temperature Programmed Reduction (TPR) experiments.

Bimetallic photocatalysts (Au<sub>x</sub>Pt<sub>y</sub>) were prepared via a two-step sol immobilization by the group of Prof. Laura Prati at University of Milan. Au/TiO<sub>2</sub> was prepared by

dissolution of  $\text{NaAuCl}_4 \cdot 2\text{H}_2\text{O}$  and Polyvinyl alcohol (PVA) solution (Au/PVA 1:0.5, w/w) to 100 mL of distilled water. After several minutes,  $\text{NaBH}_4$  (Au/ $\text{NaBH}_4$  1:4 mol/mol) was added to the mixture under vigorous stirring and reddish  $\text{Au}^0$  colloids were quickly formed, then it was immobilized by addition of titania P25 and concentrated sulfuric acid dropwise (pH 2). The catalyst was filtered, washed three times with distilled water and dried at  $80^\circ\text{C}$  for 4 h. The so synthesized Au/ $\text{TiO}_2$  powder was dispersed again in 100 mL of distilled water and a  $\text{Na}_2\text{PtCl}_6$ /PVA solution was added under stirring. Then hydrogen was bubbled (50 mL/min) under atmospheric pressure and at room temperature into the suspension and after 2 h, the slurry was filtered, and the catalyst was washed several times with distilled water and dried overnight. 1%wtAu<sub>6</sub>Pt<sub>4</sub>/P25 and 1%wtAu<sub>8</sub>Pt<sub>2</sub>/P25 were prepared in that way.

**Table 2.2.** Conditions adopted for the synthesis of photocatalysts via wetness impregnation and sol immobilization

Wetness Impregnation					
Precursor	Final loading (%wt)	Ramp ( $^\circ\text{C}/\text{min}$ )	Dwell time (min)	$\text{H}_2$ or air flow (mL/min)	Reduction T ( $^\circ\text{C}$ )
$\text{AuCl}_3$	0.36	5.0	180	$\text{H}_2$ 30	700
$\text{Pt}(\text{acac})_2$	0.36	5.0	180	$\text{H}_2$ 30	800
$\text{AuCl}_3$	1	5.0	180	Air 30	400
$\text{Pt}(\text{acac})_2$	1	5.0	180	Air 30	400
$\text{AgNO}_3$	1.0	5.0	180	30	150
$\text{AuCl}_3$	0.1	5.0	180	30	700
$\text{Pd}(\text{NO}_3)_2 \cdot 2\text{H}_2\text{O}$	0.1	5.0	180	30	300

Sol immobilization			
Catalyst	Precursor	Final loading (%wtAu+Pt)	Molar ratio
1% wtAu <sub>6</sub> Pt <sub>4</sub> /P25	NaAuCl <sub>4</sub> +		
	Na <sub>2</sub> PtCl <sub>6</sub>	0.61; 0.39	6:4
1% wtAu <sub>8</sub> Pt <sub>2</sub> /P25	NaAuCl <sub>4</sub> +		
	Na <sub>2</sub> PtCl <sub>6</sub>	0.79; 0.21	8:2

Graphitic carbon nitride was synthesised by controlled thermal decomposition of melamine (Table 2.3). About 4 g of melamine (Sigma Aldrich, 99%) are placed in a quartz crucible and decomposed in a tubular oven at high temperature (1°C/min heating ramp, 4h at 550°C or 600°C, 1°C/min cooldown) and air flow (30 mL/min). The so-formed yellow powder (bulk C<sub>3</sub>N<sub>4</sub>) is collected and grinded in a mortar. The exfoliation is carried out via sonication treatment (Table 2.3). 500 mg of bulk C<sub>3</sub>N<sub>4</sub> is added to an open-top glass reactor and stirred with 200 mL of distilled water (2.5 g/L), then, the probe that generates the ultrasound (Sonix, GEX500, Newtown, USA) is placed inside the mixture and the instrument is turned on (5h, 3s pulse, 2s rest, 0.32-1.3 MJ, 40% amplitude). The solution is then filtered and washed with distilled water three times and dried overnight at 105°C.

g-C<sub>3</sub>N<sub>4</sub>/WO<sub>3</sub> composites were prepared via precipitation assisted by ultrasound (Table 2.4). The selected amount of exfoliated carbon nitride (120W) and ammonium tungstate (Sigma Aldrich, 99.99%) precursor were added to 200 mL of distilled water under stirring and heated up to 80°C for 1h, then HNO<sub>3</sub> (Sigma Aldrich, 65%) was added dropwise until a pH below 3 was reached and the solution was sonicated (15 minutes, 0.54 MJ, 40% amplitude). The resulting mixture was stirred for 3h at 80°C and filtered and washed three times with distilled water. The collected powder was then annealed in a tubular oven at

450°C for 4h (5°C/min ramp) and under nitrogen flow (30 mL/min). With these procedures we prepared samples with nominal weight-to-weight ratio of 10%, 20%, 30% and 40%.

Graphitic carbon nitride from University of Palermo was still prepared via thermal condensation of melamine by placing 10g of it in a covered ceramic crucible and heated by 2 °C min<sup>-1</sup> up to 520 °C [3]. After maintaining this temperature for 2 h the oven was slowly cooled down. The resulted yellow powder underwent a successive heating treatment in order to obtain a thermo-exfoliated material showing an increased specific surface area with respect to the native sample. The obtained yellow g-C<sub>3</sub>N<sub>4</sub> was heated in a static air atmosphere at 520°C at 3°C min<sup>-1</sup> and maintained for 2 h at the final temperature before being cooled down. The resulted pale-yellow powder was labelled as C<sub>3</sub>N<sub>4</sub>-TE.

Binary materials composed of C<sub>3</sub>N<sub>4</sub>-TE and TiO<sub>2</sub> P25 or TiO<sub>2</sub>-exCl were prepared by mechanically mixing both components in a planetary ball mill (Retsch PM 100 CM, Haan, Germany). For that aim, 2 g of C<sub>3</sub>N<sub>4</sub>-TE were mixed up with 6 g of P25 or TiO<sub>2</sub>-exCl. The mixture was placed in a zirconia jar equipped with zirconia balls of 1 cm diameter. The mixture was rotated at 250 rpm for 1 hour inside of the planetary mill. The two composited were labelled as P25/TE and TiO<sub>2</sub>-exCl/TE.

**Table 2.3.** Receipts for the preparation of C<sub>3</sub>N<sub>4</sub>

Synthesis					
Precursor	Ramp (°C/min)	Dwell time (min)	Air flow (mL/min)	Calcination T (°C)	Yield (%)
Melamine	1.0	240	30	550	14
Melamine	1.0	240	30	600	14

Precursor	Exfoliation				Photocatalyst code
	Weight (mg)	Water volume (mL)	Exf. energy (MJ)	Time (h)	
C <sub>3</sub> N <sub>4</sub> -550	200	200	0.32	5	C <sub>3</sub> N <sub>4</sub> -550-30W
C <sub>3</sub> N <sub>4</sub> -550	200	200	0.65	5	C <sub>3</sub> N <sub>4</sub> -550-60W
C <sub>3</sub> N <sub>4</sub> -550	200	200	0.97	5	C <sub>3</sub> N <sub>4</sub> -550-90W
C <sub>3</sub> N <sub>4</sub> -550	200	200	1.30	5	C <sub>3</sub> N <sub>4</sub> -550-120W
C <sub>3</sub> N <sub>4</sub> -600	200	200	0.32	5	C <sub>3</sub> N <sub>4</sub> -600-120W

**Table 2.4.** Receipts for the preparation of C<sub>3</sub>N<sub>4</sub>/WO<sub>3</sub> composites

Precursor	Weight (g)	Support	Weight (g)	w/w %	Yield (%)
(NH <sub>4</sub> ) <sub>10</sub> H <sub>2</sub> (W <sub>2</sub> O <sub>7</sub> ) <sub>6</sub>	0.34	C <sub>3</sub> N <sub>4</sub> -550-120W	0.25	10	80%
(NH <sub>4</sub> ) <sub>10</sub> H <sub>2</sub> (W <sub>2</sub> O <sub>7</sub> ) <sub>6</sub>	0.68	C <sub>3</sub> N <sub>4</sub> -550-120W	0.25	20	80%
(NH <sub>4</sub> ) <sub>10</sub> H <sub>2</sub> (W <sub>2</sub> O <sub>7</sub> ) <sub>6</sub>	1.01	C <sub>3</sub> N <sub>4</sub> -550-120W	0.25	30	80%
(NH <sub>4</sub> ) <sub>10</sub> H <sub>2</sub> (W <sub>2</sub> O <sub>7</sub> ) <sub>6</sub>	1.35	C <sub>3</sub> N <sub>4</sub> -550-120W	0.25	40	80%

## 2.2. Immobilized photocatalysts

Titania and its modified compounds were deposited over glass tiles (26x76x1 mm) via a home-made dip coating apparatus (Figure 2.1) that allows to process up to six samples at the same (Figure 2.2). A typical immobilization experiment consists of the immersion of the glass tile(s) at the selected speed and by means of a step motor equipped with reducing gears. The solution is prepared by addition of the selected amount of titania P25 (*e.g.* 40 g into 500 mL), HCl (Sigma Aldrich, 37%) or NaOH (Sigma Aldrich, 98%), emulsion stabilizer (Disperbik®) and distilled water. The temperature and stirring of the solution were controlled by a stirring and heating plate. After the deposition, the samples were then extracted at the same speed and placed in a muffle at the selected temperature (400-

550 °C) for 3 h. Table 2.5 illustrates the results obtained by varying one or more parameters.

Co-catalyst deposition was performed with the same apparatus. The TiO<sub>2</sub>-deposited tiles were immersed again in the solution of metal precursor (*e.g.* AgNO<sub>3</sub>, CuSO<sub>4</sub>, etc.) at the selected concentration and then dried overnight in a conventional oven (105 °C) before the reduction step in a tubular oven at high temperature and under hydrogen atmosphere. Typical reduction conditions were 30 mL/min H<sub>2</sub> flow, 5°C/min heating ramp, 180 minutes of dwell time at 150 °C (Ag) or 500 °C (Cu).

**Table 2.5.** Collection of result about the photocatalyst immobilization over glass by dip coating technique

Effect of treatment					
Treatment	N° cycle	Loading (mg)	Min (mg)	Max (mg)	Loading (mg)/Cycle
unwashed	1	0.0	/	/	0.0
unwashed	1	0.7	0.6	0.8	0.7
unwashed	2	0.9	0.5	1.2	0.5
piranha+Na <sub>2</sub> CO <sub>3</sub>	1	0.1	/	/	0.1
piranha+Na <sub>2</sub> CO <sub>3</sub>	2	4.8	4.2	5.4	2.4
piranha+Na <sub>2</sub> CO <sub>3</sub>	3	2.2	0.9	4.1	0.7
piranha+Na <sub>2</sub> CO <sub>3</sub>	6	5.5	1.1	14.4	0.9
brush	1	6.3	4.0	8.6	6.3
Effect of cycles number					
N° cycle	Glass #1 (mg)	Glass #2 (mg)	Glass #3 (mg)	Glass #4 (mg)	Av. loading (mg)
1	0.7	0.6	1.2	0.4	0.7
2	0.3	1.2	1	0.5	0.8
3	0.4	0.7	0.7	0.5	0.6
4	0.5	0.6	0.3	0.6	0.5

5	1.3	1.8	1.2	0.6	1.2
6	0.4	0.2	0.8	0.2	0.4
Total	3.6	5.1	5.2	2.8	4.2
<b>Effect of parameters (2 cycles)</b>					
<b>Temp (°C)</b>	<b>pH</b>	<b>Acid/base</b>	<b>Av. loading (mg)</b>	<b>Min (mg)</b>	<b>Max (mg)</b>
20	7	/	1.5	0.9	2.2
30	7	/	1.8	0.9	3.7
50	7	/	2.8	1.6	4.1
50	3	HCl	3.6	2.7	4.9
50	3	HNO <sub>3</sub>	4.0	2.8	5.3
50	12	NH <sub>3</sub>	3.1	1.4	10.7
<b>Final optimization</b>					
<b>%w/w</b>	<b>pH</b>	<b>N° cycle</b>	<b>Av. loading (mg)</b>	<b>Min (mg)</b>	<b>Max (mg)</b>
5	7	2	3.6	2.7	4.9
5	7	3	4.8	2.6	6.4
5	7	4	8.2	7.5	9.3
5	7	5	9.9	9.1	10.7
5	7	6	10.7	9.9	11.5
<b>Effect of TiO<sub>2</sub> concentration (w/ Disperbik®)</b>					
<b>%w/w</b>	<b>pH</b>	<b>N° cycle</b>	<b>Av. loading (mg)</b>	<b>Min (mg)</b>	<b>Max (mg)</b>
5.1	7	2	2	1.0	3.1
10	7	2	4.3	3.4	5.2
15.5	7	2	12.6	6	22.9
25.3	7	2	100.6	89.1	112.8
15.2	7	1	4.3	2.7	6.9
13.7	7	1	7.2	4.8	10



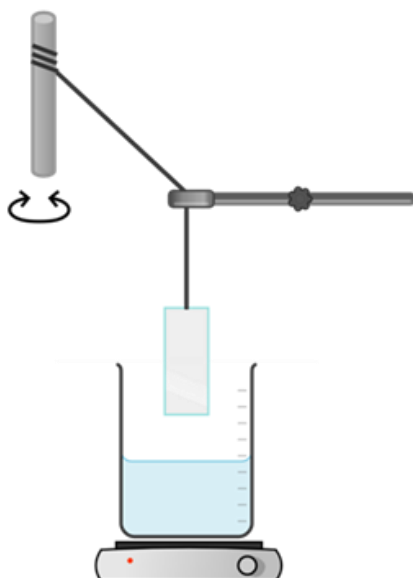


**Figure 2.1.** Schematic representation of the dip coating apparatus



**Figure 2.2.** Plastic holder used to impregnate up to six glasses at the same time

### 2.3. Materials characterization

X-ray diffraction (XRD) analyses were performed by the Rigaku Miniflex-600 horizontal-scan powder diffractometer (Tokyo, Japan) using Cu-K $\alpha$  radiation with a graphite monochromator on the diffracted beam. Crystallite size was calculated according to Scherrer equation (1).

$$(1) \quad D = (K \cdot \lambda) / (\beta \cdot \cos\theta)$$

where  $D$  is the crystal size,  $\lambda$  is the X-ray wavelength (0.154 nm with Cu K $\alpha$  generator),  $K$  is the shape factor (0.9),  $\beta$  is the width at half maximum of the peak (*i.e.* FWHM) and  $\theta$  is the Bragg angle.

N<sub>2</sub> adsorption and desorption isotherms of samples were measured with a Micromeritics ASAP2020 apparatus (Norcross, GA, USA). The BET SSA (Brunauer-Emmett-Teller Specific Surface Area) and pore volume was calculated from N<sub>2</sub> adsorption/desorption isotherms, collected at -196°C for the samples previously outgassed at 150 °C for 4h. Micropore volume was calculated according to the t-plot method. Brunauer-Emmett-Teller (BET) linearization was used in the range 0.05–0.30  $p/p^\circ$  to calculate the specific surface area ( $SSA_{BET}$ ). Barrett-Joyner-Halenda model (BJH) was used to determine pore-size distribution from the desorption branch.

Diffuse Reflectance (DR) UV-Vis spectra of samples were recorded on a Shimadzu UV-3600 Plus (Kyoto, Japan) in the range of 200-800 nm, using an integrating sphere and BaSO<sub>4</sub> as reference standard. The results were processed according to the Kubelka-Munk theory and using the Equation (2), using the reflectance spectra as input data a [4].

$$(2) \quad F(R_\infty) = (1 - R_\infty)^2 / 2R_\infty$$

$(F(R)h\nu)^{1/r}$  (with  $r = 2$  or  $1/2$  for direct and indirect band gap) was plotted versus  $h\nu$  to obtain the band gap of each sample [5].

Scanning Electron Microscopy (SEM) images and Energy Dispersive X-ray Analysis (EDX) spectra were obtained using a JSM-7900F Schottky Field Emission Scanning Electron Microscope (JEOL, Tokyo, Japan) operating at an accelerating potential of 20kV.

Absolute photoluminescence quantum yields,  $\Phi$ , were measured using a C11347 Quantaaurus Hamamatsu Photonics K.K spectrometer, equipped with a 150 W Xenon

lamp, an integrating sphere and a multichannel detector. Steady state and time-resolved fluorescence data were recorded with a FLS980 spectrofluorometer (Edinburg Instrument)

X-ray photoelectron spectroscopy (XPS) measurements were carried out on a VG Scienta SES 2002 spectrometer (Uppsala, Sweden) equipped with a monochromatic Al K $\alpha$  X-ray source (Al K $\alpha$  = 1486.6 eV) and a hemispherical analyzer (Uppsala, Sweden).

Thermogravimetric analysis was performed on Perkin Elmer TGA-7 (Waltham, Massachusetts) apparatus and under air.

## **2.4. Experimental setup for activity testing**

### **2.4.1. Photoreduction of CO<sub>2</sub>**

Photocatalytic activity tests were carried out thanks to an innovative pressurized batch photoreactor [6]. In summary, it is a stainless-steel cylinder-shaped reactor equipped with a quartz window, which allows the introduction of a coaxial lamp, and double-jacketed to better manage the temperature by recirculating water at the desired temperature (80°C, typically). The reactor is designed to operate under pressures up to 20 bar. Its internal volume is *ca.* 1.3 L, while 1.2 L of solution were used for each experiment and 0.1 L head space was left for gas accumulation and sampling. Catalyst dispersion is ensured by a magnetic stirrer set at 400 rpm and placed under the reactor. The photon source is a medium-pressure 250 W Hg vapor lamp made of two bulbs, which emits in the range of 254–364 nm. The measured average irradiance was 120 W/m<sup>2</sup> and was checked regularly by means of a photo-radiometer equipped with the prepper probe (delta OHM HD 2102.2, LP471UVA probe active in the 315-400 nm region). The optimal catalyst concentration

and catalyst/HS ratio was found in a previous work and resulted 31 mg/L and 18.6 mg<sub>cat</sub>/g<sub>HS</sub>, respectively [7].

Na<sub>2</sub>SO<sub>3</sub> (Sigma Aldrich 98%) was the main hole scavenger used and negligible CO<sub>2</sub> photoreduction has been observed without its addition. Other HSs tested were NH<sub>3</sub> (Sigma Aldrich 30%), urea (Sigma Aldrich 99%), thiourea (Sigma Aldrich 99%), 1-propanol (Sigma Aldrich 99%), 2-propanol (Sigma Aldrich 99.5%), glycerol (Sigma Aldrich 99.5%), ethylene glycol (Sigma Aldrich 99%), ethanol (Sigma Aldrich 99.8%), methanol (Sigma Aldrich 99.8%), 2-butanol (Sigma Aldrich 99.5%), acetone (Sigma Aldrich 99.5%), acetic acid (Sigma Aldrich 99.7%), triethylamine (Sigma Aldrich 99.5%), triethanolamine (Sigma Aldrich 98%) and tripropylamine (Sigma Aldrich 98%). In general, the catalyst and the HS were loaded with distilled water and the solution was saturated with CO<sub>2</sub> at the desired pressure and room temperature for one night, then the temperature and the pressure were adjusted according to the needs. The reaction starts when the lamp is switched on. All of the reported results were collected either after 24h or 6 h irradiation, as long tests allow to observe both liquid and gaseous products, while short ones do not fully consume the HS and almost only liquid products are detected. Both gas and liquid samples are taken at the beginning and at the end of the test thanks to two sampling ports mounted on the reactor. The liquid products were analyzed via a high-performance liquid chromatography (HPLC) instrument (LC-4000 series, Jasco) equipped with the proper column (2000–0 BP-OA, Benson Polymeric) and both UV (UV-4074, Jasco) and refractive index (RI-4030, Jasco) detectors have been used. The gas products were analyzed by a gas chromatograph (7820, Agilent, Palo Alto, CA, USA) equipped with a TCD detector with the proper set of configurations for the quantification of H<sub>2</sub>, CH<sub>4</sub>, and both polar and nonpolar light gases. Each test was reproducible within a

10% margin of error at maximum, as very small amount of photocatalysts were used and the proper mixing of the solution was challenging. The  $\text{Na}_2\text{SO}_4$  conversion was determined by means of iodometric titration: a selected amount of sample was mixed with a precise amount of potassium iodate water solution, then potassium iodide and diluted hydrochloric acid were added in excess. This mixture led to the production of free iodine, which was then titrated with sodium thiosulfate. All the other scavengers were analyzed by means of the same HPLC system aforementioned.

#### **2.4.2. Photoreforming of carbohydrate**

The same stainless steel photoreactor was employed. The optimal catalyst concentration and catalyst/glucose ratio was found in a previous work [8]. Negligible productivity was observed without addition of glucose or other sugars. All of the reported results were collected after 5h of irradiation. Both gas and liquid samples are taken at the beginning and at the end of the process thanks to two sampling ports mounted on the reactor. The liquid products were analyzed via a high-performance liquid chromatography equipped with the proper column (2000–0 BP-OA, Benson Polymeric) and both UV and refractive index detectors, have been used. This system also allowed for to compute the glucose conversion. The gas products were analyzed via a gas chromatograph equipped with a TCD detector with the proper set of configurations for the quantification of  $\text{H}_2$ ,  $\text{CH}_4$ , and both polar and nonpolar light gases. Each test was reproducible within a 10% margin of error at maximum, as very small amount of photocatalysts were used and the proper mixing of the solution was challenging. A more accurate glucose or sugars conversion was assessed through chemical oxygen demand (COD) and total organic carbon (TOC) analysis.

In case of COD, 5 mL of sample was mixed with 5 mL of  $\text{K}_2\text{Cr}_2\text{O}_7$  (Sigma Aldrich, 99%) water solution (0.18M) and 5.5 mL of concentrated sulfuric acid (Sigma Aldrich, 98%), then all the test tubes were digested in a bath oil at 130°C for 30 minutes. A blank sample was prepared with distilled water instead of the sample. A color shift from orange to green indicates the reduction of  $\text{Cr}^{6+}$  to  $\text{Cr}^{3+}$  ions. Then, the tubes were cooled to room temperature and the content diluted with distilled water in a volumetric flask (200 mL) and analyzed twice in a Perkin Elmer Lambda 35 double ray UV-Vis Spectrophotometer at 605 nm (upon proper calibration).

Also, a Shimadzu TOC-L CSH/CPH was used to test 50 ml aliquots of a 1:20 diluted sample prepared from the one withdrawn from the reactor. This was injected onto a platinum catalyst at 680°C in an oxygen rich atmosphere. Ultra-high purity air carrier gas transports the produced  $\text{CO}_2$  through a moisture trap and halide scrubbers to remove water vapor and halides from the gas stream, before it reaches the detector, to avoid possible interferences. A non-dispersive infrared (NDIR) detector is then used to measure the concentration of the generated  $\text{CO}_2$ .

The two simulated wastewater here employed are Black Kraft Liquor, which is rich of organic acids, and Spent Sulfite Liquor, rich of sugars. The compositions are reported in Table 2.6 and Table 2.7, however, some molecules were used in place of others, for instance, glucose and mannose are epimers so the concentration of the first one was actually increased to include also the latter.

**Table 2.6.** Composition of simulated wastewater – Black Kraft Liquor

<b>Black Kraft Liquor</b>					
<b>Real liquor composition</b>		<b>Liquor modeling</b>		<b>Representative solution</b>	
<b>Acids</b>	<b>Concentration</b>	<b>Model</b>	<b>m<sub>chemical</sub>/kg<sub>solution</sub></b>	<b>%</b>	<b>m<sub>chemical</sub>/g</b>
	<b>m<sub>chemical</sub>/kg<sub>solution</sub></b>	<b>chemical</b>			
glycolic	25	glycolic	25	12	2.16
lactic	25	lactic	25	12	2.16
3,4-dideoxypentoic	10	/	/	/	/
glucoisosaccarinic	35	gluconic	35	17	3.1
2-hydroxybutanoic	60	tartaric	60	30	5.4
3-deoxypentoic	10	/	/	/	/
xyloisosaccarinic	25	xylonic*	25	12	2.16
Others	40	levulinic	40	17	3.1
Total	230	Total	210	100	18.08

\*D-xylono-1,4-lactone

**Table 2.7.** Composition of simulated wastewater – Spent Sulfite Liquor

<b>Spent Sulfite Liquor</b>					
<b>Real liquor composition</b>		<b>Liquor modeling</b>		<b>Representative solution</b>	
<b>Sugars</b>	<b>Concentration</b>	<b>Model</b>	<b>m<sub>chemical</sub>/kg<sub>solution</sub></b>	<b>%</b>	<b>m<sub>chemical</sub>/g</b>
	<b>m<sub>chemical</sub>/kg<sub>solution</sub></b>	<b>chemical</b>			
arabinose	10	arabinose	10	2.7	0.5
xylose	60	xylose	60	16.3	2.94
mannose	120	glucose	210	56.5	10
glucose	40	glucose	/	/	/
galactose	50	glucose	/	/	/
aldonic acids	50	gluconic acid	50	13.5	2.5
acetic acid	40	acetic acid	40	11	2.0
Total	370	Total	370	1	18

### 2.4.3. Photocatalytic test with immobilized photocatalyst

Photoreduction of CO<sub>2</sub> and photoreforming of glucose tests using immobilized photocatalyst were performed in the same conditions as in case of photocatalyst in form of powder and by using the high-pressure stainless-steel photoreactor. Twelve glass slides, placed on two levels, were mounted vertically along the lamp axis so each set of six glasses was centred on one of the two lamp bulb (Figure 2.3). The samples were fixed on a custom 3D-printed support made of different materials, such as polylactic acid (PLA), polyacrylonitrile-butadiene-styrene (ABS) and polypropylene reinforced with glass fibres (PPG). The products were analysed by the same technique (HPLC and GC) as well.

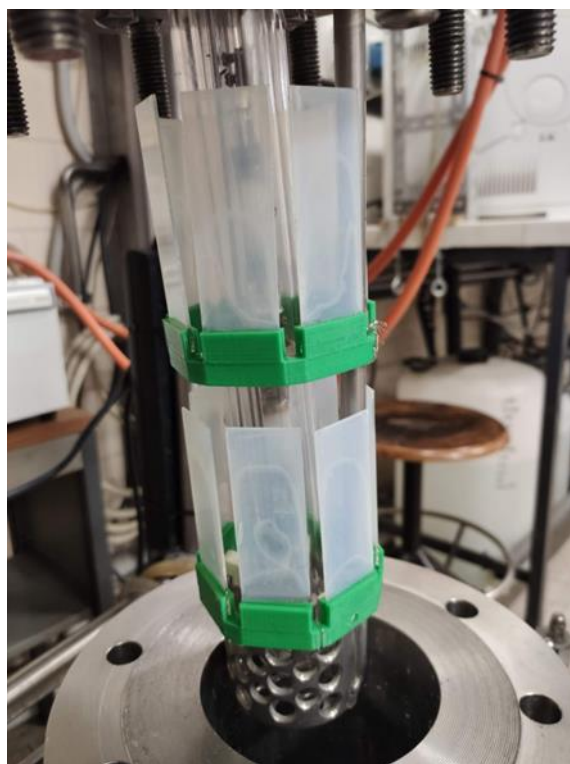


**Figure 2.3.** Custom 3D-printed support made of ABS. The support is anchored to a shaft that flanks the quartz sleeve containing the lamp.



#### 2.4.4. Photo abatement of pollutants

Diclofenac sodium salt (Sigma Aldrich, reference standard), Erythromycin (Sigma Aldrich, reference standard), Acid Orange 7 (Sigma Aldrich, 95%), Bromophenol blue (Sigma Aldrich, 95%), Amoxicillin (Sigma Aldrich, reference standard) and the other reagents such as H<sub>2</sub>O<sub>2</sub> (Sigma Aldrich, 35% v/v), iron sulfate (Sigma Aldrich, 99%), etc. were used without further purification.

Two kinds of setup were employed for this study. A small cylindrical glass reactor with a volume up to 400 mL was used in combination with an immersion lamp (Reactor B, Figure 2.4), which was fixed on the reactor cap and allowed for an efficient irradiation of the solution. The three lamps used there were (i) UVA mercury lamp (Jelosil HG 200W L, 250 W, 116 W/m<sup>2</sup>, 365 nm peak emission), (ii) UVA-LED lamp constituted of 9 emitters (Suntech 48W, 36 W/m<sup>2</sup>, 365 nm) and (iii) a visible LED lamp (Lite-On LTPL-C034UVH430, 430 nm, 1W radiant flux each LED, 12 LEDs) that emits in the blue region. The second reactor (Reactor A) has the same shape, but it is much wider and can be filled with up to 3000 mL of solution. In that case, the lamp is fixed on the top of the reactor and the irradiation occurs externally, such as in case of UV spotlight (Jelosil HG 100 AS, 125 W, 260 W/m<sup>2</sup>, 365 nm peak emission), LED visible spotlight (Yonkers, 30 W, 2700 lumen) and natural sunlight. Both the reactors were cooled down to ambient temperature by recirculating water in the external jacket, while the proper mixing of the solution was ensured by a magnetic stirrer and the temperature was monitored by means of a thermocouple connected to a display.

UV lamps performance was checked with a photo-radiometer (delta OHM HD 2102.2, LP471UVA probe active in the 315-400 nm region) and sunlight irradiance data were collected from ARPA website [9].

For each test, the selected amount of catalyst, photocatalyst and/or oxidant were added to the reactor filled with the solution of pollutant at the selected concentration, then the pH was adjusted by addition of the minimum amount of NaOH or HCl concentrated solutions (1M) and checked with pHmeter (model AMEL Instruments, Mod 2335). The solution was let to equilibrate for 30 minutes to allow the pollutant to adsorb over the photocatalyst, then, a sample is withdrawn ( $t_0$ ) and the lamp is switched on to start the reaction (Fenton reaction starts with  $H_2O_2$  addition). The reactor and the lamp are surrounded by a wood box that prevents the ambient light from entering the system.

The conversion of the pollutant was followed by means of UV-Visible analysis (Perkin Elmer Lambda 35) performed on 3 mL of the solution withdrawn from the reactor at regular intervals of time and filtered over acetate cellulose filter (0.20  $\mu m$ ) in order to remove solid particles and colloids. The concentrations were recalculated to take into account the evaporation of the solution, which was as high as 1 mL per hour when using the Reactor A. The analytical wavelenght used to determine the concentration of the selected pollutant were 278 nm (DCF), 285 nm (ERY), 486 nm (AO7) and 441 nm (BPB). A calibration curve at that wavelenght was obtained for each pollutant using  $N=5$  solutions in the range 5-100 ppm. Amoxicilline was analyzed via high pressure liquid chromatography (LC-4000 series, Jasco, Japan) using the proper column (2000–0 BP-OA, Benson Polymeric) column in combination with refractive index detector (RI-4030, Jasco). Samples eligible for toxicity test were also analysed through the Total Organic Carbon (TOC) technique to assess the presence of partially oxidated intermediates. Few millilitres of the starting solution and the processed product were filtered through cellulose-acetate filters (20  $\mu m$ ) and injected in a TOC-5000 instrument (Shimadzu, 25  $\mu m$  sample loop), where the organic fraction of injected solution was catalytically

converted at high temperature (650°C) and over a platinum supported catalyst to CO<sub>2</sub>. Then, the gas flow was analysed by means of IR spectrometer equipped with TCD detector.

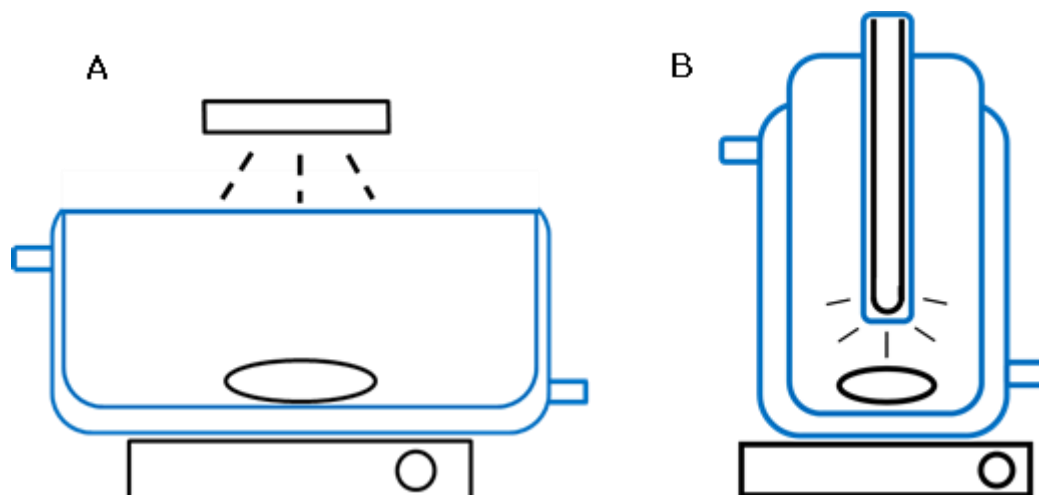


**Figure 2.4** simplified drawings of the reactor used to carry out the treatments.

#### 2.4.5. Toxicity test

The acute toxicity test of *Daphnia Magna* species was applied to verify the effectiveness of mineralization process, which can in principle lead to even more toxic byproducts through partial degradation of the starting complex molecule. Adult *Daphnia Magna* specimens were cultured (30 individuals/L) in a commercial mineral water (San Benedetto<sup>®</sup>) according to the procedure described elsewhere [31]. Toxicity of five concentrations (10, 30, 50, 70 and 100 mg/L) of each tested solution (*i.e.* untreated pollutant, direct photolysis, AOPs and photocatalytic treatment products), as well as a control (mineral water only), was tested for 48h at 20±0.5°C under a 16h light: 8h dark photoperiod. The results were analyzed in order to calculate the Lethal Concentration 50 (LC 50) at 48h using the Toxicity Relationship Analysis Program (TRAP, Version 1.30a) developed by US EPA. The treatments were carried out using an increased amount of Diclofenac (*i.e.*, 200 ppm) and 1 equivalent of H<sub>2</sub>O<sub>2</sub> in order to allow the preparation of

several diluted solutions and to assess the acute toxicity. In addition, the reaction time was increased to 24 h to completely degrade any residue of oxidant, which would have killed any crustaceans regardless of the DCF concentration, and the distilled water was replaced by commercial San Benedetto water, which is the environment in which *Daphnia Magna* is bred. All the tests were carried out using the setup A and the photo-catalyst/iron sludges were filtered after the treatment.

## References

1. Chiarello, G.L.; Rossetti, I.; Forni, L. Flame-spray pyrolysis preparation of perovskites for methane catalytic combustion. *J. Catal.* **2005**, *236*, 251–261, doi:10.1016/j.jcat.2005.10.003.
2. Bellardita, M.; García-López, E.I.; Marcì, G.; Palmisano, L. Photocatalytic formation of H<sub>2</sub> and value-added chemicals in aqueous glucose (Pt)-TiO<sub>2</sub> suspension. *Int. J. Hydrogen Energy* **2016**, *41*, 5934–5947, doi:10.1016/j.ijhydene.2016.02.103.
3. Krivtsov, I.; García-López, E.I.; Marcì, G.; Palmisano, L.; Amghouz, Z.; García, J.R.; Ordóñez, S.; Díaz, E. Selective photocatalytic oxidation of 5-hydroxymethyl-2-furfural to 2,5-furandicarboxyaldehyde in aqueous suspension of g-C<sub>3</sub>N<sub>4</sub>. *Appl. Catal. B Environ.* **2017**, *204*, 430–439, doi:10.1016/j.apcatb.2016.11.049.
4. Makuła, P.; Pacia, M.; Macyk, W. How To Correctly Determine the Band Gap Energy of Modified Semiconductor Photocatalysts Based on UV-Vis Spectra. *J. Phys. Chem. Lett.* **2018**, *9*, 6814–6817, doi:10.1021/acs.jpcllett.8b02892.
5. Tauc, J.; Grigorovici, R.; Vancu, A. Optical Properties and Electronic Structure

- of Amorphous Germanium. *Phys. Status Solidi* **1966**, *15*, 627–637,  
doi:10.1002/pssb.19660150224.
6. Galli, F.; Compagnoni, M.; Vitali, D.; Pirola, C.; Bianchi, C.L.; Villa, A.; Prati, L.; Rossetti, I. CO<sub>2</sub>photoreduction at high pressure to both gas and liquid products over titanium dioxide. *Appl. Catal. B Environ.* **2017**, *200*, 386–391, doi:10.1016/j.apcatb.2016.07.038.
  7. Bahadori, E.; Tripodi, A.; Villa, A.; Pirola, C.; Prati, L.; Ramis, G.; Rossetti, I. High pressure photoreduction of co<sub>2</sub>: Effect of catalyst formulation, hole scavenger addition and operating conditions. *Catalysts* **2018**, *8*, 430, doi:10.3390/catal8100430.
  8. Ramis, G.; Bahadori, E.; Rossetti, I. Design of efficient photocatalytic processes for the production of hydrogen from biomass derived substrates. *Int. J. Hydrogen Energy* **2021**, *46*, 12105–12116, doi:10.1016/j.ijhydene.2020.02.192.
  9. ARPA Environmental Measurements Available online:  
<https://www.arpalombardia.it/Pages/Meteorologia/Richiesta-dati-misurati.aspx#>.



### 3. Material characterization

#### 3.1. BET

The textural properties of the photocatalysts (*e.g.* BET SSA, pore volume, pore width) were obtained from N<sub>2</sub> adsorption and desorption isotherms (Table 3.4).

The shape of the curves obtained for samples of g-C<sub>3</sub>N<sub>4</sub> obtained either at 550°C and 600°C, as well as the series of composites with WO<sub>3</sub>, (Figures 3.1-3.3) is similar between the three series of materials and can be assimilated to a type IV isotherm usually associated with a mesoporous structure [1]. Furthermore, the hysteresis loop is more similar to a type H1 and only slightly similar to H3 type, which may mean that most of the porosity has cylinder shape, with a small portion of slit-like pores that come from the particle agglomeration (interparticle porosity) [2]. According to the results, the exfoliation process led to a greater surface area in case of both bulk C<sub>3</sub>N<sub>4</sub> samples obtained at 550°C and 600°C, that have a BET SSA of respectively 9 and 6 m<sup>2</sup>/g which is increased up to 28 and 20 m<sup>2</sup>/g when 120W of exfoliation power is used. Moreover, exfoliating the C<sub>3</sub>N<sub>4</sub>-500 with 30W increases the surface area to 16 m<sup>2</sup>/g, while 60W more than doubles that value and 37 m<sup>2</sup>/g are obtained. Unfortunately, there is a great interaction between the nanosheets (*e.g.* hydrogen bonds) and they tend to collapse again after the ultrasonic treatment. Although it does not seem to be beneficial to increase the power from that point of view, it is still important to compare the performance of the exfoliated materials, which will be discussed in Chapter 4. Total pore volume follows the behaviour of the specific surface area and increases as well with the exfoliation power, while the pore width actually shrinks until reaching the value of 15nm when 120W is used.

Regarding the composites, the trend is inversely proportional to the loading of  $\text{WO}_3$ , meaning that the SSA decreased from  $28 \text{ m}^2/\text{g}$  of the exfoliated g- $\text{C}_3\text{N}_4$  to  $9 \text{ m}^2/\text{g}$  when 40%  $\text{WO}_3$  is added. The same trend was reported in case of a similar series of composites loaded with 2.5 to 50% (w/w) of  $\text{WO}_3$ , though their surface area was one order of magnitude higher than our samples [3].

Regarding the  $\text{C}_3\text{N}_4$  samples from University of Palermo series, it is possible to notice from Table 3.4 that the exfoliation performed through a thermal treatment is more effective in improving the specific surface area, as the sample tested has a BET SSA around  $113 \text{ m}^2/\text{g}$ . That value is lowered when the photocatalyst is mechanically mixed with P25 ( $39 \text{ m}^2/\text{g}$ ) or  $\text{TiO}_2\text{-exCl}$  ( $76 \text{ m}^2/\text{g}$ ), though both the titania samples possess a surface area of respectively 47 and  $111 \text{ m}^2/\text{g}$ .

Titania prepared via flame spray pyrolysis shows a lower surface area and porosity than P25 when it is prepared from a 0.2M solution of  $\text{Ti}(\text{iPrO})_4$  in propionic acid, in details  $30 \text{ m}^2/\text{g}$  and  $0.105 \text{ cm}^3/\text{g}$  (Figure 3.4 and Table 3.4). On the other hand, the sample tested within the University of Palermo series and prepared from a more concentrated solution (0.7M) has an area almost doubled, that is  $67 \text{ m}^2/\text{g}$ , while the porosity is even lower ( $0.02 \text{ cm}^3/\text{g}$ ). These differences are likely to be due to the different conditions in which these photocatalysts were prepared. On the other hand, FSP- $\text{WO}_3$  has a very low area of  $3.4 \text{ m}^2/\text{g}$  (Figure 3.4), which should limit its catalytic performance since one key step of the photocatalytic process is the adsorption of the reactants over the surface of the active material. The curve reported in Figure 3.4 can be also assimilated to type IV isotherms, therefore, the samples are likely to be mesoporous.

A similar kind of isotherms (type IV, type H1 hysteresis loop) is observed even in case of titania P25 samples modified via metallization. Figure 3.5 reports some of the catalysts



from the series employed for carbohydrate photoreforming. It was observed a slight decrease of specific surface area in case of monometallic samples reduced at high temperature (*i.e.* Au and Pt), while the opposite happened to bimetallic photocatalyst prepared via sol immobilization ( $\text{Au}_x\text{Pt}_y$ ), which is likely linked to the formation of metallic nanoparticles agglomerates that increased the SSA (Table 3.4). The reduction step at high temperature of  $\text{TiO}_2$  samples was causing a collapse of the pores with a loss of specific surface area.

The same can be said for the monometallic sample loaded with palladium (0.1%Pd/P25), since the P25 was showing 47  $\text{m}^2/\text{g}$  whereas 0.1% Pd 39  $\text{m}^2/\text{g}$  [4]. Also, the strong interaction of titania, in particular the anatase phase, with metallic NPs makes the latter to fill the pores. This is true also for 1% Ag, it was synthesized at a significantly lower temperature (see Chapter 2) and the surface area resulted increased (56  $\text{m}^2/\text{g}$ ). Since the literature reported both this behavior (*i.e.* increase or decrease of surface area), it is likely that the metallization technique has an influence on the textural properties of the photocatalysts [4,5].

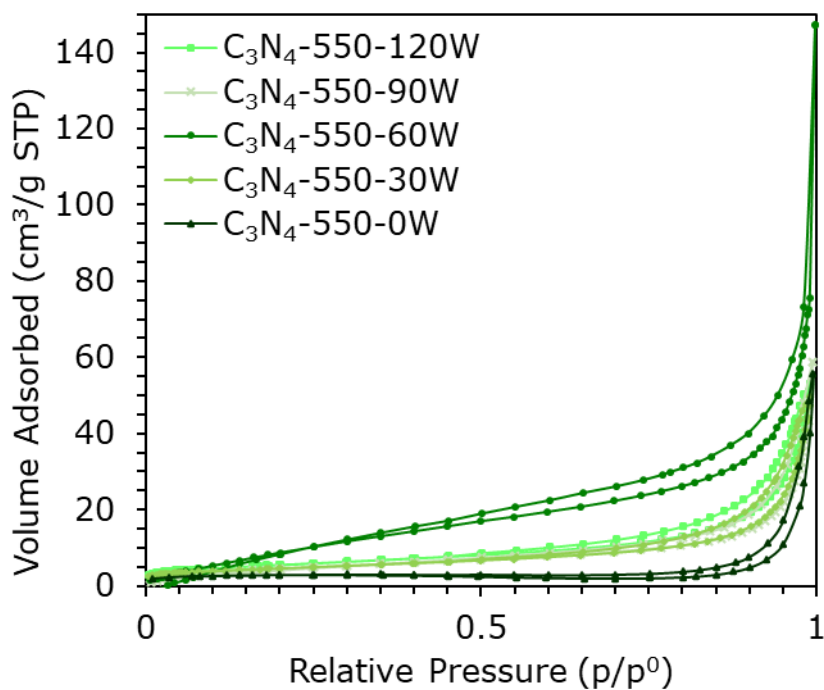


**Figure 3.1.** N<sub>2</sub> sorption curves of g-C<sub>3</sub>N<sub>4</sub> samples obtained at 550 °C and exfoliated with various power (0-120W)

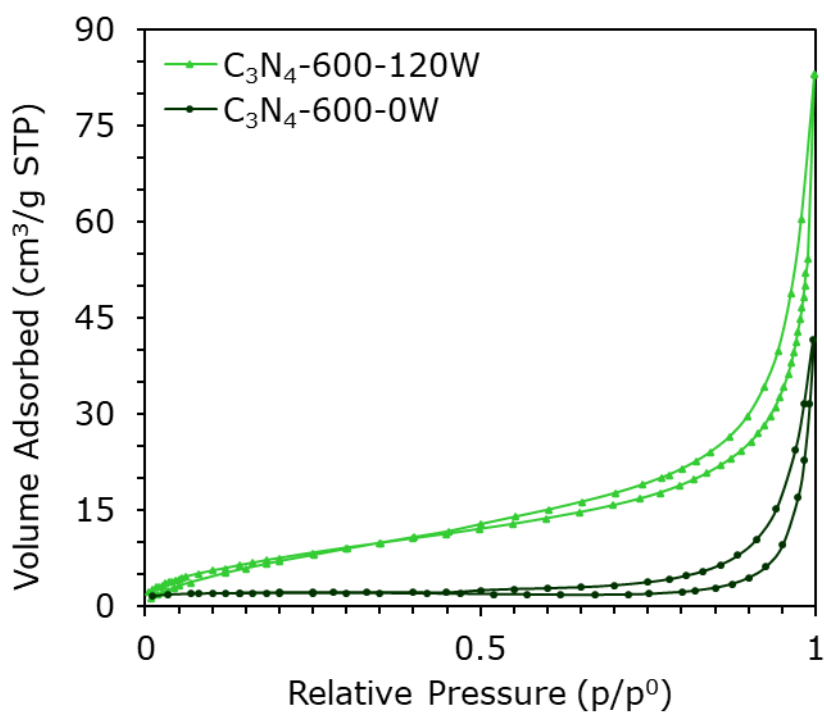


**Figure 3.2.** N<sub>2</sub> sorption curves of C<sub>3</sub>N<sub>4</sub> samples obtained at 600 °C and exfoliated (120W)

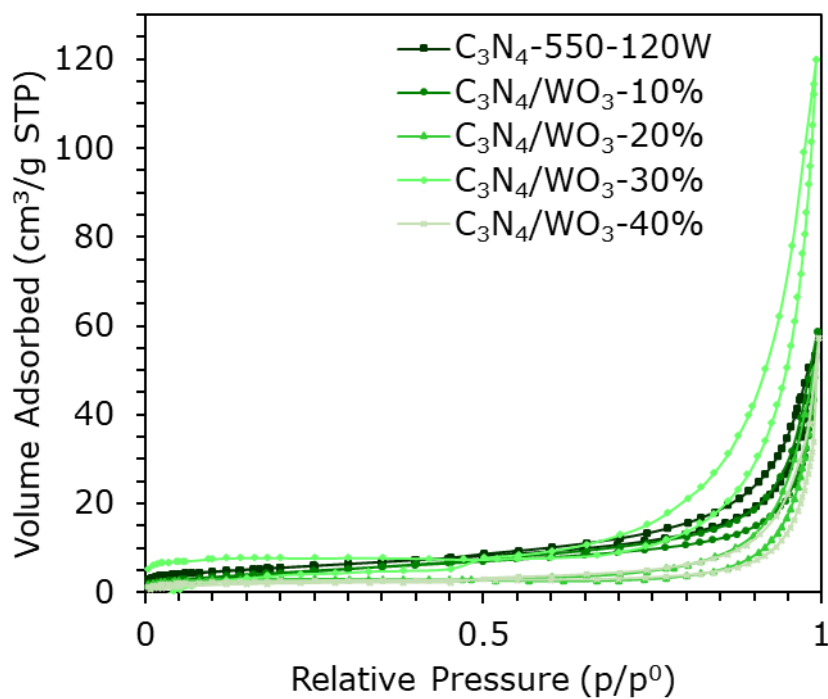


**Figure 3.3.** N<sub>2</sub> sorption curves of C<sub>3</sub>N<sub>4</sub>/WO<sub>3</sub> composite (10-40% w/w) compared with the bare g-C<sub>3</sub>N<sub>4</sub> exfoliated (120W)

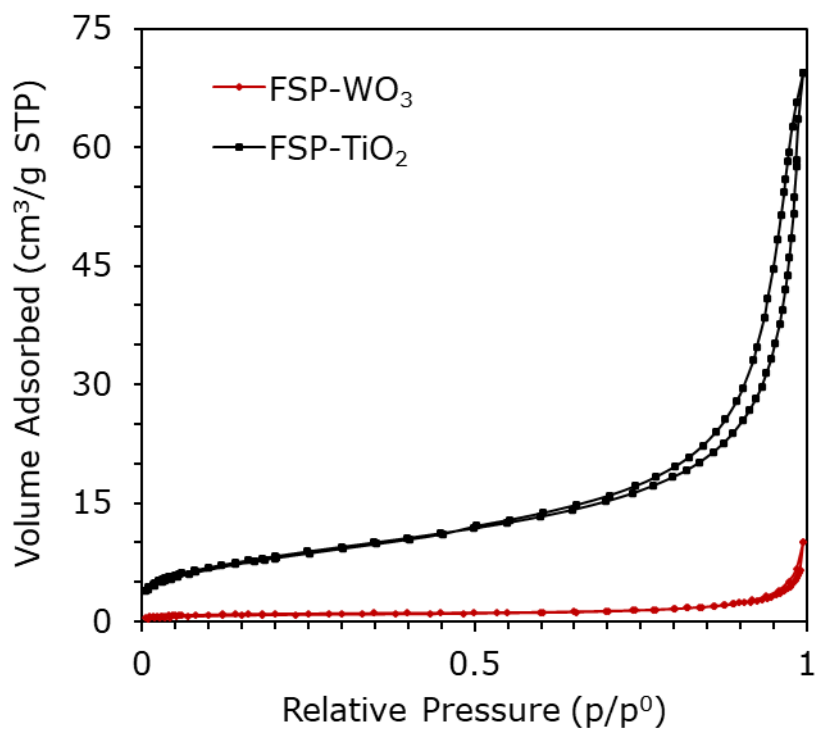


**Figure 3.4.** N<sub>2</sub> sorption curves of TiO<sub>2</sub> and WO<sub>3</sub> samples prepared via flame-spray pyrolysis

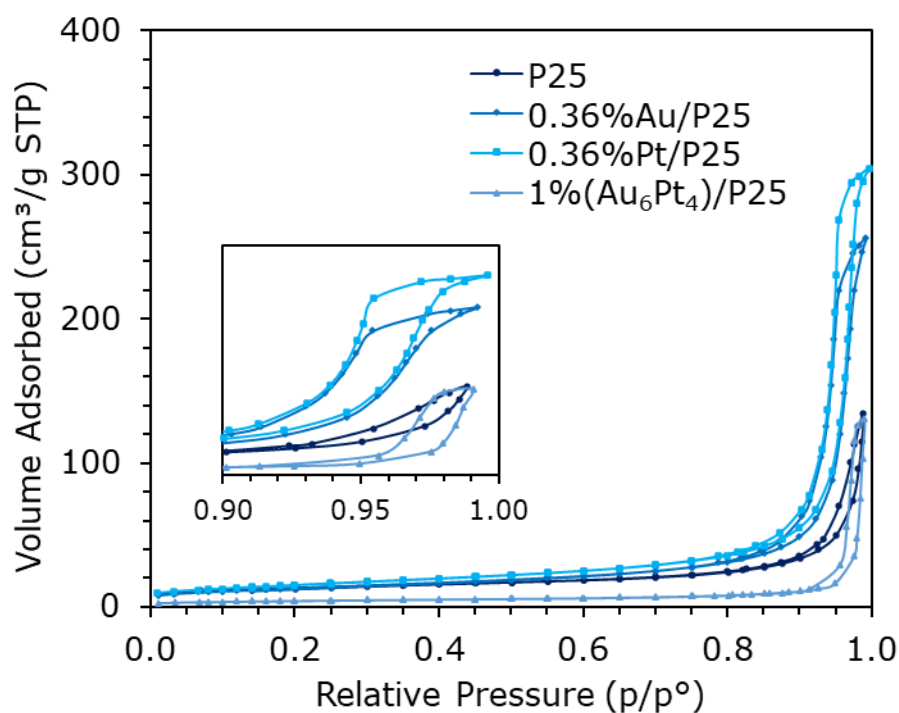


**Figure 3.5.** Adsorption and desorption N<sub>2</sub> isotherms of P25 and photocatalysts modified via metallization with gold and platinum or both

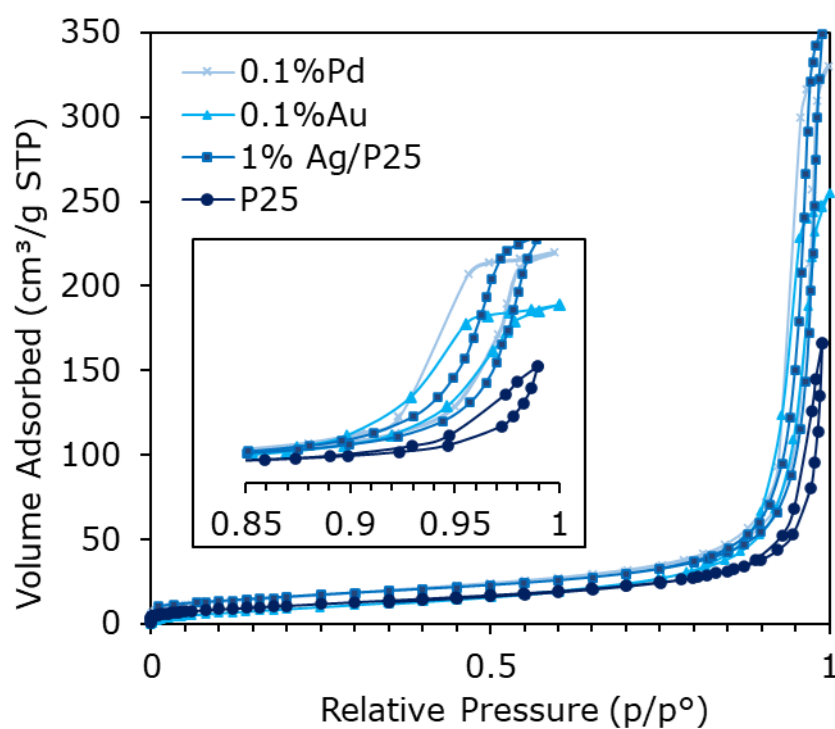


**Figure 3.6.** Adsorption and desorption N<sub>2</sub> isotherms of P25 and photocatalysts modified via metallization with palladium, gold and silver

### 3.2. XRD

C<sub>3</sub>N<sub>4</sub> samples were only partially crystalline and showed two main peaks at  $2\theta=13^\circ$  and  $2\theta=27.4^\circ$ , which were related respectively to interplane packing of linear heptazines chains and to interlayer staking of aromatic rings, in a way similar to graphite (Figure 3.7) [6,7]. It is worth to highlight that there was a shift toward higher diffraction angles of the main peak, with respect to the theoretical value reported in the JCPDS card. That shift is linked to the interplane distance and in case of the sample prepared at  $550^\circ\text{C}$  it is partially visible from the diffractogram that the exfoliation process led to a delamination of the staked sheets, though we are still far from a complete detachment [6]. C<sub>3</sub>N<sub>4</sub>-600 was more crystalline but had also a more compact structure according to the shifts of the main peak (Figure 3.8).

XRD patterns of C<sub>3</sub>N<sub>4</sub>/WO<sub>3</sub> composites showed poor crystallinity of the tungsten trioxide phase in case of samples with nominal load of 10 and 40%, as they were more similar to the pattern of the base carbon nitride exfoliated (Figure 3.7). The characteristic reflections of WO<sub>3</sub> are present in every composite. WO<sub>3</sub> was also obtained alone by decomposition of precursor in absence of C<sub>3</sub>N<sub>4</sub> and according to the reference patterns available in literature (JCPDS#020-1324 and #033-1387), it should be mainly constituted of orthorhombic phase [8,9].

On the other hand, WO<sub>3</sub> prepared via flame spray pyrolysis resulted to be more crystalline than that prepared via thermal decomposition (Figure 3.10) and both the characteristic peaks of tungsten trioxide and titanium dioxide, such as the peak of anatase near  $25^\circ$  and rutile at  $27.2^\circ$  are clearly visible in the composite TiO<sub>2</sub>/WO<sub>3</sub>-60/40.

Speaking about the series of photocatalysts from University of Palermo, the XRD patterns of the TiO<sub>2</sub> samples evidenced the coexistence of the anatase and rutile polymorphs in all

of the samples, in details, the former exhibits a principal peak at angle of  $25.3^\circ$  while the latter at  $27.4^\circ$  [10]. The peak at  $48^\circ$  further confirms the presence of the anatase structure, although FSP titania shows slightly higher percentage of rutile phase and this polymorph represents most of the structure of  $\text{TiO}_2\text{-exCl}$  (Figure 3.11). Moreover, P25 and FSP samples show high intensity peak which are associated with high crystallinity of the materials.  $\text{TiO}_2\text{exCl}$  lacks long range crystallinity, as evidenced by the broad and poorly intense reflections. The two main diffraction peaks for  $\text{C}_3\text{N}_4\text{-TE}$  at  $13^\circ$  and  $27^\circ$ , reported in Fig. 3.12 can be attributed to the (100) and (002) crystallographic planes of the material [11]. As reported in literature, the intensities of the main diffraction peak of  $\text{C}_3\text{N}_4$  is very low when it is coupled with titania, due to the high crystallinity of P25 [12].

Regarding other samples based on titania, like the monometallic titania photocatalysts loaded with silver, gold, palladium and platinum, and the bimetallic ones (Au and Pt), it is possible to notice from Figure 3.13 and 3.14 the absence of characteristic reflections attributable to these metals, that is likely to be due to the low loading compared to similar catalysts reported in literature [10]. Even in case of 1%Ag/P25, it has been already observed that silver tends to form small and distributed NPs that are not detectable by this technique [10,13].  $\text{TiO}_2$  P25 is highly crystalline, and crystallinity is retained after the metallization either via wetness impregnation or precipitation and reduction. In the first case, the thermal treatment of P25 should induce a phase transformation from anatase (>74% in all the samples) to rutile in the range  $600\text{-}800^\circ\text{C}$ , however, it has been also reported that gold and silver deposition may or may not induce this shift, which is highly dependent on calcination step and in our case it is performed under  $\text{H}_2$  atmosphere [14–17].

That is not an issue when titania is immobilized over glass slides, as the calcination temperature was set at 500 °C and the XRD pattern is comparable after the treatment (Figure 3.15). Conversely, the impregnation and subsequent reduction of silver on P25 deposited glasses determined the rising of new reflection attributable to the metallic silver phase (JCPSD card #004-0783). The estimated loading of silver in that case is 3.6%wt. and the XRD analysis of similar photocatalyst showed the same pattern [10]. On the other hand, the deposition and reduction of copper was performed with more diluted solutions (0.001-0.05M rather than 0.7M) and it is likely that the Cu NPs are too dispersed to be seen through that technique (Figure 3.16).

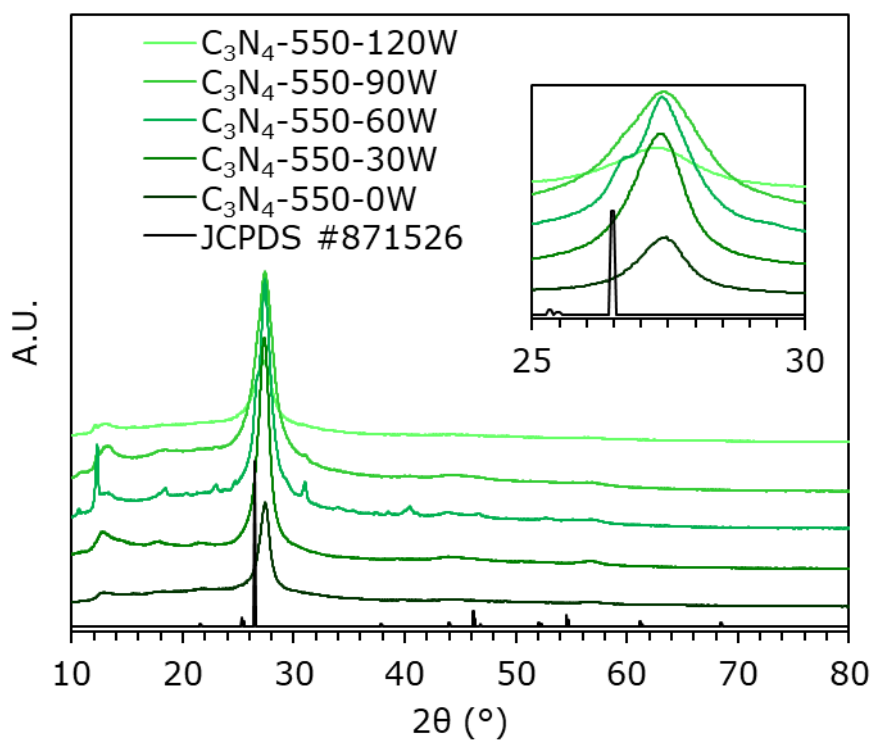


**Figure 3.7.** Diffraction patterns of  $C_3N_4$  exfoliated photocatalysts with different power (0-120W) compared with the reference XRD spectra of carbon nitride (JCPDS #871526)

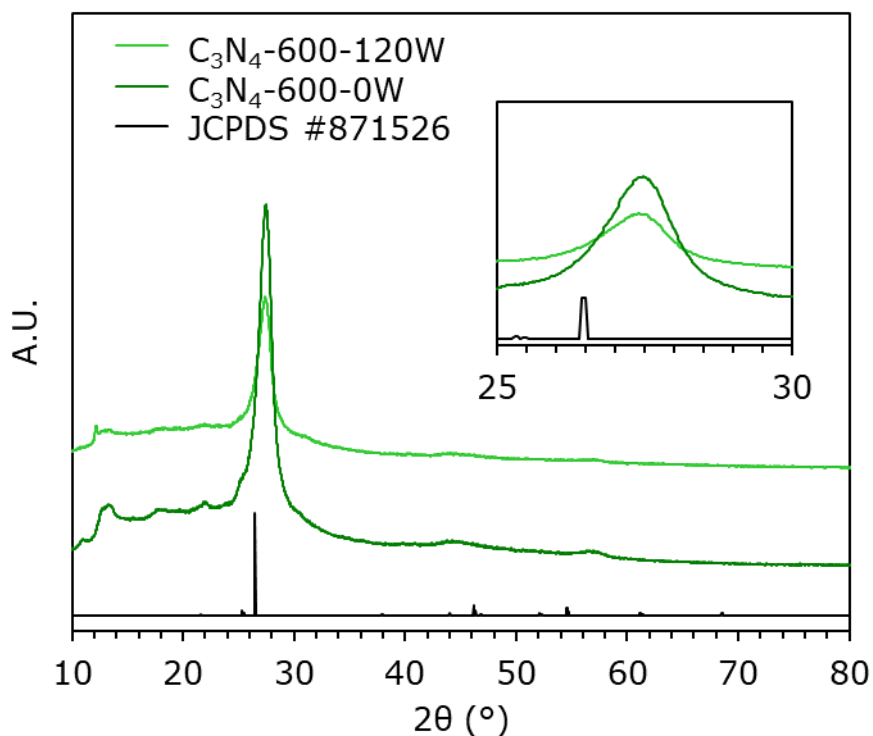


**Figure 3.8.** Diffraction patterns of  $C_3N_4$  photocatalysts synthesized at 600°C and exfoliated (0-120W)



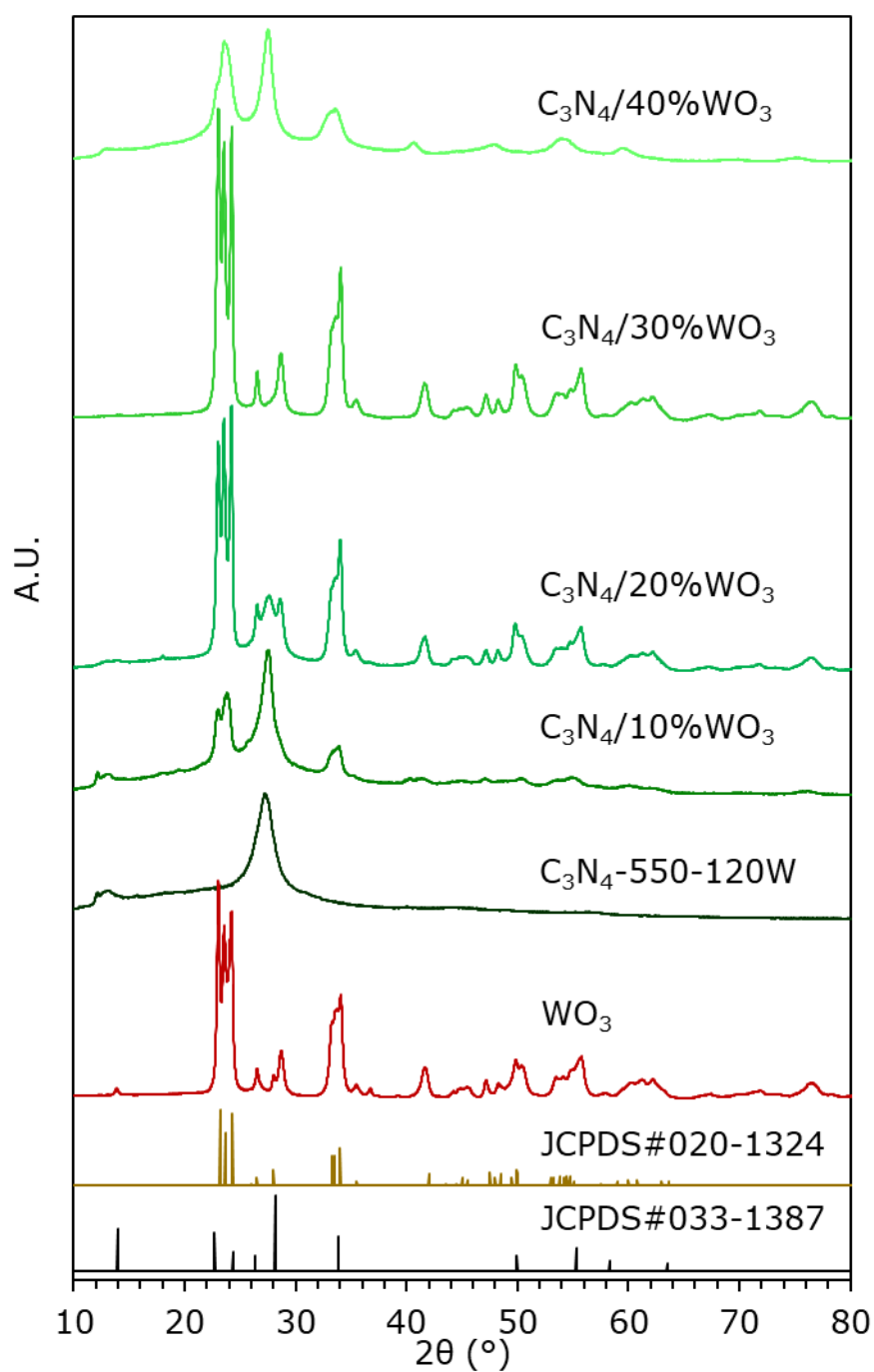


**Figure 3.9.** Diffraction patterns of C<sub>3</sub>N<sub>4</sub>/WO<sub>3</sub> composites compared with the reference pattern of orthorhombic WO<sub>3</sub> (JCPDS #020-1324) and hexagonal WO<sub>3</sub> (JCPDS #033-1387)

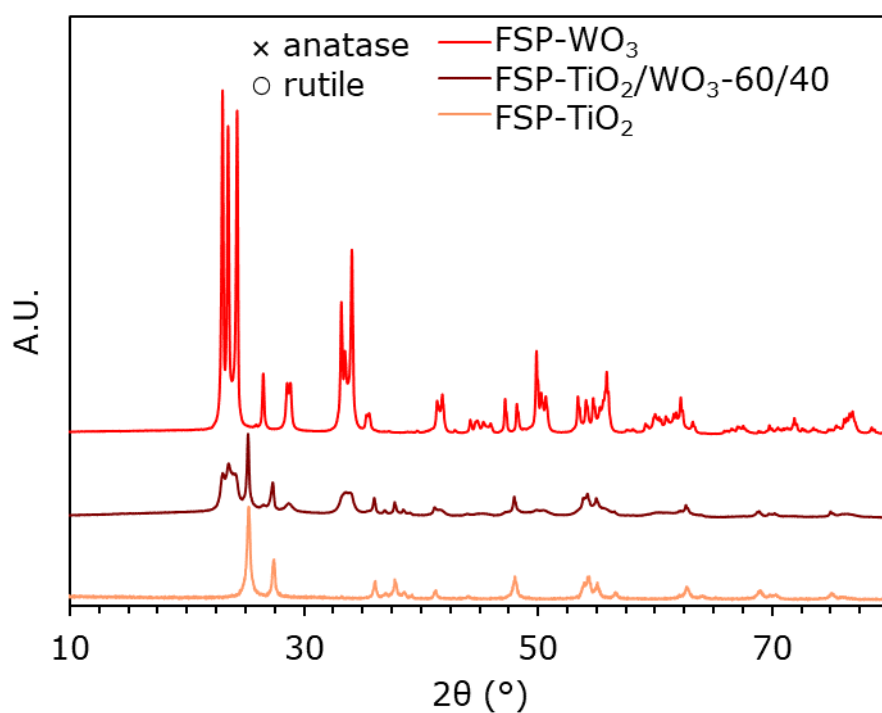


**Figure 3.10.** Diffraction patterns of FSP-TiO<sub>2</sub>, FSP-WO<sub>3</sub> and the composite

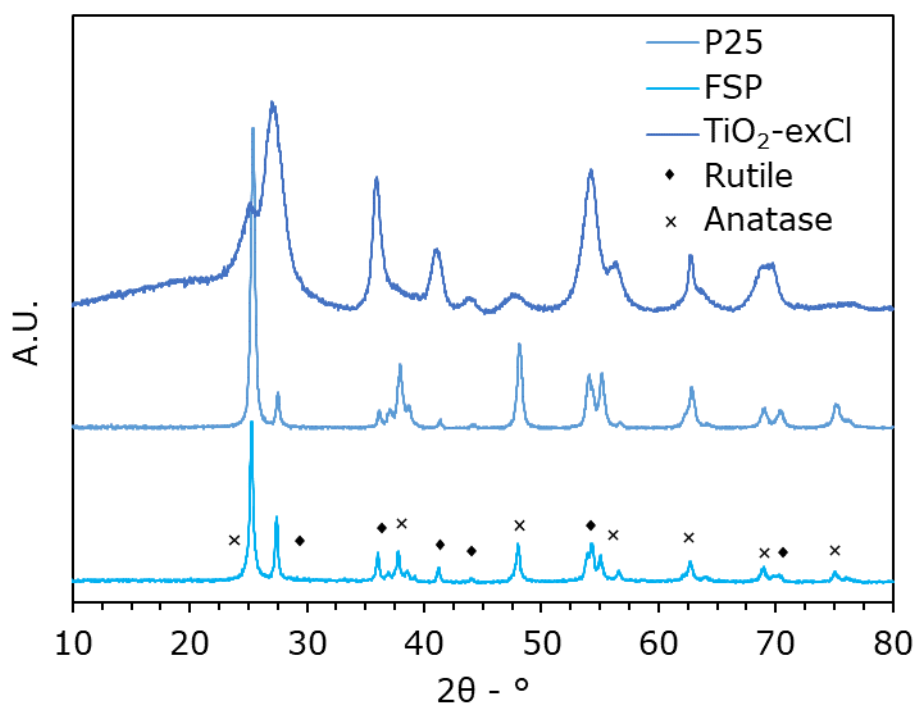


**Figure 3.11.** Diffraction patterns of P25, FSP titania and TiO<sub>2</sub>-exCl from University of Palermo

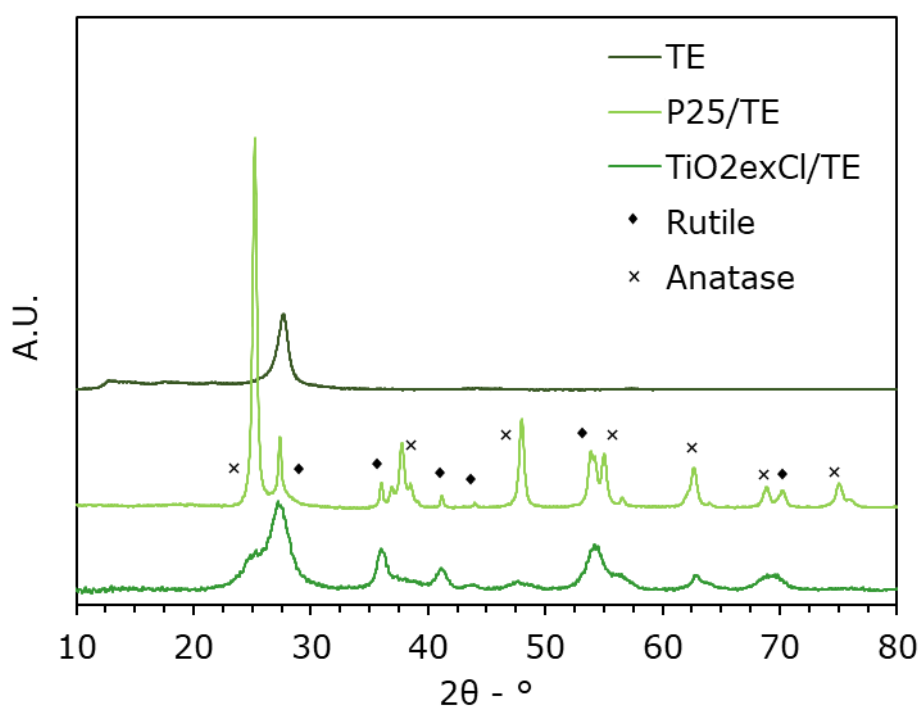


**Figure 3.12.** Diffraction patterns of g-C<sub>3</sub>N<sub>4</sub> and its composites from University of Palermo

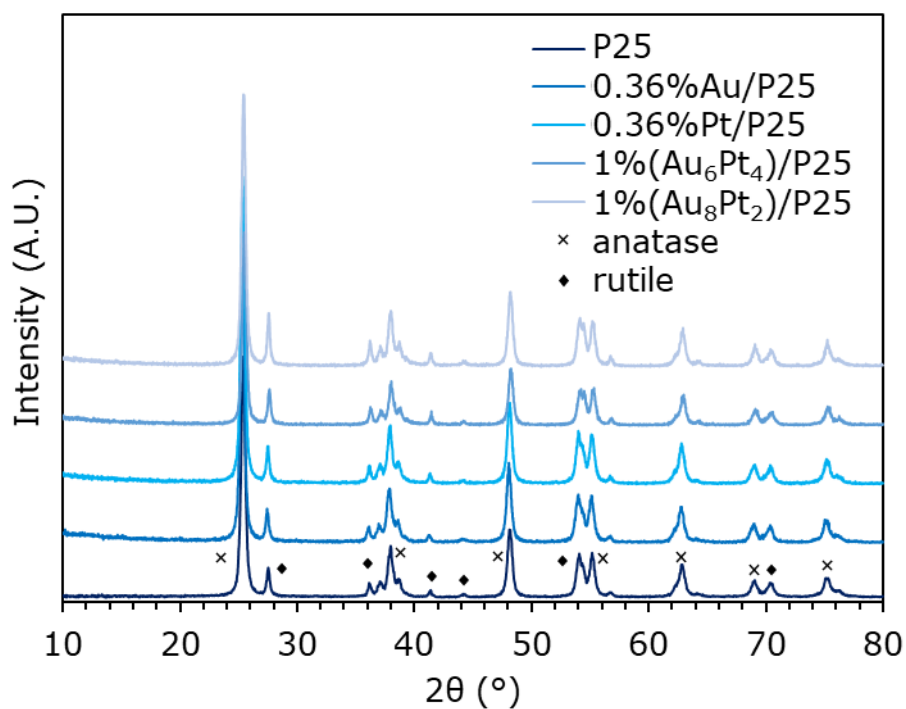


**Figure 3.13.** Diffraction patterns of metallized titania samples employed for carbohydrates photoreforming compared to the reference P25

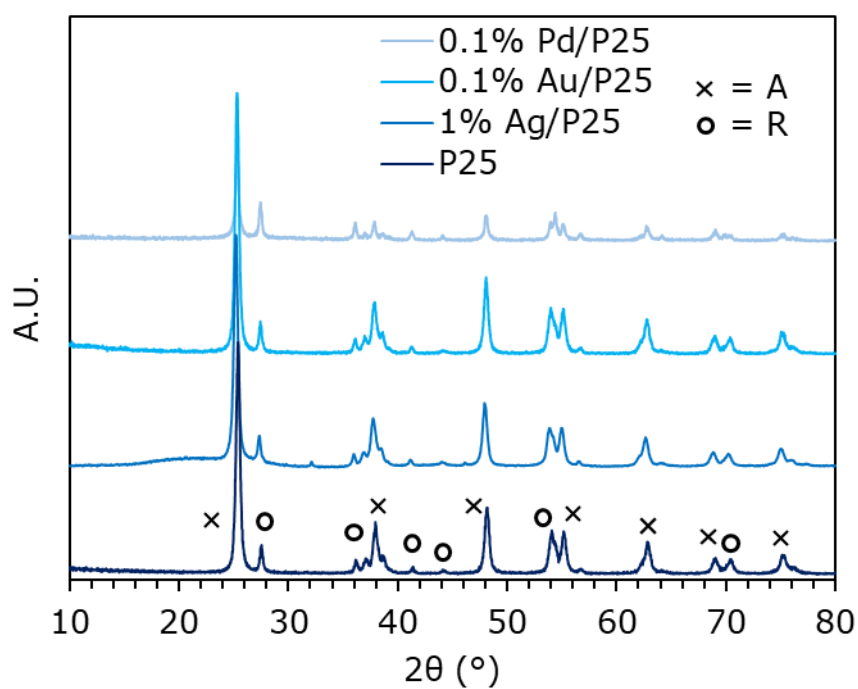


**Figure 3.14.** Diffraction patterns of titania P25 and titania photocatalysts metallized with Pd, Au and Ag

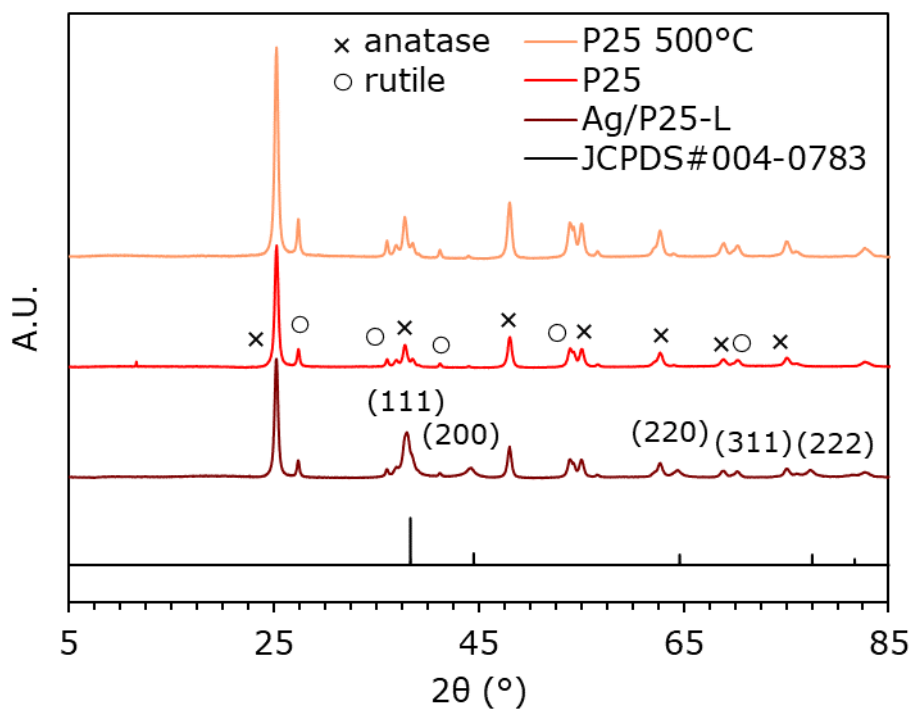


**Figure 3.15.** Diffraction patterns of P25 and Ag/P25 deposited over glass slides

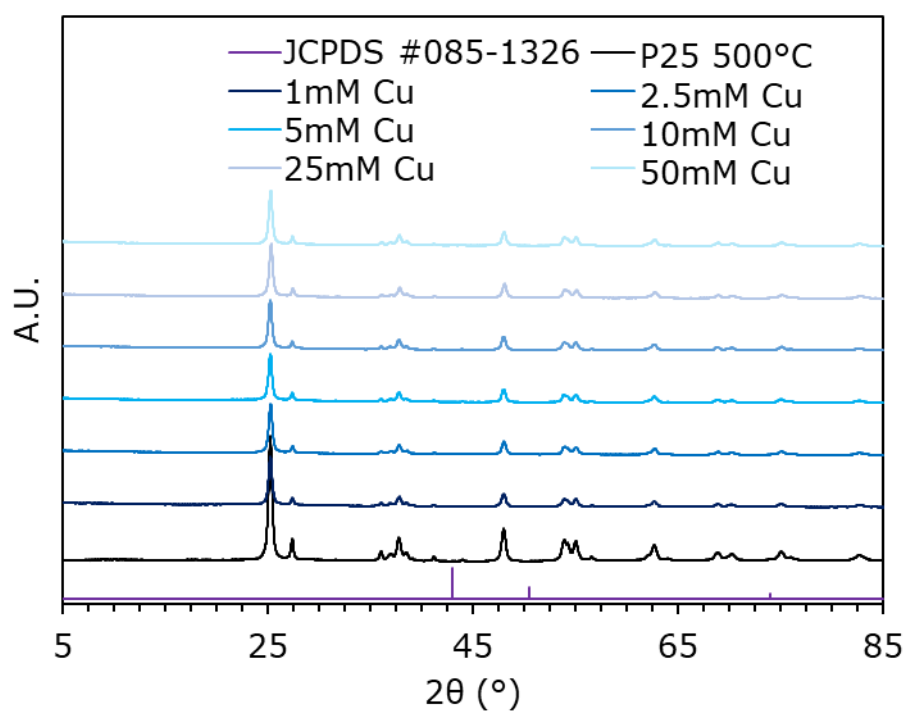


**Figure 3.16.** Diffraction patterns of P25 immobilized and calcinated compared with the same P25 impregnated with Cu (JCPDS card #085-1326 for reference)

### 3.3. DRS UV-Vis

All the samples have been diluted one-to-one or one-to-two with BaSO<sub>4</sub>, which is the reflectance standard and prevents saturation when mixed with samples that absorb too much. Therefore, the shape of the curves was not affected by the blending, but the absolute value of reflectance cannot be compared since it was highly unlikely that the mixing step was carried out exactly in the same way for each photocatalysts. The band gap of the photocatalysts was obtained from the absorption spectra illustrated in Figure 4.3 by using Kubelka-Munk and fitted with Tauc equation. The samples have all indirect band gap, thus  $r = \frac{1}{2}$  was used.

C<sub>3</sub>N<sub>4</sub> samples show a band gap within the range 2.7-2.9 eV (Figures 3.17 and 3.18). Polymeric melon, which constitutes most of the bulk C<sub>3</sub>N<sub>4</sub>, has a theoretical BG of 2.7 eV and therefore it should be able to absorb wavelength below 460 nm, in the blue region of the visible spectrum [7]. Our bulk carbon nitride obtained at 550°C has a band gap of 2.68 eV, which is very close to the theoretical value [18]. In addition, some authors report that the BG is narrower when the bulk material is exfoliated [7], while others explain the increase in BG due to the quantum confinement effect and the fact that the charges can move and recombine only within the plane and not between stacked layers [19,20]. Both our bulk materials (synthesized at 550 and 600°C) show a band gap of approximately 2.68 eV and it gradually increase with the exfoliation power up to 2.78 eV in case of C<sub>3</sub>N<sub>4</sub>-550 treated with 120W and 2.70 eV for C<sub>3</sub>N<sub>4</sub>-600 samples treated in the same conditions. A slightly higher band gap in the range 2.76-2.84 eV is observed for composite materials obtained via surface decoration of exfoliated C<sub>3</sub>N<sub>4</sub> with WO<sub>3</sub> NPs (Fig. 3.19). Bulk WO<sub>3</sub> has a theoretical band gap of 2.62 eV, however, the BG of its NPs is inversely correlated with the mean dimension of the particles and can be as high as 3.1 eV [21]. This is

common and due to the nature of the NPs, as the smaller they get the higher is the share of the atoms that belong to the surface with respect to the bulk of the material. Therefore, it is likely that a BG increase of the composites is associated with small NPs of  $\text{WO}_3$  deposited over the g- $\text{C}_3\text{N}_4$  sheets.

Figure 3.19 illustrates the Tauc plot of  $\text{TiO}_2\text{-exCl}$ ,  $\text{C}_3\text{N}_4$  from thermal exfoliation and its composites with titania. Overall, the band gap of  $\text{C}_3\text{N}_4\text{-TE}$  is higher (2.80 eV) than that of the series exfoliated through ultrasonic treatment, however, the coupling with  $\text{TiO}_2\text{-exCl}$  and P25 is effective in reducing the band gap of the composite, respectively to 2.95 eV and 2.90 eV from 3.05 eV ( $\text{TiO}_2\text{-exCl}$ ) and 3.22 eV (P25).

According to Table 3.4, the surface metallization has a positive effect (in most cases) to the band gap of the modified photocatalysts, which show a shift of the absorption toward higher wavelengths. In addition, the deposition of the metals coincides with the rise of localized surface plasmonic bands in the region 400-600 nm, due to the presence of nanocluster of reduced metal that enhance the absorption in the visible region [22–24], as reported in Fig. 3.21 and 3.22.

Regarding the samples of titania and tungsten trioxide prepared via flame spray pyrolysis, FSP titania shows a band gap narrower than commercial P25, respectively 3.1 eV and 3.22 eV, while  $\text{WO}_3$  synthesized with the same apparatus has 2.73 eV (Figure 3.23). The composite obtained by mixing the precursor in the solution that fed the burner has a BG even lower, around 2.7 eV, thus, it should be active when irradiated under visible light. Very interesting is the absorption spectra of the immobilized and impregnated P25, that was obtained by immersion in a 0.07M solution of silver nitrate (Figure 3.24). The absorption intensity increases significantly, which is usually associated with very high loading of silver NPs and an increased photocatalytic activity. That is also confirmed by

the XRD spectra, which shows reflections of  $\text{Ag}^0$  phases, and by the broad adsorption band in the visible region due to localized surface plasmonic resonance (LSPR). LSPR band is usually located around 460nm, whereas here it is broader since is likely that Ag nanocluster are formed extensively on titania NPs [22,25]. In addition, the P25 thermally treated retains its characteristic band gap (the curve differs from the one of P25 since the latter was diluted with  $\text{BaSO}_4$  during the analysis).



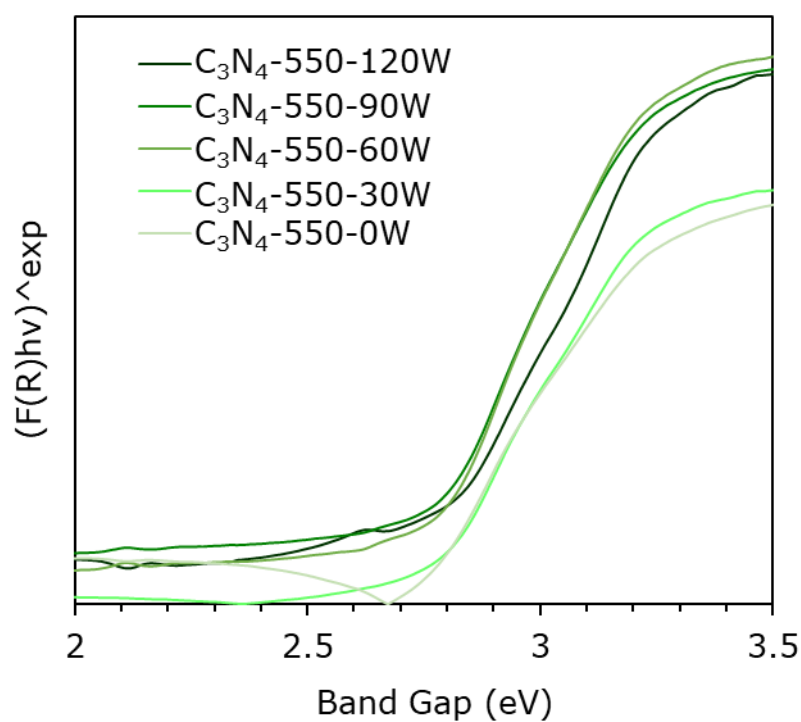


**Figure 3.17.** Tauc plot of graphitic carbon nitride-based materials synthesized at 550°C and exfoliated with different power (indirect BG)

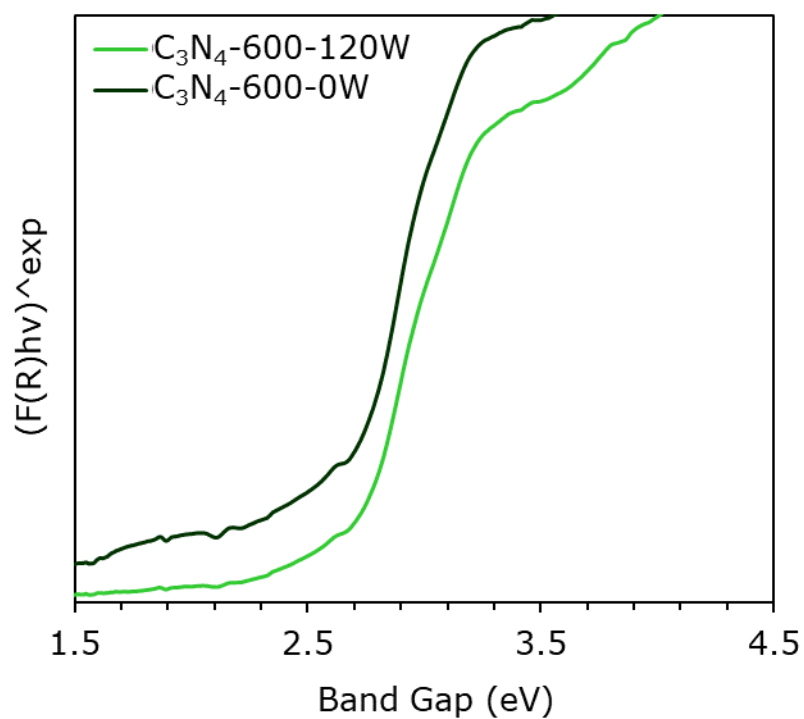


**Figure 3.18.** Tauc plot of graphitic carbon nitride-based materials synthesized at 600°C and exfoliated with different power (indirect BG)

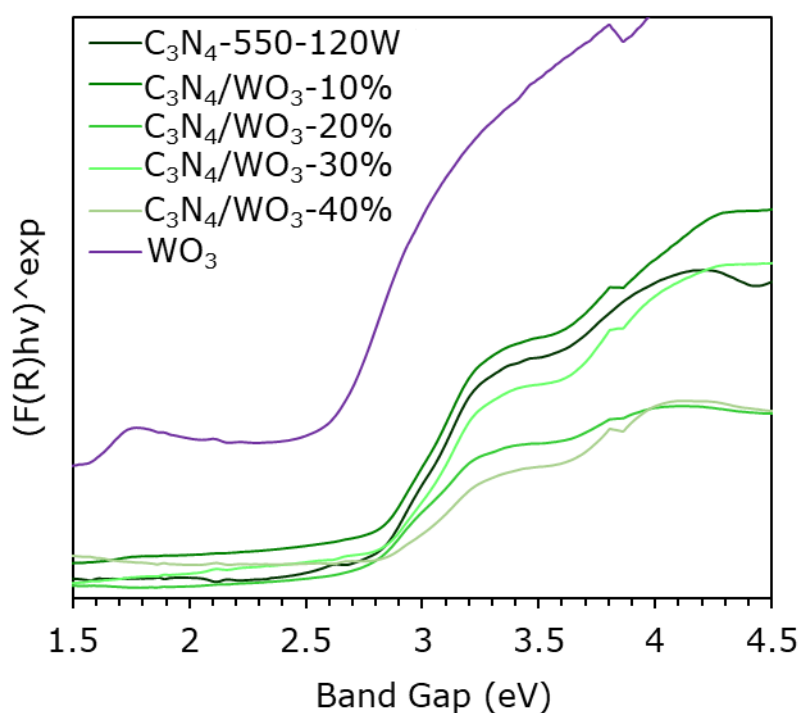


**Figure 3.19.** Tauc plot of graphitic carbon nitride/ $WO_3$  composite with different loading (10-40% w/w) compared with the base material exfoliated (indirect BG).

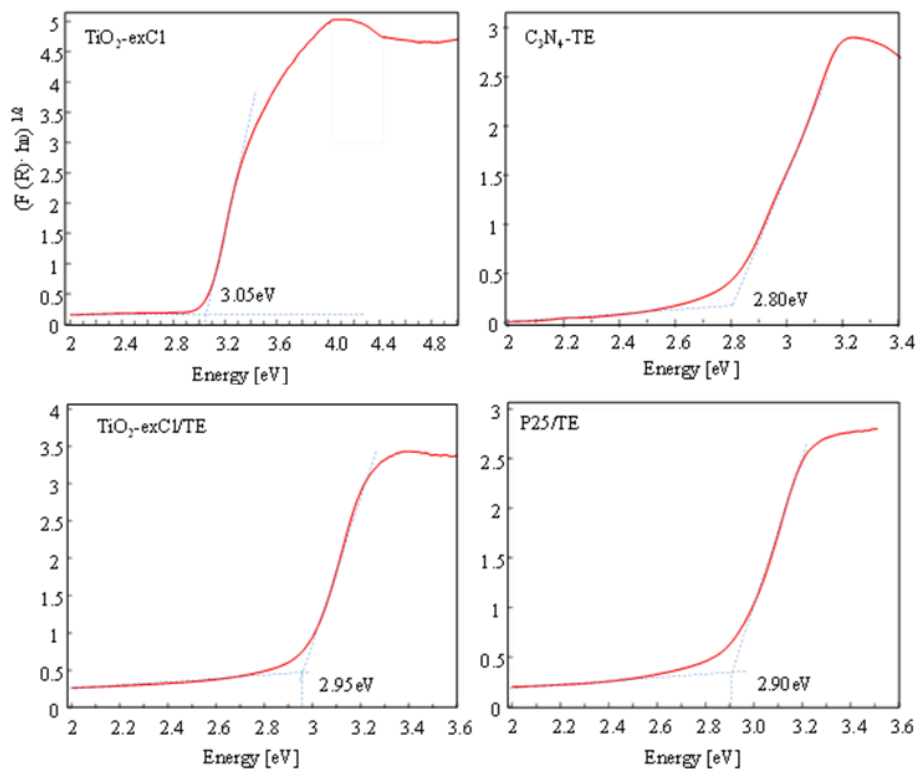


**Figure 3.20.** Tauc plot of photocatalyst from University of Palermo series

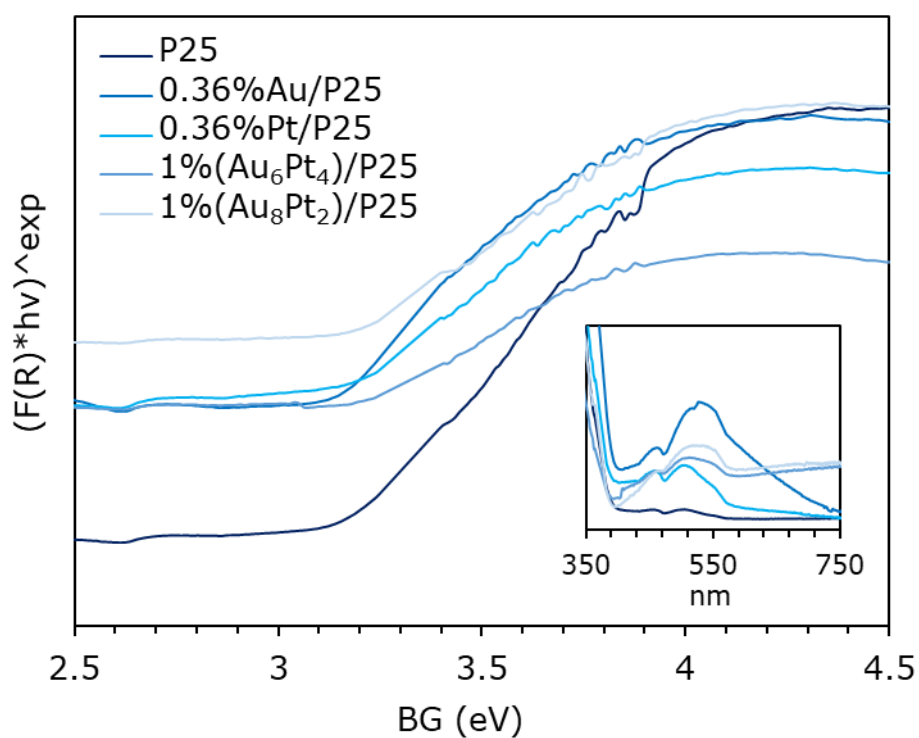


**Figure 3.21.** Band gap of M/TiO<sub>2</sub> and Au<sub>x</sub>Pt<sub>y</sub>/TiO<sub>2</sub> photocatalyst employed for photoreforming of carbohydrates

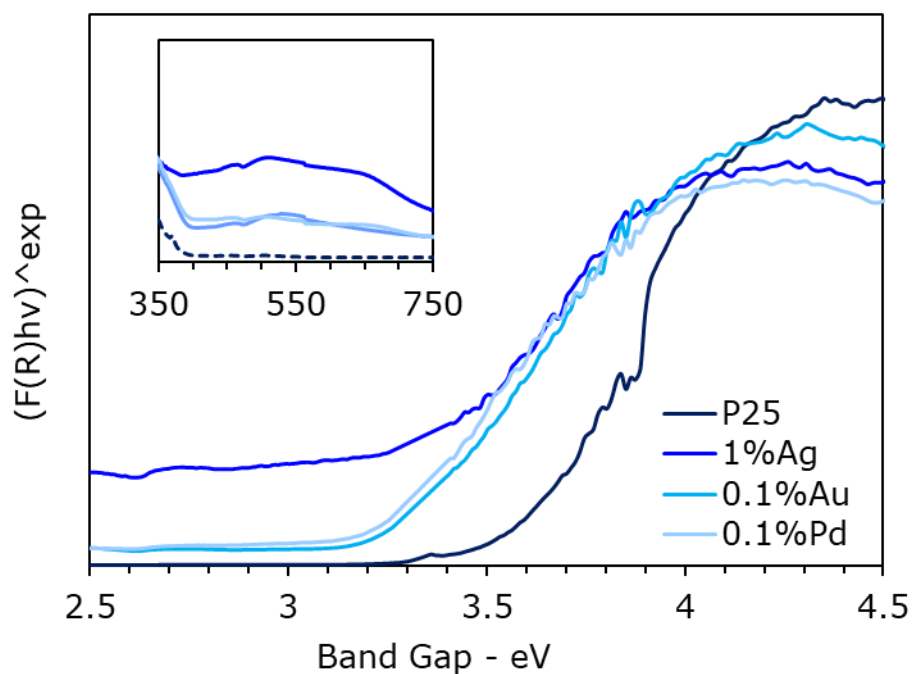


**Figure 3.22.** Band gap of M/TiO<sub>2</sub> photocatalyst employed for wastewater treatment

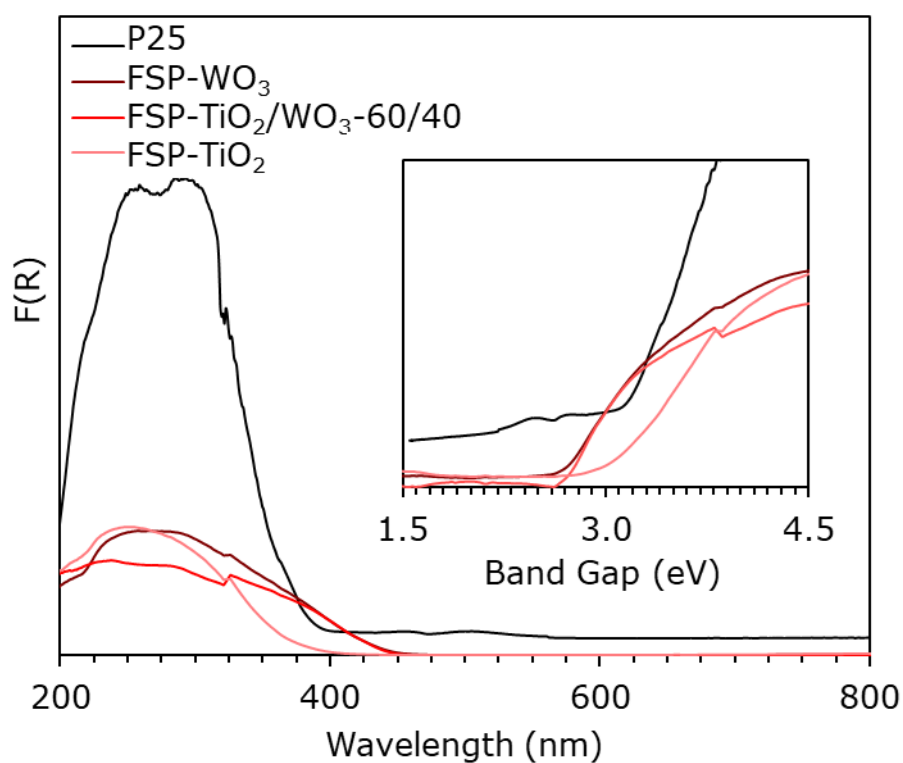


**Figure 3.23.** Tauc plot of  $\text{WO}_3$ ,  $\text{TiO}_2$  and the composite synthesized via flame-spray pyrolysis

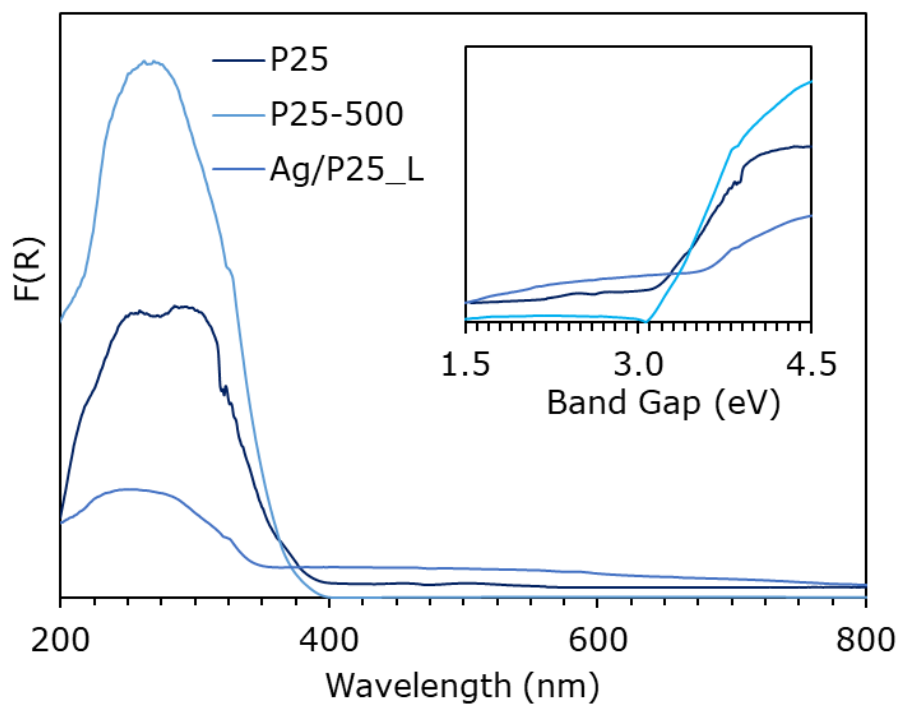


**Figure 3.24.** Band gap of immobilized titania decorated with Ag nanoparticles

### 3.4. Photoluminescence

Table 3.1 and 3.2 summarize the quantum yield (QY) measured for the series of graphitic carbon nitride and the composite with tungsten trioxide. Speaking of exfoliated carbon nitride, the QY increases with the power applied during the delamination step. In general, a lower QY is preferred for photocatalytic application, since it represents the amounts of photons emitted upon illumination and the focus of photocatalysis is on the non-radiative decays such as the realization of the electrons through the reaction. In that case, the QY of the sample treated at 30W increased with respect to bulk g-C<sub>3</sub>N<sub>4</sub> and slowly return to the initial value the more power is used during exfoliation step (*e.g.* 120W).

The series of composites have a quantum yield that significantly decreases along with the WO<sub>3</sub> loading, from the 5.8% of C<sub>3</sub>N<sub>4</sub>-550-120W to the 2% of the composite with 40% of tungsten trioxide. That translates into a higher chance that the photogenerated electron-holes couple to survive long enough to react with the species adsorbed over the photocatalyst.

**Table 3.1.** Results of quantum yield measurements for the series of exfoliated graphitic carbon nitride prepared at 550°C

Sample	Band gap (eV)	$\lambda_{\max}$ (nm) E <sub>x310nm</sub>	$\lambda_{\max}$ (nm) E <sub>x360nm</sub>	QY (%) E <sub>x310nm</sub>	QY (%) E <sub>x360nm</sub>
C <sub>3</sub> N <sub>4</sub> -550	2.68	466	466	5.8	6.6
C <sub>3</sub> N <sub>4</sub> -550-30W	2.74	442	461	7.9	8.0
C <sub>3</sub> N <sub>4</sub> -550-60W	2.76	450	460	7.2	7.2
C <sub>3</sub> N <sub>4</sub> -550-90W	2.77	443	447-455	8.2	7.2
C <sub>3</sub> N <sub>4</sub> -550-120W	2.78	439	439	6.0	6.7

**Table 3.2.** Results of quantum yield measurements for the series of composites C<sub>3</sub>N<sub>4</sub>/WO<sub>3</sub>

Sample	Band gap (eV)	$\lambda_{\text{max}}$ (nm)	QY (%) [280-300]	QY (%) [370-390]
C <sub>3</sub> N <sub>4</sub> -550-120W	2.68	439	5.9	7.0
C <sub>3</sub> N <sub>4</sub> /WO <sub>3</sub> 10%	2.80	441	5.1	6.8
C <sub>3</sub> N <sub>4</sub> /WO <sub>3</sub> 20%	2.76	438	6.8	8.0
C <sub>3</sub> N <sub>4</sub> /WO <sub>3</sub> 30%	2.82	437	3.5	6.2
C <sub>3</sub> N <sub>4</sub> /WO <sub>3</sub> 40%	2.84	439	2.0	2.9

### 3.5. TGA

Since graphitic carbon nitride is only composed by carbon and nitrogen, thermogravimetric analysis allows to understand the effectiveness of the deposition process in case of C<sub>3</sub>N<sub>4</sub>/WO<sub>3</sub> composites. Figure 3.25. illustrates the results obtained by processing those photocatalysts as well as their constituents. As expected, bare WO<sub>3</sub> did not undergo any weight loss in the selected range of temperature, while C<sub>3</sub>N<sub>4</sub> decomposition begin around 575°C and results completed around 675°C, meaning that no residues are found after the analysis. Speaking of the composite series, they all show a small weight loss at the beginning of the heating phase, which is probably due to the adsorbed water. C<sub>3</sub>N<sub>4</sub>/WO<sub>3</sub>-10%, being the sample with the least amount of oxide, showed a decomposition curve very similar to bare C<sub>3</sub>N<sub>4</sub>, but the decomposition seems to end around 725°C. In addition, the weight loss was 93%, meaning that the real loading of WO<sub>3</sub> was 7% (Table 3.2). In case of WO<sub>3</sub>/C<sub>3</sub>N<sub>4</sub>-20%, the decomposition curve is extended to even higher temperatures (775°C) and the real loading was estimated to be 23%, thus a little bit higher than expected. The last two samples, that are WO<sub>3</sub>/C<sub>3</sub>N<sub>4</sub>-30% and WO<sub>3</sub>/C<sub>3</sub>N<sub>4</sub>-40%, were found to be loaded with respectively 31% and 41% of WO<sub>3</sub>.

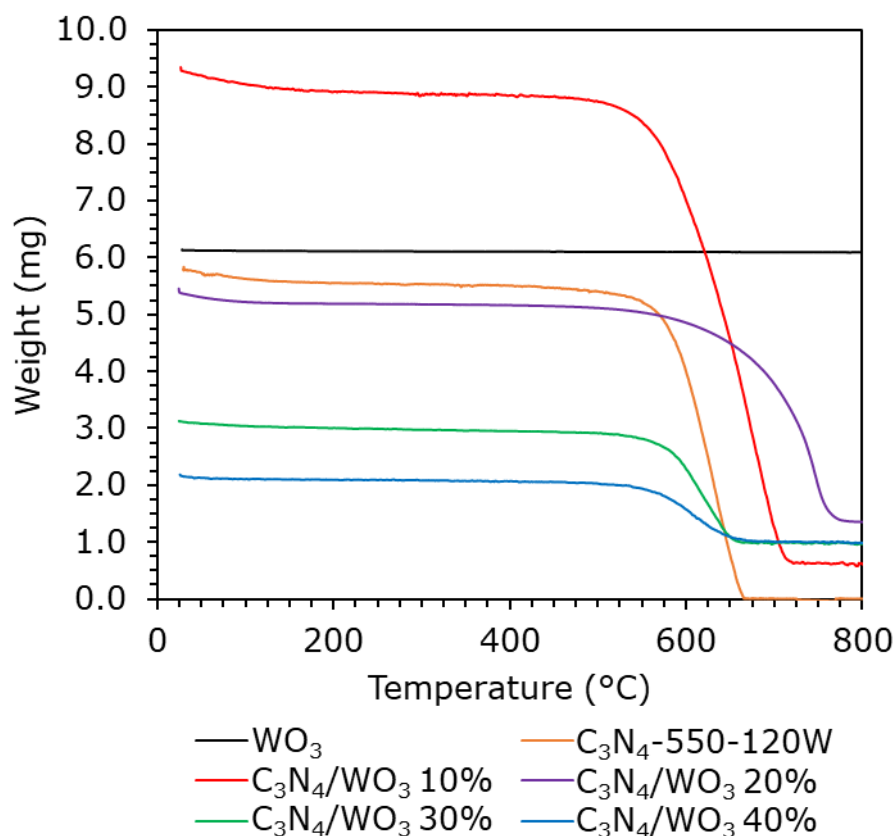


**Figure 3.25.** Results of thermogravimetric analysis performed on the bare semiconductors ( $\text{WO}_3$  and  $\text{C}_3\text{N}_4$ ) and their composites. 25-800 $^{\circ}\text{C}$ , 10 $^{\circ}\text{C}/\text{min}$ , Air flow

**Table 3.2.** Real  $\text{WO}_3$  loading calculated from TGA curves

Material	Weight loss	Real $\text{WO}_3$ loading
$\text{WO}_3$	0%	100%
$\text{C}_3\text{N}_4$ -550-120W	100%	0%
$\text{C}_3\text{N}_4/\text{WO}_3$ -10%	93%	7%
$\text{C}_3\text{N}_4/\text{WO}_3$ -20%	77%	23%
$\text{C}_3\text{N}_4/\text{WO}_3$ -30%	69%	31%
$\text{C}_3\text{N}_4/\text{WO}_3$ -40%	59%	41%

### 3.6. XPS

XPS spectra of selected photo-catalysts are illustrated in Figure 3.26. It was observed that all the analyzed samples contained organic impurities (up to 11.15%) that were associated with various organic species such as C-C, C-H, C-O, C-C=O, O=C-O, as suggested by

deconvolution of the peaks. The XPS peak intensity areas were obtained after subtracting a Shirley type background, since the component from the inelastic scattered electrons of the Ti3p and Ti3s peaks appear in the same region of Pt4f and Au4f core levels [26].

The main peak at 459 eV is due to  $\text{Ti}^{4+}$  species and overlaps with the small peak assigned to  $\text{Ti}^{3+}$  that can be found at 457 eV, especially in the spectra of 1%( $\text{Au}_6\text{Pt}_4$ )/P25 and 1%( $\text{Au}_8\text{Pt}_2$ )/P25 samples. The presence of  $\text{Ti}^{3+}$  is the consequence of the reduction step of the metallic active phase on the catalysts, which leads to partial reduction of the  $\text{Ti}^{4+}$  ion on the photo-catalyst surface itself and so modifies its electronic properties and BG values.  $\text{Ti}^{4+}$  reduction can be catalyzed by the metals here adopted, but due to the low amount of Au and Pt, the  $\text{Ti}^{3+}$  peak is barely visible on the Ti2p spectrum.

Regarding the metals, according to the shifts of the peak, they are present in the reduced state. The peaks associated with  $\text{Pt}^0$  and  $\text{Au}^0$  are characterized by a low signal-to-noise ratio, while, as expected from the higher loading, signals are more intense in the case of bi-metallic samples. The characteristic peaks of gold were identified at 84eV (4f7/2) and 88 eV (4f5/2). For platinum, peaks were detected at 71eV (4f7/2) and 74eV (4f5/2), while in the literature  $\text{Pt}^{2+}$  peaks are usually located at a slightly higher BE (ca. 72 and 75eV [27,28]. Surprisingly, the presence of reduced metal nanoclusters unveils that the photocatalysts were stable upon activation and can be stored for years without undergoing any oxidation that can potentially affect its performance [29]. In addition, traces of aluminum oxide (around 76eV) were detected in almost every sample.



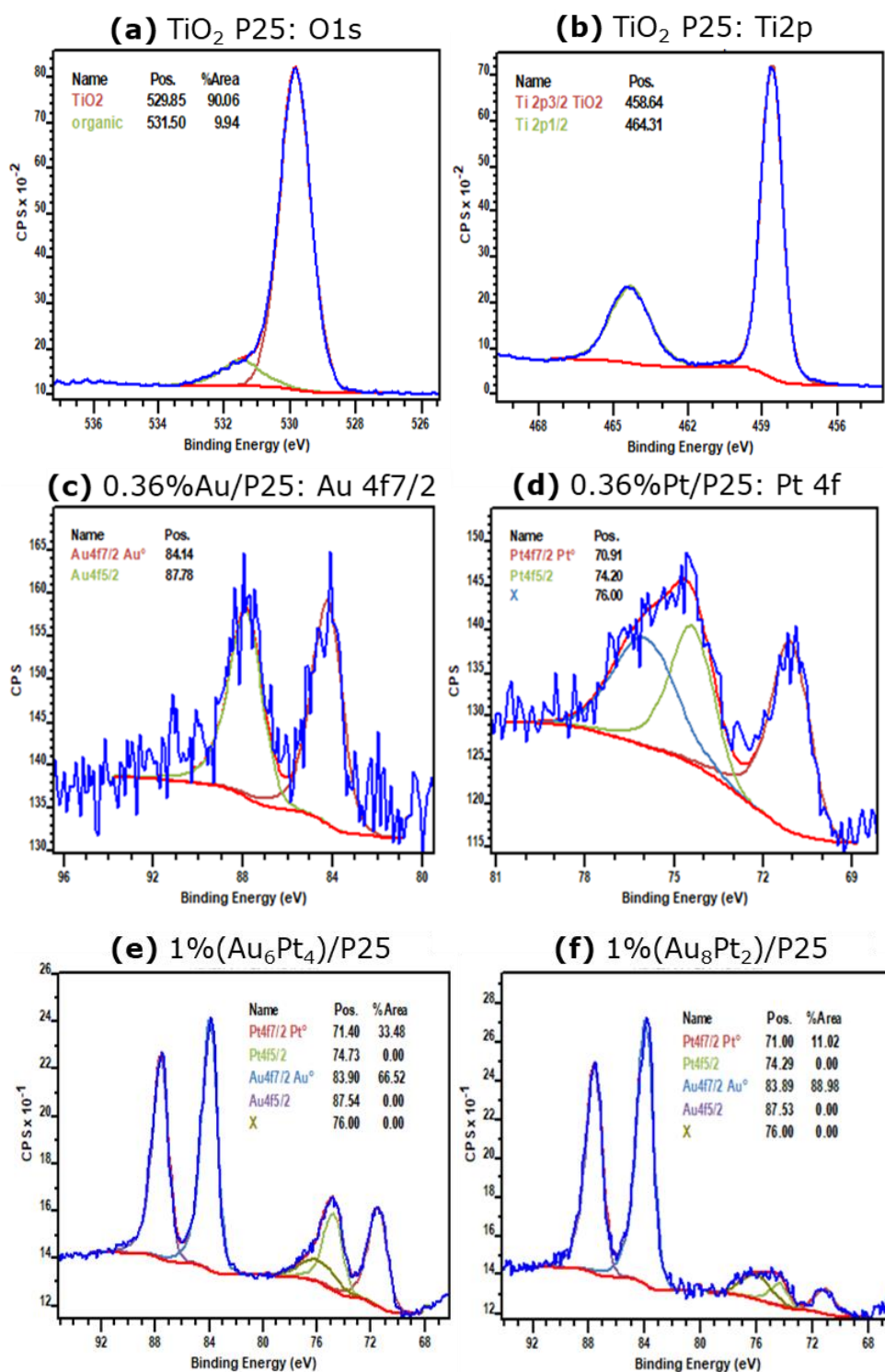


**Figure 3.26.** XPS spectra of selected photocatalysts: (a) O1s P25; (b) Ti2p P25; (c) Au4f 7/2 0.36% Au/P25; (d) Pt4f 0.36% Pt/P25; (e) Au4f and Pt4f 1%(Au<sub>6</sub>Pt<sub>4</sub>)/P25 (f) Au4f and Pt4f 1%(Au<sub>8</sub>Pt<sub>2</sub>)/P25

### 3.7. SEM-EDX

SEM-EDX analyses have been performed on selected mono and bimetallic photocatalyst (see Appendix for all the pictures). All the samples were constituted of a uniform array of titania nanoparticles ca. 20 nm in size. The composition was checked by EDX, but due to the low metal loading, it was necessary to increase the acquisition time up to 12 minutes. The metal NPs are difficultly observed through EDX spectra (Figure A10), though the presence of the metal on the catalyst surface was confirmed to be in the desired loading by XPS analysis (*vide infra*).

Elemental mapping of 1% wt. (Au<sub>6</sub>Pt<sub>4</sub>)/P25 sample highlighted only a small region of the nanoparticles in which both Au and Pt were deposited, but it was not possible to identify any metal NPs on its surface. On the other hand, a huge platinum cluster was observed on the titania surface in case of 0.36%Pt particles, while the backscatter detector (BED-C) allowed to see smaller and more abundant NPs on 0.1%molAu sample. The formation of nanocluster of tens of nanometers was already reported, but usually concerned higher metal loading than those present on the here investigated samples [26,50].

Figures A11 and A12 (see Appendix) clearly show that both C<sub>3</sub>N<sub>4</sub>-550 and C<sub>3</sub>N<sub>4</sub>-550-120W are composed of homogeneous particles and that the ultrasonic treatment caused the formation of smaller aggregates. Regarding C<sub>3</sub>N<sub>4</sub>/WO<sub>3</sub> composites (Figures A13-A16), the white disc-like spots on the surface of the graphitic carbon nitride were identified as WO<sub>3</sub> particles via EDX analysis (Figures A17 and A18). As expected, the number of WO<sub>3</sub> particles grows among the series, however, the composite loaded with 30% appears to be less homogeneous than the others.

Figures A1-A3 illustrate the growth of titania NPs that are thermally treated after the deposition over glass and after the second impregnation cycle aimed to metallize the

surface with silver. In addition, the Ag loading was checked qualitatively via EDX, which confirmed the presence of the metal (2.2%) along with traces of Si that are probably due to glass debris. The same technique was used to confirm the presence of copper on the glasses impregnated with  $\text{CuSO}_4$  0.025M, that is around 0.8%.

### 3.8. FT-IR

FTIR spectra were obtained for the series of photocatalyst from University of Palermo (Figure 3.27, the contribute of KBr was subtracted). The analysis of  $\text{C}_3\text{N}_4$ -TE confirmed the carbon nitride structure, showing the major bands of this structure such as those attributable to C-N-C and C-NH-C units (*i.e.* 1632, 1560, 1410, 1325, 1250  $\text{cm}^{-1}$ ) typical for the stretching vibrations modes of heptazine heterocyclic ring ( $\text{C}_6\text{N}_7$ ) units as long as the absorption at 887 and 804  $\text{cm}^{-1}$  corresponding to the N-H deformation mode and a bending mode of the triazine units respectively [30]. Figure 3.27 shows also a broad band ranging from 3500 to 3000  $\text{cm}^{-1}$  which can be attributed to O-H and N-H stretching, due to the presence of hydroxyl adsorbed species and free amino groups on the surface. The N-H stretching confirms the existence of NH and/or  $\text{NH}_2$  groups caused by incomplete polycondensation of the  $\text{C}_3\text{N}_4$  [31]. The IR transitions attributed to the heptazine heterocyclic ring are less defined and wider in the composites indicative of a disorder in the carbon nitride layered structure after the ball milling process in the presence of both titania containing samples. It is particularly true for the P25/TE sample, for which the SEM micrographs evidenced a uniform coverage of  $\text{C}_3\text{N}_4$  by titania nanoparticles. In Figure 3.29 also the FTIR of the bare  $\text{TiO}_2$ -exCl sample is shown evidencing the absence of bands in the heptazine range, the presence of water and the transitions due to the cut-off at ca. 900  $\text{cm}^{-1}$  due to the Ti-O-Ti bonds in the oxide sample.

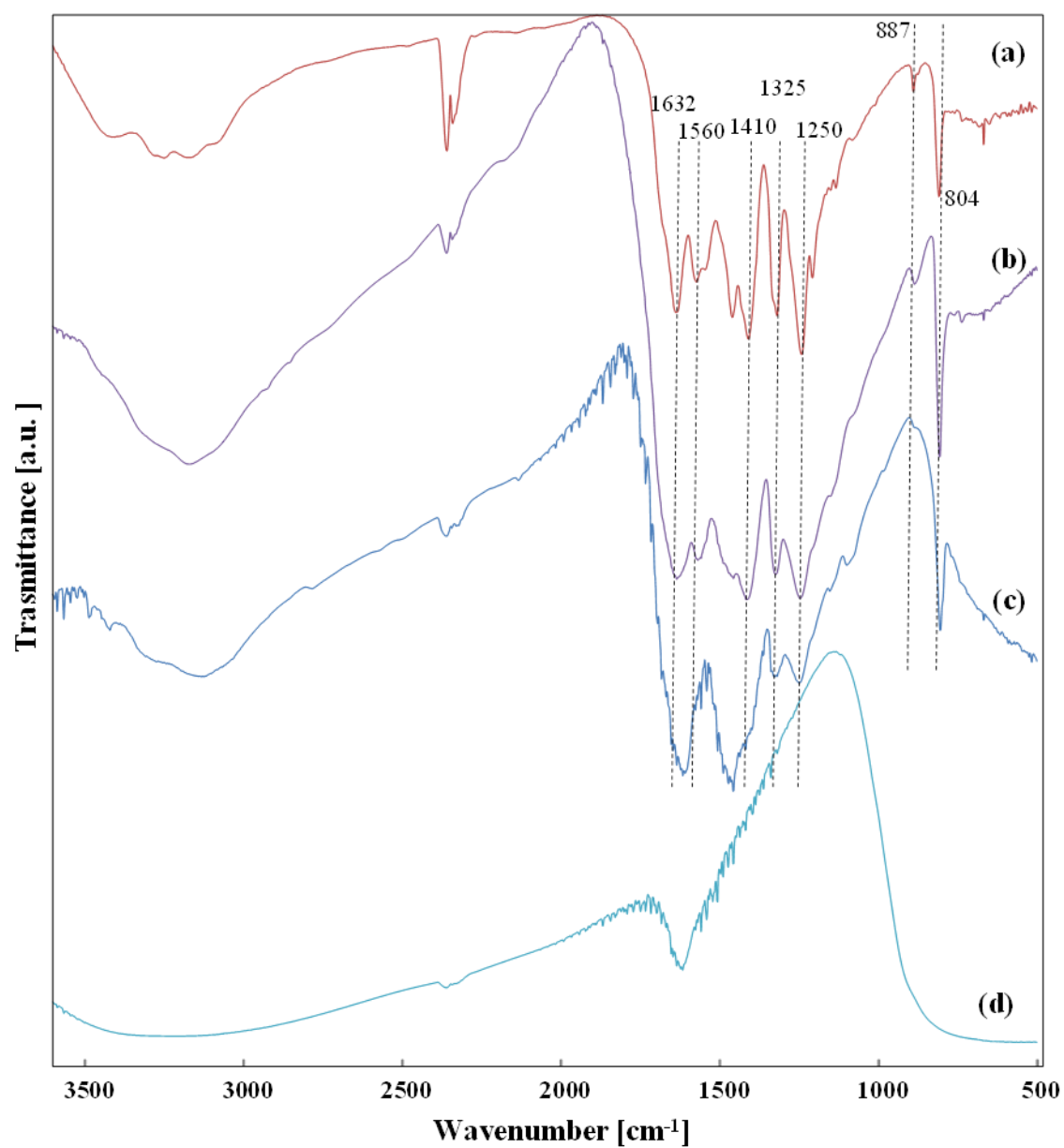


**Figure 3.27.** FTIR spectra of (a) C<sub>3</sub>N<sub>4</sub>-TE sample; (b) TiO<sub>2</sub>-exCl/TE; (c) P25/TE and (d) bare TiO<sub>2</sub>-exCl

**Table 3.4.** Textural and optical properties of all the photocatalysts employed

Sample	BET SSA (m <sup>2</sup> /g)	Total pore volume (cm <sup>3</sup> /g)	BJH ads. pore width (nm)	Crystallite size (nm)	Phase %	BG (eV)
P25	47	0.257	35	15(A);26(R)	78(A);22(R)	3.22
P25-500	/	/	/	18(A);25(R)	90(A);10(R)	3.22
Ag/P25-L	/	/	/	19(A);28(R)	92(A);8(R)	3.60
FSP-TiO <sub>2</sub>	30	0.109	14	22(A);27(R)	A(70); R(30)	3.10
FSP-WO <sub>3</sub>	3.4	0.015	35	43	Orthorhombic	2.73
TiO <sub>2</sub> /WO <sub>3</sub> 60/40	/	/	/	32(A);33(R)	A(75); R(25)	2.70
C <sub>3</sub> N <sub>4</sub> -600-0W	6.1	0.027	32	3.9	/	2.68
C <sub>3</sub> N <sub>4</sub> -600-120W	20	0.083	15	3.1	/	2.70
C <sub>3</sub> N <sub>4</sub> -550-0W	9.0	0.032	47	4.8	/	2.68
C <sub>3</sub> N <sub>4</sub> -550-30W	16	0.078	17	5.2	/	2.74
C <sub>3</sub> N <sub>4</sub> -550-60W	37	0.225	15	3.8	/	2.76
C <sub>3</sub> N <sub>4</sub> -550-90W	30	0.150	16	2.8	/	2.77
C <sub>3</sub> N <sub>4</sub> -550-120W	28	0.130	15	2.2	/	2.78
C <sub>3</sub> N <sub>4</sub> /WO <sub>3</sub> 10%	16	0.091	15	81	/	2.80
C <sub>3</sub> N <sub>4</sub> /WO <sub>3</sub> 20%	11	0.077	30	74	/	2.76
C <sub>3</sub> N <sub>4</sub> /WO <sub>3</sub> 30%	30	0.186	20	82	/	2.82
C <sub>3</sub> N <sub>4</sub> /WO <sub>3</sub> 40%	9	0.088	21	77	/	2.84
WO <sub>3</sub>	/	/	/	20	Orthorhombic	2.65
FSP-TiO <sub>2</sub> -PAL	67	0.020	18	20(A);25(R)	A(65); R(35)	3.20
TiO <sub>2</sub> -exCl	111	/	6	/	Poorly cryst.	3.05
C <sub>3</sub> N <sub>4</sub> -TE	113	0.019	22	/	Poorly cryst.	2.80
TiO <sub>2</sub> -exCl/TE	76	0.036	6	/	Poorly cryst.	2.95
P25/TE	39	0.002	12	17(A);17(R)	A(85); R(15)	2.90
0.1% Au/P25	38	0.394	32	18(A);66(R)	86(A);14(R)	3.14
0.1% Pt/P25	35	0.474	38	19(A);65(R)	86(A);14(R)	3.18
1% (Au <sub>6</sub> Pt <sub>4</sub> )/P25	45	0.467	38	20(A);82(R)	81(A);19(R)	3.22

1% (Au <sub>8</sub> Pt <sub>2</sub> )/P25	52	0.480	42	20(A);87(R)	80(A);20(R)	3.19
Sample	BET SSA (m <sup>2</sup> /g)	Total pore volume (cm <sup>3</sup> /g)	BJH ads. pore width (nm)	Crystallite size (nm)	Phase %	BG (eV)
1% Ag/P25	56	0.266	36	17(A);15(R)	89(A);11(R)	3.25
0.1% Pd/P25	39	0.511	32	19(A);25(R)	74(A);26(R)	3.14

## References

1. Cychosz, K.A.; Thommes, M. Progress in the Physisorption Characterization of Nanoporous Gas Storage Materials. *Engineering* **2018**, *4*, 559–566, doi:10.1016/j.eng.2018.06.001.
2. Zdravkov, B.D.; Čermák, J.J.; Šefara, M.; Janků, J. Pore classification in the characterization of porous materials: A perspective. *Cent. Eur. J. Chem.* **2007**, *5*, 385–395, doi:10.2478/s11532-007-0017-9.
3. Han, X.; Xu, D.; An, L.; Hou, C.; Li, Y.; Zhang, Q.; Wang, H. WO<sub>3</sub>/g-C<sub>3</sub>N<sub>4</sub> two-dimensional composites for visible-light driven photocatalytic hydrogen production. *Int. J. Hydrogen Energy* **2018**, *43*, 4845–4855, doi:10.1016/j.ijhydene.2018.01.117.
4. Bagheri, S.; Muhd Julkapli, N.; Bee Abd Hamid, S. Titanium dioxide as a catalyst support in heterogeneous catalysis. *Sci. World J.* **2014**, *2014*, 1–21, doi:10.1155/2014/727496.
5. Naik, B.; Manoratne, C.H.; Chandrashekhar, A.; Iyer, A.; Prasad, V.S.; Ghosh, N.N. Preparation of TiO<sub>2</sub>, Ag-doped TiO<sub>2</sub> nanoparticle and TiO<sub>2</sub>-SBA-15 nanocomposites using simple aqueous solution-based chemical method and study of their photocatalytical activity. *J. Exp. Nanosci.* **2013**, *8*, 462–479, doi:10.1080/17458080.2011.597435.

6. Alwin, E.; Kočí, K.; Wojcieszak, R.; Zieliński, M.; Edelmannová, M.; Pietrowski, M. Influence of high temperature synthesis on the structure of graphitic carbon nitride and its hydrogen generation ability. *Materials (Basel)*. **2020**, *13*, 1–19, doi:10.3390/ma13122756.
7. Wang, X.; Maeda, K.; Thomas, A.; Takanabe, K.; Xin, G.; Carlsson, J.M.; Domen, K.; Antonietti, M. A metal-free polymeric photocatalyst for hydrogen production from water under visible light. *Nat. Mater.* **2009**, *8*, 76–80, doi:10.1038/nmat2317.
8. Huang, L.; Xu, H.; Li, Y.; Li, H.; Cheng, X.; Xia, J.; Xu, Y.; Cai, G. Visible-light-induced WO<sub>3</sub>/g-C<sub>3</sub>N<sub>4</sub> composites with enhanced photocatalytic activity. *Dalt. Trans.* **2013**, *42*, 8606–8616, doi:10.1039/c3dt00115f.
9. Li, Y.; Li, F.; Li, C.; Wei, W.; Jiang, D.; Zhu, L.; Sun, D.; Zhang, X.; Ruan, S. The preparation of Cr<sub>2</sub>O<sub>3</sub>@WO<sub>3</sub> hierarchical nanostructures and their application in the detection of volatile organic compounds (VOCs). *RSC Adv.* **2015**, *5*, 61528–61534, doi:10.1039/c5ra06667k.
10. Leong, K.H.; Gan, B.L.; Ibrahim, S.; Saravanan, P. Synthesis of surface plasmon resonance (SPR) triggered Ag/TiO<sub>2</sub> photocatalyst for degradation of endocrine disturbing compounds. *Appl. Surf. Sci.* **2014**, *319*, 128–135, doi:10.1016/j.apsusc.2014.06.153.
11. Praus, P.; Svoboda, L.; Smetana, B. Exfoliated nanosheets of graphitic carbon nitride: Study of structure and morphology. In Proceedings of the NANOCON 2016 - Conference Proceedings, 8th International Conference on Nanomaterials - Research and Application; 2016; pp. 92–97.
12. Elbanna, O.; Fujitsuka, M.; Majima, T. G-C<sub>3</sub>N<sub>4</sub>/TiO<sub>2</sub> Mesocrystals Composite

- for H<sub>2</sub> Evolution under Visible-Light Irradiation and Its Charge Carrier Dynamics. *ACS Appl. Mater. Interfaces* **2017**, 9, 34844–34854, doi:10.1021/acsami.7b08548.
13. Kowalska, E.; Janczarek, M.; Rosa, L.; Juodkazis, S.; Ohtani, B. Mono- and bi-metallic plasmonic photocatalysts for degradation of organic compounds under UV and visible light irradiation. *Catal. Today* **2014**, 230, 131–137, doi:10.1016/j.cattod.2013.11.021.
  14. Fernandes MacHado, N.R.C.; Santana, V.S. Influence of thermal treatment on the structure and photocatalytic activity of TiO<sub>2</sub> P25. *Catal. Today* **2005**, 107–108, 595–601, doi:10.1016/j.cattod.2005.07.022.
  15. Khore, S.K.; Kadam, S.R.; Naik, S.D.; Kale, B.B.; Sonawane, R.S. Solar light active plasmonic Au@TiO<sub>2</sub> nanocomposite with superior photocatalytic performance for H<sub>2</sub> production and pollutant degradation. *New J. Chem.* **2018**, 42, 10958–10968, doi:10.1039/c8nj01410h.
  16. Bowering, N.; Croston, D.; Harrison, P.G.; Walker, G.S. Silver modified degussa P25 for the photocatalytic removal of nitric oxide. *Int. J. Photoenergy* **2007**, 2007, 1–8, doi:10.1155/2007/90752.
  17. Tian, B.; Zhang, J.; Tong, T.; Chen, F. Preparation of Au/TiO<sub>2</sub> catalysts from Au(I)-thiosulfate complex and study of their photocatalytic activity for the degradation of methyl orange. *Appl. Catal. B Environ.* **2008**, 79, 394–401, doi:10.1016/j.apcatb.2007.11.001.
  18. Kessler, F.K.; Zheng, Y.; Schwarz, D.; Merschjann, C.; Schnick, W.; Wang, X.; Bojdys, M.J. Functional carbon nitride materials-design strategies for electrochemical devices. *Nat. Rev. Mater.* **2017**, 2, 17030,

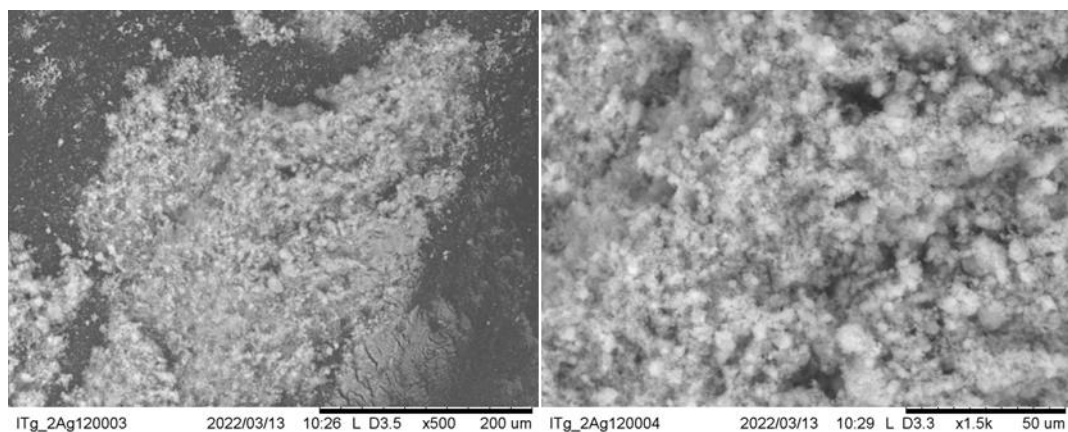


doi:10.1038/natrevmats.2017.30.

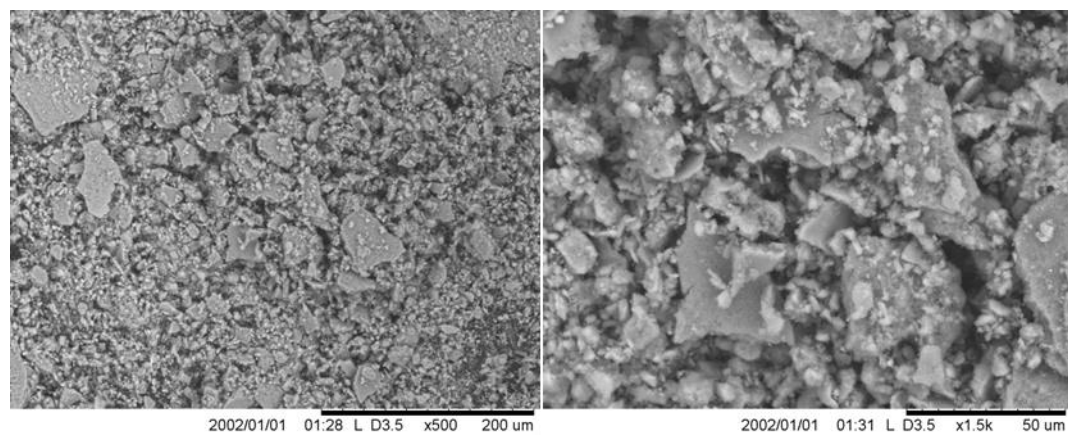
19. Jiang, H.; Li, Y.; Wang, D.; Hong, X.; Liang, B. Recent Advances in Heteroatom Doped Graphitic Carbon Nitride (g-C<sub>3</sub>N<sub>4</sub>) and g-C<sub>3</sub>N<sub>4</sub>/Metal Oxide Composite Photocatalysts. *Curr. Org. Chem.* **2020**, *24*, 673–693, doi:10.2174/1385272824666200309151648.
20. Yin, S.; Han, J.; Zhou, T.; Xu, R. Recent progress in g-C<sub>3</sub>N<sub>4</sub> based low cost photocatalytic system: Activity enhancement and emerging applications. *Catal. Sci. Technol.* **2015**, *5*, 5048–5061, doi:10.1039/c5cy00938c.
21. Kwong, W.L.; Savvides, N.; Sorrell, C.C. Electrodeposited nanostructured WO<sub>3</sub> thin films for photoelectrochemical applications. *Electrochim. Acta* **2012**, *75*, 371–380, doi:10.1016/j.electacta.2012.05.019.
22. Petica, A.; Florea, A.; Gaidau, C.; Balan, D.; Anicai, L. Synthesis and characterization of silver-titania nanocomposites prepared by electrochemical method with enhanced photocatalytic characteristics, antifungal and antimicrobial activity. *J. Mater. Res. Technol.* **2019**, *8*, 41–53, doi:10.1016/j.jmrt.2017.09.009.
23. Sandulescu, A.; Anastasescu, C.; Papa, F.; Raciulete, M.; Vasile, A.; Spataru, T.; Scarisoreanu, M.; Fleaca, C.; Mihailescu, C.N.; Teodorescu, V.; et al. Advancements on basic working principles of photo-driven oxidative degradation of organic substrates over pristine and noble metal-modified TiO<sub>2</sub>. Model case of phenol photo oxidation. *Catalysts* **2021**, *11*, 487, doi:10.3390/catal11040487.
24. Liu, Z.; Jia, B.; Zhang, Y.; Haneda, M. Engineering the Metal-Support Interaction on Pt/TiO<sub>2</sub> Catalyst to Boost the H<sub>2</sub>-SCR of NO<sub>x</sub>. *Ind. Eng. Chem. Res.* **2020**, *59*, 13916–13922, doi:10.1021/acs.iecr.0c01792.
25. Liu, L.; Zhang, X.; Yang, L.; Ren, L.; Wang, D.; Ye, J. Metal nanoparticles

- induced photocatalysis. *Natl. Sci. Rev.* **2017**, *4*, 761–780, doi:10.1093/nsr/nwx019.
26. Tougaard, S. Quantitative analysis of the inelastic background in surface electron spectroscopy. *Surf. Interface Anal.* **1988**, *11*, 453–472, doi:10.1002/sia.740110902.
  27. Kruse, N.; Chenakin, S. XPS characterization of Au/TiO<sub>2</sub> catalysts: Binding energy assessment and irradiation effects. *Appl. Catal. A Gen.* **2011**, *391*, 367–376, doi:10.1016/j.apcata.2010.05.039.
  28. Yu, F.; Wang, C.; Ma, H.; Song, M.; Li, D.; Li, Y.; Li, S.; Zhang, X.; Liu, Y. Revisiting Pt/TiO<sub>2</sub> photocatalysts for thermally assisted photocatalytic reduction of CO<sub>2</sub>. *Nanoscale* **2020**, *12*, 7000–7010, doi:10.1039/c9nr09743k.
  29. Subramanian, V.; Wolf, E.E.; Kamat, P. V. Influence of metal/metal ion concentration on the photocatalytic activity of TiO<sub>2</sub> - Au composite nanoparticles. *Langmuir* **2003**, *19*, 469–474, doi:10.1021/la026478t.
  30. Niu, P.; Zhang, L.; Liu, G.; Cheng, H.M. Graphene-like carbon nitride nanosheets for improved photocatalytic activities. *Adv. Funct. Mater.* **2012**, *22*, 4763–4770, doi:10.1002/adfm.201200922.
  31. García-López, E.I.; Abbasi, Z.; Di Franco, F.; Santamaria, M.; Marci, G.; Palmisano, L. Selective oxidation of aromatic alcohols in the presence of C<sub>3</sub>N<sub>4</sub> photocatalysts derived from the polycondensation of melamine, cyanuric and barbituric acids. *Res. Chem. Intermed.* **2021**, *47*, 131–156, doi:10.1007/s11164-020-04330-5.

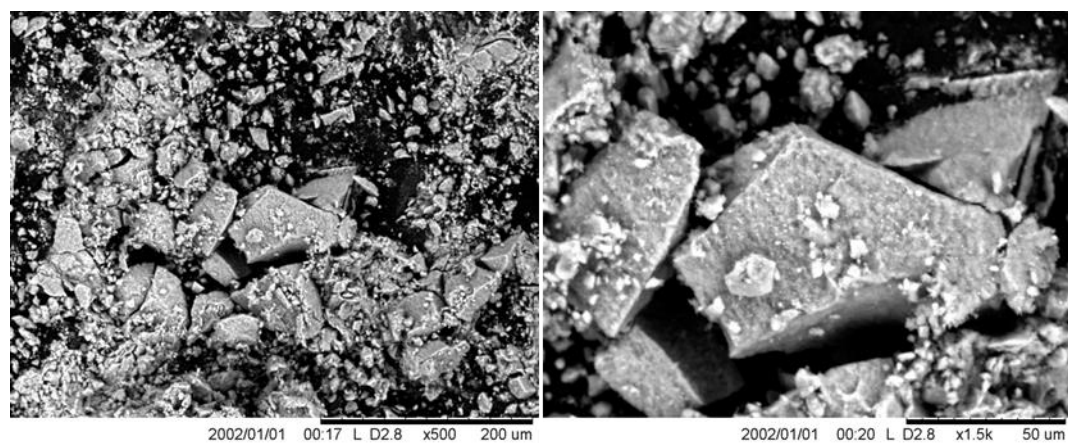
## Appendix A



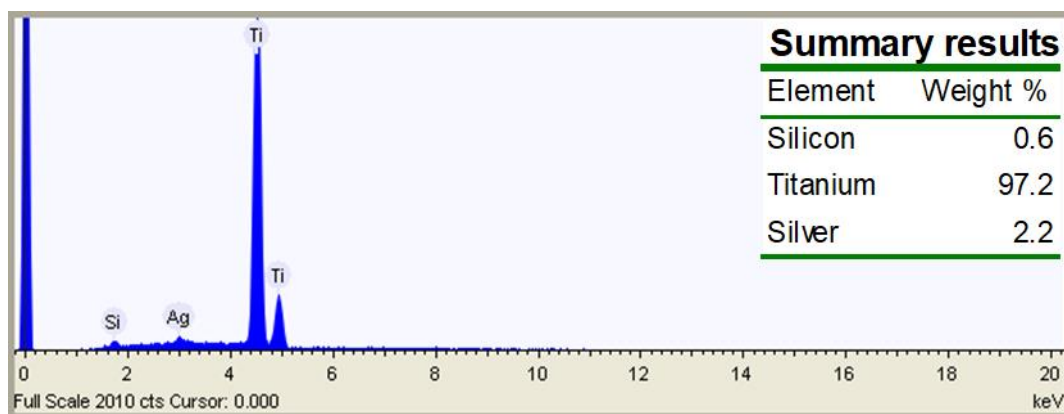
**Figure A1.** SEM images of TiO<sub>2</sub> P25



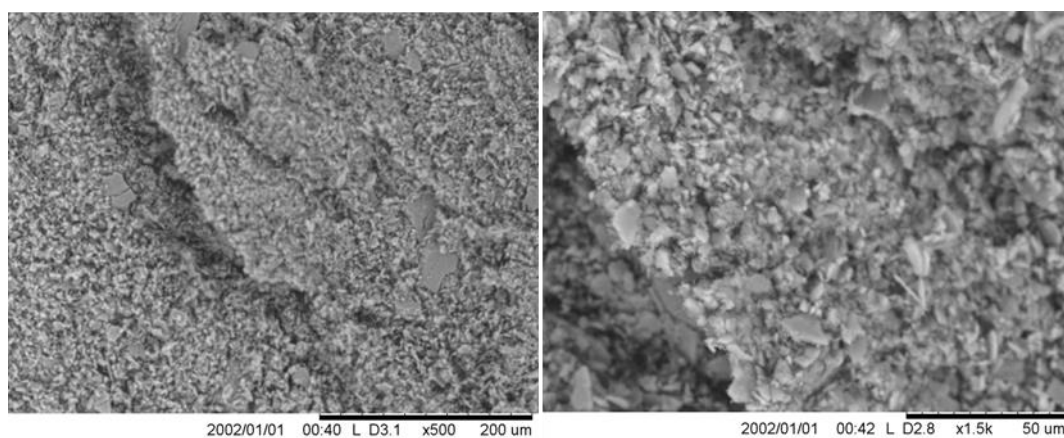
**Figure A2.** SEM images of P25 coated on glass and thermally treated at 500° (P25-500)



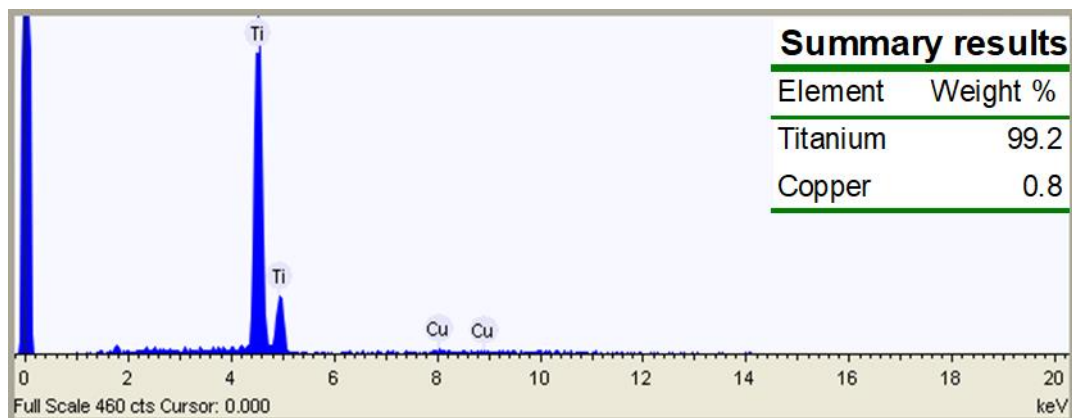
**Figure A3.** SEM images of P25 coated on glass and metallized with silver (Ag/P25-L)



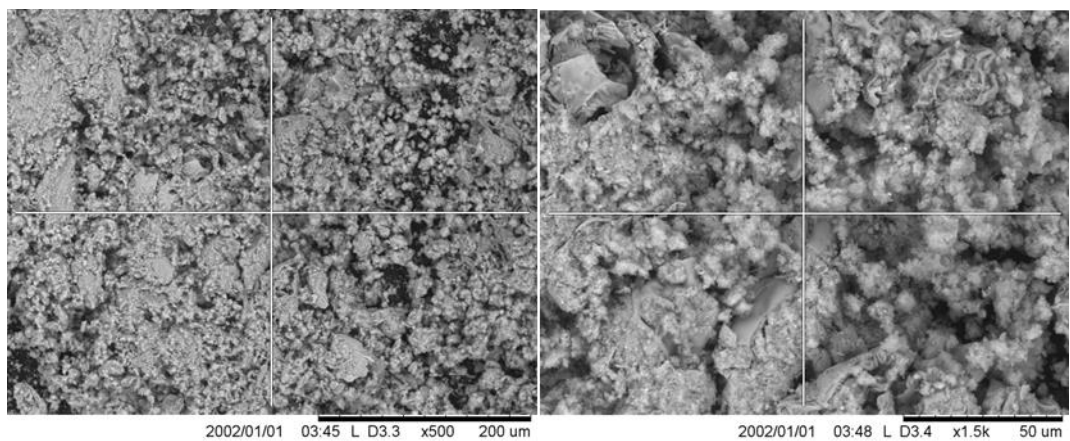
**Figure A4.** SEM-EDX of P25 coated on glass and metallized with silver (Ag/P25-L)



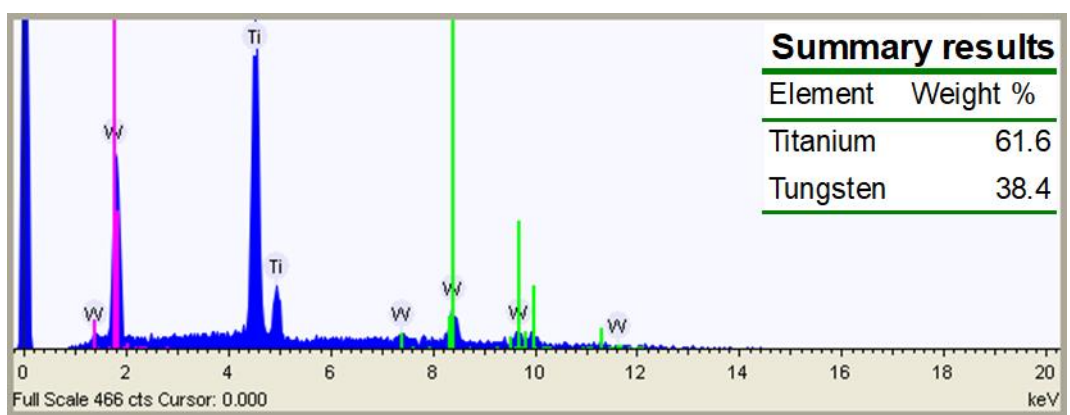
**Figure A5.** SEM images of P25 coated on glass and metallized with copper



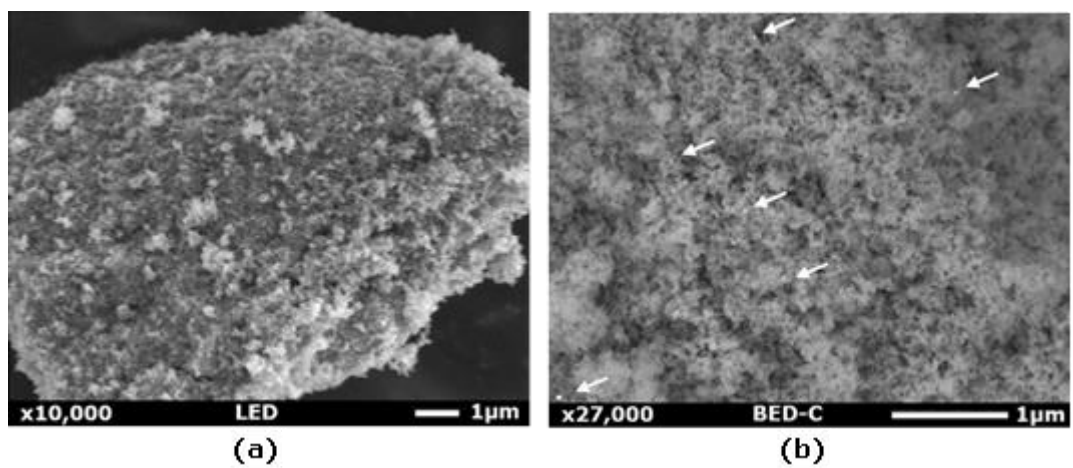
**Figure A6.** SEM-EDX of P25 coated on glass and metallized with copper



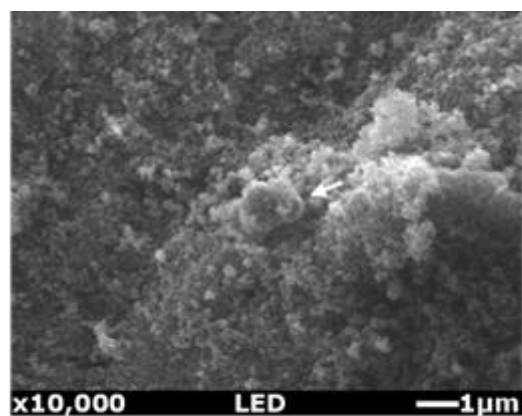
**Figure A7.** SEM images of FSP-TiO<sub>2</sub>/WO<sub>3</sub>-60/40



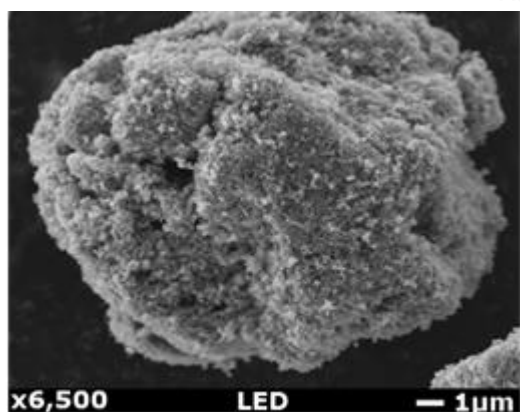
**Figure A8.** SEM-EDX of FSP-TiO<sub>2</sub>/WO<sub>3</sub>-60/40



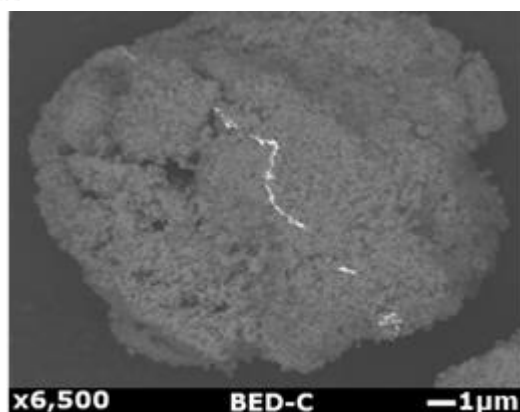




(c)

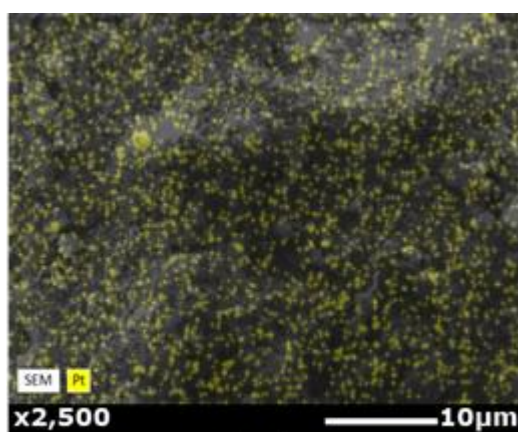


(d)

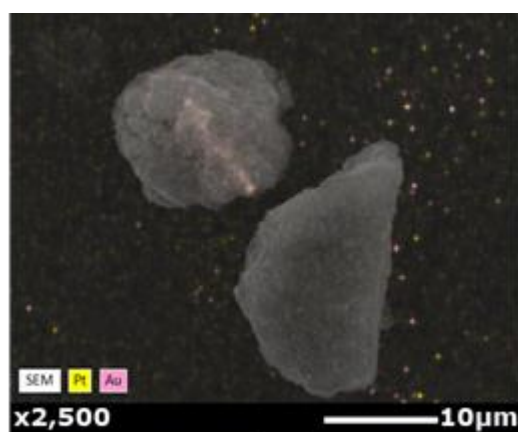


(e)

**Figure A9.** SEM images of (a) 0.36% Au/P25, (c) 0.36% Pt/P25 and (d) and 1% wt. (Au<sub>6</sub>Pt<sub>4</sub>)/P25. (b) and (e) have been taken using backscatter detector (BED-C)



(a)



(b)

**Figure A10.** SEM-EDX images of (a) 0.36% Pt/P25 and (b) 1% wt. (Au<sub>6</sub>Pt<sub>4</sub>)/P25

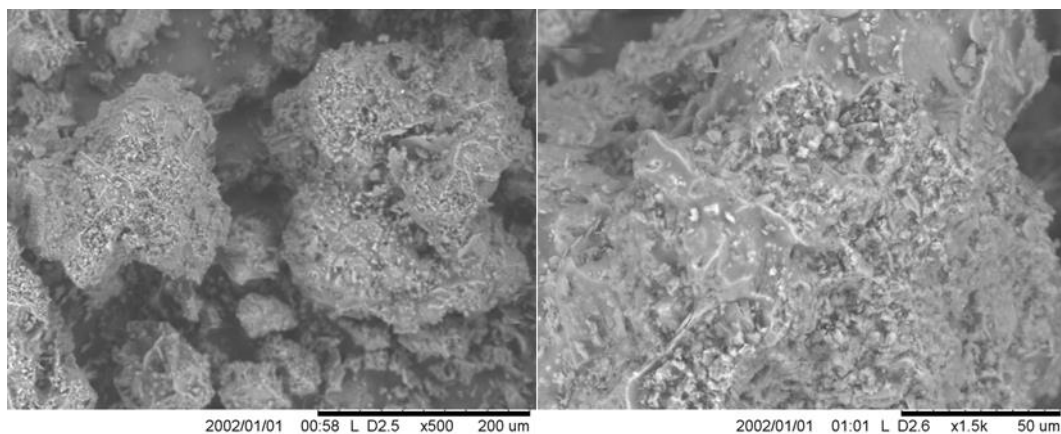


**Figure A11.** SEM images of g-C<sub>3</sub>N<sub>4</sub>-550

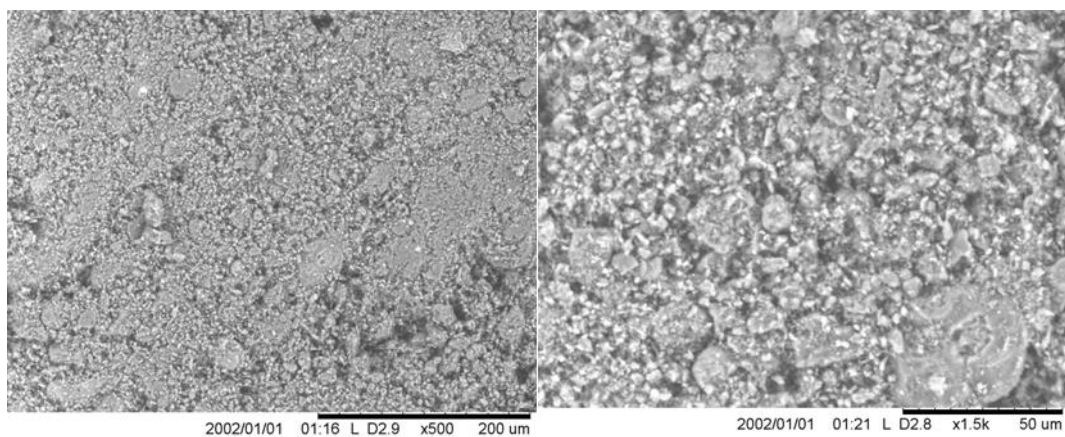


**Figure A12.** SEM images of g-C<sub>3</sub>N<sub>4</sub>-550-120W

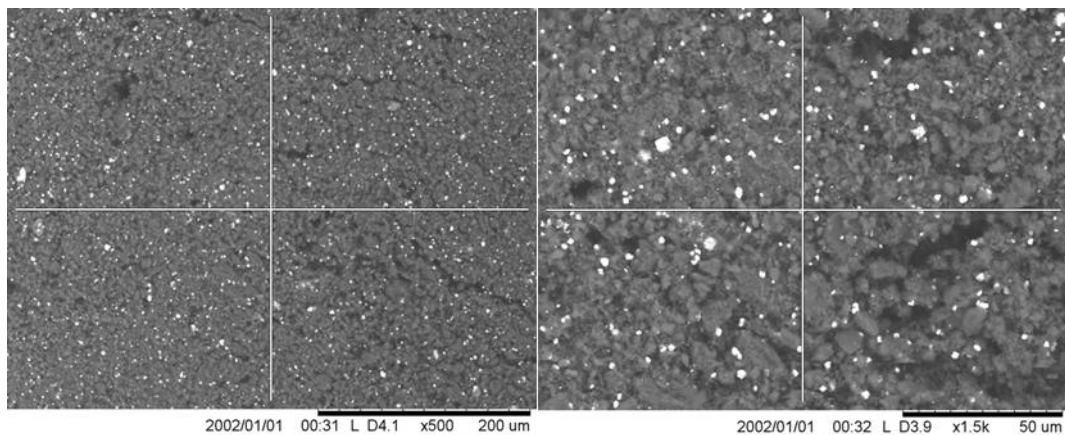


**Figure A13.** SEM images of g-C<sub>3</sub>N<sub>4</sub>/WO<sub>3</sub>-10%

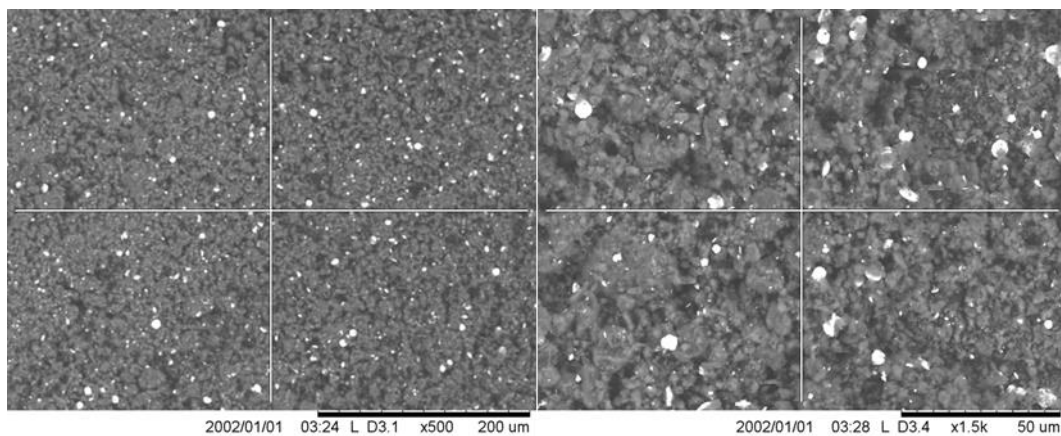


**Figure A14.** SEM images of g-C<sub>3</sub>N<sub>4</sub>/WO<sub>3</sub>-20%

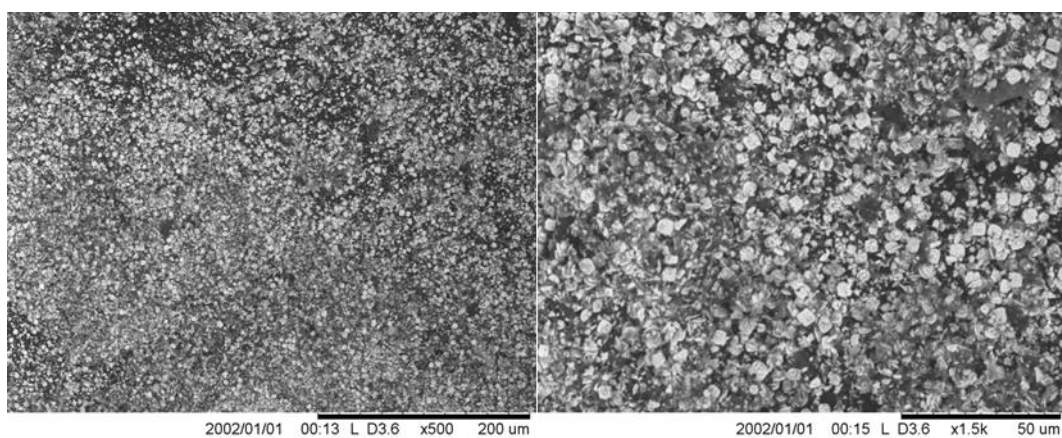


**Figure A15.** SEM images of g-C<sub>3</sub>N<sub>4</sub>/WO<sub>3</sub>-30%

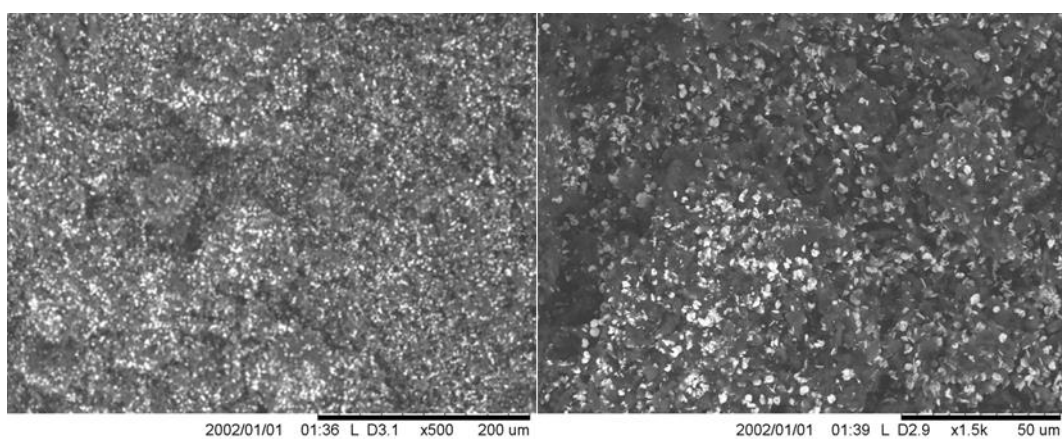


**Figure A16.** SEM images of g-C<sub>3</sub>N<sub>4</sub>/WO<sub>3</sub>-40%



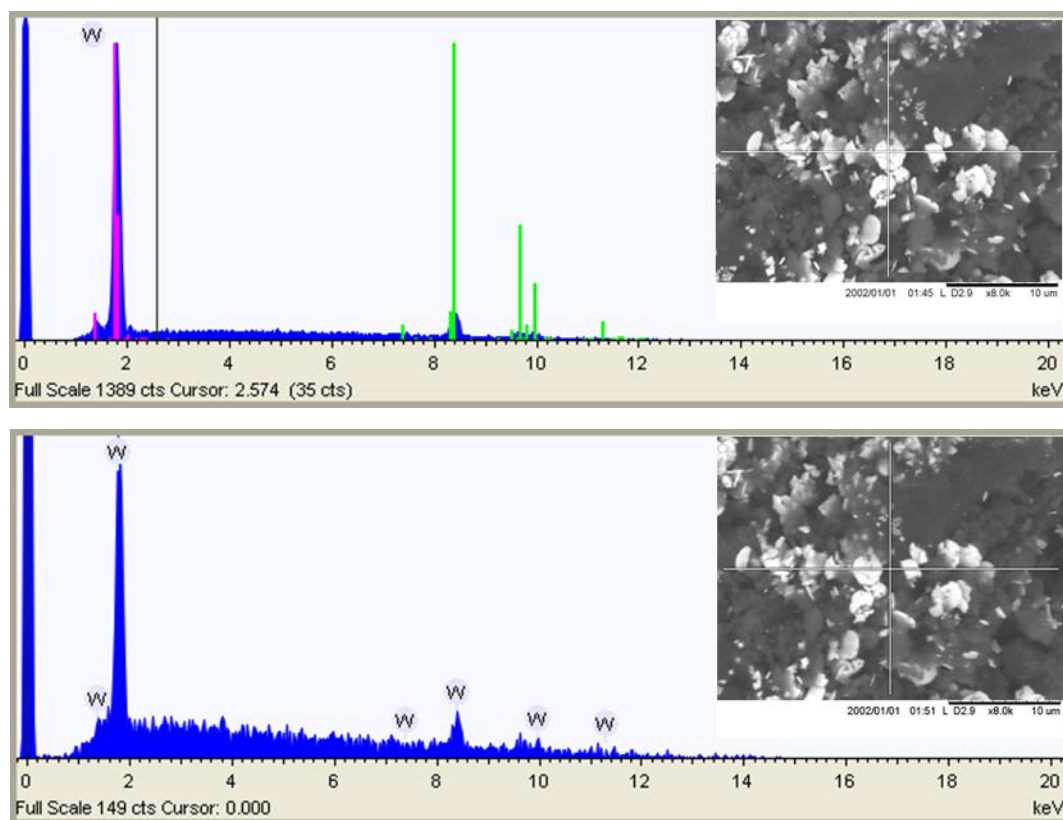


**Figure A16.** SEM-EDX of  $\text{g-C}_3\text{N}_4/\text{WO}_3\text{-40\%}$  on two different spots

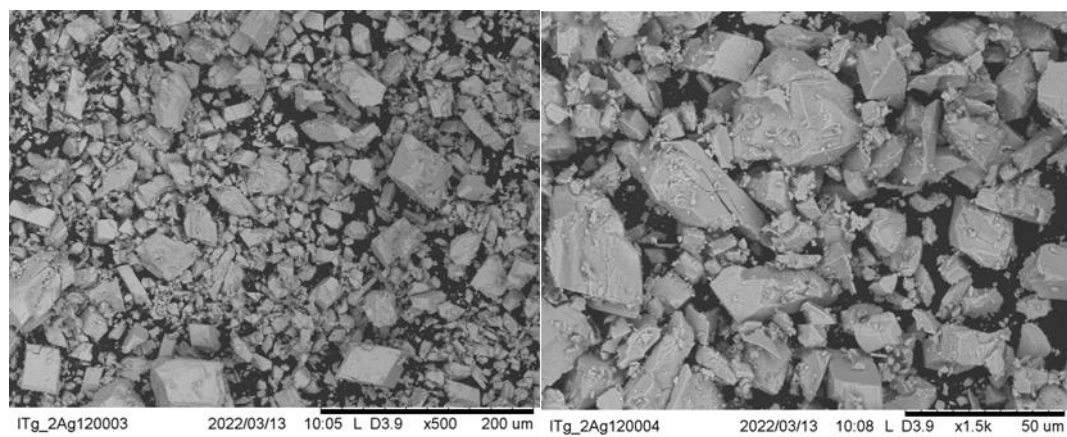


**Figure A17.** SEM images of bare  $\text{WO}_3$  prepared via thermal decomposition



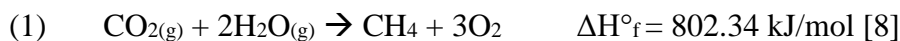
## 4. CO<sub>2</sub> photo-reduction

### 4.1. Introduction

It is pointless to affirm that carbon dioxide is the plague of our century, since the evidence of its noxious effects over the ecosystem of our planet keep adding up, and they cannot be ignored anymore. Indeed, the CO<sub>2</sub> concentration into atmosphere, which was less than 300 ppm back in 1900, surpassed the 400 ppm threshold in the 2015 [1]. Among the most obvious effects of this 25% increase since the pre-industrial era, we can find the global warming, as the average temperature of the planet has grown 1 °C in the past 150 years [2]. It may not seem a lot, however, given the huge mass involved, it means that the humanity has been able, to a small extent, to terraform our planet by modifying permanently its biome and climate and so entering the Anthropocene era [3]. Other repercussions include the acidification of the oceans and potentially risk to human health, since the pH of the blood is regulated through the CO<sub>2</sub>-bicarbonate buffer system [4].

The reason why the carbon dioxide is massively emitted into atmosphere is connected with the energetic content of carbon sources, like wood in the past and fossil fuels nowadays, which provide a reliable, stable and easily transportable source of energy. We are heavily dependent on oil, gas and carbon, and only few countries completely shifted the political agenda to include a sustainable growth of the respective economies [5]. Almost three-quarters of the CO<sub>2</sub> emitted are related to the Energy sector (namely heavy industries, power plants, transportation and buildings), while the rest is mainly released by the agriculture, land use and the cement sector [6]. Most of these are point sources and the carbon dioxide is dispersed in air since it is the most cost-effective way to get rid of this problematic product. In fact, the CO<sub>2</sub> is quite unreactive at standard temperature and pressure, as reported in Equation 1, and there are few uses for it, such as in carbonated

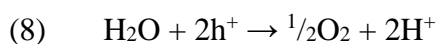
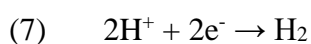
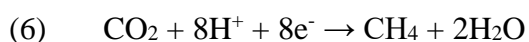
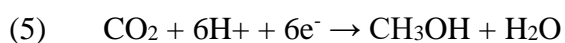
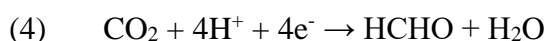
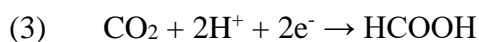
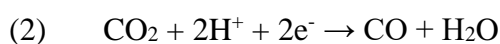
drinks and to enhance plant growth, whereas most of the effort to limit its emission is directed toward Carbon Capture and Sequestration (CCS) technologies and thermochemical conversion [7].



The sequestration of the carbon dioxide naturally occurs via acidification of the oceans and the photosynthesis performed by the plants. Still, half of the yearly emissions of this gas is free to accumulate [9]. In this regard, CCS techniques offer a long-term solution with a low environmental impact, since the CO<sub>2</sub> is converted into carbonate through interaction with the minerals present in the soil (*i.e.* rocks rich of calcium and magnesium), either in the production site or where the ores are extracted. Anyhow, the most used CCS method in the last twenty years is the underground sequestration in sedimentary formations, which, in shorts, means that whenever a barrel of oil is pumped out through the wells, from 0.3 to 0.6 tons of CO<sub>2</sub> are injected into the oilfield [10]. In that case, we refer to CO<sub>2</sub> enhanced oil recovery (CO<sub>2</sub>-EOR), which, unfortunately, is mostly performed using carbon dioxide from high concentrated sources, such as natural CO<sub>2</sub> gas fields [11].

On the other hand, most of the industries emits diluted CO<sub>2</sub>, since it is the results of the combustion of hydrocarbons using air. That exhaust gasses can be used to enhance plant growth in a process known as “yield boosting” [12], which increases the crop production up to one third, though it also depends on other parameters such as the temperature and the kind of crop [13]. Overall, if we take into account the whole market usage of carbon dioxide, its value barely reaches the 230 Mt [14] vs the 35 billion tons emitted each year [15]. Thus, it is crucial to invest in new technologies that allow to convert huge amounts of diluted CO<sub>2</sub> in a practical and economically sustainable way.

Among the possible solutions, CO<sub>2</sub> photoreduction is gaining traction since it is seen as a convenient way to use and store the energy from the sunlight and simultaneously get rid of this molecule [16,17]. In details, by using heterogeneous photocatalysis it is possible to adsorb and reduce the carbon dioxide over the photocatalysts surface, provided that its band gap can match the redox potential of the reaction. Regarding that, the injection of electrons can lead to a broad spectrum of products, as it is summarized by Equations 2-6. For instance, after addition of two photoexcited electrons it is theoretically possible to obtain carbon monoxide or formic acid, which are valuable commodities. Going further with the reduction, formaldehyde, methanol and methane are achieved, and all these molecules are valuable to the market. Although there is still an open discussion about the kind of electron transfer, which can be single or multiple, these are the main products that can be obtained by photoreduction of CO<sub>2</sub> in liquid or gas phase, however, there are also competing reactions such as the reduction of H<sup>+</sup> to molecular hydrogen (Equation 7) [17].



As intuitive, this process depends on many factors, including the irradiance of the light source, the temperature, the pressure, the reaction media, the kind of photocatalyst and its textural properties (surface area, adsorption properties, etc.). Our work focus on the high-pressure liquid-phase photoreduction of CO<sub>2</sub> using both TiO<sub>2</sub> and C<sub>3</sub>N<sub>4</sub> based materials.

The ideal reaction medium is water, since it is abundant and inexpensive and in theory should be able to be used as hole scavenger (HS), that is a sacrificial electron donor that reacts with the photogenerated hole in order to prevent its accumulation, anyhow, this reaction (Equation 8) is kinetically slow and severely limits the performance of the photoreduction process. In order to overcome that limitation, photoreduction treatments were conducted in alternative solvents, like methanol and ethanol, which consume the holes while providing a preferential reaction path toward certain products [18]. A critical step is surely the adsorption of carbon dioxide over the photocatalyst surface, and the setup here adopted employs a high-pressure stainless steel photoreactor that allows to work with pressure up to 20 bar. This further increases the dissolution of CO<sub>2</sub> into water and shifts the adsorption equilibria, leading to greater performance with respect to conventional systems [19]. Moreover, a sacrificial hole scavenger was added to the mixture, both inorganic hole scavengers such as sodium sulfite and ammonia, and organic ones like 2-propanol, acetone, acetic acid and others. This allowed to explore different products distributions and possibly find future alternatives. On the other hand, the pH at which the process is carried out influences the results, *in primis* because the solubility of CO<sub>2</sub> further increases at high pH and also for the role that carbonate and bicarbonate ions have in the adsorption and reduction steps [20].

Countless papers report the photoreduction of CO<sub>2</sub> in water using either TiO<sub>2</sub> or its modified forms [21,22]. Mizuno et al. [23] reported a modest yield of methanol and methane by using TiO<sub>2</sub> with carbonated water either in neutral or basic conditions, achieving a higher productivity when a modest CO<sub>2</sub> pressure was applied. Others reported an enhanced photoreduction when titania was used as a support for silver nanoparticles (up to 5%wt) and illuminated under UV light to obtain methanol, carbon monoxide,

methane and hydrogen [24], while Pd-loaded titania can lead to formation of formic acid [25]. Titania band gap limits its applicability, though. One of the possible replacements is represented by graphitic carbon nitride, whose band gap (2.9-2.7 eV) allows the absorption of visible light wavelengths and was already successfully tested in some previous works [26]. Mao et al. reported high yield of methanol after 12h of irradiation under simulated sunlight [27], while Ohno obtained the same product by compounding  $\text{WO}_3$  and g- $\text{C}_3\text{N}_4$  [28]. Compounding is advantageous, both for titania and graphitic carbon nitride, as the so-formed heterojunction allows to improve the photocatalytic performance of the material, which in general has a lower recombination rate of the photogenerated charges and a lower band gap.

In this thesis the photocatalytic activity is reported for various photocatalysts composed of  $\text{TiO}_2$ , g- $\text{C}_3\text{N}_4$ ,  $\text{WO}_3$  and several materials based on these and modified with the aim to obtain better performance.

## 4.2. Results and discussion

### 4.2.1. CO<sub>2</sub> photoreduction tests with TiO<sub>2</sub>, g-C<sub>3</sub>N<sub>4</sub>-TE and composites

#### 4.2.1.1. Effect of pH

During the photoreduction process, the carbon dioxide or the carbonate species can be adsorbed over the titanium dioxide surface by acid-base interaction with the hydroxylic groups or the coordinated Ti centers on the photocatalyst (acidic) [29,30]. In case of graphitic carbon nitride, some DFT calculations proposed that the adsorption of CO<sub>2</sub> on an ideal surface occurs via physisorption and interaction with the bi-coordinated nitrogen of the triazine/heptazine unit, which represents the building block of g-C<sub>3</sub>N<sub>4</sub> [31]. Anyway, real carbon nitride samples are not perfect surface and are often present -NH<sub>2</sub> and -NH moieties on the surface that coordinates with the CO<sub>2</sub> molecule and facilitate its adsorption via acid-base interactions [32].

That being said, it is intuitive to think that the pH at which the test is performed has a great influence on its result, not limited by the mere fact that a higher pH lead to a greater dissolution of CO<sub>2</sub> in the solvent, which is water. Indeed, carbon dioxide or carbonate can be reduced into HCOOH, CH<sub>3</sub>OH, HCHO and many other compounds through a multi-step electron addition that is influenced by the pH itself (among the other parameters). Indeed, at basic pH the formate ion is preferentially formed and then eventually reduced to formaldehyde and methane [33], with the process that is energetically uphill and is mainly limited by the adsorption of CO<sub>2</sub> over the photocatalyst surface [34,35].

In our case, it was decided to adjust the initial pH of the solution by addition of sodium hydroxide and in order to favor the production of formic acid, which is a valuable product. That was chosen since from early tests it was also found that the overall productivity of



organics was greater at pH=14 with respect to the tests at native pH and the overall stored energy in the formed products was superior as well [36–38].

#### 4.2.1.2. Effect of pressure

In general, it was decided to work with two values of pressure, that are 8 and 18 bar, as examples of high and intermediate pressure testing conditions. Also, as already said, the pH was increased by addition of sodium hydroxide in order to improve even more the solubility of the carbon dioxide and to favor the formation of formic acid. Negligible amounts of liquid or gaseous products were detected without addition of the photocatalyst, the hole scavenger or when the lamp was switched off. Typical photocatalyst and HS concentrations were respectively 31 mg/L and 1.67 g/L and the reaction time was usually 24h or 6h, if not differently specified.

Figures 4.1 and 4.2 illustrates the effect of the pressure on the activity of several titania and  $C_3N_4$  photocatalysts from University of Palermo. It is evident from the graph that the productivity of  $HCOOH$ , and in a lower degree  $H_2$ , increases along with the pressure, which improves the adsorption of the reactants over the photocatalyst surface.  $TiO_2$ -exCl sample increases its productivity of formic acid by 64% when pressure was increased from 8 to 18 bar, which is less than the gain that was observed in case of the benchmark P25 (+91%) and FSP titania (+240%). In terms of absolute value of productivity,  $TiO_2$ -exCl seems to be the most active photocatalyst with almost 12 mol/kg<sub>cat</sub>·h (at 18 bar), followed by FSP (7.5 mol/kg<sub>cat</sub>·h) and P25 (*ca.* 6.5 mol/kg<sub>cat</sub>·h). The trend is not the same for hydrogen production, however,  $H_2$  is mainly generated once the HS is almost fully consumed, and the organics present in the reaction medium start to react as hole scavengers themselves [39]. During these tests, due to the long reaction time (24h) the

HS conversion was always higher than 95% and so both liquid and gaseous products were observed. On the other hand, formaldehyde and methanol were not detected, as one should expect in these conditions. The activity of TiO<sub>2</sub>-exCl may be higher than the other samples as it exhibits a lower band gap (3.05 eV), so that, being the light source polychromatic, it can theoretically absorb more radiation than other titania samples. In addition, its specific surface area (111 m<sup>2</sup>/g) was significantly higher than both P25 (47 m<sup>2</sup>/g) and FSP titania (67 m<sup>2</sup>/g).

Thermally exfoliated graphitic carbon nitride (TE g-C<sub>3</sub>N<sub>4</sub>) and its composites with TiO<sub>2</sub>-exCl perform very differently at low pressure but similarly at 18 bar. Actually, the productivity of formic acid for TE sample was 15% lower at high pressure, which is compensated by the 3-fold increase of H<sub>2</sub> concentration. Conversely, TiO<sub>2</sub>-exCl produced 2.5-times more formic acid (with respect to 8 bar) and P25/TE doubled its performance, achieving the highest productivity among the series (13.5 mol/kg<sub>cat</sub> h). P25/TE composite has a slightly higher band gap than the bare C<sub>3</sub>N<sub>4</sub> (2.9 eV vs 2.8 eV) and a lower surface area, therefore, these results cannot be explained by the differences in the textural or optical properties. The Z-scheme that results when these two photocatalysts are electrically connected sees the photogenerated electrons migrate from titania to C<sub>3</sub>N<sub>4</sub>, as its CB is located at more negative potential with respect to TiO<sub>2</sub>, and this improves the charge separation and so the efficiency of the photocatalyst [40]. By contrast, pure C<sub>3</sub>N<sub>4</sub> has a high electrical conductivity along the nanosheets and the photogenerated charges tend to recombine rather than react with the adsorbed CO<sub>2</sub>.

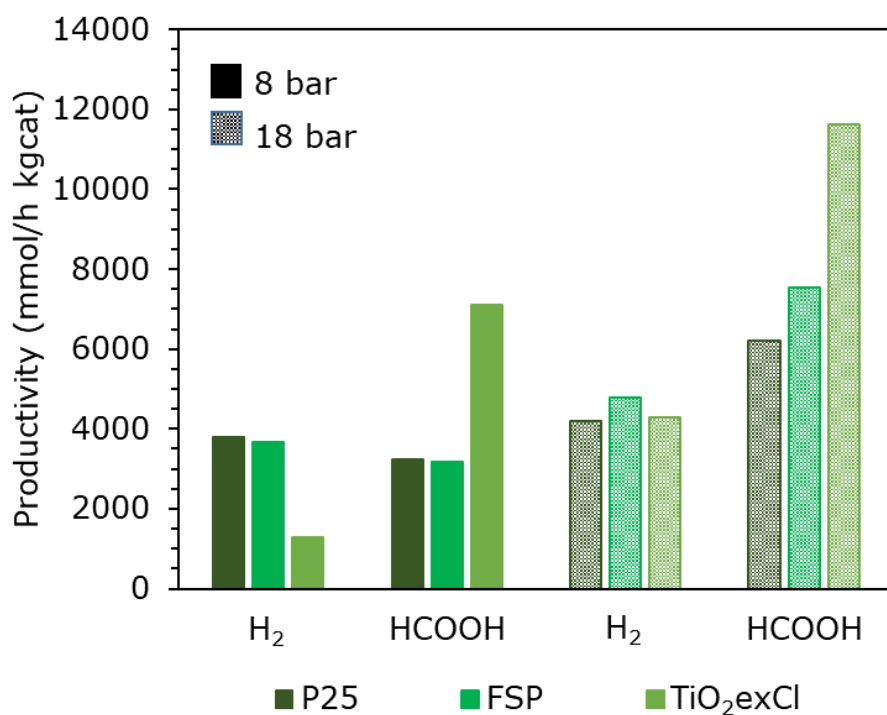


**Figure 4.1.** Effect of pressure on productivity at 8 and 18 bar for TiO<sub>2</sub> samples. 24h, pH=14, 31 mg/L of photocatalyst and 1.67 g/L of HS

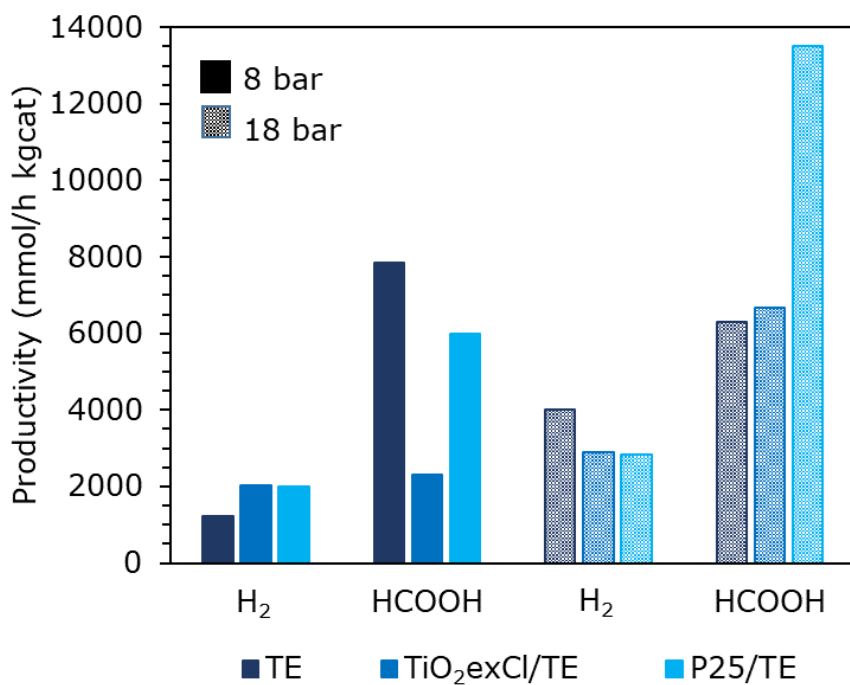


**Figure 4.2.** Effect of pressure on productivity at 8 and 18 bar for TE-C<sub>3</sub>N<sub>4</sub> and its composites with different TiO<sub>2</sub>. 24h, pH=14, 31 mg/L of photocatalyst and 1.67 g/L of HS

#### 4.2.1.3. Effect of HS concentration

The amount of HS added to the photoreactor was optimized by using P25 as photocatalyst, thus, in order to prevent the consumption of formic acid formed *in situ*, further tests were carried out with an increased concentration of HS, up to 5 g/L (Figure 4.3), while keeping the pressure at 18 bar. The activity of the two composites (*i.e.* TiO<sub>2</sub>-exCl and P25/TE) greatly improved when the concentration of the HS was tripled, in particular, TiO<sub>2</sub>-exCl/TE achieved a HCOOH productivity of 26 mol/kg<sub>cat</sub> h (+92% from the previous result) and for P25/TE it increased over two-times (29 mol/kg<sub>cat</sub> h). As expected, the productivity of H<sub>2</sub> in both cases was substantially lower when the HS concentration was increased. It is likely that the lower performance of the composite with TiO<sub>2</sub>-exCl is related to its low crystallinity, as there are evidence of an highly efficient charge separation when C<sub>3</sub>N<sub>4</sub> is couple with TiO<sub>2</sub> nanocrystals [41].

Although the HS concentration was increased by three-fold, its conversion was still above 95%. In light of that, the reaction time was lowered from 24h to 6h to avoid the fully consumption of the HS.

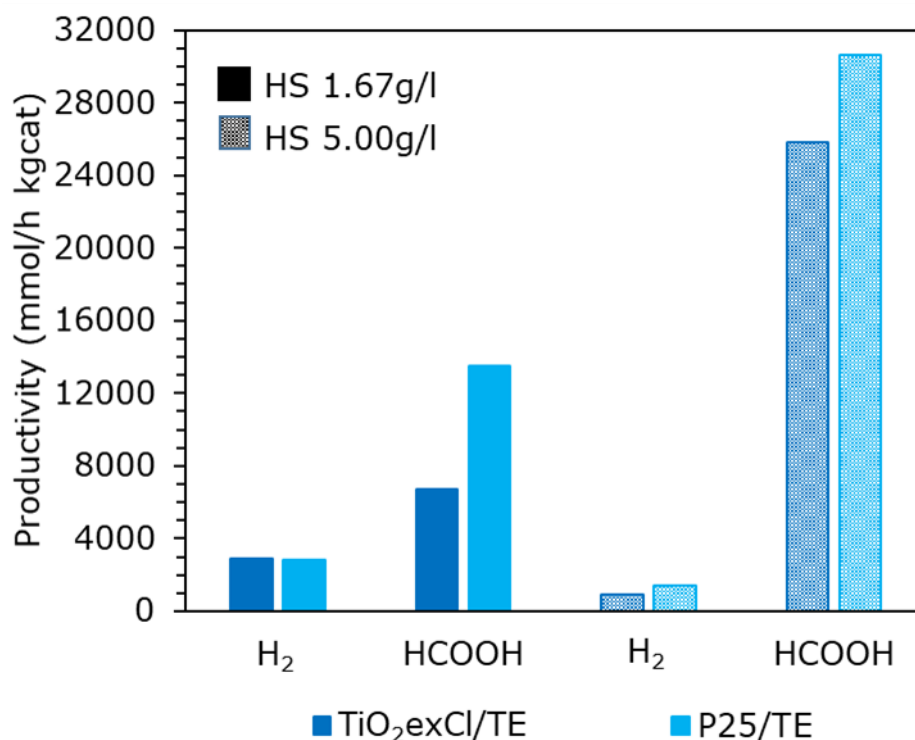


**Figure 4.3.** Effect of hole scavenger concentration on products distribution and productivity (1.67 and 5 g/L). 24h, pH=14, 31 mg/L of photocatalyst

#### 4.2.1.4. Effect of reaction time

So far, the one-day long test allowed to observe the productivity of hydrogen along with formic acid, however, a series of shorter tests allowed to better understand the real activity of these photocatalysts in terms of the formic acid productivity. The graphs of Figures 4.4 and 4.5 illustrate the results of the photoreduction performed over 6h of illumination at 18 bar of CO<sub>2</sub> and with 1.67 g/L of photocatalyst. The most evident consequence is that the hydrogen productivity dropped to zero, or below 400 mmol/kg<sub>cat</sub> h in case of the composites, which is in line with the conversion of the hole scavenger (Figure 4.5) that was lower than 80% in every case analyzed. In those conditions, the activity of TiO<sub>2</sub>-exCl, TiO<sub>2</sub>-exCl/TE and P25/TE was quite similar (HCOOH  $\approx$  40 mol/kg<sub>cat</sub> h), while the

rest of the photocatalysts (P25, FSP and TE) did not achieve more than 16 mol/kg<sub>cat</sub> h. With respect to the previous case (*i.e.* 18 bar and 24h), the productivity of formic acid for each catalyst increased respectively by +260% for P25, +180% for FSP, +230% for TiO<sub>2</sub>-exCl, +220% for TE, +420% TiO<sub>2</sub>-exCl/TE and +200% for P25/TE.

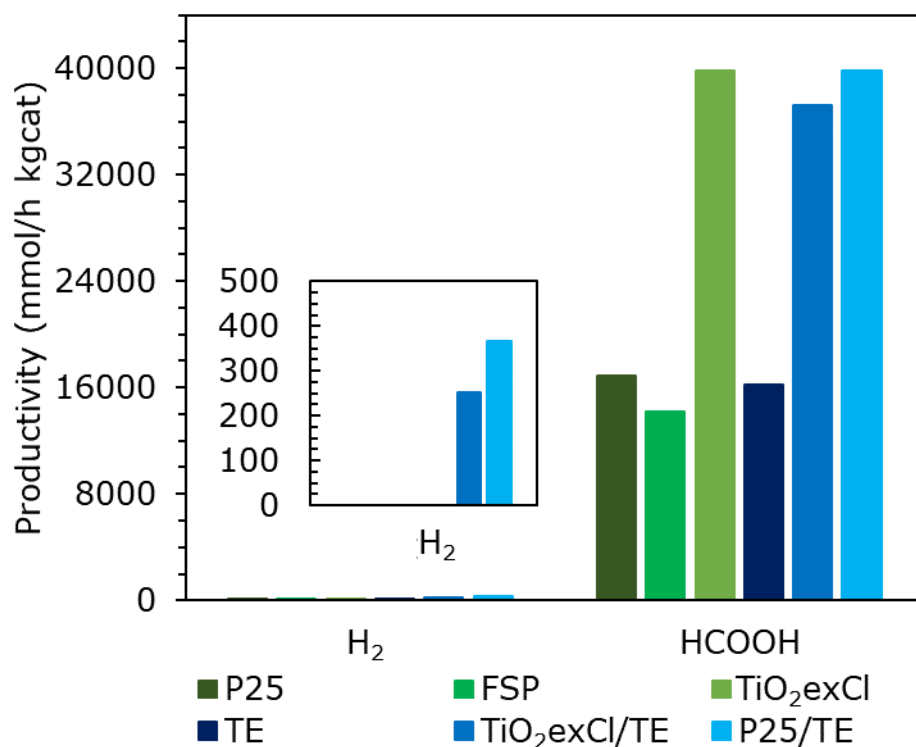


**Figure 4.4.** Tests performed at 18 bar, 6 h, pH=14, 31 mg/l of photocatalyst and 1.67g/l of HS concentration

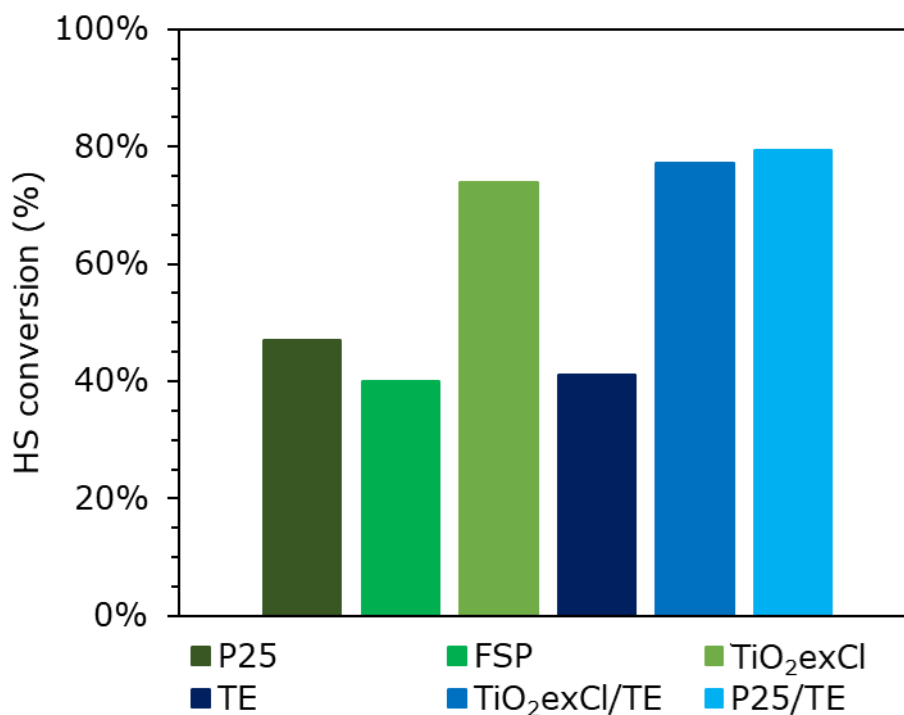


**Figure 4.5.** HS conversion in case of shorter tests (6h)

#### 4.2.1.5. Economic assessment of photocatalytic process

A technology such as the one proposed in this manuscript will theoretically allow to convert the energy from the sunlight into the energy of the chemical bonds, which is particularly interesting since it opens the possibility for the long-term storage of the solar energy. This point is particularly interesting as existing technologies based on renewables, like photovoltaic and wind, are characterized by a discontinuous and not reliable production of energy that is not economically feasible to store, unlike chemicals. Given the context, it could be quite interesting to make a rough estimate of the amount of energy that a photocatalyst is able to convert, from light to chemicals. As an example, the maximum measured HCOOH productivity of the composite photocatalyst P25/TE was 39.8 mol/kg<sub>cat</sub> h, that is about 9.1 mmol or 0.42 g of formic acid dissolved in the volume of the reactor ( $MM_{\text{HCOOH}}=46.03$  g/mol). If we consider that the higher heating value

(HHV) of this organic acid is 5.5 kJ/g, the energetic content of the product from the photoreduction is around 2.3kJ, of course without considering the small amount of hydrogen detected during the test. The input energy is represented by the lamp, which is powered by a 250W power supply, and although most of the energy is dissipated as heat rather than UV light, we can calculate that after 6h (or 21'600 seconds) of test the energy consumed is 5.4 MJ. From here, the efficiency can be defined as follows (Eq. 1):

$$\text{Energy Efficiency (on lamp power) (\%)} = \frac{E_{HCOOH}(J)}{E_{lamp}(W) \text{ time (s)}} \cdot 100 \quad (\text{Eq. 1})$$

$$\text{Energy Eff. (on irradiance) (\%)} = \frac{E_{HCOOH}(J)}{E_{irr.} \left( \frac{J}{h \ m^2} \right) \text{ time (h)} \tilde{S} (m^2)} \cdot 100 \quad (\text{Eq. 2})$$

If the conditions described above are used as input data for Eq. 1, the result is a 0.04% conversion efficiency. This is quite low, especially if compared with commercial PVs system that are able to reach efficiency around 20%.

Anyway, the efficiency of the energy storage can also be calculated as described by Eq. 2, and so by referring to the real irradiance of the lamp, that is lower than power consumption. This is important if one is planning to understand the feasibility in case natural solar radiation is used. Considering the reactor geometry (S is the mean irradiated surface) and the lamp irradiance, the calculated efficiency is about 1.2%.

#### 4.2.2. CO<sub>2</sub> photoreduction tests with g-C<sub>3</sub>N<sub>4</sub> and WO<sub>3</sub> composites

Based on the interesting results obtained over carbon nitrides and its visible light absorption, this type of catalysts was deepened. The photocatalysts presented in this section were prepared via controlled thermal decomposition of melamine either at 550°C



or 600°C, and subsequently delaminated via ultrasonic treatment. Indeed, bulk carbon nitride has low surface area, that can be increased by exfoliation. Exfoliation was carried out in the previous paragraphs through thermal treatment, while here we considered ultrasounds (US) as a method to delaminate the materials. The so-formed exfoliated graphitic carbon nitride samples were labeled depending on the exfoliation US power and are C<sub>3</sub>N<sub>4</sub>-550-0W, C<sub>3</sub>N<sub>4</sub>-550-30W, C<sub>3</sub>N<sub>4</sub>-550-60W, C<sub>3</sub>N<sub>4</sub>-550-90W, C<sub>3</sub>N<sub>4</sub>-550-120W, C<sub>3</sub>N<sub>4</sub>-600-0W and C<sub>3</sub>N<sub>4</sub>-600-120W. As reported later in this section, C<sub>3</sub>N<sub>4</sub>-550-120W shows the highest activity among the series (in the selected conditions) and so it was used to synthesize a further series of composites with WO<sub>3</sub> and different loading (w/w %), namely 10%, 30%, 30% and 40%. The logic was the same of the other composites already reported (e.g. P25/TE), since the Z-scheme allows for an efficient charge separation and actually increases the lifetime of the photogenerated charges, we expected that WO<sub>3</sub> and C<sub>3</sub>N<sub>4</sub> could form an efficient heterojunction for charge transfer. Furthermore, they are both visible responsive materials, opening the way to visible light application.

All the tests gave negligible productivity when the catalyst was not added to the reactor, as well as when the HS was not present in the solution, and both are required to perform the treatment. Furthermore, negligible productivity was achieved when operating in dark conditions.

#### **4.2.2.1. Tests with exfoliated g-C<sub>3</sub>N<sub>4</sub>**

Figure 4.6 illustrates the activity, in terms of productivity of the two most abundant products of CO<sub>2</sub> photoreduction (*i.e.* HCOOH and H<sub>2</sub>) carried out with the series of exfoliated graphitic carbon nitride and compared with the benchmark P25. Methanol, formaldehyde and CO were detected in traces. The tests were still 24h-long, therefore,

almost full consumption of the HS was achieved in each experiment. From the graph of Figure 4.6 it is possible to observe that the amount of formic acid detected at the end of the treatment increased along with the exfoliation power and was always higher than the benchmark P25. That is true for both samples obtained at 550°C and 600°C. In particular, C<sub>3</sub>N<sub>4</sub>-550-120W achieved the highest productivity of formic acid, that is over 8 mol/kg<sub>cat</sub> h or 2.5-times the productivity obtained with P25 (at 8 bar), while H<sub>2</sub> productivity was almost equal in both cases (over 3.5 mol/kg<sub>cat</sub> h). C<sub>3</sub>N<sub>4</sub>-600-0W and C<sub>3</sub>N<sub>4</sub>-600-120W samples performed the same as their 550°C counterpart, however, their H<sub>2</sub> productivity was lower (1.2 mol/kg<sub>cat</sub> h).

The band gap slightly increased when higher exfoliation power was applied, from 2.68 eV for C<sub>3</sub>N<sub>4</sub>-550°C-0W photocatalyst to 2.78 eV of the sample exfoliated at 120W, whereas the shift was almost not visible in case of C<sub>3</sub>N<sub>4</sub>-600-120W (2.68 eV to 2.70 eV), thus, it is likely that this is not the factor that determines the activity. On the other hand, the delamination step is effective in increasing the specific surface area of the photocatalyst and porosity (mainly due to interparticle porosity), from 9 m<sup>2</sup>/g of the base carbon nitride (550°C) to 37 m<sup>2</sup>/g of the sample exfoliated at 60W. As intuitive, this has a positive effect on the activity of the photocatalyst due to the greater adsorption of CO<sub>2</sub> and larger surface area exposed to light [27].

In contrast to the activity results, the quantum yield of the exfoliated catalysts was higher than the bulk C<sub>3</sub>N<sub>4</sub>, which means the photoexcited electrons were more likely to relax through the emission of light rather than dissipating the energy as heat or rather participate in the reaction with the adsorbed species. The differences in QY do not reflect in the productivity results, other factors should be taken into consideration (*e.g.* textural properties, band gap, etc.).

The fact that the tests were carried out over 24h poses some limits to the comparison of the data, since the HS consumption was close to 100%. However, that reaction time was specifically selected to observe both liquid and gaseous products.

Regarding that aspect, the graph of Figure 4.7 reports the results of several tests halted at different time, namely 2, 5, 6 and 24 hours. Between the 6th hour and the end of the test, the conversion of the hole scavenger keeps going up and simultaneously the concentration of formic acid decreases, although only by 19% from its peak value. Since most of the formic acid was accumulated and only a fraction was converted into hydrogen and carbon monoxide, a day-long test is still useful to compare the performance of different materials. From the same data reported in Figure 4.7, it is possible to calculate that the conversion efficiency is similar to the case reported in the previous paragraph. Since the absolute amount of formic acid obtained (around 9.1 mmol) after 6h with g-C<sub>3</sub>N<sub>4</sub>-120W is the same of the previous case in which we considered the P25/TE composite, the calculated efficiency of the energy storage will result in the same value.

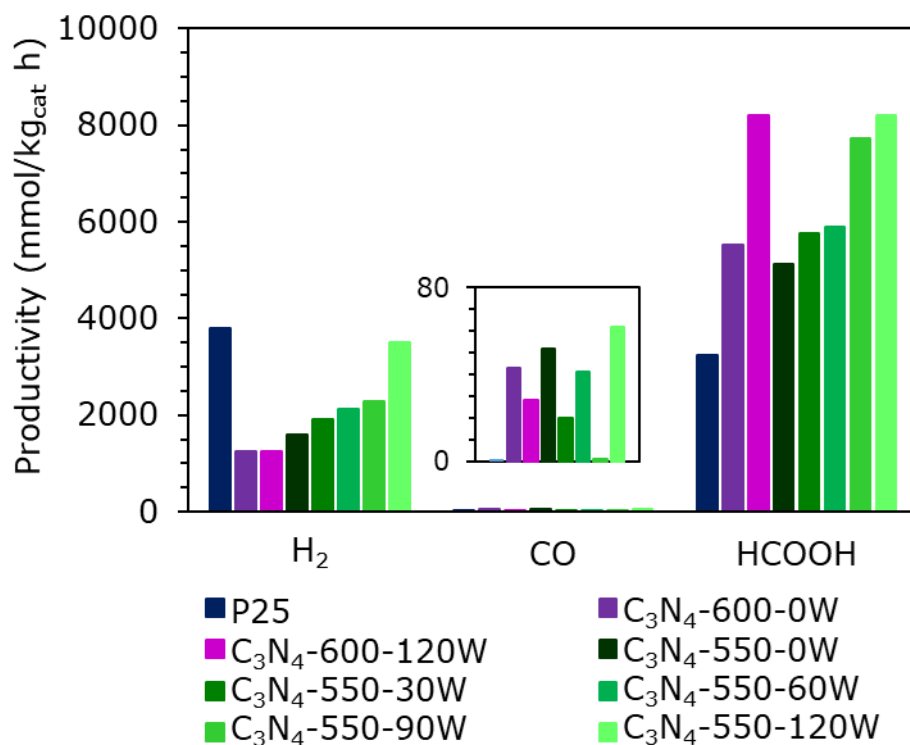


**Figure 4.6.** Productivity results of base C<sub>3</sub>N<sub>4</sub> and exfoliated photocatalyst. 1.2L, pH=14, 31 mg/L photocatalyst, 1.67 g/L Na<sub>2</sub>SO<sub>3</sub>, 24h

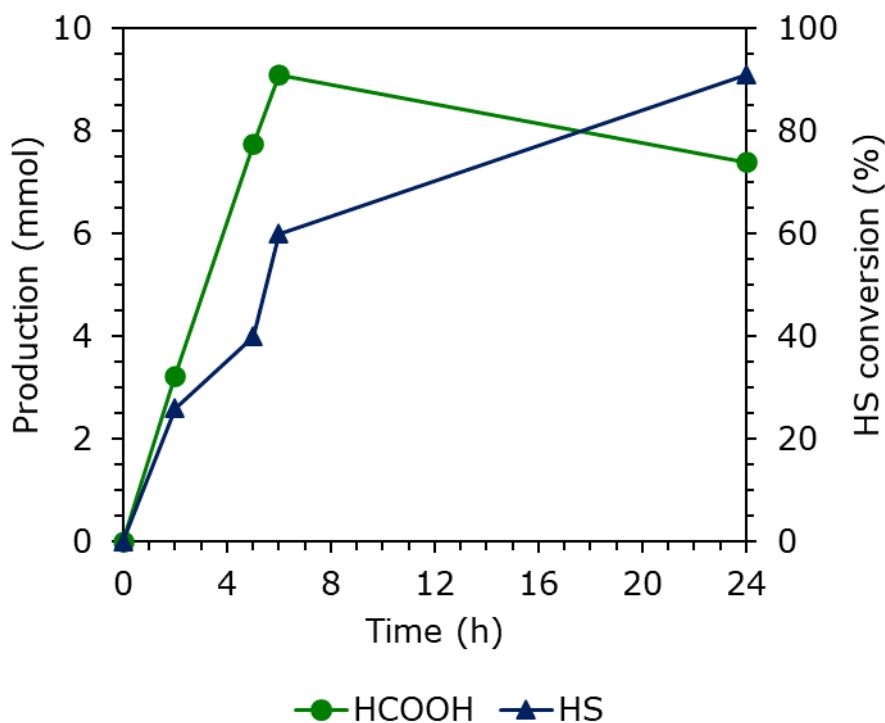


**Figure 4.7.** Production of formic acid and consumption of the HS over time. 1.2L, pH 14, 31 mg/L of C<sub>3</sub>N<sub>4</sub>-120W, 1.67 g/L Na<sub>2</sub>SO<sub>3</sub>

#### 4.2.2.2. Tests with C<sub>3</sub>N<sub>4</sub>/WO<sub>3</sub> composites

WO<sub>3</sub> was selected as a co-catalyst due to its chemical stability and low band gap (around 2.7 eV, depending on NPs size). A direct Z-scheme (or rather type-II heterojunction) is formed when it is coupled with g-C<sub>3</sub>N<sub>4</sub> and this may be a method to increase the activity of the resulting photocatalyst [42], preventing charges recombination. Moreover, the position of the valence band of tungsten trioxide is below (more positive) than that of g-C<sub>3</sub>N<sub>4</sub>, which enhances the photooxidation capabilities of the photocatalyst, while the photoexcited electrons in the conduction band are quenched by the holes present on carbon nitride nanosheets and so, improving the separation of the charges [43].

Here, we tested the photocatalytic activity of four different composites based on C<sub>3</sub>N<sub>4</sub>-550-120W and prepared via sonication/precipitation and thermal decomposition that are loaded with WO<sub>3</sub> in the range 10-40% (w/w). That preparation technique is a well-known method that allows for an intimate contact between the two materials [42]. Figure 4.8 illustrates the results of the CO<sub>2</sub> photoreduction carried out in the same conditions adopted for the series of g-C<sub>3</sub>N<sub>4</sub> photocatalyst. Generally speaking, the productivity of formic acid of the composite materials was always lower than the bare C<sub>3</sub>N<sub>4</sub> (nearly 8.5 mol/kg<sub>cat</sub> h) and only slightly higher than bare WO<sub>3</sub> (6.5 mol/kg<sub>cat</sub> h), except in case of C<sub>3</sub>N<sub>4</sub>/WO<sub>3</sub>-10% which produced less HCOOH and more hydrogen and methane. Speaking of the gaseous phase, small but significant amounts of methane were detected in every case and, in addition, the highest amount of CO measured was tripled (0.25 mol/kg<sub>cat</sub> h) with respect to the tests with exfoliated carbon nitride alone. To obtain the most from these photocatalysts, it is likely to be required a proper tuning of the textural properties, such as surface area, porosity and so on.

Ohno et al. reported the performance of g-C<sub>3</sub>N<sub>4</sub>/WO<sub>3</sub> composite obtained via sonication and irradiated under visible light and its activity expressed as CH<sub>3</sub>OH production was 30% higher than the sole carbon nitride [28]. In our case, the high pH (=14) favors the formation of formic acid rather than methanol and the increased pressure greatly affected the productivity of the former. It can be seen that within the series of the composites the specific surface, the total pore volume and the pore size did not change dramatically, which may be the reason why the activity of those materials was similar. The band gap was not a discriminant factor here, since all the photocatalysts were activated by the same UV lamp emitting at 365 nm peak. On the other hand, the quantum yield decreased with the amount of WO<sub>3</sub>, which should impact positively the performance of the photocatalyst.

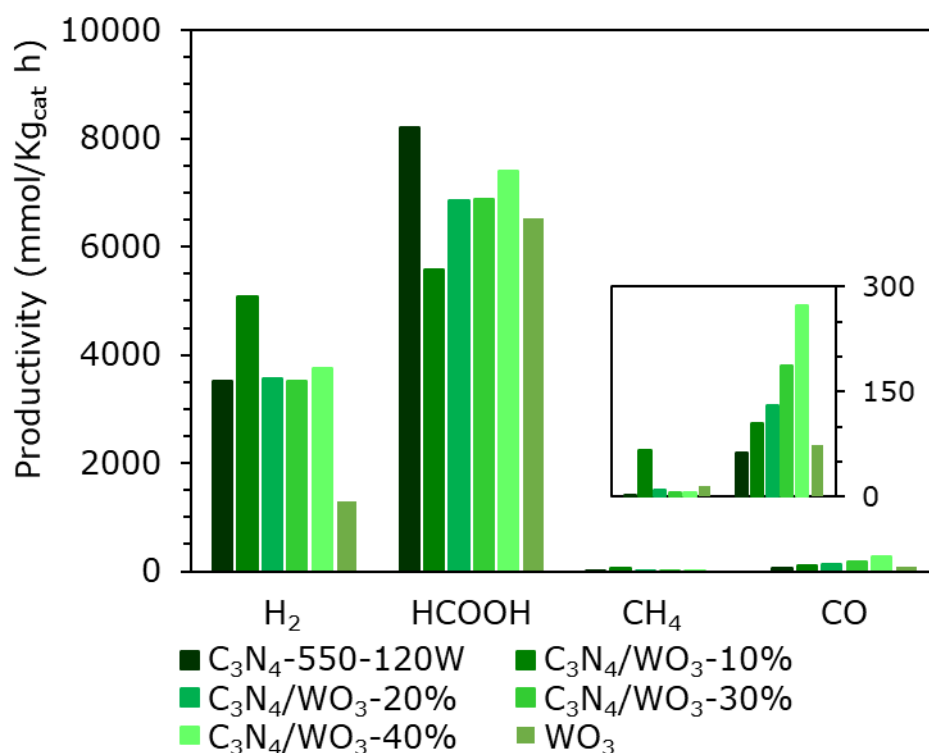


**Figure 4.8.** Productivity results of C<sub>3</sub>N<sub>4</sub>/WO<sub>3</sub> composites. 1.2L, pH=14, 31 mg/L photocatalyst, 1.67 g/L Na<sub>2</sub>SO<sub>3</sub>, 24h

#### 4.2.3. CO<sub>2</sub> photoreduction tests with catalysts synthesized via FSP

Considering the performance of WO<sub>3</sub>, the productivity of HCOOH was lower than that of carbon nitride and titania, but overall satisfactory and deserving some deepening. Being a completely inorganic material, tungsten trioxide can be synthesized by flame-spray pyrolysis, which is a robust method to obtain oxide nanoparticles. Also, it allows to prepare mixed compounds by tuning the proportion between the precursor that are fed to the burner. Here we present the results obtained with both the bare tungsten and titanium oxides and of one example of composite containing 60% TiO<sub>2</sub> and 40% WO<sub>3</sub>, on a weight basis. Indeed, titanium dioxide can be prepared with the same apparatus and the heterojunction between the two is expected greatly improve the activity.

As reported in Figure 4.10, WO<sub>3</sub> was active alone and its performance was comparable to that of titania synthesized in the same conditions, around 14 mol of formic acid per hour of reaction and kilogram of photocatalyst, with the HS conversion that was roughly 40% for each test (18 bar, 6h). On the other hand, the composite resulted to be much more active and outperformed both its constituents by reaching a productivity of almost 37 mol/kg<sub>cat</sub> h, and the HS conversion exceeded the 90%. In all the cases, only traces of hydrogen were detected according to the incomplete conversion of the sulphite. According to literature, the intimate contact between the TiO<sub>2</sub> and WO<sub>3</sub> phases forms a Z-scheme heterojunction which suppresses the charge recombination and increases the efficiency with respect to the single constituents [44] (Figure 4.9). Also, WO<sub>3</sub> has a conduction band higher (more positive) than TiO<sub>2</sub>, while the position of the VB allows the migration of the holes to the counterpart of the Z-scheme [45,46]. Lastly, WO<sub>3</sub> is more acidic than TiO<sub>2</sub>, therefore, it should interact preferentially with the carbonate ions dissolved [45]. That reason and the fact that the band gap of the composite was lower

with respect to both the single oxides (2.7 eV), are likely to be the explanation for the activity of the composite.

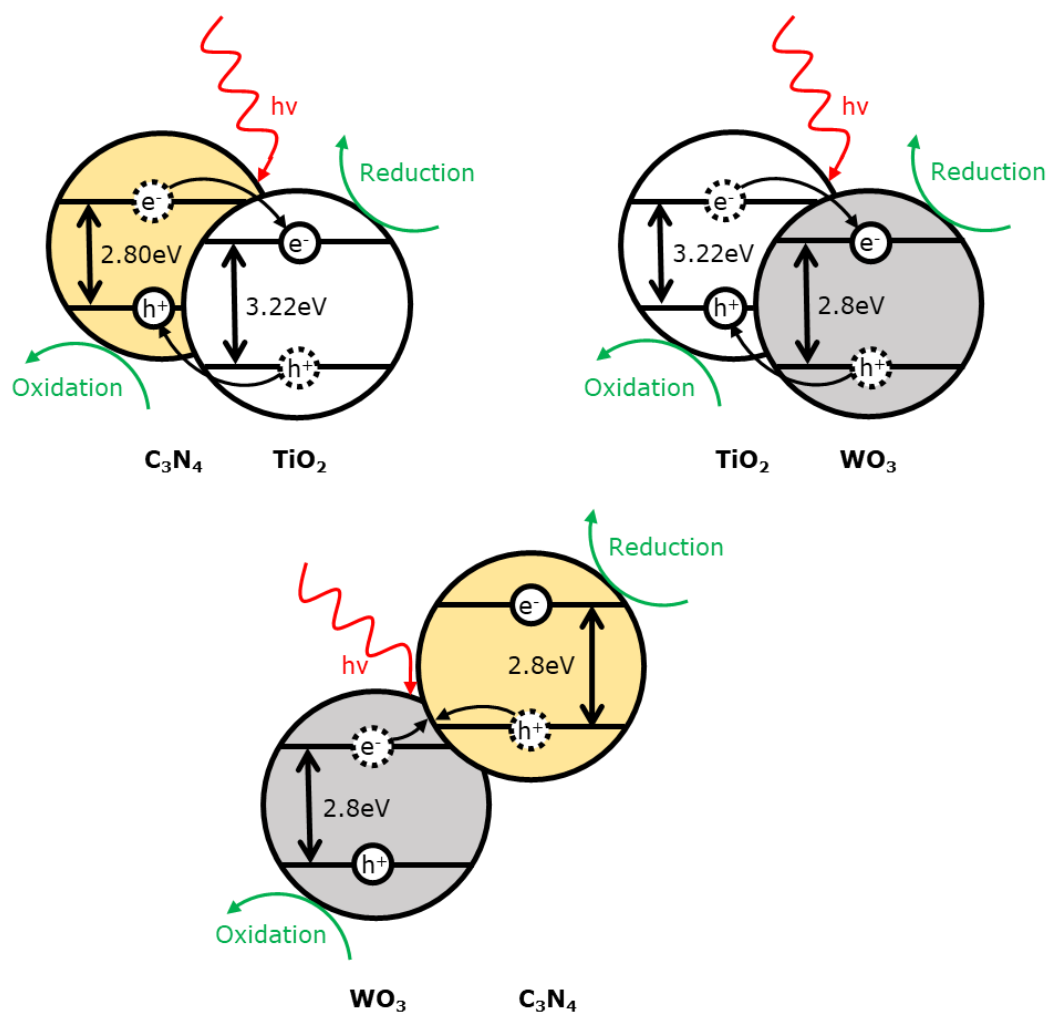


**Figure 4.9.** Heterojunction scheme of  $\text{TiO}_2/\text{C}_3\text{N}_4$ ,  $\text{TiO}_2/\text{WO}_3$  and  $\text{C}_3\text{N}_4/\text{WO}_3$  composites



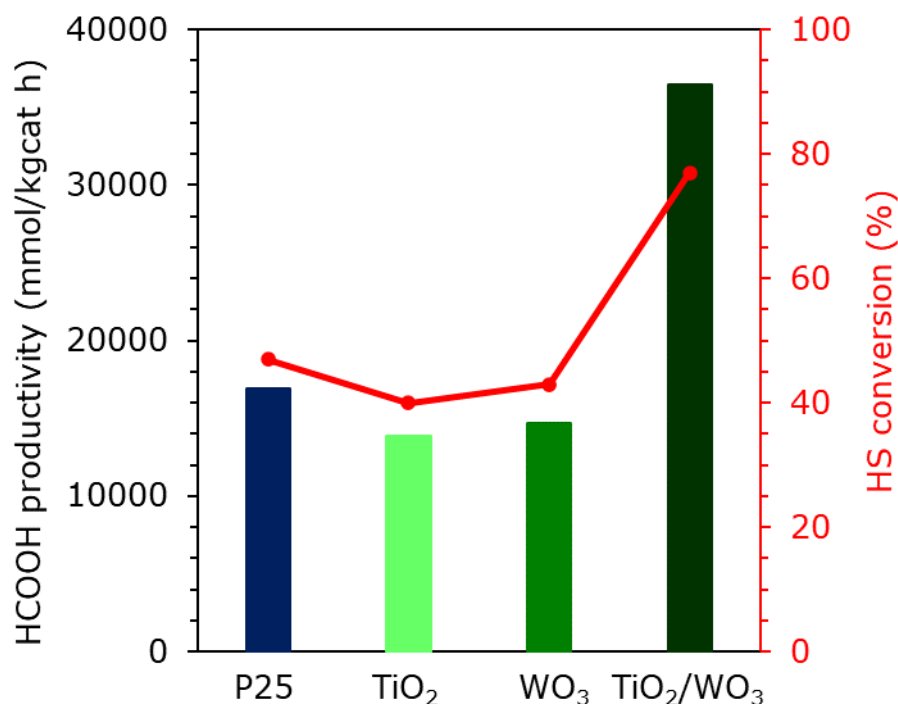


**Figure 4.10.** Productivity results of CO<sub>2</sub> photoreduction using FSP-TiO<sub>2</sub>, FSP-WO<sub>3</sub> and the FSP-prepared composite TiO<sub>2</sub>/WO<sub>3</sub> 40/60 %w/w. 1.2L, pH=14, 31 mg/L photocatalyst, 18 bar, 6h, 1.67 g/L Na<sub>2</sub>SO<sub>3</sub>

#### 4.2.4. Comparison with other photocatalysts

The activity of the photocatalysts reported in this manuscript can be compared with a series of materials based on titanium dioxide that was previously tested in the same photoreactor. Briefly, the series was composed by metallized titania prepared via wetness impregnation and loaded with one metal (Au, Pt, Ag or Cu) or titania modified with two metals (Au/Pt and Au/Ag) via sol-immobilization [37]. For the sake of comparison, only the productivity results of the test carried out at 8 bar and for 24h will be considered.

In the aforementioned previous work, it was found that the most active mono- and bi-metallic titania photocatalysts were 0.1% mol Pt/P25 and 1% wt. (Au<sub>2</sub>Ag<sub>8</sub>)/P25, where the

former achieved productivities of 5.5 mol/kg<sub>cat</sub> h (HCOOH) and 4.1 mol/kg<sub>cat</sub> h (H<sub>2</sub>) and the latter reached 9.53 mol/kg<sub>cat</sub> h (HCOOH) and 4.50 mol/kg<sub>cat</sub> h (H<sub>2</sub>).

Making comparisons with the other photocatalyst reported in literature is not an easy task, given the unique setup that is presented in this work and that allows to obtain high productivities of chemicals thanks to the pressure applied during the test, the high temperature and the powerful UVA lamp. In addition, the amount of photocatalyst added to the reactor is one order of magnitude lower than the concentration usually adopted. For instance, Tseng et al reported the formation of methanol (0.020 mol/kg<sub>cat</sub> h) upon illumination of a water solution saturated with CO<sub>2</sub> under slightly pressure (ca. 1.3 bar) and by using Cu/TiO<sub>2</sub> as photocatalyst [47]. The author did not exclude the presence of other gaseous products and liquid organics which are, unfortunately, not detectable by using that setup (0.2 L).

Kočí [48] observed the evolution of hydrogen, carbon monoxide and methane from CO<sub>2</sub> saturated solution treated with g-C<sub>3</sub>N<sub>4</sub> loaded with 3% wt. of Pt nanoparticles. Again, the absolute production values are quite interesting, but those results were obtained by employing large amount of photocatalyst (1 g/L).

**Table 4.1.** Collection of results regarding the photoreduction of CO<sub>2</sub> carried out with different catalyst from our group and from literature

Photocatalyst	[Cat.] mg/l	Light source	HS	Conditions	Productivity mol/kg <sub>cat</sub> ·h	Ref.
P25	31	UVA-157	Na <sub>2</sub> SO <sub>3</sub>	80°C; 8bar;	HCOOH-3.24	This
		W/m <sup>2</sup>		pH14; 24h	H <sub>2</sub> -3.80	work
C <sub>3</sub> N <sub>4</sub> -550-120W	31	UVA-157	Na <sub>2</sub> SO <sub>3</sub>	80°C; 8bar;	HCOOH-8.20	This
		W/m <sup>2</sup>		pH14; 24h	H <sub>2</sub> -3.52	work
C <sub>3</sub> N <sub>4</sub> /WO <sub>3</sub> -40%	31	UVA-157	Na <sub>2</sub> SO <sub>3</sub>	80°C; 8bar;	HCOOH-7.39	This
		W/m <sup>2</sup>		pH14; 24h	H <sub>2</sub> -3.77	work
TE-C <sub>3</sub> N <sub>4</sub>	31	UVA-157	Na <sub>2</sub> SO <sub>3</sub>	80°C; 8bar;	HCOOH-7.85	This
		W/m <sup>2</sup>		pH14; 24h	H <sub>2</sub> -1.22	work
0.1% mol Pt/P25	31	UVA-157	Na <sub>2</sub> SO <sub>3</sub>	80°C; 8bar;	HCOOH-5.50	[37]
		W/m <sup>2</sup>		pH14; 24h	H <sub>2</sub> -4.10	
1% wt. (Au <sub>2</sub> Ag <sub>8</sub> )/P25	31	UVA-157	Na <sub>2</sub> SO <sub>3</sub>	80°C; 8bar;	HCOOH-9.53	[37]
		W/m <sup>2</sup>		pH14; 24h	H <sub>2</sub> -4.50	
6% wt. Cu/TiO <sub>2</sub>	750	UVC-8W	NaOH	50°C; 1.3 bar	CH <sub>3</sub> OH-0.020	[47]
				pH14; 6h		
3%Pt/g-C <sub>3</sub> N <sub>4</sub>	1000	UVC-8W	NaOH	rt; 1.2 bar;	H <sub>2</sub> -0.025	[48]
				pH14; 8h	CO-0.0012	
					CH <sub>4</sub> -0.0038	

#### 4.2.5. Test with different hole scavenger

Despite being an inexpensive product and easily oxidable, sodium sulfite may not be the best choice when it comes to scale up the process to an industrial level as it is obtained via a synthetic route and it accumulates inside the reactor as sulfate. Therefore, other HS were tested in order to find potential alternatives, such as glycerin which is widely available from natural sources. The candidate alternative HS should be easily oxidizable as well though interaction with the holes of the used semiconductors, be possibly of renewable origin and it should lead to gas phase products not interfering with the reaction. The results obtained by using different HS while keeping the same molar amount are reported in Figure 4.11 (exact concentration are reported in appendix).

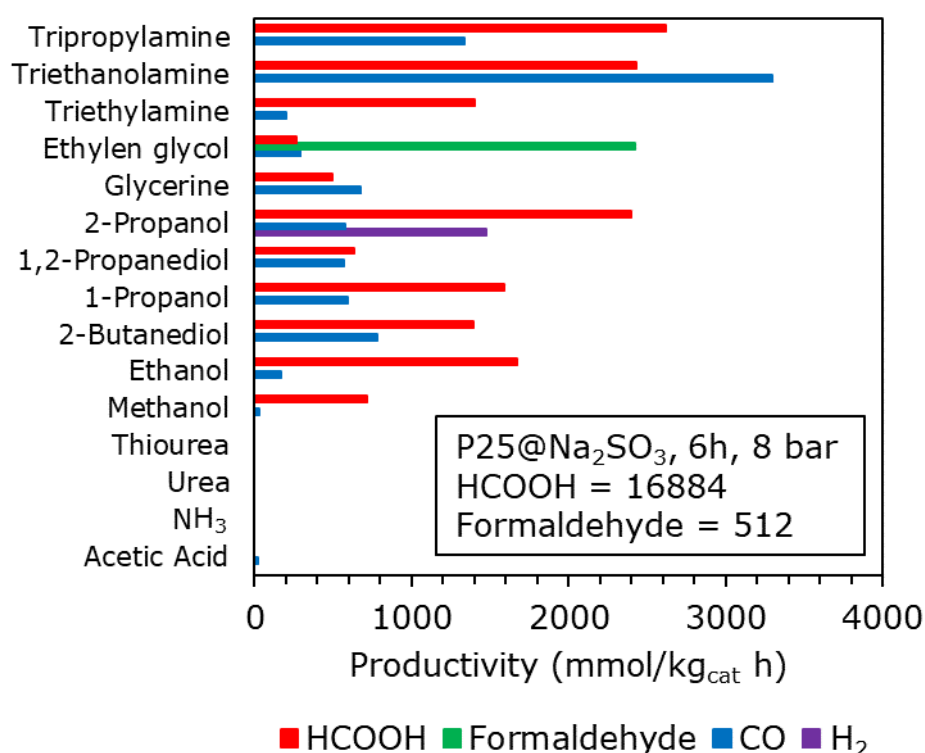


**Figure 4.11.** Productivity results of CO<sub>2</sub> photoreduction using P25 and various HS. 1.2L, 8 bar, pH 14, 31 mg/L photocatalyst, 6h

The first promising candidate was ammonia, as it can be dissolved in the reaction medium and its selective oxidation product is molecular nitrogen, which would have solved the problem of accumulation that we were facing when sodium sulfite is oxidized to sulfate. Unfortunately, ammonia gave negligible productivity of the main products (either gaseous or liquid), even when the pressure was increased to 18 bar or when it was added in larger excess. Other authors suggest that during the photooxidation treatment, ammonia reacts poorly with the photogenerated holes and rather combines with hydroxyl radicals [49]. If NH<sub>3</sub> is not adsorbed and oxidized on the photocatalyst surface, the holes accumulate and the efficiency of the CO<sub>2</sub> photoreduction decrease dramatically. Similar studies highlighted that without the presence of oxygen or hydrogen peroxide the photocatalytic oxidation of ammonia does not occur [50].

Analogous compounds easy to handle, such as urea and thiourea, gave poor activity too, and only traces of products (*i.e.* hydrogen and formic acid) were detected. Urea would have been a good source of ammonia that releases only gaseous products upon oxidation, however, it still reacts mainly with OH• rather than directly with the holes on titania surface [51] and a similar explanation can be hypothesized in case of thiourea.

On the other hand, organics with amine moieties, namely tripropylamine, triethanolamine and triethylamine were tested. All these HS are formed during fermentation of biomass containing proteins and free amino acids and can be a valid bio-based substitute to the inorganic Na<sub>2</sub>SO<sub>3</sub> [56]. When tested, they induced the formation of both formic acid and carbon monoxide, however, these were not the main products since great amount of ethane was detected in case of NEt<sub>3</sub> and N(EtOH)<sub>3</sub>, while NPr<sub>3</sub> surprisingly achieved a productivity of 129 mol/kg<sub>cat</sub> h of C<sub>2</sub>H<sub>6</sub> (Figure 4.12). Also, smaller amounts of methane and ethylene were detected. Triethylamine reacts directly over titanium dioxide surface [52] and it is very likely that the same applies to tripropylamine too. This difference in activity and the huge productivity of ethane cannot be easily explained, for the many factors that needs to be taken into account during the photocatalyzed CO<sub>2</sub> photoreaction. The literature that covers the photoreforming of amine is scarce and the experiments are performed in conditions different from our setup. It can be said that the interaction between the HS and the surface of the photocatalyst plays a crucial role in the whole process and may favor the formation of specific products, as formic acid and CO, which are obtained through the same pathway [53], while ethane is probably one of the stable intermediates that are able to desorb from the photocatalyst surface once formed. As an example, similar studies at ambient temperature and pressure using triethylamine as solvent and Pt-TiO<sub>2</sub> catalyst unveiled the formation of CO and CH<sub>4</sub> along with hydrogen

[54] and it was also reported that triethanolamine leads to significantly better yield of those. In addition, Satoshi et al. [55] observed a similar activity trend ( $\text{NPr}_3 > \text{NEt}_3$ ) and they explained these differences with the fact that on its way to the full oxidation (mineralization),  $\text{NH}_4^+$  is formed as intermediate and it mainly reacts with the photogenerated radicals. Conversely, triethanolamine may interact with hydroxyl group of titania surface, leading to stronger adsorption.

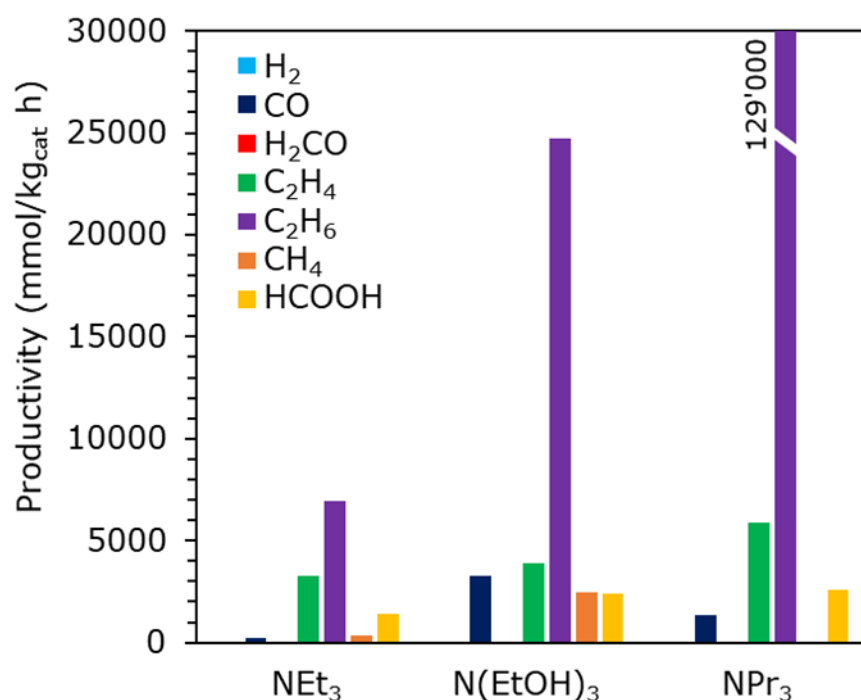


**Figure 4.12.** Productivity results of  $\text{CO}_2$  photoreduction using P25 and triethylamine (1.60 g/L), triethanolamine (2.37 g/L) or tripropylamine (2.27 g/L). 1.2L, 8 bar, pH 14, 31 mg/L photocatalyst, 6h

The third class of HS that was explored is the group of alcohols, both mono- and polyalcohols. Methanol is the benchmark of the series, being the simplest alcohol, and the productivity of formic acid and hydrogen (the two main products) was respectively 0.72 and 0.32 mol/kg<sub>cat</sub> h after 6h of reaction (Figure 4.13). By using ethanol instead, the

productivity rose dramatically as the one of formic acid increased to 1.67 and hydrogen to 0.17 mol/kg<sub>cat</sub> h. Propanol and 2-propanol behave similarly to ethanol in terms of HCOOH and CO production, with the secondary alcohol being more active. In case of both these alcohols, ethane was detected as the main product (roughly 40 mol/kg<sub>cat</sub> h), along with smaller amounts of ethylene and methane (with iPrOH as HS). Butanol gave the best performance among the series, being the productivity of ethane and ethylene respectively three and five times higher than that of propanol. Some authors suggested that the ability to serve as hole scavenger for water reduction follows the trend of hydrophilicity, therefore, methanol should be more active than ethanol and butanol should be the least suitable HS [57]. Others state that methanol is effective as HS only once it is activated by reaction with radicals (*e.g.* OH•) [58]. A more detailed overview is reported by Toe et al. [59]. Briefly, it is suggested that the first critical step is represented by the formation of a radical on the hydroxyl group or the alkyl chain, then it comes the interaction between the alcohol and the functional groups on the surface of the photocatalysts. This could explain why methanol achieved such low productivities with respect to butanol, since the latter stabilizes (slightly) better the radicals formed via hyperconjugation effect. Then, the same authors reported that mass transfer plays a crucial role, especially for the selectivity of the products, and according to the results we have evidence that the photooxidation led to the formation of C2 hydrocarbons that desorb and accumulate in the head space of the reactor. A proper tuning of the photocatalyst textural properties is required to boost the production of formic acid, which is the final stage of multiple reaction pathway and the oxidation to gaseous species (*e.g.* CO and CO<sub>2</sub>) [59].

Figure 4.13 illustrates the productivities obtained in case of polyalcohol, that are 1,2-propanediol, ethylene glycol and glycerin. The propanediol behaved similarly to isopropyl alcohol, and ethane was the main product along with ethylene and methane. Ethylene glycol follows an unique reaction path due to its structure, indeed, in that environment one of the hydroxyl groups is oxidated to aldehyde and the subsequent reaction with two photogenerated holes splits this intermediates into one molecule of formaldehyde and one of formic acid [60]. In our case, the amount of formaldehyde is significantly higher than that of formic acid and it is likely that the interaction with the photocatalyst surface is more favorable for the adsorption, and so the complete oxidation, of the acid [59].

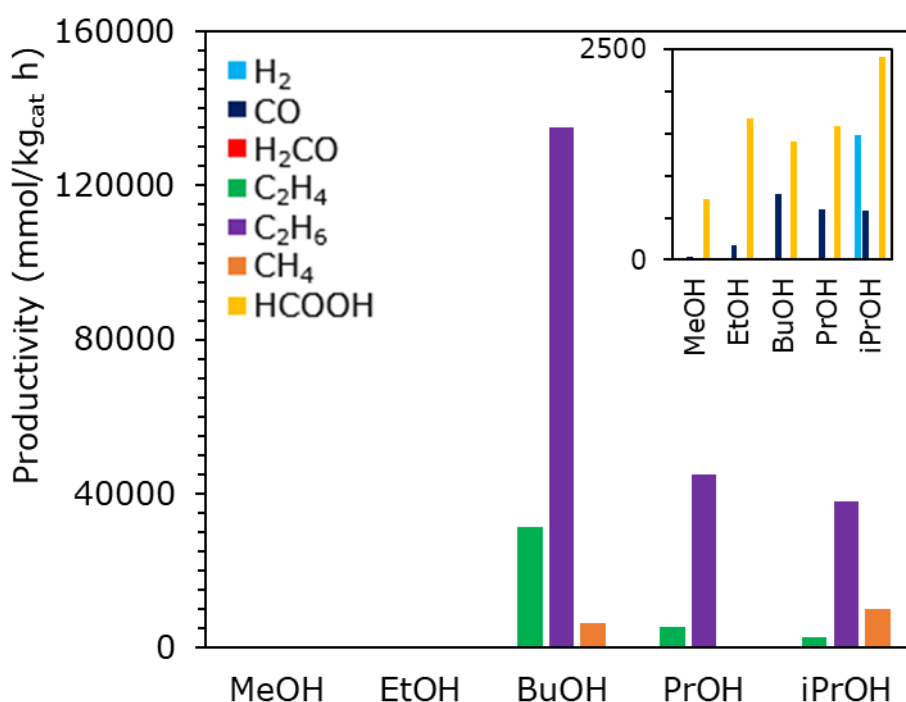


**Figure 4.13.** Productivity results of CO<sub>2</sub> photoreduction using P25 and methanol (0.51 g/L), ethanol (0.73 g/L), propanol (0.95 g/L), 2-propanol (0.95 g/L) or butanol (1.2 g/L). 1.2L, 8 bar, pH 14, 31 mg/L photocatalyst, 6h



Lastly, glycerin was not so active as hole scavenger (Figure 4.14), indeed, the productivity of ethane was below 3 mol/kg<sub>cat</sub> h. Glycerin can undergo the oxidation of the primary alcohol to aldehyde, which then leads to ethylene glycol or glycolic acid. On the other hand, it was reported the oxidation of the secondary alcohol to dihydroxyacetone (DHA), which appears to be a stable intermediate, but HPLC analysis did not reveal its presence [59]. Like in case of amines, alcohols are produced through inexpensive route such as fermentation and constitutes a valid alternative HS, thus, we decided to further test the capabilities of isopropanol as a HS [61].

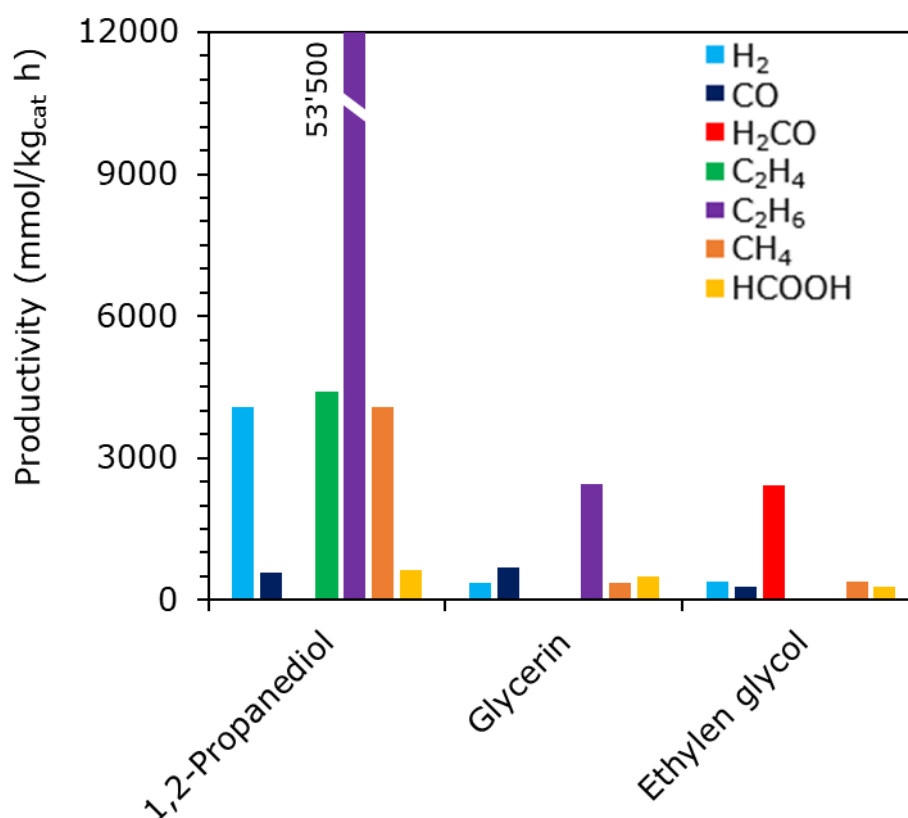
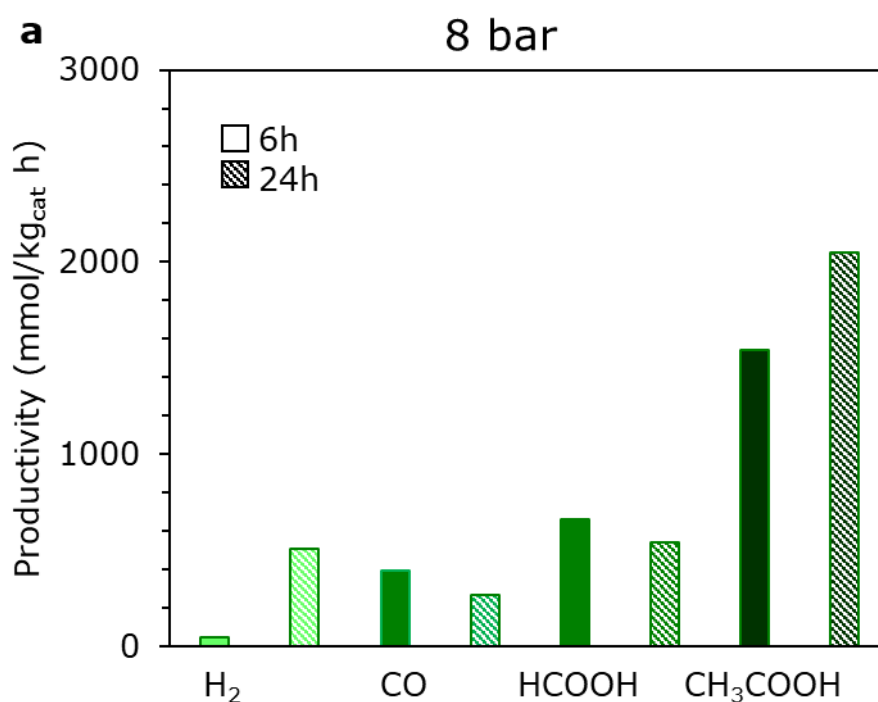


**Figure 4.14.** Productivity results of CO<sub>2</sub> photoreduction using P25 and 1,2-propandiol (1.2 g/L), glycerin (1.46 g/L), ethylene glycol (0.99 g/L). 1.2L, 8 bar, pH 14, 31 mg/L photocatalyst, 6h

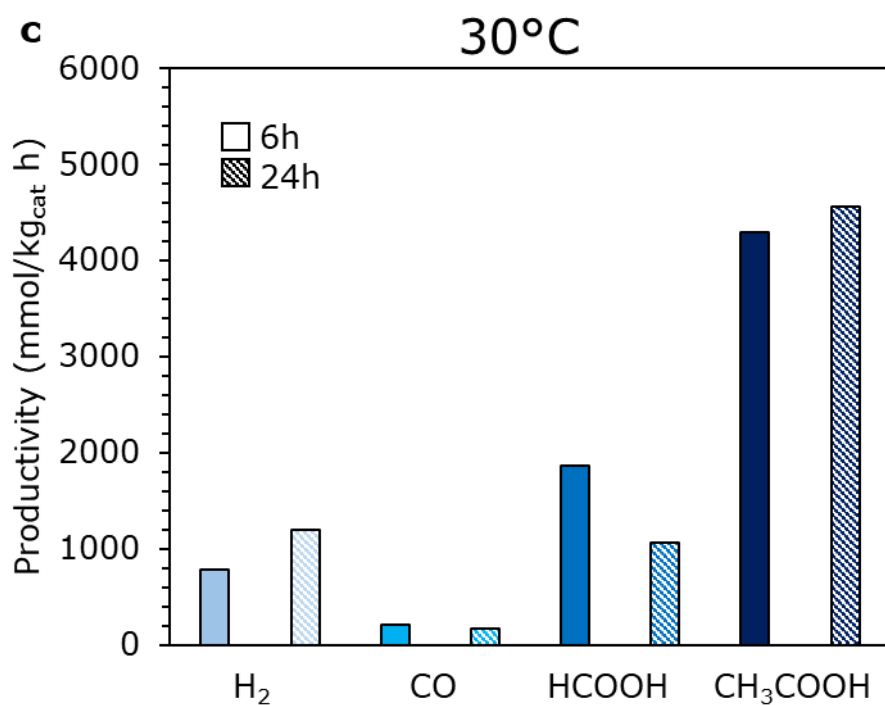
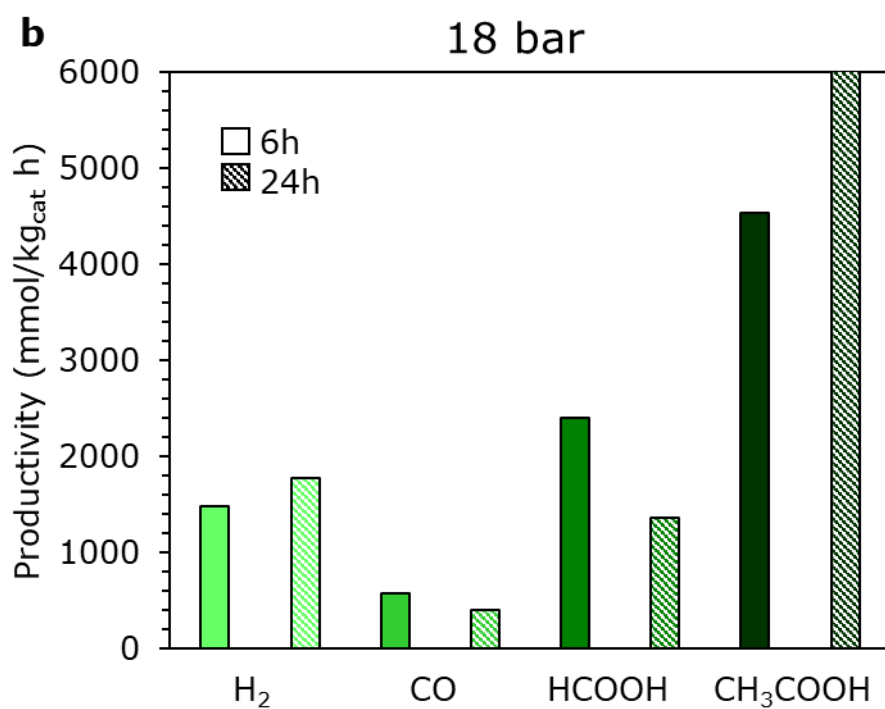
Figure 4.15a illustrates the results of the photoreduction carried out during a whole day, along with the previous results obtained with a short test of 6h. During the first quarter of the test, most of the products were composed of carbon monoxide, formic acid and acetic acid, and the latter was observed only in case of two HS, that are 2-propanol and 1,2-propanediol. According to well-established reaction mechanisms of organic chemistry, acetic acid should be the oxidation product of ethanol, while oxidation of a secondary alcohol such as 2-propanol should lead to acetone. To obtain acetic acid, acetone must be further oxidized, supposedly by adsorption of acetone on titania surface via interaction with the surface oxygen and formation of ketene intermediate, which then ejects a methyl radical, leaving an acetate bound to the surface [62]. It is observed that after 24h, the hydrogen and acetic acid productivity increased and CO and formic acid were lower, with the conversion of 2-propanol that increased from 28.4% to 36.4%. HCOOH was probably decomposed to CO or rather used as HS itself, in competition with 2-propanol. Furthermore, when the pressure was increased from 8 bar to 18 bar (Figure 4.15b), the trend of the products distribution was the same, while in general the productivity was higher and even small amounts of methanol were detected, which may be due to the mechanism that involves the formation of a methyl radical [63]. For instance, acetic acid productivity was three-times higher and the HS conversion as well, from 19.6% to 68.7%. Figure 4.15c shows what happen when the temperature decreased from 80°C to 30°C. A high temperature was chosen in order to maximize the productivity when using P25 in combination with Na<sub>2</sub>SO<sub>3</sub>, however, with the current setup the productivity of all the products was only a bit lower than the test at 80°C, meaning that the pressure was a parameter by far more critical than the temperature, as the reaction kinetics is probably not limited by that. The HS conversion was slightly lower, around 18% after 6h and 50%

after 24h. Given that results, it was decided to halve the amount of 2-propanol added to the reactor, from 1.2 to 0.6 mL and the results are reported in Figure 4.14d. Overall, it was found a lower productivity for every compound, such as -40% for H<sub>2</sub> after 6h and -16% after 24h or -14% and -20% respectively for acetic acid. On the other hand, CO and HCOOH scored a higher productivity after 24h of test, respectively +5% for carbon monoxide and +58% for formic acid, and the conversion of HS after 6h and 24h was 26% and 86.7%. Being close to fully consumption, the photocatalyzed reaction is likely to slow down.

Interestingly, adding a second hole scavenger more easily oxidable, that is Na<sub>2</sub>SO<sub>3</sub>, greatly boosted the formic acid productivity by ten times (Figure 4.15e). Also, acetone was detected, which is a hypothesized intermediate in the 2-propanol oxidation. Whereas after 12h the sodium sulfite was fully consumed, while the alcohol reached a 5.5% conversion after 6h and 18.4% after 24h. Conversely, when both HS were used under a



nitrogen blank test instead of CO<sub>2</sub> only small amount of hydrogen and acetic acids were detected, confirming the role of CO<sub>2</sub> in products formation.



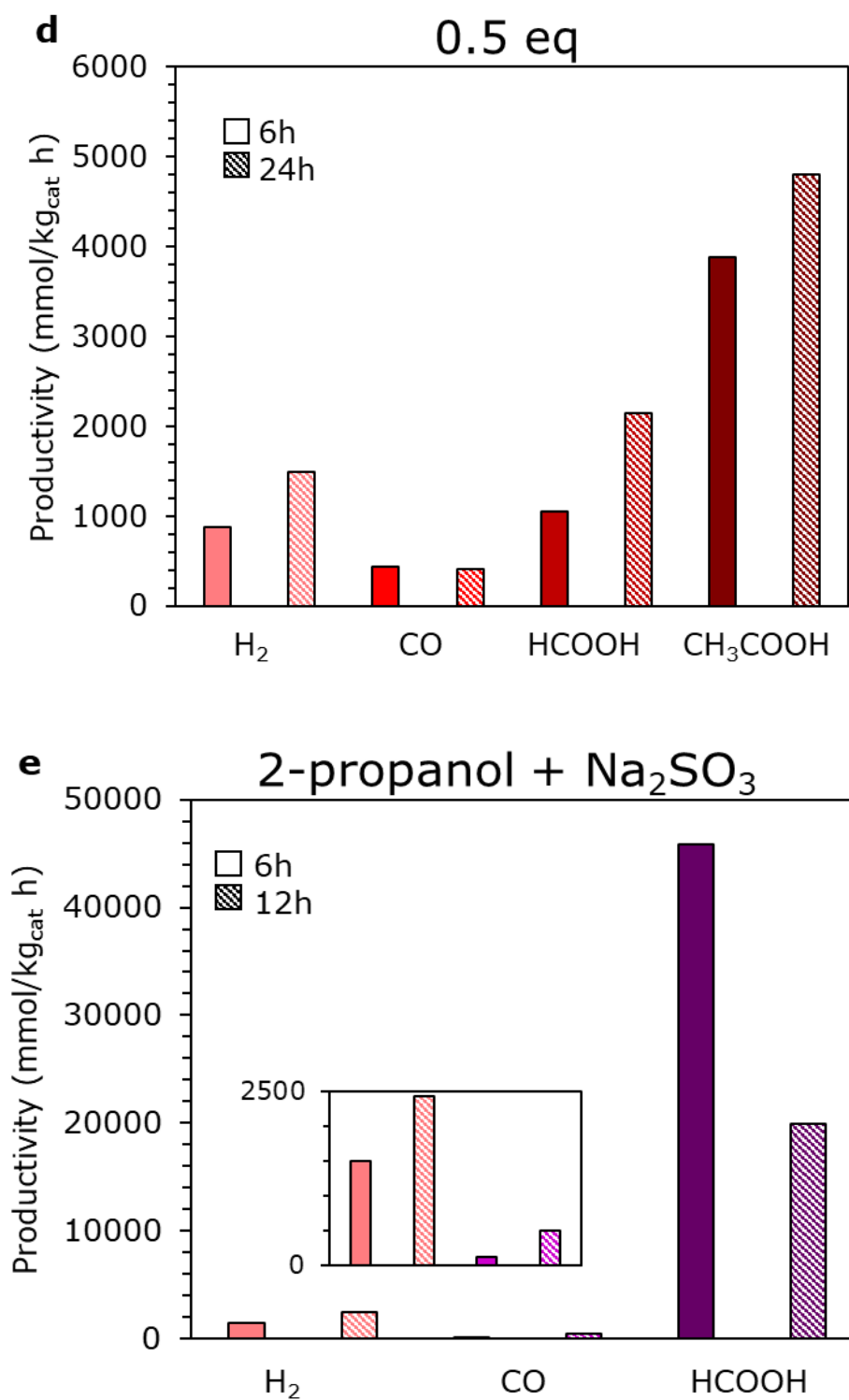


**Figure 4.15.** Productivity results of several CO<sub>2</sub> photoreduction tests using P25 and isopropanol under different conditions. 1.2L, pH 14, 31 mg/L photocatalyst, 8-18 bar, 6-24h, 0.47-0.95 g/L of isopropyl alcohol

### 4.3 Conclusions

Through the help of an innovative photoreactor that works at high pressure, we were able to test several promising photocatalysts for the CO<sub>2</sub> photoreduction to liquid products. Graphitic carbon nitride was prepared through a simple route that requires a thermal treatment of melamine and a treatment in water with ultrasounds, then possibly further functionalized by deposition of tungsten trioxide nanoparticles over its surface. A second set of catalysts based on C<sub>3</sub>N<sub>4</sub> exfoliated, either thermally or with US, and compounded with TiO<sub>2</sub> or WO<sub>3</sub> was tested as well.

It was observed that the activity of the exfoliated material, expressed as the formic acid productivity, follows the energy of exfoliation, as the sample obtained at 120W was significantly more effective in reducing the CO<sub>2</sub> with respect to the base material, while the temperature of synthesis (550°C vs 600°C) had a little impact on the activity. Compounding with WO<sub>3</sub> did not bring advantages and the performance was even lower when C<sub>3</sub>N<sub>4</sub> was combined with 10%w/w tungsten trioxide. On the other hand, non-negligible amount of methane was detected, and it is likely that under different conditions the catalyst can perform better than the single components.

The same conditions were used to test the series of thermally exfoliated C<sub>3</sub>N<sub>4</sub> and titanium dioxide, where the best performers were titanium dioxide from TiCl<sub>4</sub> hydrolysis (*i.e.* TiO<sub>2</sub>-exCl) and TE-C<sub>3</sub>N<sub>4</sub>. In addition, the highest activity was found when the pressure was increased from 8 bar to 18 bar and the reaction time was shortened to 6h, since more CO<sub>2</sub> is dissolved into water and the HS conversion is lower than 100%, thus avoiding the consumption of formic acid by the photocatalyst itself.

The test carried out using titania P25 in combination with various organic and inorganic hole scavengers highlighted that the choice of the HS is not trivial and also that it is

difficult to find valuable alternatives to the  $\text{Na}_2\text{SO}_3$ . One of the most attractive HS was ammonia, in principle, which failed to show any activity probably due to its oxidation mechanism, and it was found that the performance of the system when alcohols are used as HS vary widely depending on the number of functionality and their arrangement on the molecule. 2-propanol was found to shift the products distribution toward acetic acid, which is still a valuable commodity. In general, the structure of the HS was found to influence widely the products distribution and the productivity, and in some cases we achieved remarkable productivities of ethane, ethylene and methane.

Finally, although the results here reported are not directly comparable with others reported in literature due to the unique setup that was employed, we were able to achieve productivities results significantly higher with respect to similar processes operated at lower temperature and pressure and with greater photocatalyst concentration (up to two orders of magnitude).

## References

1. GISTEMP Team, N.G.I. for S.S. <https://data.giss.nasa.gov/gistemp/>.
2. Lenssen, N.J.L.; Schmidt, G.A.; Hansen, J.E.; Menne, M.J.; Persin, A.; Ruedy, R.; Zyss, D. Improvements in the GISTEMP Uncertainty Model. *J. Geophys. Res. Atmos.* **2019**, *124*, 6307–6326, doi:10.1029/2018JD029522.
3. Subramanian, M. Humans versus Earth: the quest to define the Anthropocene. *Nature* **2019**, *572*, 168–170, doi:10.1038/d41586-019-02381-2.
4. Duarte, C.M.; Jaremko, L.; Jaremko, M. Hypothesis: Potentially Systemic Impacts of Elevated  $\text{CO}_2$  on the Human Proteome and Health. *Front. Public Heal.* **2020**, *8*, doi:10.3389/fpubh.2020.543322.

5. Scoones, I. The Politics of Sustainability and Development. *Annu. Rev. Environ. Resour.* **2016**, *41*, 293–319, doi:10.1146/annurev-environ-110615-090039.
6. <https://www.climatewatchdata.org/data-explorer/historical-emissions?historical-emissions-data-sources=cait&historical-emissions-gases=all-ghg&historical-emissions-regions=All%20Selected&historical-emissions-sectors=total-including-lucf%2Ctotal-including-l> Available online: <https://ourworldindata.org/emissions-by-sector> (accessed on Apr 19, 2022).
7. Raza, A.; Gholami, R.; Rezaee, R.; Rasouli, V.; Rabiei, M. Significant aspects of carbon capture and storage – A review. *Petroleum* **2019**, *5*, 335–340, doi:10.1016/j.petlm.2018.12.007.
8. *Lange's Handbook of Chemistry*; Speight, J.G., Ed.; 17th editi.; McGraw-Hill Education: New York, 2017; ISBN 9781259586095.
9. Kelemen, P.; Benson, S.M.; Pilorgé, H.; Psarras, P.; Wilcox, J. An Overview of the Status and Challenges of CO<sub>2</sub> Storage in Minerals and Geological Formations. *Front. Clim.* **2019**, *1*, doi:10.3389/fclim.2019.00009.
10. McGlade, C. Can CO<sub>2</sub>-EOR really provide carbon-negative oil? Available online: IEA (2019), Can CO<sub>2</sub>-EOR really provide carbon-negative oil?, IEA, Paris <https://www.iea.org/commentaries/can-co2-eor-really-provide-carbon-negative-oil>.
11. Dipietro, P.; Balash, P. A Note on Sources of CO<sub>2</sub> Supply for Enhanced-Oil-Recovery Operations Available online: <http://www.gctelegram.com/News/>.
12. Kimball, B.A.; Idso, S.B. Increasing atmospheric CO<sub>2</sub>: effects on crop yield, water use and climate. *Agric. Water Manag.* **1983**, *7*, 55–72, doi:10.1016/0378-3774(83)90075-6.



13. Idso, S.B.; Kimball, B.A.; Anderson, M.G.; Mauney, J.R. Effects of atmospheric CO<sub>2</sub> enrichment on plant growth: the interactive role of air temperature. *Agric. Ecosyst. Environ.* **1987**, *20*, 1–10, doi:10.1016/0167-8809(87)90023-5.
14. <https://www.iea.org/reports/putting-co2-to-use>.
15. <https://ourworldindata.org/co2-emissions>.
16. Pachaiappan, R.; Rajendran, S.; Senthil Kumar, P.; Vo, D.V.N.; K.A. Hoang, T. A review of recent progress on photocatalytic carbon dioxide reduction into sustainable energy products using carbon nitride. *Chem. Eng. Res. Des.* **2022**, *177*, 304–320, doi:10.1016/j.cherd.2021.11.006.
17. Wang, W.-N.; Soulis, J.; Yang, Y.J.; Biswas, P. Comparison of CO<sub>2</sub> Photoreduction Systems: A Review. *Aerosol Air Qual. Res.* **2014**, *14*, 533–549, doi:10.4209/aaqr.2013.09.0283.
18. Liu, B.J.; Torimoto, T.; Yoneyama, H. Photocatalytic reduction of CO<sub>2</sub> using surface-modified CdS photocatalysts in organic solvents. *J. Photochem. Photobiol. A Chem.* **1998**, *113*, 93–97, doi:10.1016/S1010-6030(97)00318-3.
19. Conte, F.; Rossetti, I.; Ramis, G.; Vaulot, C.; Hajjar-garreau, S.; Bennici, S. Low Metal Loading (Au, Ag, Pt, Pd) Photo-Catalysts Supported on TiO<sub>2</sub> for Renewable Processes. *Materials (Basel)*. **2022**, *15*, 2915, doi:10.3390/ma15082915.
20. Thompson, W.A.; Sanchez Fernandez, E.; Maroto-Valer, M.M. Review and Analysis of CO<sub>2</sub> Photoreduction Kinetics. *ACS Sustain. Chem. Eng.* **2020**, *8*, 4677–4692, doi:10.1021/acssuschemeng.9b06170.
21. Mao, J.; Li, K.; Peng, T. Recent advances in the photocatalytic CO<sub>2</sub> reduction over semiconductors. *Catal. Sci. Technol.* **2013**, *3*, 2481–2498,

- doi:10.1039/c3cy00345k.
22. Rawool, S.A.; Yadav, K.K.; Polshettiwar, V. Defective TiO<sub>2</sub> for photocatalytic CO<sub>2</sub> conversion to fuels and chemicals. *Chem. Sci.* **2021**, *12*, 4267–4299, doi:10.1039/d0sc06451c.
  23. Mizuno, T.; Adachi, K.; Ohta, K.; Saji, A. Effect of CO<sub>2</sub> pressure on photocatalytic reduction of CO<sub>2</sub> using TiO<sub>2</sub> in aqueous solutions. *J. Photochem. Photobiol. A Chem.* **1996**, *98*, 87–90, doi:10.1016/1010-6030(96)04334-1.
  24. Kočí, K.; Matějů, K.; Obalová, L.; Krejčíková, S.; Lacný, Z.; Plachá, D.; Čapek, L.; Hospodková, A.; Šolcová, O. Effect of silver doping on the TiO<sub>2</sub> for photocatalytic reduction of CO<sub>2</sub>. *Appl. Catal. B Environ.* **2010**, *96*, 239–244, doi:10.1016/j.apcatb.2010.02.030.
  25. Goren, Z.; Willner, I.; Nelson, A.J.; Frank, A.J. Selective photoreduction of CO<sub>2</sub>/HCO<sub>3</sub><sup>-</sup> to formate by aqueous suspensions and colloids of Pd-TiO<sub>2</sub>. *J. Phys. Chem.* **1990**, *94*, 3784–3790, doi:10.1021/j100372a080.
  26. Yin, S.; Han, J.; Zhou, T.; Xu, R. Recent progress in g-C<sub>3</sub>N<sub>4</sub> based low cost photocatalytic system: Activity enhancement and emerging applications. *Catal. Sci. Technol.* **2015**, *5*, 5048–5061, doi:10.1039/c5cy00938c.
  27. Mao, J.; Peng, T.; Zhang, X.; Li, K.; Ye, L.; Zan, L. Effect of graphitic carbon nitride microstructures on the activity and selectivity of photocatalytic CO<sub>2</sub> reduction under visible light. *Catal. Sci. Technol.* **2013**, *3*, 1253–1260, doi:10.1039/c3cy20822b.
  28. Ohno, T.; Murakami, N.; Koyanagi, T.; Yang, Y. Photocatalytic reduction of CO<sub>2</sub> over a hybrid photocatalyst composed of WO<sub>3</sub> and graphitic carbon nitride (g-C<sub>3</sub>N<sub>4</sub>) under visible light. *J. CO<sub>2</sub> Util.* **2014**, *6*, 17–25,

- doi:10.1016/j.jcou.2014.02.002.
29. Cao, Y.; Hu, S.; Yu, M.; Yan, S.; Xu, M. Adsorption and interaction of CO<sub>2</sub> on rutile TiO<sub>2</sub>(110) surfaces: A combined UHV-FTIRS and theoretical simulation study. *Phys. Chem. Chem. Phys.* **2015**, *17*, 23994–24000, doi:10.1039/c5cp04013b.
  30. He, H.; Zapol, P.; Curtiss, L.A. A theoretical study of CO<sub>2</sub> anions on anatase (101) surface. *J. Phys. Chem. C* **2010**, *114*, 21474–21481, doi:10.1021/jp106579b.
  31. Zhu, B.; Zhang, L.; Xu, D.; Cheng, B.; Yu, J. Adsorption investigation of CO<sub>2</sub> on g-C<sub>3</sub>N<sub>4</sub> surface by DFT calculation. *J. CO<sub>2</sub> Util.* **2017**, *21*, 327–335, doi:10.1016/j.jcou.2017.07.021.
  32. Kessler, F.K.; Zheng, Y.; Schwarz, D.; Merschjann, C.; Schnick, W.; Wang, X.; Bojdys, M.J. Functional carbon nitride materials-design strategies for electrochemical devices. *Nat. Rev. Mater.* **2017**, *2*, 17030, doi:10.1038/natrevmats.2017.30.
  33. Qin, G.; Zhang, Y.; Ke, X.; Tong, X.; Sun, Z.; Liang, M.; Xue, S. Photocatalytic reduction of carbon dioxide to formic acid, formaldehyde, and methanol using dye-sensitized TiO<sub>2</sub>film. *Appl. Catal. B Environ.* **2013**, *129*, 599–605, doi:10.1016/j.apcatb.2012.10.012.
  34. Halmann, M.; Ulman, M.; Mackoft, A.; Aurian-Blajent, B. Photoreduction of Carbon Dioxide to Formic Acid, Formaldehyde, Methanol, Acetaldehyde and Ethanol Using Aqueous Suspensions of Strontium Titanate with Transition Metal Additives. *Int. J. Sol. Energy* **1982**, *1*, 213–222, doi:10.1080/01425918208909887.

35. Kwawu, C.R.; Aniagyei, A.; Konadu, D.; Antwi, B.Y. Mechanisms of CO<sub>2</sub> reduction into CO and formic acid on Fe (100): a DFT study. *Mater. Renew. Sustain. Energy* **2021**, *10*, 9, doi:10.1007/s40243-021-00194-w.
36. Conte, F.; Tripodi, A.; Rossetti, I.; Ramis, G. Feasibility study of the solar-promoted photoreduction of CO<sub>2</sub> to liquid fuels with direct or indirect use of renewable energy sources. *Energies* **2021**, *14*, 2804, doi:10.3390/en14102804.
37. Conte, F.; Villa, A.; Prati, L.; Pirola, C.; Bennici, S.; Ramis, G.; Rossetti, I. Effect of Metal Cocatalysts and Operating Conditions on the Product Distribution and the Productivity of the CO<sub>2</sub> Photoreduction. *Ind. Eng. Chem. Res.* **2022**, *61*, 2963–2972, doi:10.1021/acs.iecr.1c02514.
38. Bahadori, E.; Tripodi, A.; Villa, A.; Pirola, C.; Prati, L.; Ramis, G.; Rossetti, I. High pressure photoreduction of CO<sub>2</sub>: Effect of catalyst formulation, hole scavenger addition and operating conditions. *Catalysts* **2018**, *8*, 430, doi:10.3390/catal8100430.
39. Islam, J.B.; Furukawa, M.; Tateishi, I.; Katsumata, H.; Kaneco, S. Photocatalytic reduction of hexavalent chromium with nanosized TiO<sub>2</sub> in presence of formic acid. *ChemEngineering* **2019**, *3*, 1–10, doi:10.3390/chemengineering3020033.
40. Yu, J.; Wang, S.; Low, J.; Xiao, W. Enhanced photocatalytic performance of direct Z-scheme g-C<sub>3</sub>N<sub>4</sub>-TiO<sub>2</sub> photocatalysts for the decomposition of formaldehyde in air. *Phys. Chem. Chem. Phys.* **2013**, *15*, 16883–16890, doi:10.1039/c3cp53131g.
41. Elbanna, O.; Fujitsuka, M.; Majima, T. G-C<sub>3</sub>N<sub>4</sub>/TiO<sub>2</sub> Mesocrystals Composite for H<sub>2</sub> Evolution under Visible-Light Irradiation and Its Charge Carrier Dynamics. *ACS Appl. Mater. Interfaces* **2017**, *9*, 34844–34854,

doi:10.1021/acsami.7b08548.

42. Zhang, X.; Wang, X.; Meng, J.; Liu, Y.; Ren, M.; Guo, Y.; Yang, Y. Robust Z-scheme g-C<sub>3</sub>N<sub>4</sub>/WO<sub>3</sub> heterojunction photocatalysts with morphology control of WO<sub>3</sub> for efficient degradation of phenolic pollutants. *Sep. Purif. Technol.* **2021**, 255, 117693, doi:10.1016/j.seppur.2020.117693.
43. Han, X.; Xu, D.; An, L.; Hou, C.; Li, Y.; Zhang, Q.; Wang, H. WO<sub>3</sub>/g-C<sub>3</sub>N<sub>4</sub> two-dimensional composites for visible-light driven photocatalytic hydrogen production. *Int. J. Hydrogen Energy* **2018**, 43, 4845–4855, doi:10.1016/j.ijhydene.2018.01.117.
44. Rehman, Z.U.; Bilal, M.; Hou, J.; Butt, F.K.; Ahmad, J.; Ali, S.; Hussain, A. Photocatalytic CO<sub>2</sub> Reduction Using TiO<sub>2</sub>-Based Photocatalysts and TiO<sub>2</sub> Z-Scheme Heterojunction Composites: A Review. *Molecules* **2022**, 27, 2069, doi:10.3390/molecules27072069.
45. Kumar, S.G.; Rao, K.S.R.K. Comparison of modification strategies towards enhanced charge carrier separation and photocatalytic degradation activity of metal oxide semiconductors (TiO<sub>2</sub>, WO<sub>3</sub> and ZnO). *Appl. Surf. Sci.* **2017**, 391, 124–148, doi:10.1016/j.apsusc.2016.07.081.
46. Klara, P.; dela Rosa, F.M.; Kovačić, M.; Kušić, H.; Štanger, U.L.; Fresno, F.; Dionysiou, D.D.; Bozic, A.L. Recent achievements in development of TiO<sub>2</sub>-based composite photocatalytic materials for solar driven water purification and water splitting. *Materials (Basel)*. **2020**, 13, 1338, doi:10.3390/ma13061338.
47. Tseng, I.H.; Chang, W.C.; Wu, J.C.S. Photoreduction of CO<sub>2</sub> using sol-gel derived titania and titania-supported copper catalysts. *Appl. Catal. B Environ.* **2002**, 37, 37–48, doi:10.1016/S0926-3373(01)00322-8.

48. Kočí, K.; Dang Van, H.; Edelmannová, M.; Reli, M.; Wu, J.C.S. Photocatalytic reduction of CO<sub>2</sub> using Pt/C<sub>3</sub>N<sub>4</sub> photocatalysts. *Appl. Surf. Sci.* **2020**, *503*, 144426, doi:10.1016/j.apsusc.2019.144426.
49. Ren, H.T.; Liang, Y.; Han, X.; Liu, Y.; Wu, S.H.; Bai, H.; Jia, S.Y. Photocatalytic oxidation of aqueous ammonia by Ag<sub>2</sub>O/TiO<sub>2</sub> (P25): New insights into selectivity and contributions of different oxidative species. *Appl. Surf. Sci.* **2020**, *504*, 144433, doi:10.1016/j.apsusc.2019.144433.
50. Lee, J.; Park, H.; Choi, W. Selective photocatalytic oxidation of NH<sub>3</sub> to N<sub>2</sub> on platinumized TiO<sub>2</sub> in water. *Environ. Sci. Technol.* **2002**, *36*, 5462–5468, doi:10.1021/es025930s.
51. Park, S.; Lee, J.T.; Kim, J. Photocatalytic oxidation of urea on TiO<sub>2</sub> in water and urine: mechanism, product distribution, and effect of surface platinumization. *Environ. Sci. Pollut. Res.* **2019**, *26*, 1044–1053, doi:10.1007/s11356-017-8380-3.
52. Huang, A.; Cao, L.; Chen, J.; Spiess, F.J.; Suib, S.L.; Obee, T.N.; Hay, S.O.; Freihaut, J.D. Photocatalytic degradation of triethylamine on titanium oxide thin films. *J. Catal.* **1999**, *188*, 40–47, doi:10.1006/jcat.1999.2617.
53. Fu, J.; Jiang, K.; Qiu, X.; Yu, J.; Liu, M. Product selectivity of photocatalytic CO<sub>2</sub> reduction reactions. *Mater. Today* **2020**, *32*, 222–243, doi:10.1016/j.mattod.2019.06.009.
54. Das, R.; Chakraborty, S.; Peter, S.C. Systematic Assessment of Solvent Selection in Photocatalytic CO<sub>2</sub> Reduction. *ACS Energy Lett.* **2021**, *6*, 3270–3274, doi:10.1021/acsenergylett.1c01522.
55. Horikoshi, S.; Watanabe, N.; Mukae, M.; Hidaka, H.; Serpone, N. Mechanistic examination of the titania photocatalyzed oxidation of ethanolamines. *New J.*

- Chem.* **2001**, 25, 999–1005, doi:10.1039/b102186i.
56. Visciano, P.; Schirone, M. Update on Biogenic Amines in Fermented and Non-Fermented Beverages. *Foods* **2022**, 11, 353, doi:10.3390/foods11030353.
  57. Denisov, N.; Yoo, J.E.; Schmuki, P. Effect of different hole scavengers on the photoelectrochemical properties and photocatalytic hydrogen evolution performance of pristine and Pt-decorated TiO<sub>2</sub> nanotubes. *Electrochim. Acta* **2019**, 319, 61–71, doi:10.1016/j.electacta.2019.06.173.
  58. Guzman, F.; Chuang, S.S.C.; Yang, C. Role of methanol sacrificing reagent in the photocatalytic evolution of hydrogen. *Ind. Eng. Chem. Res.* **2013**, 52, 61–65, doi:10.1021/ie301177s.
  59. Toe, C.Y.; Tsounis, C.; Zhang, J.; Masood, H.; Gunawan, D.; Scott, J.; Amal, R. Advancing photoreforming of organics: Highlights on photocatalyst and system designs for selective oxidation reactions. *Energy Environ. Sci.* **2021**, 14, 1140–1175, doi:10.1039/d0ee03116j.
  60. Berto, T.F.; Sanwald, K.E.; Eisenreich, W.; Gutiérrez, O.Y.; Lercher, J.A. Photoreforming of ethylene glycol over Rh/TiO<sub>2</sub> and Rh/GaN:ZnO. *J. Catal.* **2016**, 338, 68–81, doi:10.1016/j.jcat.2016.02.021.
  61. Liew, F.E.; Nogle, R.; Abdalla, T.; Rasor, B.J.; Canter, C.; Jensen, R.O.; Wang, L.; Strutz, J.; Chirania, P.; De Tissera, S.; et al. Carbon-negative production of acetone and isopropanol by gas fermentation at industrial pilot scale. *Nat. Biotechnol.* **2022**, 40, 335–344, doi:10.1038/s41587-021-01195-w.
  62. Henderson, M.A. Photooxidation of acetone on TiO<sub>2</sub>(110): Conversion to acetate via methyl radical ejection. *J. Phys. Chem. B* **2005**, 109, 12062–12070, doi:10.1021/jp0507546.

63. Shen, M.; Henderson, M.A. Identification of the active species in photochemical hole scavenging reactions of methanol on TiO<sub>2</sub>. *J. Phys. Chem. Lett.* **2011**, *2*, 2707–2710, doi:10.1021/jz201242k.

## Appendix B

Photocatalyst	Time (h)	CO <sub>2</sub> pressure (bar)	HS conc. (g/L)	HS conversion (%)	Other conditions	Productivity mol/kg <sub>cat</sub> ·h
P25	24	8	Na <sub>2</sub> SO <sub>3</sub> 1.67g/L	>95	80°C; pH14	HCOOH-3.24 H <sub>2</sub> -3.80
P25	24	18	Na <sub>2</sub> SO <sub>3</sub> 1.67g/L	>95	80°C; pH14	HCOOH-6.21 H <sub>2</sub> -4.20
FSP	24	8	Na <sub>2</sub> SO <sub>3</sub> 1.67g/L	>95	80°C; pH14	HCOOH-3.18 H <sub>2</sub> -3.67
FSP	24	18	Na <sub>2</sub> SO <sub>3</sub> 1.67g/L	>95	80°C; pH14	HCOOH-7.53 H <sub>2</sub> -4.77
TiO <sub>2</sub> -exCl	24	8	Na <sub>2</sub> SO <sub>3</sub> 1.67g/L	>95	80°C; pH14	HCOOH-7.09 H <sub>2</sub> -1.28
TiO <sub>2</sub> -exCl	24	18	Na <sub>2</sub> SO <sub>3</sub> 1.67g/L	>95	80°C; pH14	HCOOH-11.6 H <sub>2</sub> -4.29
TE-C <sub>3</sub> N <sub>4</sub>	24	8	Na <sub>2</sub> SO <sub>3</sub> 1.67g/L	>95	80°C; pH14	HCOOH-7.85 H <sub>2</sub> -1.22
TE-C <sub>3</sub> N <sub>4</sub>	24	18	Na <sub>2</sub> SO <sub>3</sub> 1.67g/L	>95	80°C; pH14	HCOOH-6.31 H <sub>2</sub> -4.00
TiO <sub>2</sub> -exCl/TE	24	8	Na <sub>2</sub> SO <sub>3</sub> 1.67g/L	>95	80°C; pH14	HCOOH-2.32 H <sub>2</sub> -2.01
TiO <sub>2</sub> -exCl/TE	24	18	Na <sub>2</sub> SO <sub>3</sub> 1.67g/L	>95	80°C; pH14	HCOOH-6.68 H <sub>2</sub> -2.90
P25/TE	24	8	Na <sub>2</sub> SO <sub>3</sub> 1.67g/L	>95	80°C; pH14	HCOOH-6.00 H <sub>2</sub> -2.01
P25/TE	24	18	Na <sub>2</sub> SO <sub>3</sub> 1.67g/L	>95	80°C; pH14	HCOOH-13.5 H <sub>2</sub> -2.85
TiO <sub>2</sub> -exCl/TE	24	18	Na <sub>2</sub> SO <sub>3</sub> 5.00g/L	>95	80°C; pH14	HCOOH-25.8 H <sub>2</sub> -0.90 CO-0.014
P25/TE	24	18	Na <sub>2</sub> SO <sub>3</sub> 5.00g/L	>95	80°C; pH14	HCOOH-30.7



						H <sub>2</sub> -1.42 CO-0.011
P25	6	18	Na <sub>2</sub> SO <sub>3</sub> 1.67g/L	47	80°C; pH14	HCOOH-16.9 H <sub>2</sub> -0
FSP	6	18	Na <sub>2</sub> SO <sub>3</sub> 1.67g/L	40	80°C; pH14	HCOOH-14.2 H <sub>2</sub> -1
Photocatalyst	Time (h)	CO <sub>2</sub> pressure (bar)	HS conc. (g/L)	HS conversion (%)	Other conditions	Productivity mol/kg <sub>cat</sub> ·h
TiO <sub>2</sub> -exCl	6	18	Na <sub>2</sub> SO <sub>3</sub> 1.67g/L	74	80°C; pH14	HCOOH-39.8 H <sub>2</sub> -1
TE	6	18	Na <sub>2</sub> SO <sub>3</sub> 1.67g/L	41	80°C; pH14	HCOOH-16.2 H <sub>2</sub> -1
TiO <sub>2</sub> -exCl/TE	6	18	Na <sub>2</sub> SO <sub>3</sub> 1.67g/L	77	80°C; pH14	HCOOH-37.2 H <sub>2</sub> -0.25
P25/TE	6	18	Na <sub>2</sub> SO <sub>3</sub> 1.67g/L	79	80°C; pH14	HCOOH-39.8 H <sub>2</sub> -0.37
C <sub>3</sub> N <sub>4</sub> -600-0W	24	8	Na <sub>2</sub> SO <sub>3</sub> 1.67g/L	>95	80°C; pH14	HCOOH-5.53 H <sub>2</sub> -1.25 CO-0.043
C <sub>3</sub> N <sub>4</sub> -600-120W	24	8	Na <sub>2</sub> SO <sub>3</sub> 1.67g/L	>95	80°C; pH14	HCOOH-8.20 H <sub>2</sub> -1.24 CO-0.028
C <sub>3</sub> N <sub>4</sub> -550-0W	24	8	Na <sub>2</sub> SO <sub>3</sub> 1.67g/L	>95	80°C; pH14	HCOOH-5.12 H <sub>2</sub> -0.16 CO-0.052
C <sub>3</sub> N <sub>4</sub> -550-30W	24	8	Na <sub>2</sub> SO <sub>3</sub> 1.67g/L	>95	80°C; pH14	HCOOH-5.77 H <sub>2</sub> -1.92 CO-0.020
C <sub>3</sub> N <sub>4</sub> -550-60W	24	8	Na <sub>2</sub> SO <sub>3</sub> 1.67g/L	>95	80°C; pH14	HCOOH-5.90 H <sub>2</sub> -2.13 CO-0.041
C <sub>3</sub> N <sub>4</sub> -550-90W	24	8	Na <sub>2</sub> SO <sub>3</sub> 1.67g/L	>95	80°C; pH14	HCOOH-7.73 H <sub>2</sub> -2.29 CO-0
C <sub>3</sub> N <sub>4</sub> -550-120W	24	8	Na <sub>2</sub> SO <sub>3</sub> 1.67g/L	>95	80°C; pH14	HCOOH-8.20 H <sub>2</sub> -3.52 CO-0.062

C <sub>3</sub> N <sub>4</sub> -550-120W	2	8	Na <sub>2</sub> SO <sub>3</sub> 1.67g/L	26	80°C; pH14	HCOOH-52.3 H <sub>2</sub> -0
C <sub>3</sub> N <sub>4</sub> -550-120W	5	8	Na <sub>2</sub> SO <sub>3</sub> 1.67g/L	40	80°C; pH14	HCOOH-50.0 H <sub>2</sub> -0
C <sub>3</sub> N <sub>4</sub> -550-120W	6	8	Na <sub>2</sub> SO <sub>3</sub> 1.67g/L	60	80°C; pH14	HCOOH-49.7 H <sub>2</sub> -0
Photocatalyst	Time (h)	CO <sub>2</sub> pressure (bar)	HS conc. (g/L)	HS conversion (%)	Other conditions	Productivity mol/kg <sub>cat</sub> ·h
C <sub>3</sub> N <sub>4</sub> /WO <sub>3</sub> -10%	24	8	Na <sub>2</sub> SO <sub>3</sub> 1.67g/L	>95	80°C; pH14	HCOOH-5.58 H <sub>2</sub> -5.07 CO-0.104 CH <sub>4</sub> -0.067
C <sub>3</sub> N <sub>4</sub> /WO <sub>3</sub> -20%	24	8	Na <sub>2</sub> SO <sub>3</sub> 1.67g/L	>95	80°C; pH14	HCOOH-6.87 H <sub>2</sub> -3.58 CO-0.131 CH <sub>4</sub> -0.009
C <sub>3</sub> N <sub>4</sub> /WO <sub>3</sub> -30%	24	8	Na <sub>2</sub> SO <sub>3</sub> 1.67g/L	>95	80°C; pH14	HCOOH-6.89 H <sub>2</sub> -3.52 CO-0.187 CH <sub>4</sub> -0.006
C <sub>3</sub> N <sub>4</sub> /WO <sub>3</sub> -40%	24	8	Na <sub>2</sub> SO <sub>3</sub> 1.67g/L	>95	80°C; pH14	HCOOH-7.39 H <sub>2</sub> -3.77 CO-0.273 CH <sub>4</sub> -0.006
WO <sub>3</sub>	24	8	Na <sub>2</sub> SO <sub>3</sub> 1.67g/L	>95	80°C; pH14	HCOOH-6.51 H <sub>2</sub> -1.28 CO-0.074 CH <sub>4</sub> -0.015
FSP-TiO <sub>2</sub>	6	18	Na <sub>2</sub> SO <sub>3</sub> 1.67g/L	40	80°C; pH14	HCOOH-13.9 H <sub>2</sub> -0
FSP-WO <sub>3</sub>	6	18	Na <sub>2</sub> SO <sub>3</sub> 1.67g/L	43	80°C; pH14	HCOOH-14.7 H <sub>2</sub> -0
TiO <sub>2</sub> /WO <sub>3</sub> 60/40	6	18	Na <sub>2</sub> SO <sub>3</sub> 1.67g/L	77	80°C; pH14	HCOOH-36.5 H <sub>2</sub> -0
P25	6	8	CH <sub>3</sub> COOH 0.76 g/L	/	80°C; pH14	HCOOH-0 H <sub>2</sub> -0 CO-0.023
P25	6	8	NH <sub>3</sub>	/	80°C; pH14	HCOOH-0

P25	6	8	0.51 g/L Urea	/	80°C; pH14	H <sub>2</sub> -0 HCOOH-0
P25	6	8	0.42 g/L Thiourea	/	80°C; pH14	H <sub>2</sub> -0 HCOOH-0
P25	6	8	1.6 g/L Methanol	/	80°C; pH14	H <sub>2</sub> -0 HCOOH-0.718 CO-0.032

Photocatalyst	Time (h)	CO <sub>2</sub> pressure (bar)	HS conc. (g/L)	HS conversion (%)	Other conditions	Productivity mol/kg <sub>cat</sub> ·h
P25	6	6	2-Butanol 1.2 g/L	/	80°C; pH14	HCOOH-1.40 CO-0.779 C <sub>2</sub> H <sub>6</sub> -135 C <sub>2</sub> H <sub>4</sub> -31.5 CH <sub>4</sub> -6.4
P25	6	8	1-Propanol 0.95 g/L	/	80°C; pH14	HCOOH-1.59 CO-0.594 C <sub>2</sub> H <sub>6</sub> -44.9 C <sub>2</sub> H <sub>4</sub> -5.47
P25	6	8	1,2-Propanediol 1.2 g/L	/	80°C; pH14	HCOOH-0.631 CO-0.566 C <sub>2</sub> H <sub>6</sub> -53.5 C <sub>2</sub> H <sub>4</sub> -4.40 CH <sub>4</sub> -4.08
P25	6	8	2-Propanol 0.95 g/L	19.6	80°C; pH14	HCOOH-2.40 H <sub>2</sub> -1.45 CO-0.579 C <sub>2</sub> H <sub>6</sub> -38.0 C <sub>2</sub> H <sub>4</sub> -2.65 CH <sub>4</sub> -10
P25	6	8	Glycerin 1.46		80°C; pH14	HCOOH-0.491 CO-0.673 C <sub>2</sub> H <sub>6</sub> -2.46 CH <sub>4</sub> -0.358
P25	6	8	Ethyl glycol 0.99 g/L		80°C; pH14	HCOOH-0.265 CO-0.288 HCOH-2.42 CH <sub>4</sub> -0.385

P25	6	8	Triethylamine 1.60 g/L	80°C; pH14	HCOOH-1.40 CO-0.204 C <sub>2</sub> H <sub>6</sub> -6.91 C <sub>2</sub> H <sub>4</sub> -3.25 CH <sub>4</sub> -0.337
P25	6	8	Triethanolamine 2.37 g/L	80°C; pH14	HCOOH-2.43 CO-3.29 C <sub>2</sub> H <sub>6</sub> -24.7 C <sub>2</sub> H <sub>4</sub> -3.88 CH <sub>4</sub> -2.493
P25	6	8	Tripopylamine 2.27 g/L	80°C; pH14	HCOOH-2.62 CO-1.33 C <sub>2</sub> H <sub>6</sub> -129 C <sub>2</sub> H <sub>4</sub> -5.86 CH <sub>4</sub> -0.056

---

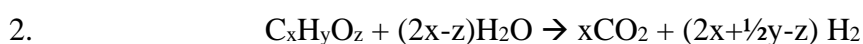
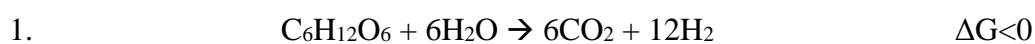
## 5. Carbohydrate photoreforming

### 5.1. Introduction

As already mentioned, there is a need for an inexpensive, reliable and sustainable source of energy that will free us from the dependence on fossil fuels. It is not necessary to reinvent the wheel and just by looking to nature it is possible to observe that the plants, through the evolution, have mastered the way to convert the sunlight radiation into chemical energy via the formation of polymeric sugars such as cellulose. Indeed, natural fibers and wood have had a key role during the human evolution, before the era of synthetic products, and in many countries, these are still the main source of energy and raw materials.

The European commission estimated in 2018 that roughly 956 MT of dry waste biomass were produced by the twenty-eight countries of the union, of which 54% was food and 46% was composed of residues such as leaves and stems [1]. These residues are important to maintain a sufficient carbon level in the soil and in some cases may be marketable, for instance when used to feed animals, but most of it is left to decompose while it could be further valorized with chemical treatments. Generally, speaking, dry biomass has a higher heating value that falls in the range 14-19 MJ/kg, while for reference, the coal can be as high as 30 MJ/kg. Therefore, there is a potential source of energy that we are not taking advantage of. One of the most adopted processes to treat biomass is fermentation, which requires sugary feedstock such as sugar cane or corn, though that kind of biomass source is becoming of concern due to their value as a food. Conversely, lignocellulosic materials do not pose ethical problem but they require pretreatments (delignification), like partial hydrolysis, that convert the biomass into something more digestible by yeast and bacteria [2,3]. The resulting alcohols and other platform molecules are then used in traditional

petrochemical processes, including polymers and pharmaceuticals, that lately have been described as “biorefinery” [4]. The integrated biorefinery is particularly promising since it could serve as alternative source of chemicals and fuels, therefore valorizing the biomass and lowering the consumption of fossil resources. Being lignocellulosic biomass widely available almost everywhere, it follows that this kind of system are quite scalable. Of course, that kind of transformation can also be carried out by means of light-driven processes that reform the biomass and that operate at ambient temperature and pressure, in contrast to more energy-intensive processes like gasification. Rao et al. [4] summarised the state of the art regarding the photoreforming of glucose and cellulosic material in general by using titanium dioxide and other photocatalysts. Leaving out the latter, by tuning the characteristics of TiO<sub>2</sub> and the conditions of the treatment it is possible to convert sugars into countless feedstock, including, formic acid, arabinose, glucuronic acid, glycerol, and many other acids, aldehydes and liquid products. In addition, metal loaded titania-based photocatalysts are particularly known to induce the production of hydrogen from water when sugars are used as hole scavenger [5], since the oxidation of glucose and similar compounds is more favorable from a thermodynamic point of view with respect to oxidation of water (Eq. 1). Equation 2 is applicable to a broader range of compounds.



Our group has been working with glucose photoreforming in liquid by using a high-pressure stainless-steel photoreactor (see Chapter 2) equipped with UVA lamp [6] and loaded with titanium dioxide P25 or metallized titania photocatalyst (Pt, Au, Ag, Pd). In the selected conditions, the main product of the gaseous phase was hydrogen along with

small amounts of ethylene and carbon monoxide. In this chapter, it will be discussed the photocatalytic performance of that system when mono and bimetallic titania-based photocatalysts are used to treat glucose and more complex organic mixtures, that are Kraft black liquor and Spent sulphite liquor deriving from a potential big source of sugar-containing waste waters such as the paper industry [7]. The composition of these two sugar-rich wastewaters from the pulp industry was replicated and tested for photoreforming to better understand the behavior of the photocatalyst under real-life conditions, which is particularly interesting in that case since the global pulp market reached levels of production around 160 Mt in 2013 and thus comparable amounts of wastewater were generated [8]. Although the contaminated water is no longer discharged directly into the rivers and lakes, the main concern of the regulators is the presence of chlorinated compound rather than the carbon content of the effluents, that can still pose a hazard to aquatic life and the whole ecosystem in general [8].

## **5.2. Result and discussion**

### **5.2.1. Effect of catalysts composition and metal loading**

The starting point of this work are the optimized conditions found by our research group, which were 80°C, 5 bar of N<sub>2</sub>, 5 g/L of HS (glucose) and 0.25 g/L of photocatalyst [6,9,10]. From here, the kind of hole scavenger and the pH was modified or not depending on the kind of test. Table 5.1a reports the results of several experiments with glucose and mono- and bimetallic titania photocatalysts, compared with the benchmark P25. Figure 5.1 clearly shows that the deposition of metallic nanoparticles over titania surface has a positive effect both on hydrogen productivity and glucose conversion, with the former that increased up to seven times in case of 0.36wt.%Pt/P25 and five times when

0.36wt.% Au/P25 was used. Pt is likely to be more active for the hydrogen evolution since its overpotential for hydrogen activation is lower than that of gold. In addition, the work function of Pt is higher than Au (6.4 vs. 5.1 eV) and so the electron trapping effect is enhanced in the first case. The main byproducts were CO<sub>2</sub> and CO, with more or less similar concentration for all the catalysts considered, with the sole exception of P25. Other gaseous products were detected in traces (*e.g.* methane, ethylene, ethane), among which ethane was the most abundant one.

An additional sample of 0.36wt.% Pt/P25 was prepared by performing a second reduction treatment at 700°C, in an attempt to further reduce the titania surface (promoted by the co-catalyst) and produce more oxygen vacancies, which is known to have a positive effect on the band gap of the material. Figures 5.1a and 5.1b illustrate that the product distribution was almost the same than for the 0.36wt.% Pt/P25 sample and only the hydrogen productivity was slightly increased. Speaking of bimetallic samples, despite the expectation it is clear than they performed worse than the mono metallic photocatalysts, at least in case of 0.36wt.% Pt/P25 sample, and a higher metal loading was detrimental to both the glucose conversion and hydrogen productivity, with the differences in activity that are probably due to the electronic properties of each material, as the textural ones were almost identical.

Figure 5.1c shows the cumulative production of hydrogen over the 5h of test, from which is clear that there was not significant deactivation during the experiments and the H<sub>2</sub> amount increased almost linearly by the time.

Zhao et al. [11] reported 6250 mmol/kg<sub>cat</sub> h while using Au/TiO<sub>2</sub> prepared via sol-immobilization and under simulated solar radiation, and the products distribution was aligned with our findings. Other authors [12] reported that the activity of bimetallic



loaded titania photocatalysts reduced at high temperature under  $H_2$  decreased by 40% when the platinum and gold content was increased from 0.5% wt to 1% wt, though it was still higher than the monometallic ones loaded with 1% wt of metal and reduced in the same conditions.

### 5.2.2. Effect of pH

The pH of the solution affects how the photocatalyst surface is charged. As an example, pH lower than the point of zero charge of P25 ( $pH_{pzc}$ ) leads to adsorption of  $H^+$  ions and the surface will be charged positively. Conversely, when working at pH above the point of zero charge of titania, the negative ions will be repelled by the photocatalysts, for the deprotonated hydroxyl group that populate the surface. So far, we worked without adjusting the pH of the glucose solution, that was around 6.5 once the sugar is dissolved in water, however, both the simulated wastewaters were characterized by an acidic pH and thus it was necessary to evaluate the effect of this parameter on the performance of the system.

Therefore, glucose photoreforming with P25 was carried out at pH 3.5, 5, 7 and 12.5 (Figure 5.2a). The test at pH 12.5 gave negligible hydrogen productivity and it was not possible to calculate the glucose conversion via chromatography due to the formation of a huge number of unidentified intermediates, indeed, at the end of the process the solution turned from clear to a brownish color, whose scent was like caramel. At that pH there is a low concentration of  $H^+$  ions and glucose are in its deprotonated form ( $PZC_{glu}$  12.3) thus, it cannot reach the titania surface due to electrostatic repulsion. Also, it was reported in literature that the degradation of glucose in alkaline environment tends to produce

oligomers, which ability to be adsorbed and oxidated over the photocatalysts surface are not known [13].

The hydrogen productivity was suppressed as well at pH 3.5, being the PZC of titania around 6-6.5 [14] and  $H^+$  are repelled by its surface groups in their acidic form [15]. Again, the evolution of  $H_2$  increased linearly with the irradiation time (Figure 5.2b), while  $CO_2$  seems to be the main product at pH different from 7, meaning that the reaction path was mainly oxidative, and among the other possible compounds, only traces of CO and ethylene were detected. Moreover, the TOC analysis unveiled that the HS conversion is low at this pH (Table 5.1), and the glucose is oxidated to arabinose and many other sugars rather than to  $CO_2$ .

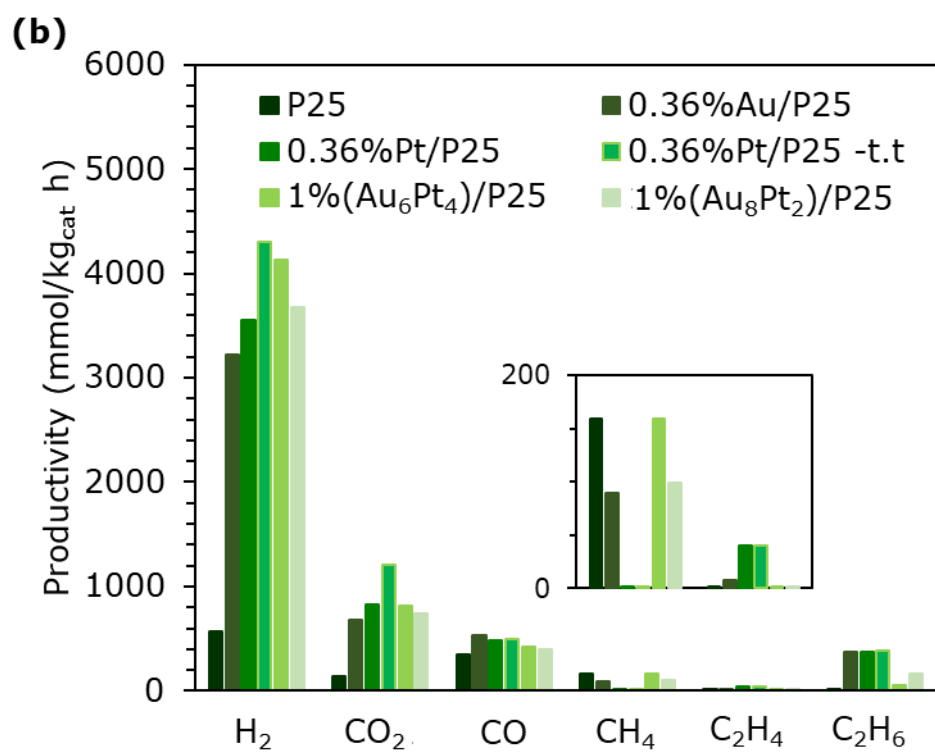
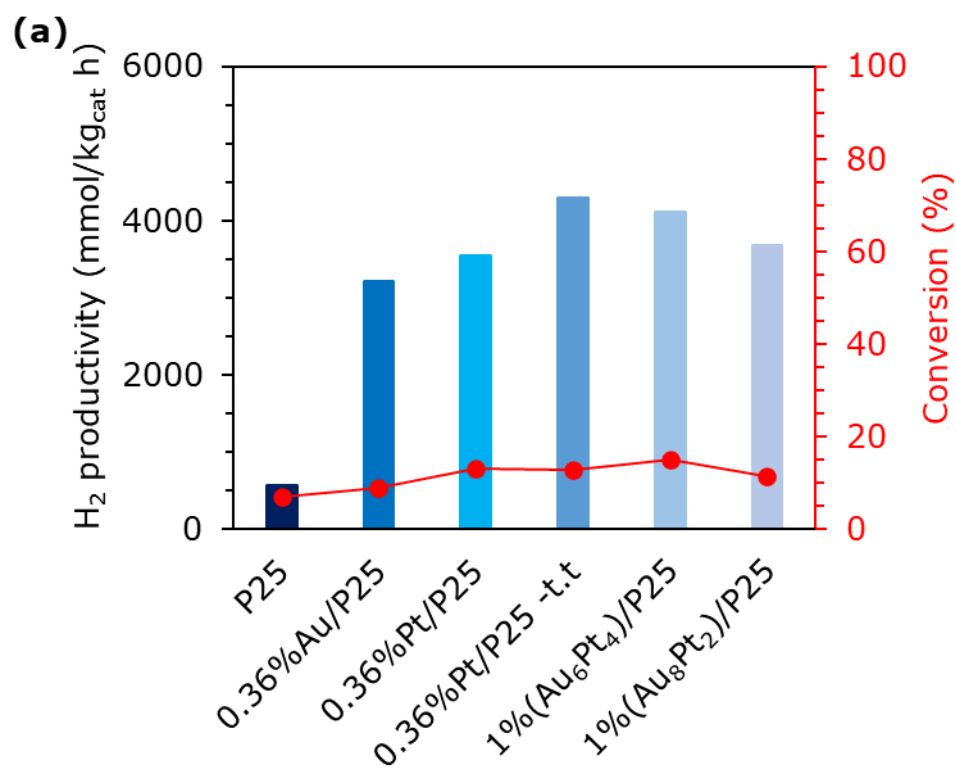
### **5.2.3. Photoreforming of wastewater from pulp industry**

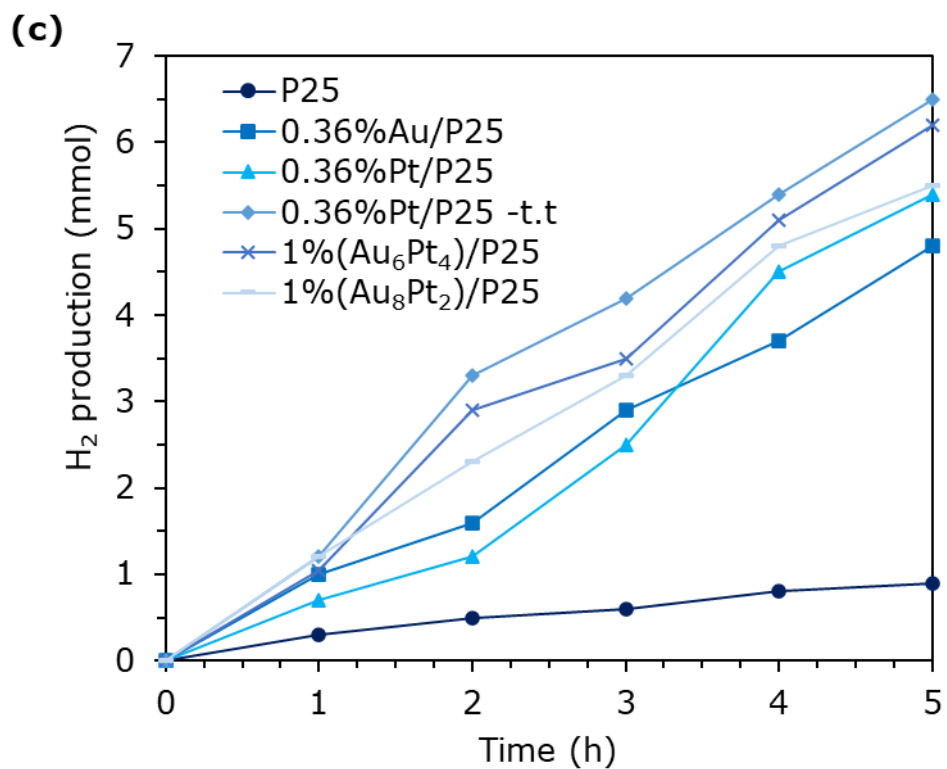
Before treating Black Kraft Liquor and Spent Sulfite Liquor, we used tartaric acid as a model molecule for wastewater containing organic acids. As reported in Figure 5.3, the tartaric acid conversion was five times higher than glucose (*ca.* 40%), when the same conditions were applied, and the TOC conversion increased as well, from 0.7% to 12.2%. In addition, the productivity of  $CO_2$  rose dramatically up to 6 mol/kg<sub>cat</sub> h and also the amount of ethane detected, around 2.7 mol/kg<sub>cat</sub> h, was impressive. A similar behaviour was already reported in literature in case of cellulose hydrolysate rich of tartaric acid that was photoreformed under UV with  $SrTiO_3$  [16]. The presence of the latter was found to be crucial to increase the hydrogen productivity since its hydroxymethyl moieties can be easily oxidated by the photogenerated holes on photocatalysts surface, though lignin-based hydrolysate showed lower  $H_2$  productivity despite being rich of tartaric acid. In our

case, the high CO<sub>2</sub> and ethane productivity may be the consequence of the double decarboxylation of tartaric acid followed by dehydroxylation of the so formed ethanediol. Then, we proceeded with the test of both the simulated wastewater, whose concentration was around 15 g/L. During a previous work, our group already investigated the effect of glucose concentration up to 8 g/L, which impacted negatively on the hydrogen productivity due to the “surface crowding effect”, which is when the surface of the photocatalyst is highly populated by glucose molecule that desorb before undergoing the full oxidation cycle. Since the re-adsorption is less probable in that environment, the consequences are an overall low activity [17].

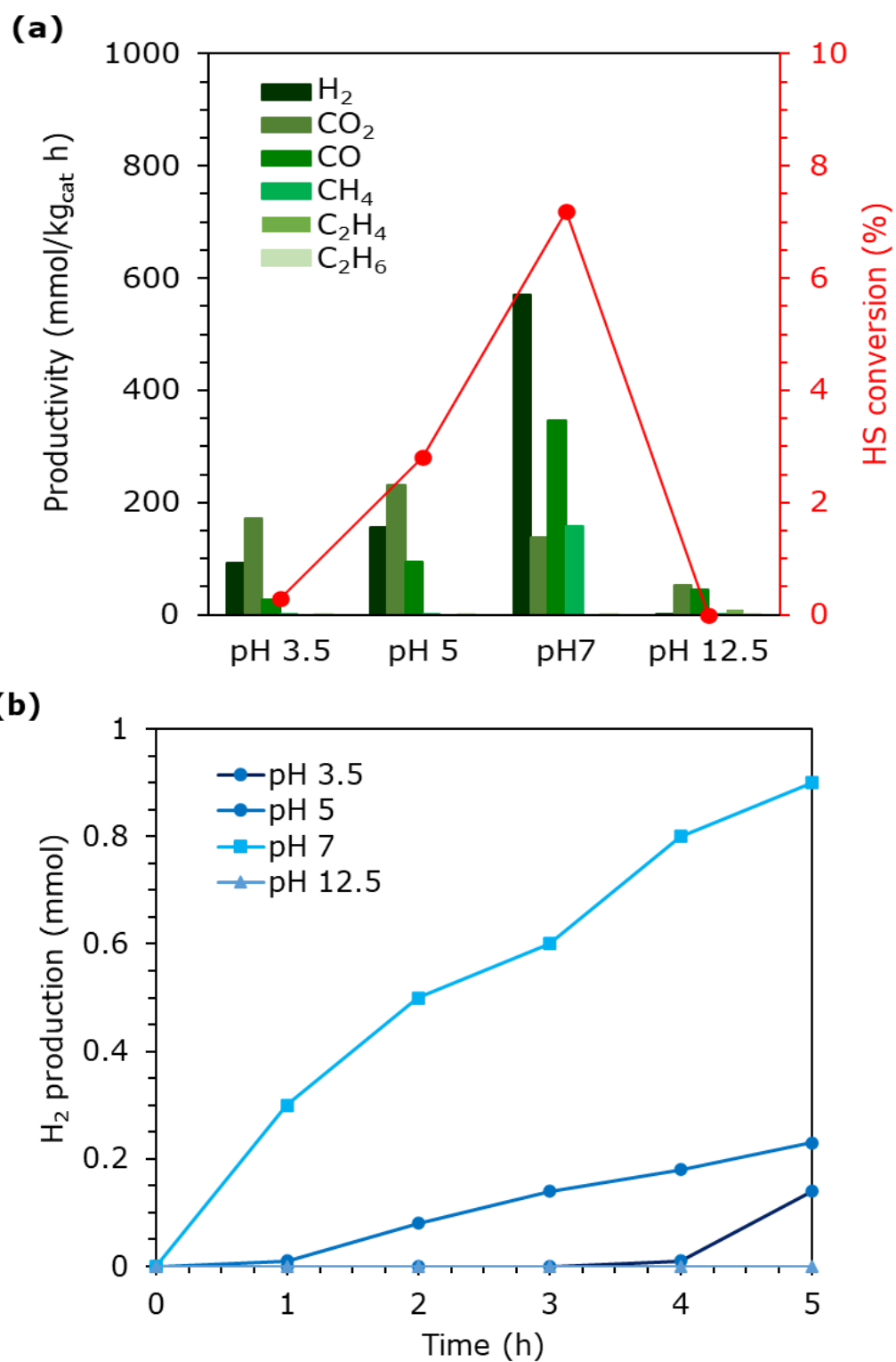
The photoreforming of Black Kraft Liquor led to high productivities of CO<sub>2</sub> and ethane, both in case of monometallic photocatalyst loaded with Pt and bimetallic 1wt.%(Au<sub>6</sub>Pt<sub>4</sub>), *i.e.* the best performing when testing the model glucose molecule (Figure 5.4a). The values observed were higher even than the benchmark glucose/P25 and the ethane productivity was respectively 4.6 and 3.45 mol/kg<sub>cat</sub> h. In addition, TOC conversion was significantly higher than the benchmark, almost ten times, while in general other products never reached productivities above the mmol/kg<sub>cat</sub> h. The presence of that amounts of ethane can be ascribed again to the decarboxylation-dehydroxylation steps, in particular, the decomposition of formic acid (already detected when using glucose as HS) and oxalic acid is known to lead to formation of methane and ethane [11]. The evolution of the main gaseous species (*i.e.* H<sub>2</sub> and C<sub>2</sub>H<sub>6</sub>) was monitored during the test, and it was found that the amount of products continuously rose, though the curve of hydrogen diverged from the one of ethane and tended to reach a plateau, while the other curve surge at the end of the process (Figure 5.4b).

On the other hand, the results after processing Sulfite Spent Liquor (Figure 5.5) were not as good as Black Kraft Liquor, as hydrogen was not the main product (ca. 100 mmol/kg<sub>cat</sub> h) and mostly CO<sub>2</sub> and methane were detected, although with productivities below 500 mmol/kg<sub>cat</sub> h. Conversely, the TOC conversion was higher than the benchmark, around 10%. Again, the formation of oligomers that deposit or are difficult to desorb may be the cause of the low activity.

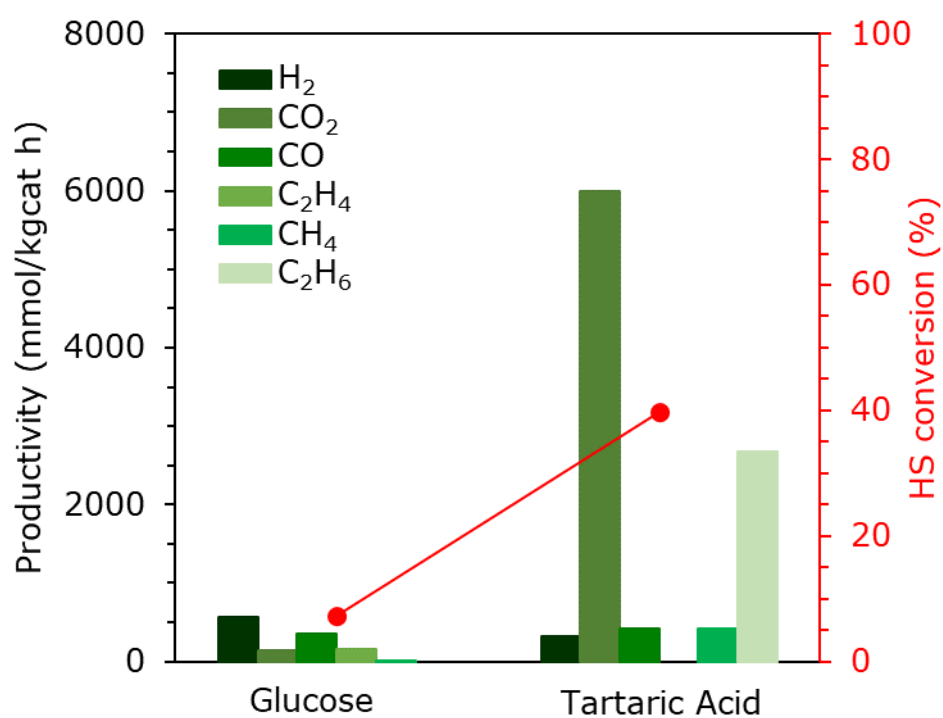




**Figure 5.1.** (a) Glucose conversion and hydrogen productivity of selected monometallic photocatalysts; (b) productivity of other gaseous species; (c) evolution of hydrogen over the time of the test. t.t. stands for thermal treatment

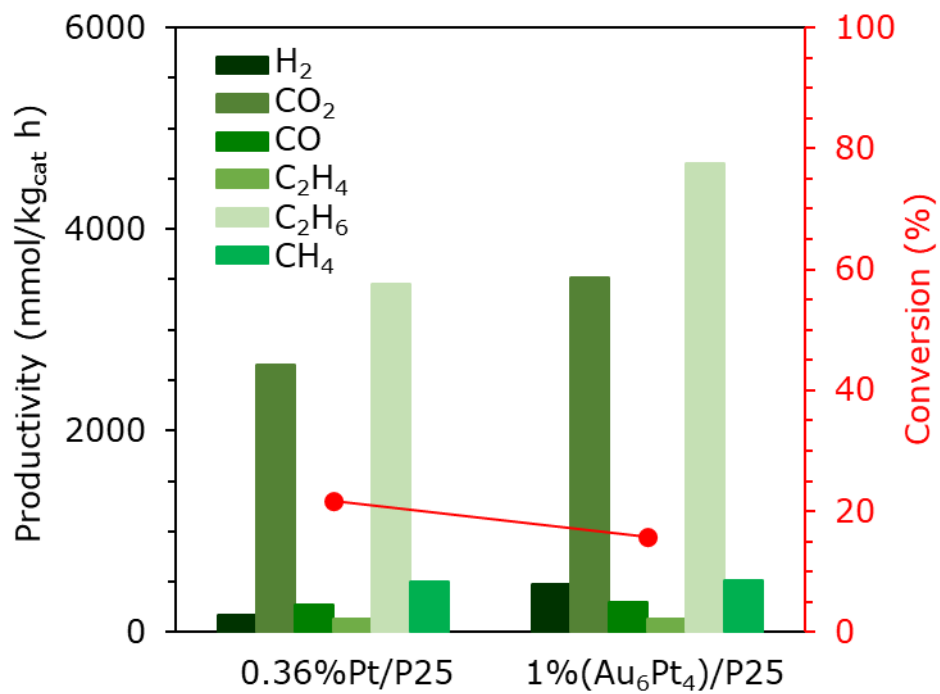


**Figure 5.2.** (a) Glucose conversion and hydrogen productivity of P25 under different pH; (b) evolution of hydrogen over the time for tests carried out between pH 3 and 12.5



**Figure 5.3.** Photoreforming of glucose and tartaric acid by using TiO<sub>2</sub>-P25

**(a)**





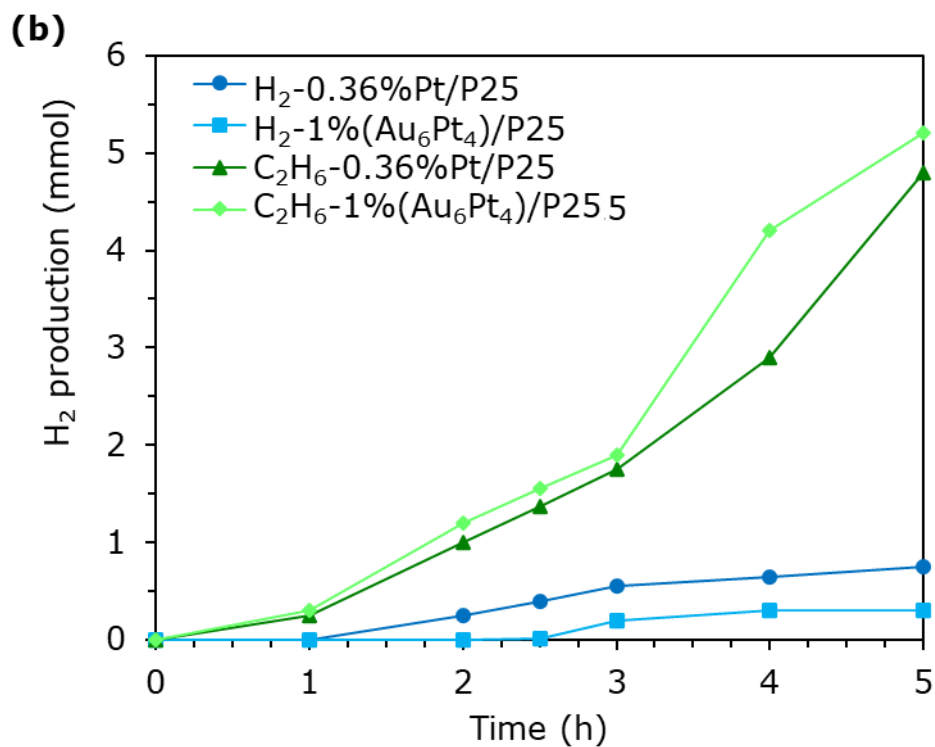


**Figure 5.4.** (a) photoreforming of simulated Black Kraft Liquor by using 0.36wt.%Pt/P25 and 1wt.%(Au<sub>6</sub>Pt<sub>4</sub>)/P25 photocatalysts; (b) evolution of main products over the test

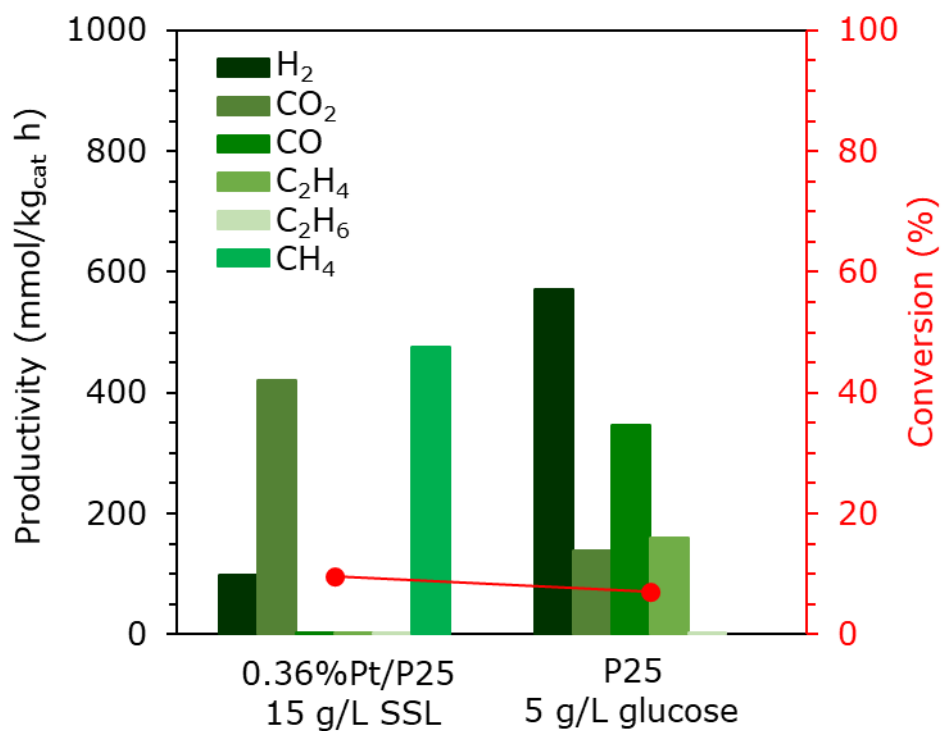


**Figure 5.5.** Photoreforming of simulated Spent Sulfite Liquor by using 0.36wt.%Pt/P25 and comparison with benchmark P25 and glucose

**Table 5.1.** Summary of activity tests. Productivity is mmol/kg<sub>cat</sub> h. HS = hole scavenger;

GL = glucose; TA = tartaric acid; BL = black kraft liquor; SS = spent sulfite liquor

Catalyst	HS	pH	Conversion HS	Conversion TOC	Arabinose	H <sub>2</sub>	CO <sub>2</sub>	CO	C <sub>2</sub> H <sub>4</sub>	CH <sub>4</sub>	C <sub>2</sub> H <sub>6</sub>
			%	%							
P25	GL	3.5	0.3	0.7	9.9	92.6	171.7	27.32	0	0	0
P25	GL	5	2.8	/	17.4	155.2	232.2	94.9	65.7	0	0
P25	GL	7	7.2	/	34.6	571.1	139.1	346.1	159	1.41	0
P25	GL	12.5	/	/	/	0	52.2	44.7	0	9.6	0
0.36wt.% Au/P25	GL	7	8.9	/	68.5	3225	685.8	532.6	89.3	7.2	371.8
0.36wt.% Pt/P25	GL	7	13.2	/	97.2	3549	830.3	438.4	/	39.8	376.8
1wt.% Au/P25	GL	7	4.7	0.3	27.1	721.1	129.9	117.7	/	6.2	71
1wt.% Pt/P25	GL	7	7.5	1.4	65.7	1522	382	289	50.8	27.7	409.5
1wt.% (Au <sub>6</sub> Pt <sub>4</sub> )/P25	GL	7	15.2	/	109	4124	810.2	422.9	159.1	/	59.4
1wt.% (Au <sub>8</sub> Pt <sub>2</sub> )/P25	GL	7	11.4	/	85.4	3679.2	741.3	396.7	98.8	1.2	158.4
P25	TA	2-3	39.7	12.2	/	324.9	5992.9	415.6	/	412.5	2669.9
1wt.% (Au <sub>6</sub> Pt <sub>4</sub> )/P25	BK	2-3	/	21.7	/	170.4	2659.2	275.6	135.2	507.3	3450
1wt.% Au/P25	BK	2-3	/	15.8	/	480.6	3517.6	303.6	129.1	511.6	4651
1wt.% Pt/P25	SS	3	/	9.7	/	98.4	419.9	/	/	476.1	/

### 5.3. Conclusions

We explored the possibility to obtain hydrogen and other gaseous compounds of interest (mainly ethane) via photoreforming of solutions containing glucose, tartaric acid and simulated wastewater produced by pulp processing. It was found that titania P25 photocatalysts loaded with noble metals, such as 0.36wt.%Pt/P25 and 1wt.%(Au<sub>x</sub>Pt<sub>y</sub>)/P25 were quite active in the photoreforming process, at least to what concerns the conversion of glucose and hydrogen productivity. In particular, 1wt.%(Au<sub>6</sub>Pt<sub>4</sub>)/P25 achieved a productivity over 4000 mmol/kg<sub>cat</sub>·h of the H<sub>2</sub>, thus positioning above similar results already reported in literature [15].

In general, the conversion of the HS was low, thus, further studies should be carried out in order to overcome the kinetic limitations, with more attention dedicated to the composition of the photocatalysts itself, as superior textural properties of bimetallic photocatalyst actually led to lower performance than monometallic Pt/P25.

Tartaric acid led to a different product distribution with respect to glucose, as the main product was CO<sub>2</sub> along with ethane, however, when starting from waste solution this could still come as a valorization.

In general, the photodegradation of hydroxylated carboxylic acid was found to be easier, in terms of conversion, with respect to sugars, as highlighted by the treatment of the two simulated liquors and despite a pH correction may be necessary in order to achieve the best productivity of the desired products.

## References

1. Camia, A.; Robert, N.; Eds. Biomass production, supply, uses and flows in the European Union. *Publ. Off. Eur. Union* **2018**, 1–126, doi:10.2760/181536.
2. Hossain, N.; Zaini, J.H.; Mahlia, T.M.I. A review of bioethanol production from plant-based waste biomass by yeast fermentation. *Int. J. Technol.* **2017**, 8, 5–18, doi:10.14716/ijtech.v8i1.3948.
3. Pfab, E.; Filiciotto, L.; Luque, R. The Dark Side of Biomass Valorization: A Laboratory Experiment to Understand Humin Formation, Catalysis, and Green Chemistry. *J. Chem. Educ.* **2019**, 96, 3030–3037, doi:10.1021/acs.jchemed.9b00410.
4. Navakoteswara Rao, V.; Malu, T.J.; Cheralathan, K.K.; Sakar, M.; Pitchaimuthu, S.; Rodríguez-González, V.; Mamatha Kumari, M.; Shankar, M.V. Light-driven transformation of biomass into chemicals using photocatalysts – Vistas and challenges. *J. Environ. Manage.* **2021**, 284, 111983, doi:10.1016/j.jenvman.2021.111983.
5. Rioja-Cabanillas, A.; Valdesueiro, D.; Fernández-Ibáñez, P.; Byrne, J.A. Hydrogen from wastewater by photocatalytic and photoelectrochemical treatment. *J Phys Energy* **2021**, 3, 012006, doi:10.1088/2515-7655/abceab.
6. Ramis, G.; Bahadori, E.; Rossetti, I. Design of efficient photocatalytic processes for the production of hydrogen from biomass derived substrates. *Int. J. Hydrogen Energy* **2021**, 46, 12105–12116, doi:10.1016/j.ijhydene.2020.02.192.
7. Conte, F.; Casalini, G.; Prati, L.; Ramis, G.; Rossetti, I. Photoreforming of model carbohydrate mixtures from pulping industry wastewaters. *Int. J. Hydrogen Energy* **2022**, doi:10.1016/j.ijhydene.2021.12.260.

8. Cabrera, M.N. Pulp Mill Wastewater: Characteristics and Treatment. In *Biological Wastewater Treatment and Resource Recovery*; InTech, 2017.
9. Bahadori, E.; Ramis, G.; Zanardo, D.; Menegazzo, F.; Signoretto, M.; Gazzoli, D.; Pietrogiacomini, D.; Di Michele, A.; Rossetti, I. Photoreforming of glucose over CuO/TiO<sub>2</sub>. *Catalysts* **2020**, *10*, 477, doi:10.3390/catal10050477.
10. Rossetti, I.; Bahadori, E.; Tripodi, A.; Villa, A.; Prati, L.; Ramis, G. Conceptual design and feasibility assessment of photoreactors for solar energy storage. *Sol. Energy* **2018**, *172*, 225–231, doi:10.1016/j.solener.2018.02.056.
11. Zhao, H.; Liu, P.; Wu, X.; Wang, A.; Zheng, D.; Wang, S.; Chen, Z.; Larter, S.; Li, Y.; Su, B.L.; et al. Plasmon enhanced glucose photoreforming for arabinose and gas fuel co-production over 3DOM TiO<sub>2</sub>-Au. *Appl. Catal. B Environ.* **2021**, *291*, 120055, doi:10.1016/j.apcatb.2021.120055.
12. Gallo, A.; Montini, T.; Marelli, M.; Minguzzi, A.; Gombac, V.; Psaro, R.; Fornasiero, P.; Dal Santo, V. H<sub>2</sub> production by renewables photoreforming on Pt-Au/TiO<sub>2</sub> catalysts activated by reduction. *ChemSusChem* **2012**, *5*, 1800–1811, doi:10.1002/cssc.201200085.
13. De Bruijn, J.M.; Kieboom, A.P.G.; van Bekkum, H. Alkaline Degradation of Monosaccharides Part VII. A Mechanistic Picture. *Starch - Stärke* **1987**, *39*, 23–28, doi:10.1002/star.19870390107.
14. Bahadori, E.; Conte, F.; Tripodi, A.; Ramis, G.; Rossetti, I. Photocatalytic selective oxidation of ammonia in a semi-batch reactor: Unravelling the effect of reaction conditions and metal co-catalysts. *Catalysts* **2021**, *11*, 1–15, doi:10.3390/catal11020209.
15. Fu, X.; Long, J.; Wang, X.; Leung, D.Y.C.; Ding, Z.; Wu, L.; Zhang, Z.; Li, Z.;

- Fu, X. Photocatalytic reforming of biomass: A systematic study of hydrogen evolution from glucose solution. *Int. J. Hydrogen Energy* **2008**, 33, 6484–6491, doi:10.1016/j.ijhydene.2008.07.068.
16. Wang, W.; Cheng, B.; Zhao, M.; Anthony, E.; Luque, R.; Dionysiou, D.D. Boosting H<sub>2</sub> yield from photoreforming of lignocellulose by thermo-alkaline hydrolysis with selective generation of a key intermediate product: Tartaric acid. *Energy Convers. Manag.* **2022**, 257, 115444, doi:10.1016/j.enconman.2022.115444.
17. Sanwald, K.E.; Berto, T.F.; Eisenreich, W.; Jentys, A.; Gutiérrez, O.Y.; Lercher, J.A. Overcoming the Rate-Limiting Reaction during Photoreforming of Sugar Aldoses for H<sub>2</sub>-Generation. *ACS Catal.* **2017**, 7, 3236–3244, doi:10.1021/acscatal.7b00508.

## 6. Photo abatement of pollutants

### 6.1. Introduction

Now more than ever, the Earth's capacity to autoregulate and maintain environmental conditions that enabled the human development is in danger. Due to huge utilization of fossil fuels and the mass industrialization, fresh water and also clean air are something that in most part of the world ones cannot be taken for granted [1]. Chemical pollutants have been released since the early days of industrialization and carbon dioxide only accounts for a fraction of them, less than 20%, as we humans have synthesized and used more than 140'000 type of chemicals and mixture of them in the last 150 years, while thousands new molecules are discovered on an annual basis [2]. Without taking into account the geological impact of mining operations, roughly 220 billion of tons of chemicals per year are released into the environment and the traces of them are everywhere, since those compounds were found in human blood, deep seas, high mountains and arctic pole, with effects on both the biosphere and the human health [3]. Even if we stop today each source of pollution, all the chemicals already released will be around for a long time, up to hundreds of years [4]. These persistent pollutants, often organic molecules (POPs), were chemicals intentionally produced to perform one task or accidentally released as a result of an industrial process, like dioxins produced after incineration of municipal waste [5]. A great example of a worldwide adopted chemical is DDT, which stands for 1,1'-(2,2,2-Trichloroethane-1,1-diyl)bis(4-chlorobenzene), and it is a chlorinated organic molecule intensively used as insecticide. Although its effectiveness is not under discussion and it helped to eradicate diseases like malaria, it was banned by US in 1972 and we are now left to deal with the consequences of its residues dispersed in the environment, with well-known effects on animal reproduction.

Half a century since the ban and we are still fighting its noxious effects [6]. What is more concerning is that every chemical that is used nowadays may become a persistent pollutant in the future if it is not specifically designed to be degradable in the environment (and there is also an open discussion about that [7]). This is why back in 2005 the European Commission promoted the NORMAN project, which can be summarized as a permanent network of institutional entities (universities, research centers) and industry partners with the goal of helping the policy makers to be proactive when it comes to chemical pollution [8]. NORMAN database includes more than 900 molecules, and it is updated continuously with new concerning pollutants.

The first obvious carrier of these noxious compounds is wastewater. Whether it comes from city sewers, dumped by industries or after agricultural use, water dissolves and carries around huge quantities of chemicals. Existing treatments are usually composed of three to five stages in which solid particles are removed and the organic matter is digested via biological processes, then the final stage is often a sand filtration and disinfection of the wastewater [9]. The overall efficiency is highly dependent on the amount of water to be treated (huge amounts of rainwater dilutes sewage and both are directly released into water streams) and on the biological oxygen demand (BOD) of the sewage. For instance, only 30% to 70% of pharmaceuticals are removed by traditional suspended sludge process [10]. Thus, there is a need for effective and inexpensive treatments for the removal of POPs along with other chemicals released by industries, especially for those countries in which there are poor regulations about the industrial activities and that will benefit the most from innovative solutions.

In this chapter, treatments based on photocatalysis are compared with more traditional advanced oxidation processes (AOPs), such as Fenton, Photo-Fenton and UV/H<sub>2</sub>O<sub>2</sub> [11].



Indeed, heterogeneous photocatalysis does not require expensive apparatus or much of resources that are used in advanced wastewater treatment plants, especially when it is combined with sunlight. The active material is able to produce *in situ* the oxidant species (mainly hydroxyl radical OH•) or rather to adsorb and degrade the pollutants on its surface by reaction with photogenerated holes. Conversely, in conventional AOPs the oxidation is carried out by activation of H<sub>2</sub>O<sub>2</sub>, which is added to the wastewater and then decomposed to hydroxyl radicals via catalysis (Fenton), light (UV/H<sub>2</sub>O<sub>2</sub>) or both (Photo-Fenton), according to the following reactions (1-4).

- (1)  $\text{H}_2\text{O}_2 + \text{Fe}^{2+} \rightarrow \text{OH}^- + \text{OH}^\bullet + \text{Fe}^{3+}$
- (2)  $\text{H}_2\text{O}_2 + \text{Fe}^{3+} \rightarrow \text{HO}_2^\bullet + \text{H}^+ + \text{Fe}^{2+}$
- (3)  $\text{H}_2\text{O}_2 + \text{Fe}^{3+} + h\nu \rightarrow \text{HO}_2^\bullet + \text{H}^+ + \text{Fe}^{2+}$
- (4)  $\text{H}_2\text{O}_2 + h\nu \rightarrow 2\text{HO}^\bullet$

The reaction 2 is kinetically slow and in Photo-Fenton process it is assisted by light (reaction 3) [12]. Reaction 4 is the only one that occurs during UV/H<sub>2</sub>O<sub>2</sub> treatment, as the UV light is powerful enough to cleave the oxygen-oxygen bond directly.

The pollutants that were selected for this study are Diclofenac (DCF), Erythromycin (ERY), Acid Orange 7 (AO7) and Amoxicillin (AMX). DCF is a nonsteroidal anti-inflammatory drug (NSAID) used to alleviate pain and to treat inflammatory diseases. About 1443 tons per year are used worldwide and most of them is excreted unaltered through urine and then into wastewater, with an average concentration of 57.1 µg/L for surface water, 13.4 µg/L for ground water and 10.2 µg/L in case of seawater [13]. If these values do not pose a threat to human life, the presence of DCF may significantly alter the life of animals, aquatic organisms and plants [14]. In addition, conventional treatments are not effective for its mineralization [15–17].

On the other hand, the abuse of antibiotics like Erythromycin and Amoxicillin is believed to be the cause of superbugs, which are bacteria resistant toward conventional medical treatment [18]. Again these are only partially mineralized by wastewater treatment plants, and it was observed its adsorption over solid particles, which is a huge problem as sewage sludges are used as fertilizer for crops and from there it may be released again [19,20]. Even though the concentration of the aforementioned antibiotics in wastewater is way below the toxic level for humans, the problem is amplified due to its bioaccumulation up to the food chain, thus, we all end up eating fishes and crustaceous in which the ERY and AMX concentration is hundred times more than that of polluted water [18].

Dyes are widely employed in textile industry, however, after the dying process up to 15% of these molecules is found unbound in the wastewater, with concentration from 10 to 200 mg/L. Given that an industrial district like the one in Tamilnadu (India) produces more than 100 million liters of wastewater each day, failing to disposed or to treat such huge amount of contaminated water is dangerous for the environment, in which dyes like Acid Orange 7 affects the growth and the wellness of aquatic species [21,22].

Titania and its derived composites have been used extensively in the purification of wastewater [23,24].  $\text{TiO}_2$  and  $\text{Ag/TiO}_2$  were tested under UVA irradiation for their antimicrobial activity [25], while Pazoki et al. reported the photodegradation of a steroid by using a similar photocatalyst [26]. Furthermore,  $\text{Au/TiO}_2$  was employed for the detoxification of wastewater from parabens [27]. The same can be said for  $\text{C}_3\text{N}_4$  and  $\text{TiO}_2/\text{C}_3\text{N}_4$  composites, that were successfully applied for the photodegradation on bisphenol A [28] and methyl orange dye [29] under simulated solar light.

Diclofenac sodium salt was degraded by means of photocatalytic treatment with P25 [30] and many other doped photocatalysts based on it [16]. Amoxicillin was degraded by tin-

doped titania under UVC radiation [31]. On the other hand, very few studies focus on the photooxidation of Erythromycin despite its wide adoption as a drug.

As already said, in this work the photodegradation of these emerging pollutants (*i.e.* Diclofenac, Erythromycin and AO7) was optimized and compared with the performance of more traditional AOPs. In addition, the treatment was carried out with different setups, including UV, visible and sunlight irradiation and glass reactors of 0.3 L and 3 L, which firstly scale-up typical bench-scale reactors that can be found commonly in literature. Such setup allows to better understand the behavior of the system in conditions that are more similar to an industrial treatment, as inexpensive photocatalysts were used. Lastly, the effectiveness of the oxidation processes was evaluated both by following the pollutant conversion and also by carrying out *in vitro* toxicity test using *Daphnia Magna* as a benchmark to assess the quality of the treated wastewater. Given the sensibility of these animals to the environment in which they grow, their survival indicates whether the treatments efficiently lowered the initial toxicity regardless of the reaction path and of the intermediates and byproducts formed.

## **6.2. Results and discussion**

### **6.2.1. Photocatalytic test**

Tests performed under dark conditions and without catalyst, hydrogen peroxide or both gave a negligible conversion of the pollutant. When the photocatalyst was added to the reactor containing the simulated wastewater, the concentration of the latter decreased in the first 30 minutes as the pollutant was adsorbed over the material, therefore, the lamp was switched on once stable conditions were reached.

## **6.2.2. Diclofenac**

### **6.2.2.1. Direct photolysis**

From the results of previous similar investigation [32], it was decided to carry out the first test using 100ppm of DCF to assess the effect of the UV light on its decomposition (Reactor B). The solution turned from clear to brown color and the absorbance increased over time (+20% after 3h), as direct photolysis of DCF is well known for forming species that absorb greatly at the selected wavelength [33].

After that, we scaled up the process by using reactor A in combination with an equivalent amount of hydrogen peroxide, which was added in order to promote the mineralization, and both UV and LED spotlights were used (Figure 4.5). The addition of the oxidant is equal to the stoichiometric amount of  $\text{H}_2\text{O}_2$  required to oxidize 100ppm of DCF (30 mg) and correspond to roughly 0.8 mL of  $\text{H}_2\text{O}_2$  30% v/v.

As expected, the visible light emitted by LEDs was not able to cleave directly the oxygen-oxygen bond in  $\text{H}_2\text{O}_2$  and the conversion was below 5%. A similar result was obtained with the external UV spotlight, despite in theory it should be able to activate  $\text{H}_2\text{O}_2$ . It is likely that most of the radiation was attenuated by the airgap between the bulb and the solution and by the adsorption of the solution itself, which limited the conversion to roughly 5%. Lastly, Reactor B and the immersed UV lamp seemed to be the best choice, since this powerful lamp that can irradiate effectively the whole solution was able to convert 90% of the Diclofenac after 15 minutes of treatment, then the reaction slowed down significantly until reaching a plateau.

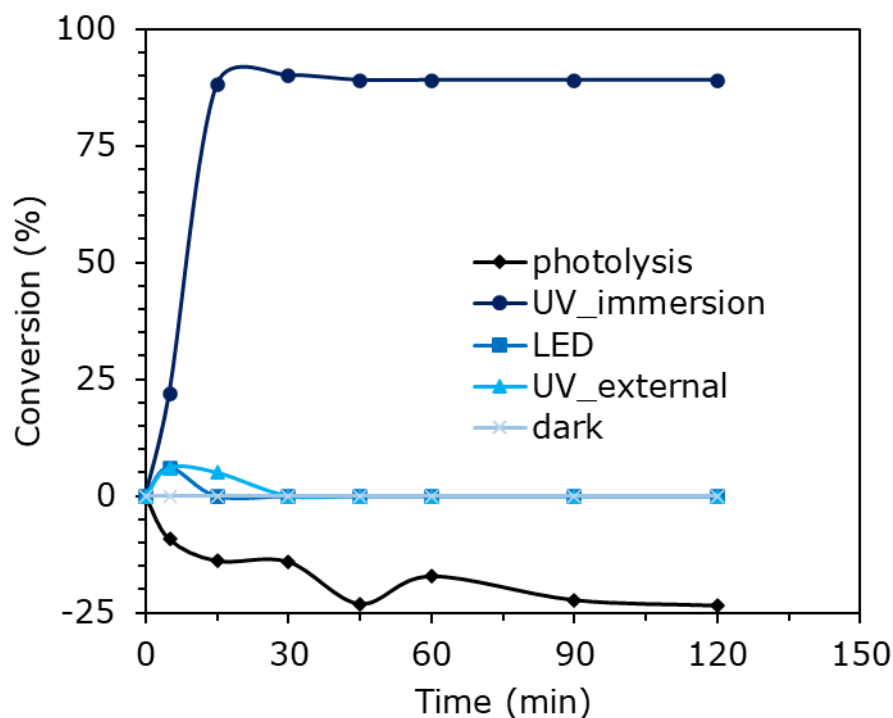


**Figure 6.1.** Results of photolysis and Light/UV treatment. 100ppm DCF, pH 6.5, 0.8 mL H<sub>2</sub>O<sub>2</sub> 30% v/v, 300mL reactor B, 1000mL reactor A

#### 6.2.2.2. Photo-Fenton reaction: Effect of DCF concentration

Photo-Fenton under visible light (reactor A) already proved to be effective with other kinds of organic pollutants [32], so it was used here to explore its feasibility with the selected pollutant and setup. The impact of pollutant concentration on reaction time was investigated by treatment of four solutions with different concentration in the range 12-100 ppm. The graph of Figure 6.2 illustrates that the initial reaction rate was faster for 50 and 100 ppm solutions and after over 5h of treatment the final conversion of DCF was respectively 88% and 75%. Several papers report that the degradation of pharmaceuticals follows the Langmuir Hinshelwood kinetics [30], unless their concentration is so high that a zero-order kinetics is observed. On the other hand, 12 ppm solution reaches a conversion plateau way sooner, about 24% after 3h of reaction and a similar situation is

faced by 25 ppm solution, which cannot overcome the 36% conversion after 4h. This is related to the low concentration of these two solutions [34], however, this behavior is not common and deserve further investigations. Indeed, it has been reported that direct photolysis (and photocatalysis) lead preferentially to the formation of the dimer carbazole as an early intermediate, which absorb at the same wavelength of DCF and is more recalcitrant [35]. On the other hand, the photodegradation via Photo-Fenton treatment follows a different path involving a quinone imine form, that is more degradable [36]. Anyway, 100 ppm was chosen as the benchmark for the following tests, as it allows to observe easily the conversion of the target molecule over a reasonable timespan.

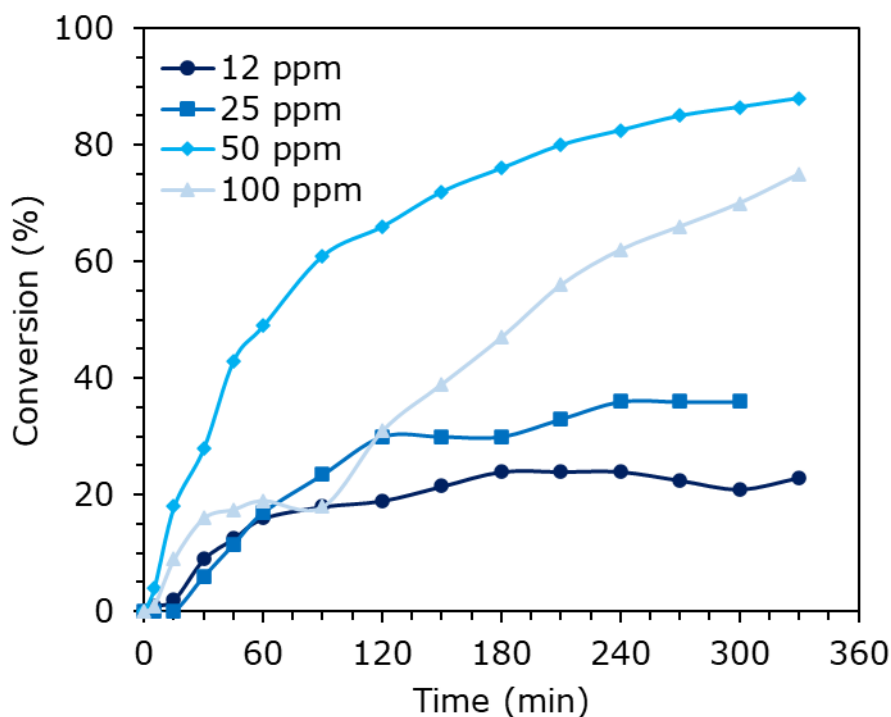


**Figure 6.2.** Photo-Fenton treatment of DCF in the concentration range 12-100 ppm. pH 6.5, 0.8 mL H<sub>2</sub>O<sub>2</sub> 30% v/v, 54 ppm FeSO<sub>4</sub>, LED, reactor A

#### **6.2.2.3. Effect of $\text{Fe}^{2+}$ concentration**

Conversely,  $\text{Fe}^{2+}$  concentration (it was used  $\text{FeSO}_4$  as iron source) was found to not affect greatly the Photo-Fenton process and its concentration was kept at 54 ppm (see Appendix for more details). In any case, working with high amounts of iron salt may not be the best way to boost the effectiveness of the treatment from an industrial point of view, due to the formation of sludges in the process which have to be filtered before releasing the wastewater into the water streams, and this may be challenging [37].

#### **6.2.2.4. Effect of hydrogen peroxide concentration**

Then, we tested the effect of an increased amount of hydrogen peroxide on the reaction rate. It was found that increasing the amount of hydrogen peroxide from 0.8 mL to 1.6 mL did not affect the conversion, even under UV. It has already been reported that the photodegradation of DCF under UVC and in presence of  $\text{H}_2\text{O}_2$  is effective, and that was explained by a degradation path that involves a first step promoted by the UV light (direct photolysis) which in turns generated an intermediate that is more susceptible of reaction with the hydroxyl radicals [38]. Therefore, according to that model, increasing the concentration of  $\text{H}_2\text{O}_2$  is not beneficial since the reaction is still bottlenecked by the first step.

#### **6.2.2.5. Effect of pH**

The next step was to understand at which pH the pollutant was more easily degraded, thus, along with the test at neutral pH two more treatments were performed with a basic (pH 12) and acid (pH 3) environment, whose results are reported in Figure 6.3. It is not surprising that at pH 12 the performance was quite poor, since at that pH the iron

precipitates as hydroxide and sludges are formed, which inhibits the Photo-Fenton process. At pH 3 the process was more effective, although the conversion curve almost matched that of pH 7. Since our goal is to find an inexpensive, simple and effective treatment to mineralize recalcitrant organics, there is no need to add an acid to the wastewater if that leads only to a slightly faster reaction in the first two hours of degradation. Direct photolysis was reported to occur faster at pH 3 than neutral condition, and this was explained by the fact that the DCF was mainly present as the protonated form rather than the conjugated base [39]. In our case, the Photo-Fenton process generates hydroxyl radicals that oxidize the pollutant regardless of its ionic form.

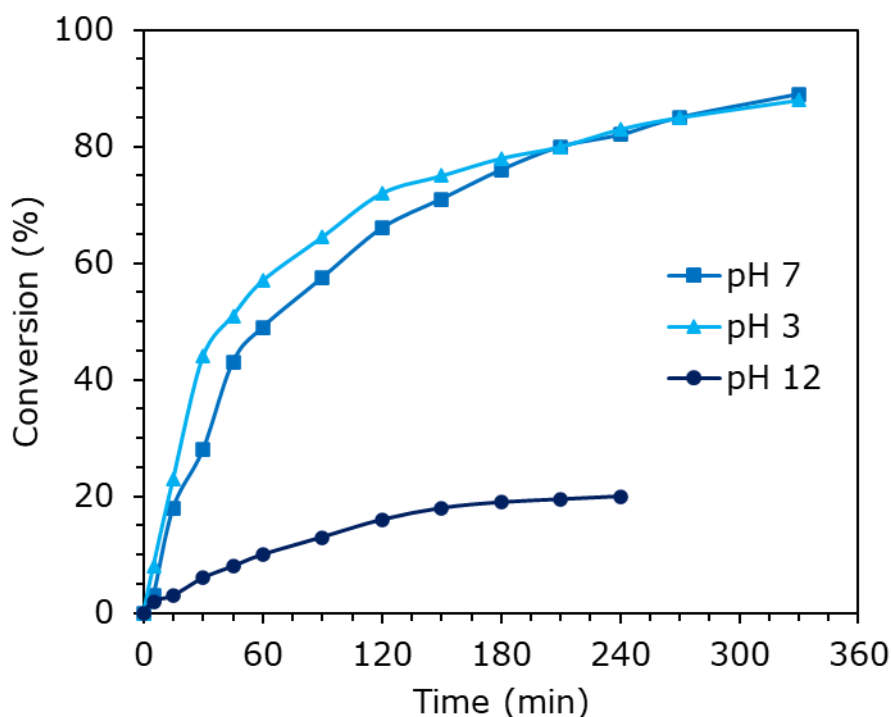


**Figure 6.3.** Photo-Fenton treatment of DCF at pH 3, 7 and 12. 100 ppm DCF solution, 0.8 mL H<sub>2</sub>O<sub>2</sub> 30% v/v, 54 ppm FeSO<sub>4</sub>, LED, reactor A



#### 6.2.2.6. Effect of irradiation system

After the tuning of these parameters, Fenton, Photo-Fenton under visible light, UV light and sunlight were tested and compared (Figure 6.4). Despite an initial reaction rate similar among the series, the treatments carried out under ultraviolet radiation were the most effective in converting Diclofenac (it is worth to remember that the solution was clear during the whole process), with both reaching a plateau around 80% conversion after 2h of reaction. This includes also the treatment under sunlight, since this radiation source is polychromatic and carries a non-negligible portion of UV light. In that particular day, from 10 am to 2 pm the average irradiance was  $544 \text{ W/m}^2$ , however, this is not the value that one can expect every day, since the irradiance varies greatly, and it is also affected by the weather and the season.

Surprisingly, it was observed that the treatment under LED spotlight was effective, though it required a long reaction time as 80% conversion was reached after 3h and a half. As expected, Fenton reaction was the slowest and least effective treatment, being limited by the regeneration of the  $\text{Fe}^{2+}$  that is necessary to promote the hydrogen peroxide decomposition. That regeneration is catalyzed by light in the Photo-Fenton process, anyhow, Fenton treatment may be taken into consideration in case of wastewaters characterized by a strong color that hinders the penetration of the light.

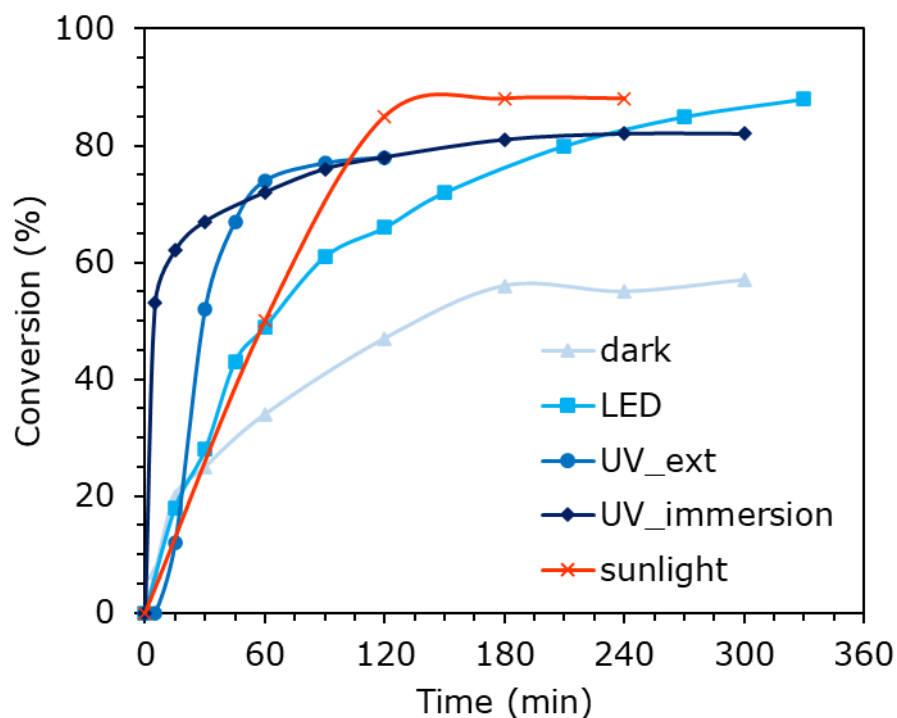


**Figure 6.4.** Fenton and Photo-Fenton treatments of 100 ppm DCF solution with both reactor A and B. pH 7, 0.8 mL H<sub>2</sub>O<sub>2</sub> 30% v/v, 54 ppm FeSO<sub>4</sub>

#### 6.2.2.7. Photocatalysis with TiO<sub>2</sub> and M/TiO<sub>2</sub>

It is well-known that the heterogeneous photocatalyst is able to promote the oxidation either by reaction of the adsorbed species with the photogenerated holes or the production in situ of reactive radicals such as the hydroxyl one. Thus, early tests were performed without addition of H<sub>2</sub>O<sub>2</sub> and under UV radiation, since the selected photocatalysts are not activated by visible light. The results reported in Figure 6.5 illustrate the bare P25 is the best performer among the series. According to the graph, P25 carries out most of the conversion (65%) in the first hour of reaction, until reaching a plateau of 72% after 2h. The initial reaction rate is fast also in case of 0.1% Au (55% @15 minutes) however, the conversion drops at its minimum after 2h before rising again to 45% at 5h. This weird behavior may be linked to the formation of byproducts that absorb at the same wavelength

of DCF. Unfortunately, the activity of 0.1% Pd and 1% Ag was quite low and the final conversion was around 10%. That results are opposite to what is reported in literature, as, for instance, Kim et al. reported the degradation of organic pollutants to be enhanced by the metallization of titania with palladium and, to a smaller extent, with gold, though their loading was significantly higher (1% on a weight basis) [40]. Our samples containing Au and Pd are prepared via reduction at high temperature, and despite their band gap is lower than the benchmark P25 (3.14 eV), that alone is not the only parameter that influence the catalytic performance since the SSA for both these modified materials was inferior to that of bare titania, respectively 39 and 32 m<sup>2</sup>/g vs 47 m<sup>2</sup>/g. Indeed, modified catalysts prepared via photo-deposition technique showed greater activity than the unmodified ones [40,41]. 1% Ag was prepared at a significantly lower temperature (150°C) but it had a low porosity, likely due to the silver deposited into the pores. It may be that this metallization technique is not suitable to obtain photocatalysts active for this kind of treatment, despite the good performance in case of CO<sub>2</sub> photoreduction and glucose photo reforming [42].

To boost the conversion, hydrogen peroxide was added to the mixture, which is still preferable than the Photo-Fenton treatment, as the catalyst can be filtered away or rather immobilized over a solid surface. The initial reaction rate was high for every catalyst except P25 (Figure 6.6). The latter showed an induction time of the order of minutes and converted slightly above 40% of the pollutant after 3h of treatment, which was still higher than the 30% conversion obtained with 0.1% Pd within the same time. Both 1% Ag and 0.1% Au performed better at the beginning of the reaction, then, the conversion rose up to 90% at 6h. Again, this can be explained by the fast degradation of Diclofenac, in particular the cleavage of the amine bridge, and the formation of intermediates that were

more resistant toward degradation [33]. It has already been reported that when a photocatalyst based on titanium dioxide is used, the decomposition of  $\text{H}_2\text{O}_2$  occurs mostly via a photocatalyzed reaction rather than direct splitting [43], however, the complete understanding of the degradation pathway is beyond the scope of this work, especially since the aim is to degrade a broad spectrum of pollutants. In any case, it is interesting to see that silver loaded photocatalyst behave similarly to 0.1% Au, as the former costs significantly less than gold.

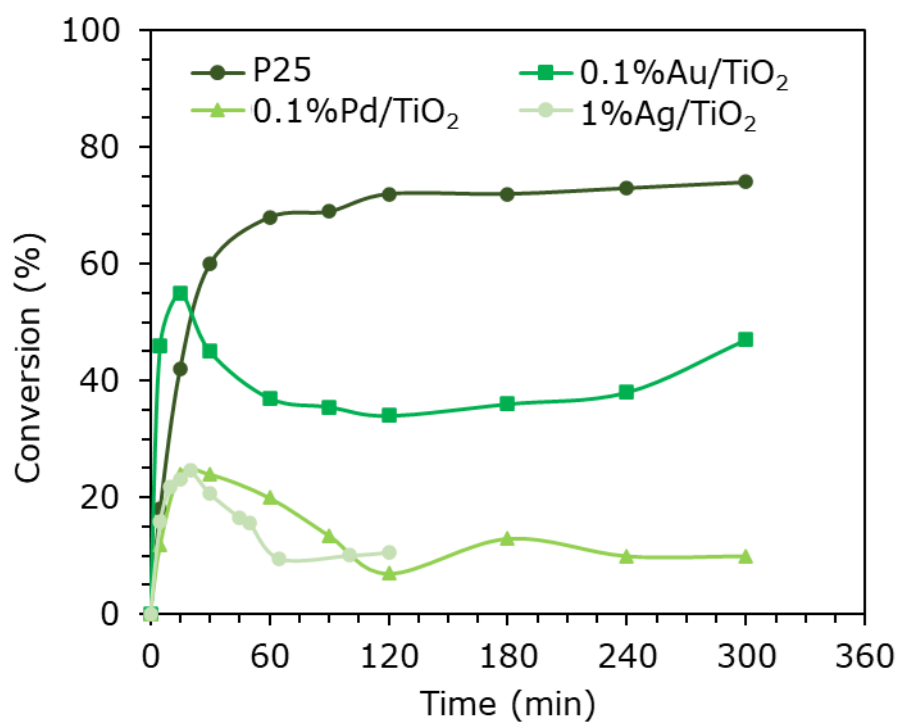


**Figure 6.5.** Photocatalytic treatment using TiO<sub>2</sub> and M/TiO<sub>2</sub> photocatalysts. 200 ppm catalyst, 100 ppm DCF pH 7, reactor A with external UV lamp

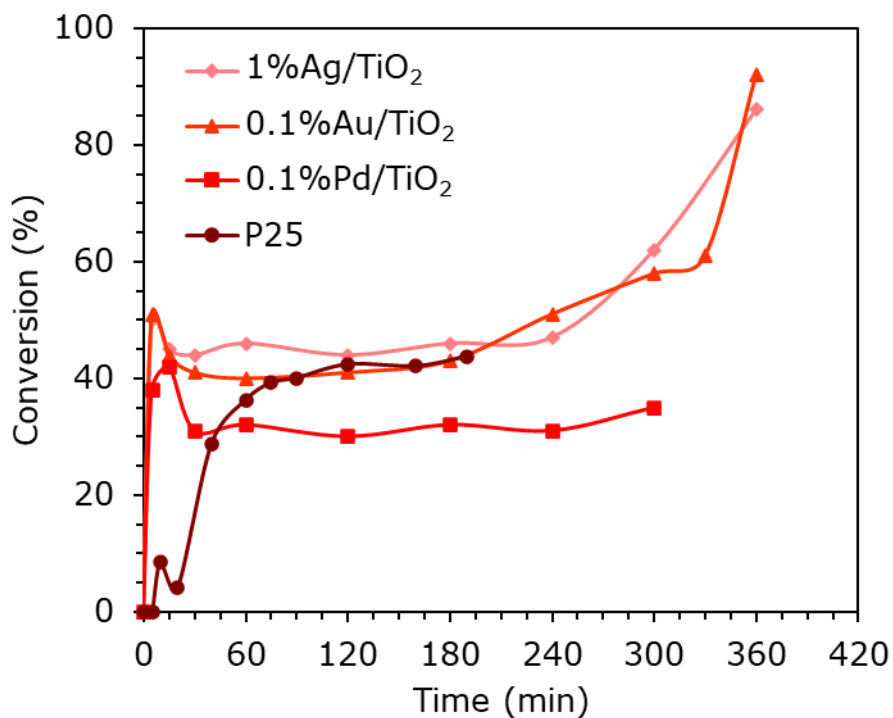


**Figure 6.6.** Photocatalytic treatment using TiO<sub>2</sub> and M/TiO<sub>2</sub> and H<sub>2</sub>O<sub>2</sub>. 200 ppm catalyst, 100 ppm DCF pH 7, 0.8 mL H<sub>2</sub>O<sub>2</sub> 30% v/v, reactor A with UV spotlight

#### **6.2.2.8. Comparison between heterogeneous and homogeneous treatments**

Further tests were conducted to compare Photo-Fenton and photocatalytic treatments. Based on our experience and past investigations, we selected three setups, that are (i) Photo-Fenton under visible LED lamp, (ii) P25 with immersed UV lamp and (iii) 0.1% Au/P25 with H<sub>2</sub>O<sub>2</sub> and external UV spotlight, and the results are reported in Figure 6.7. P25 was the best performing under UV light and without addition of external hydrogen peroxide and again in this the most active catalysts in the optimized conditions. On the other hand, both heterogeneous treatment with 0.1% Au/P25 and Photo-Fenton could not reach over 70% conversion after 5h of irradiation, though the first one was much faster at the beginning while in the second case the conversion rose steadily during the whole process. Anyway, photocatalytic treatments may be the best solution for short and effective treatments that aim to reduce the toxicity (toxicity tests will be discussed later in this paragraph).

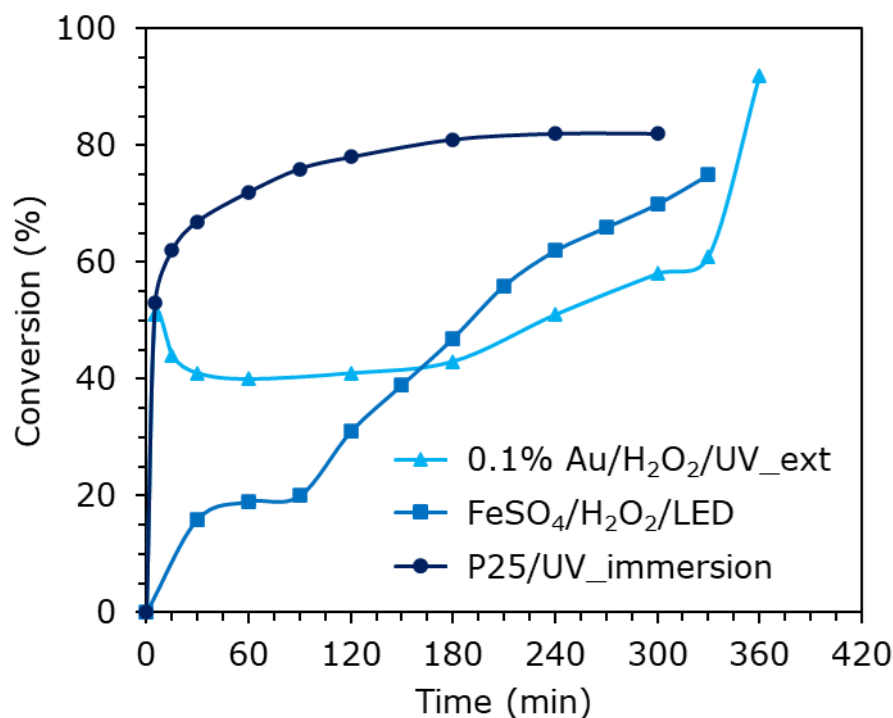


**Figure 6.7.** Conversion results of Photo-Fenton and Photocatalyzed treatments. 100 ppm DCF, 6.5 pH, 0.8 mL H<sub>2</sub>O<sub>2</sub> 30% v/v, 200 ppm of photocatalyst or 54 ppm of FeSO<sub>4</sub>

### 6.2.3. Erythromycin

This antibiotic was treated by both Photo-Fenton and photocatalyzed treatment, using 0.8 mL of H<sub>2</sub>O<sub>2</sub>, 28 ppm of FeSO<sub>4</sub> and 200 ppm of Au/P25 photocatalyst (Figure 6.8). The test with Photo-Fenton was carried with half of the amount of pollutant and catalyst, though the ratio between them is the one used with DCF. Both treatments (Photo-Fenton and photocatalytic) were effective, in particular, through photo-Fenton the conversion quickly reaches the 80% in around 30 minutes and increases marginally during the rest of the test. In case of photocatalytic treatment, the photo abatement of erythromycin is slower and after half a hour less than 40% of the pollutant is converted, while this value increases to 70% after 4h.

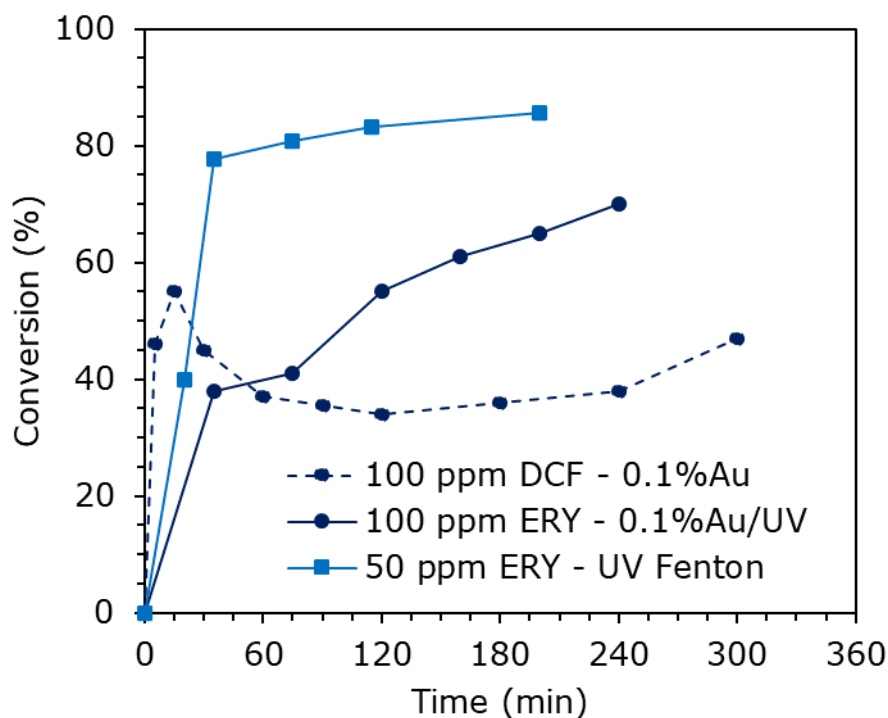


**Figure 6.8.** Conversion results of Photo-Fenton and Photocatalyzed treatments carried out with respectively 50 ppm and 10 ppm of ERY, 6.5 pH, 0.8 mL H<sub>2</sub>O<sub>2</sub> 30% v/v (Photo-Fenton), 200 ppm of photocatalyst or 28 ppm of FeSO<sub>4</sub>, reactor A with UV spotlight

#### 6.2.3.1. Toxicity test

The conversion performance alone does not assess the effectiveness of the treatment in reducing the toxicity of the solution containing Diclofenac, as the degradation by-products can still be noxious and lead to harmful compounds. Thus, in order to estimate the validity of each treatment, the solutions after photocatalytic treatments were tested for assessing the acute toxicity using *Daphnia Magna* as model species (Figure 6.9). The exposure to DCF alone (200 ppm) induced the complete mortality of daphnids after 48 h of exposure (Figure 13). These results agreed with previous studies performed on the same biological model, reporting that the effect concentration for the 50% of individuals (EC<sub>50</sub>) of DCF ranged between 9 e 123 mg/L [44–46]. Our companion study estimated



that the EC<sub>50</sub> of the DCF sodium salt used in this experiment was  $78.42 \pm 5.21$  mg/L (95% confidence intervals = 72.10 – 84.50). The results of the acute toxicity tests suggested that some of the photocatalytic treatments were highly efficient in degrading DCF and reducing its toxicity. Although Photo-Fenton reaction with visible light might be successful in the mineralization of DCF, the visible light was not able to cleave the bonds of H<sub>2</sub>O<sub>2</sub>, resulting in the complete mortality of daphnids at the end of the exposure. The exposure to solutions from photolysis of DCF with UV light alone returned a mortality up to the 40% of individuals. The shift in the color of the solution, from clear to brown, with an increase in the absorbance at 278 nm, can be supposed being due to the formation of by-products that could affect the health of daphnids. Similar results were obtained testing the toxicity of the solution deriving from photocatalyzed treatment with P25 and under UV light, where a decrease in viability as low as 50% after 48h was noted. In contrast, the highest survival of daphnids was obtained at the end of the experiments with the solutions from 0.1% Au/P25 under UV light and Photo-Fenton under UV treatments, whereby <10% and no mortality occurred after 48 hrs. That same photocatalyzed treatment performed worse than bare titania P25 when tested for shorter reaction time and optimized parameter, however, the modified titania is clearly superior to the benchmark, as it efficiently mineralized the pollutant and lowered the toxicity of the solution to one-tenth of its original value. The Photo-Fenton treatment has proven to be effective in degrading DCF and decreasing its acute toxicity, but the formation of iron sludges at the end of the treatment represents an issue to be addressed.

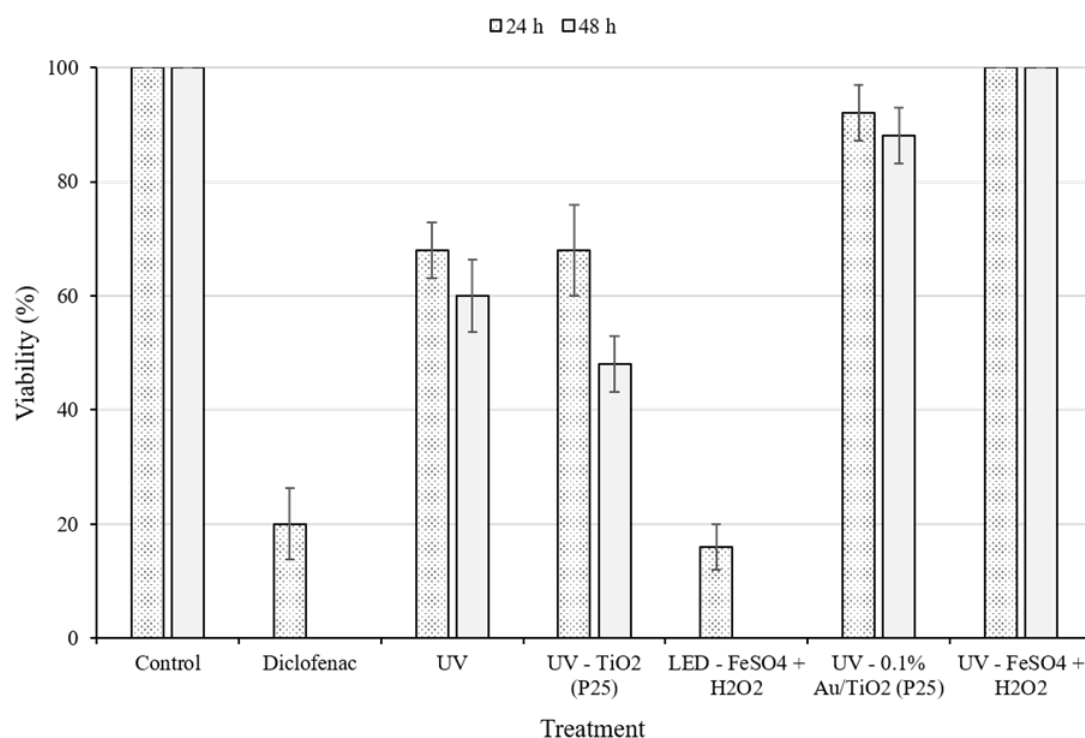


**Figure 6.9.** Results of toxicity tests performed on samples treated with different processes and catalysts. Percentage of survival of *Daphnia Magna* individuals after the 48h exposure to solutions deriving from different photocatalytic treatments for removing DCF from the water.

#### 6.2.4. Acid Orange, Bromophenol Blue, Amoxicillin

Titanium dioxide in combination with a powerful UV spotlight has proved to be a good and reliable system to carry out photo-abatement treatment, however, it still has some limitations, including the wide band gap of titanium dioxide and the huge power consumption of the UV light bulb, which dissipates most of the energy in the form of heat. By contrast, materials like the aforementioned graphitic carbon nitride represent the novel generation of photocatalysts, since it is obtained as easily as TiO<sub>2</sub> and its band gap is way lower. Thus, we replaced titanium dioxide-based materials with g-C<sub>3</sub>N<sub>4</sub> obtained from thermal condensation of melamine and it was coupled with a new illumination

system constituted of LEDs that emits at 365nm (UV-LED). The latter is more efficient than traditional mercury lamp and also more flexible when it comes to adapt the lamp to the reactor. To estimate the potential of that system, it was tested the photodegradation of Acid Orange 7, which is a non-reactive azo dye used in hair coloring and wool processing. It was selected since its characteristic color is a strong indicator of the goodness of the photodegradation process and it is quite easy to degrade even via photolysis, so it is a good benchmark.

#### **6.2.4.1. Catalysts comparison**

The very first tests were used to compare the performance of g-C<sub>3</sub>N<sub>4</sub> with that of P25, therefore, reactor B was used in combination with UV-LED lamp and the results are reported in Figure 6.10. Direct photolysis, though effective in the discoloration of the solution, is a very time-consuming process and after almost 3h of exposure the conversion of AO7 was still below 8%. Conversely, the mineralization increases steadily when using P25 and the 40% conversion was reached within 5h and a half. From the graph it is clear that the graphitic carbon nitride, at least our benchmark prepared at 550°C and exfoliated, was the top performer, since within the same time span of P25 the conversion was above 70% and still rising. The UV-LEDs emit at 365 nm, which is a wavelength that is able to activate titania P25. Some report that the photodegradation capabilities of TiO<sub>2</sub> is greater than g-C<sub>3</sub>N<sub>4</sub> under simulated sunlight [47], others obtained better performance when P25 was used for treatment of river water and pyridine [48,49]. In our case, the difference in activity was not negligible. Anyway, one of the main advantages of using the carbon nitride is the narrow band gap (2.73 eV), that corresponds to an absorption threshold of roughly 450 nm and so it should be active under blue light. Thus, the same test was carried

out by substituting the LED-365nm lamp with a LED lamp that emits at 430 nm (Figure 6.10). Surprisingly, the degradation of AO7 did not occur, despite it has been reported a modest activity of  $C_3N_4$  from melamine in case of bilirubin degradation under greenlight [50].

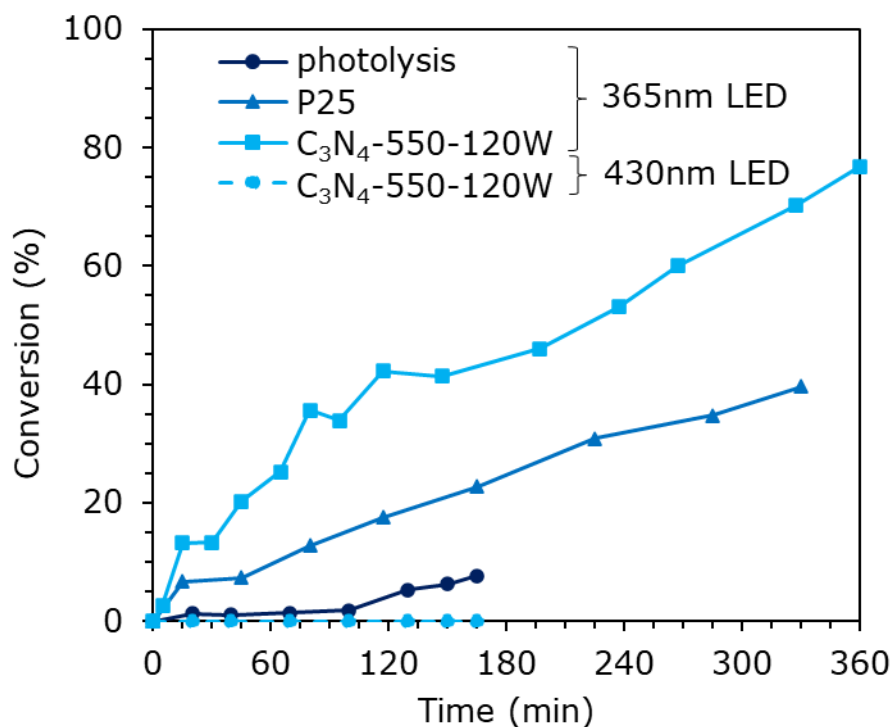


**Figure 6.10.** Conversion results of photolysis and photodegradation of AO7. 300 mL, 50 ppm of pollutant, 6.5 pH, rt, 125 ppm of photocatalyst, LED-UV lamp (365nm)

Figure 6.11 illustrates what happened to the system when an equivalent amount (*i.e.* theoretical amount required to oxidize the pollutant) of hydrogen peroxide was added to the system. The performance of all the setups improved, with UV/H<sub>2</sub>O<sub>2</sub> treatment that reached 27% conversion after 4h and g-C<sub>3</sub>N<sub>4</sub>-550-120W raised over 75%. Noteworthy, was the 100% conversion obtained with H<sub>2</sub>O<sub>2</sub> and P25 after 4h. Acid Orange is particularly susceptible to be degraded by H<sub>2</sub>O<sub>2</sub> [51], while other authors reported that

the photodegradation of phenol was quite effective when  $\text{TiO}_2$  and hydrogen peroxide were used together [52] due to a mixture of direct decomposition on the titania surface and oxidation by  $\text{H}_2\text{O}_2$ . On the other hand, the  $\text{C}_3\text{N}_4$  itself is known to activate the hydrogen peroxide, although a co-catalyst (like metal NPs deposited on the nanosheets) is required to improve its efficiency [53]. Indeed, photodegradation of organics was only slightly accelerated by addition of the oxidant, as it is likely that most of the reaction involved the species adsorbed over the photocatalyst itself.

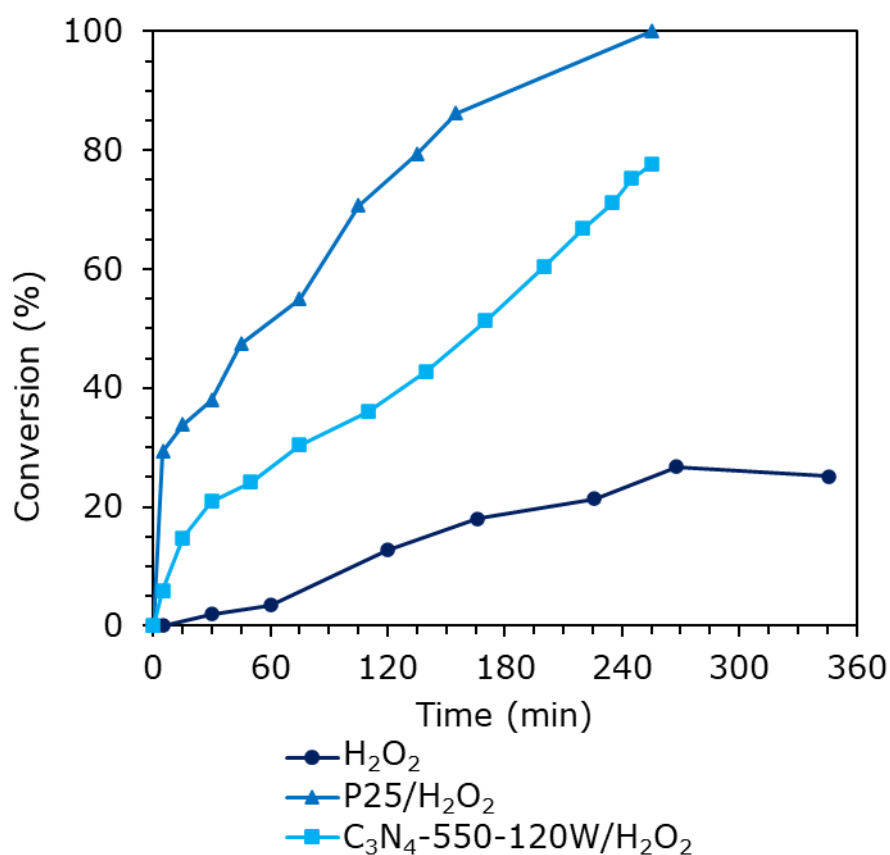


**Figure 6.11.** Conversion results of photolysis and photodegradation of AO7. 300 mL, 50 ppm of pollutant, 6.5 pH, rt, 0.3 mL  $\text{H}_2\text{O}_2$  30% v/v, 125 ppm of photocatalyst, LED-UV lamp (365nm)

#### 6.2.4.2. Effect of pollutant irradiation system

For the sake of comparison, Figure 6.12 illustrates the performance of photodegradation carried out with P25 when different lamps were used, in details, UV-LED immersed lamp ( $48 \text{ W/m}^2$ ) and UV-spotlight ( $260 \text{ W/m}^2$ ). The UV-spotlight clearly outperformed the UV-LED immersion lamp, however, this does not take into account the power consumption of the first system, which is more than five-fold that of LEDs. Moreover, the longer reaction time may be due to the different irradiance of the two systems, since the immersed lamp was able to illuminate the reactor volume more efficiently, but its irradiance was six times lower than that of the UV spotlight. In any case, the addition of hydrogen peroxide, even in lower amount of the stoichiometric value, was an effective way to compensate the lower irradiance.

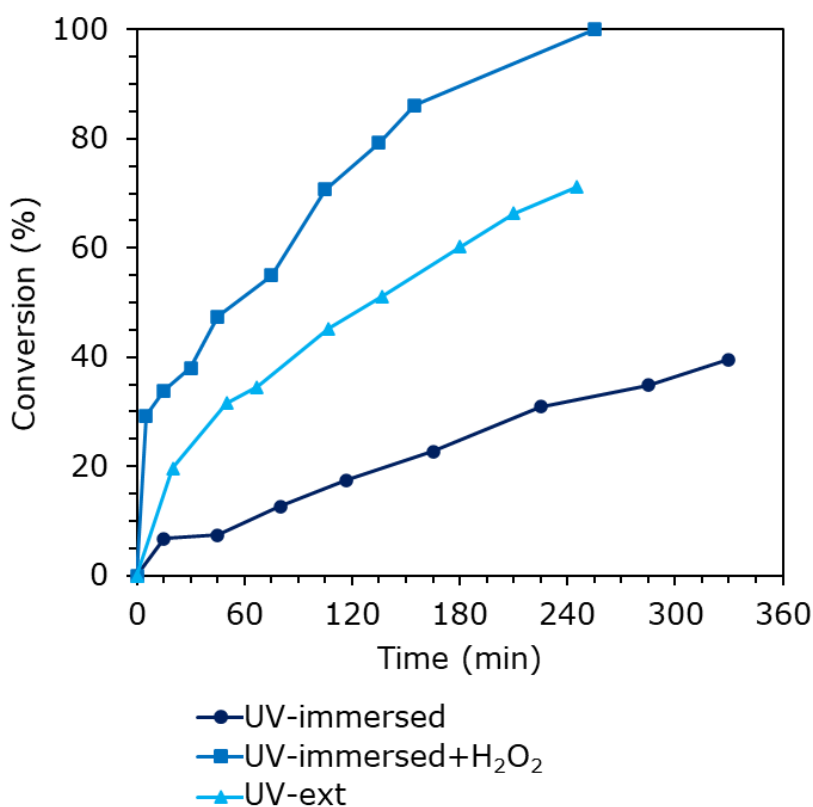


**Figure 6.12.** Conversion results of photolysis and photodegradation of AO7. 300 mL, 50 ppm of pollutant, 6.5 pH, rt, 0.3 mL H<sub>2</sub>O<sub>2</sub> 30% v/v, 125 ppm of P25, LED-UV lamp (365nm) or UV-spotlight

#### 6.2.4.3. Effect of pollutant concentration

As expected, a reduction of the concentration of AO7 impacts positively on the reaction time. Figure 4.17 illustrates that the reaction time required to fully degrade the pollutant passed from 4h to less than 2h, when the concentration was lowered from 25 to 15 ppm. On the other hand, the shape of the curve in the early stage of the reaction was similar in case of 40 ppm and 50 ppm pollutant, which may be due to the system that is already working at its maximum degradation rate.

Conversely, decreasing the concentration of photocatalyst (the same exfoliated  $C_3N_4$  obtained at  $550^\circ C$ ) has the opposite effect, since 50 ppm of catalyst prolonged the treatment by more than two-fold when compared to 125 ppm of photocatalyst.

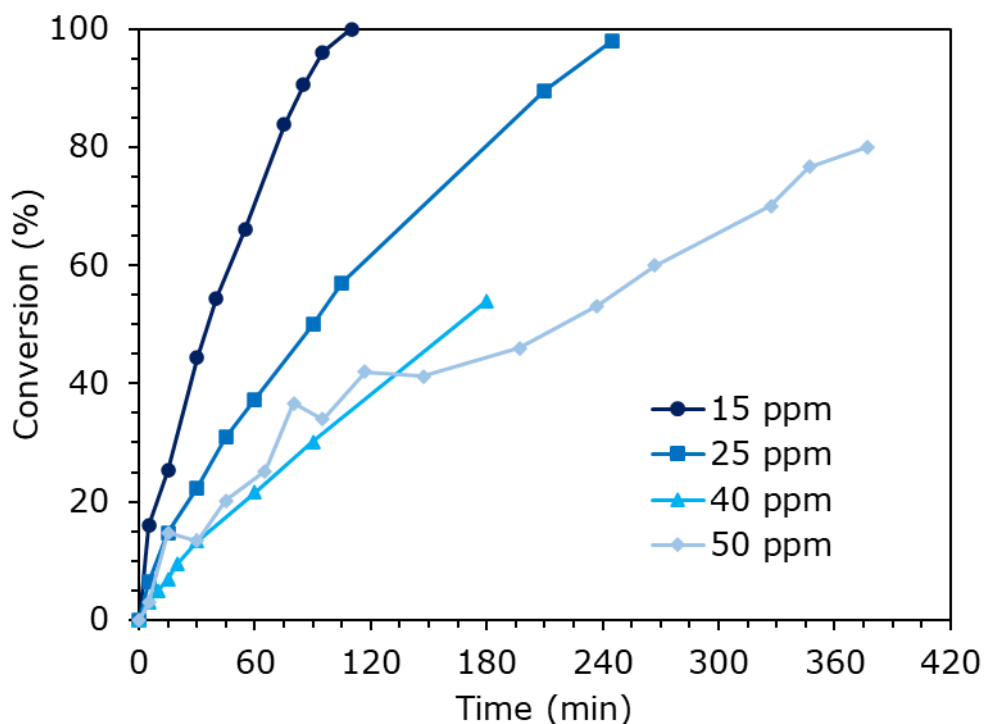


**Figure 6.13.** Conversion results of photodegradation of AO7 in the range 15-50 ppm. 300 mL, 6.5 pH, rt, 125 ppm of  $g-C_3N_4$ -550-120W, LED-UV lamp (365nm)

#### 6.2.4.4. Effect of pollutant nature

Even if one may be tempted to find the right balance between concentration and time, the context in which the photodegradation occurs is still far from a real-case scenario. Indeed, when tap water is used for the preparation of the solution with 125 ppm of  $C_3N_4$ -550-120W, the time required to exceed the 90% conversion became 5h instead of 85 minutes. Thus, maximizing the amount of photocatalyst added to the mixture is crucial for the success of the treatment, as real wastewaters contain multiple pollutants, either organic (pharmaceuticals, pesticides, dyes, microplastic, etc.) and inorganic (ammonia, nitrate, nitrite, chloride, etc., besides various cations) that compete for the degradation process and lower the efficiency of the treatment of a specific pollutant.

In that regard, a second pollutant was added to the reaction mixture, that is Bromophenol blue (BPB), a dye extensively used in laboratories and a marker which absorbs at a different wavelength than AO7 (441 nm instead of 486 nm). The photodegradation was carried out with 15 ppm of AO7 and 25 ppm of BPB (different amounts due to solubility issues), and the results are reported in Figure 6.14. It is evident that the presence of a second molecule in the system worsened the conversion of AO7, which reached a 77% conversion plateau after more than 4h of irradiation. When AO7 was the only pollutant, a similar conversion was reached within 80 minutes. Also, from the graph it is possible to note that there is an induction time of 10 minutes in which the photodegradation of AO7 seems to be inhibited. Conversely, the degradation of BPB proceeds during the whole process and slightly less than 50% of the pollutant was degraded after 5h of reaction. Despite the longer reaction time required, overall, it seems that the photoreactor can carry out the simultaneous degradation of the two pollutants.



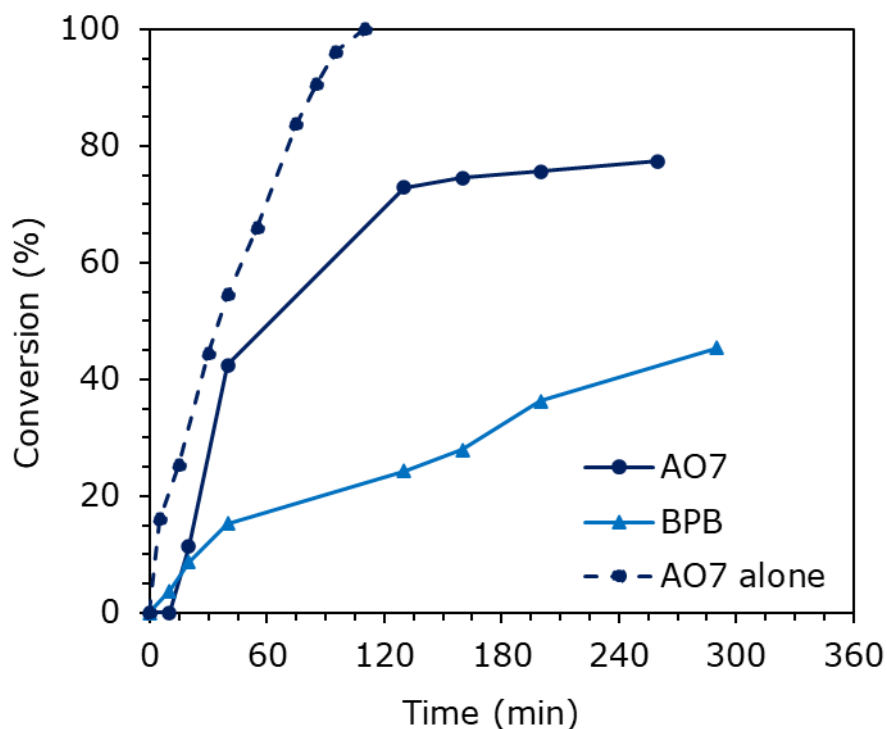


**Figure 6.14.** Conversion results of photodegradation of 15 ppm of AO7 and 25 ppm of BPB. 300 mL, 6.5 pH, rt, 125 ppm of g-C<sub>3</sub>N<sub>4</sub>-550-120W, LED-UV lamp (365nm)

#### 6.2.4.5. Effect of exfoliation power

Further tests highlighted the differences of activity between carbon nitride samples exfoliated with different power. The non-exfoliated material (C<sub>3</sub>N<sub>4</sub>-550-0W, Figure 6.15) is the benchmark here and it converted almost 90% of AO7 within 160 minutes. Similar results were obtained irrespectively of the calcination temperature and with low exfoliation power. On the other hand, when the exfoliation power increased to 120W, the same 90% degradation was obtained in 70 minutes.

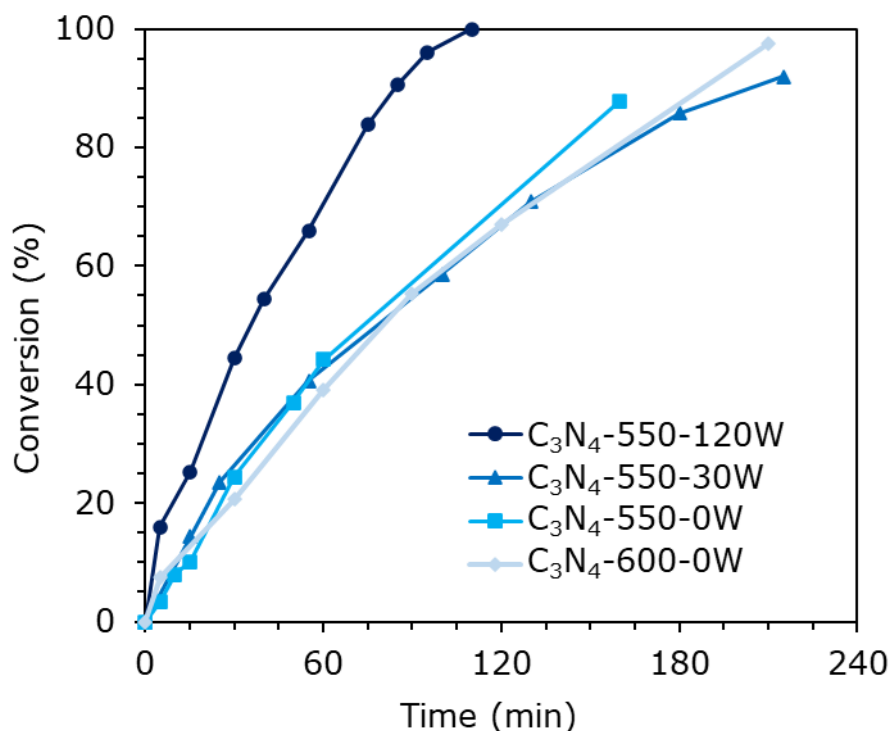


**Figure 6.15.** Conversion results of photodegradation of 15 ppm of AO7 using different exfoliated C<sub>3</sub>N<sub>4</sub>-550 samples. 6.5 pH, rt, 125 ppm of photocatalysts, LED-UV lamp (365nm)

#### 6.2.4.6. Effect of photocatalyst concentration

While keeping the same amount of AO7 (15 ppm), the concentration of photocatalyst C<sub>3</sub>N<sub>4</sub>-550-120W was lowered to 50 ppm, and the results are reported in Figure 6.16. From the graph it can be observed that the reaction time increased when the photocatalyst was more diluted, as one should expect from a photocatalyzed process, and with 50 ppm of photocatalyst 4h and a half are required to reach 90% conversion. We performed a further test with a solution prepared with tap water, which determined a loss in performance and a longer reaction time, according to the graph of Figure 6.16.

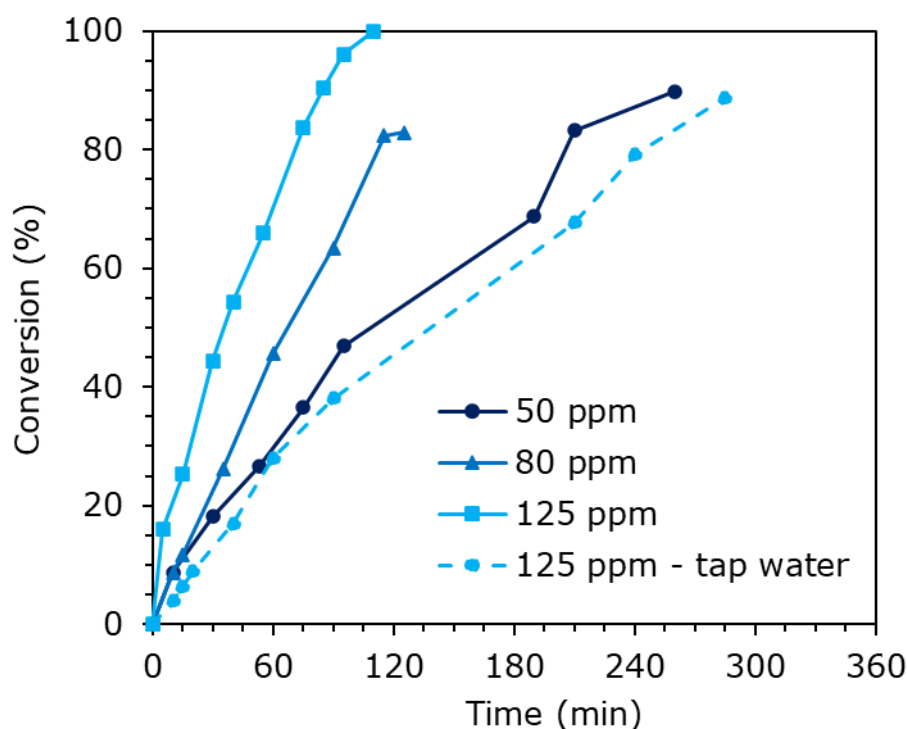


**Figure 6.16.** Conversion results of photodegradation of 15 ppm of AO7 using  $C_3N_4$ -550-120W in the range 50-125 ppm, with distilled or tap water. 6.5 pH, rt, 125 ppm of photocatalysts, LED-UV lamp (365nm)

#### 6.2.4.7. Photo-Fenton

Also in this case, Photo-Fenton was performed in various conditions and the performance compared with those of photocatalyzed treatments.

Figure 6.17 illustrates the results of the Photo-Fenton carried out at acid and native pH, while basic pH was ignored due to low performance in previous tests. Without adjusting the pH, the conversion increased linearly and after 90 minutes more than 23% of the AO7 was converted. The performance increased greatly at pH=3, with over 85% of conversion within 90 minutes and almost 100% conversion after 2h of treatment. In order to further reduce the time required to complete the photodegradation, we increased the amount of iron sulfate by 50%, from 20 to 30 ppm, while keeping the pH at 3, and so a complete

conversion was reached within 40 minutes. AO7 is a quite good base ( $\text{pK}_{\text{a}1}$  8.26,  $\text{pK}_{\text{a}2}$  11.4), so it is likely that the differences between the two setups are due the degree of protonation of the molecule of pollutant.

On the other hand, tests performed at different concentration of pollutant unveiled that with these conditions, small amounts such as 15 and 25 ppm were quickly degraded (100% in less than 40 minutes), while doubling the concentration of AO7 had an effect more detrimental to the reaction time, which increased to 2h. By contrast, the photocatalyzed treatment with  $\text{C}_3\text{N}_4$  and 25 ppm of AO7 took more than 4h to complete the degradation, though that degradation did not involve hydrogen peroxide.

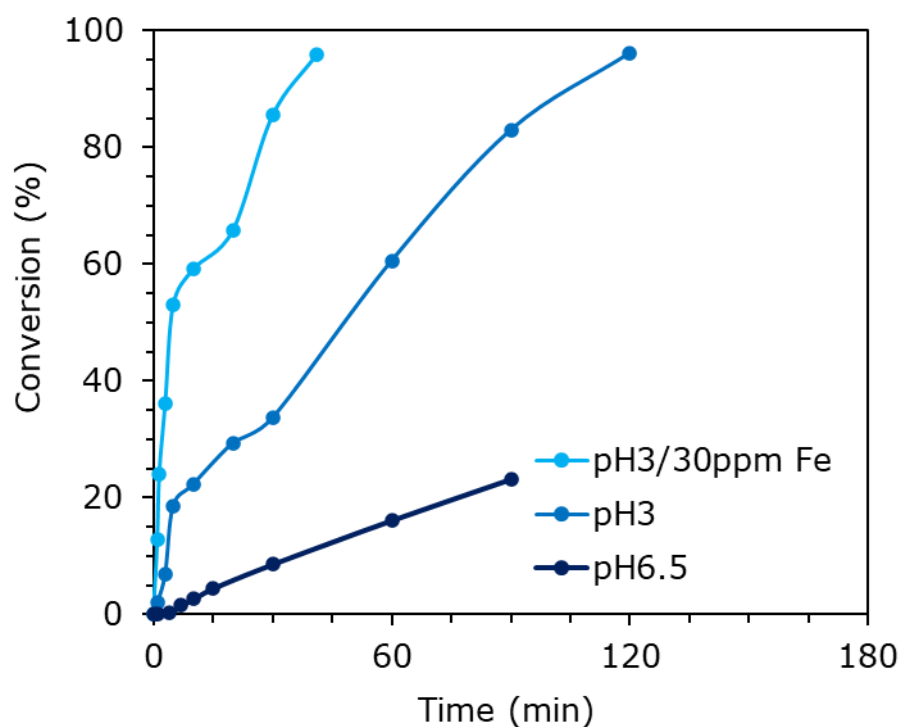


**Figure 6.17.** Conversion results of Photo-Fenton of 50 ppm of AO7 at pH 3 and 6.5. 300 mL, 20 ppm of  $\text{FeSO}_4$ , 0.3 mL  $\text{H}_2\text{O}_2$  30% v/v, LED-UV lamp (365nm)

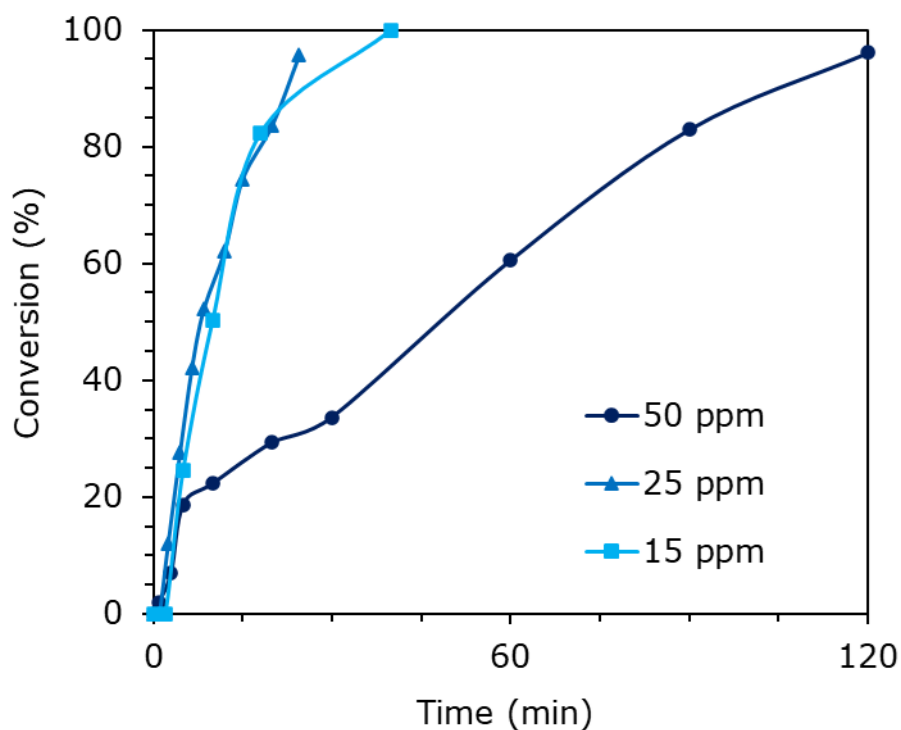


**Figure 6.18.** Conversion results of Photo-Fenton of AO7 in the range 15-50 ppm. pH 3. 20 ppm of  $\text{FeSO}_4$ , 0.3 mL  $\text{H}_2\text{O}_2$  30% v/v, LED-UV lamp (365nm)

### 6.2.5. Tests and acute toxicity with Amoxicillin

So far, the behavior of graphitic carbon nitride photocatalyst was studied by using Acid Orange 7 as model, whose conversion can be rapidly checked through UV-Vis analysis. On the other hand, we were interested in the mineralization of other kinds of pollutant, such as Amoxicillin (an antibiotic) that do not have a strong adsorption in the UV-Vis range. Therefore, we decided to carry out the photodegradation of this pharmaceutical with different treatments (listed below) and to analyze the efficiency of the photooxidation via TOC analysis and toxicity test with *Daphnia Magna*.

- Untreated sample of AMX
- Photolysis with immersed UV-Led lamp (365 nm, 36 W/m<sup>2</sup>)
- Photolysis with UV-spotlight (UVA, 116 W/m<sup>2</sup>)
- Photocatalysis with UV-spotlight (UVA, 116 W/m<sup>2</sup>) and C<sub>3</sub>N<sub>4</sub>-550-120W
- Photo-Fenton with immersed UV-Led lamp (365 nm, 36 W/m<sup>2</sup>)
- Photo-Fenton with UV-spotlight (UVA, 116 W/m<sup>2</sup>)

Therefore, a total of six tests were performed in order to assess the capability of the system in case of Amoxicillin degradation (Figure 6.18 and Table 6.1). The tests involved the treatment of 200 ppm of AMX at native pH in either reactor A (1000 mL) or B (300 mL), whereas the concentration of the catalyst was respectively 125 ppm for C<sub>3</sub>N<sub>4</sub>-550-120W and 20 ppm for FeSO<sub>4</sub>. Also, 0.3 mL of H<sub>2</sub>O<sub>2</sub> was added in case of Photo-Fenton process. Pollutant concentration was increased since EC<sub>50</sub> test involves the exposure of the daphnids to several treated solution with different dilution factor and being AMX not so

toxic toward this aquatic species, an excessive dilution would have caused a survivability close to 100% regardless of its presence.

As already mentioned, AMX is not particularly toxic toward daphnids (48h-EC50 is greater than 1000 mg/L according to the datasheet) and a  $95\pm5\%$  survivability was achieved with the untreated solution (Figure 6.19). Then, we exposed the daphnids to two solutions that were irradiated with UV light by means of the immersed UV-LED lamp and the UV-spotlight, which resulted in a lower survivability in the first case ( $85\pm5\%$ ) and still  $95\pm5\%$  for the second setup. Moreover, according to the data reported in Table 6.1 about the mineralization of the pollutant, roughly 3% of the organic carbon present was converted to CO<sub>2</sub> in case of the UV-LED lamp, while that percentage increases to 4.54% in case of the external UV lamp. The survivability was similar in both cases, thus, the differences in the mineralization process were likely to be linked to the mean irradiance of the two system, since the spotlight was much more powerful despite being less efficient in illuminating the solution. Regarding the photodegradation via photocatalysis, the mineralization according to TOC analysis was around 4.8% for the setup with the immersed UV lamp and 4.1% for the UV spotlight. The survivability, though, was not affected by the treatment, and that could mean that (i) the AMX converted was completely mineralized or (ii) the AMX was converted to other intermediates and partially mineralized, which is still acceptable given that the acute toxicity of the solution did not increase. Lastly, the two treatments based on photo-Fenton achieved the highest value of mineralization, respectively 20.6% for the immersed UV-LED lamp and 15.6% for the external one. Moreover, none of the daphnids died during the exposure to the treated solutions (100% survivability) and if any intermediate was formed during the process, it was less toxic than the AMX itself. This also confirms indirectly that most, if

not all, of the added hydrogen peroxide was decomposed, since that oxidant is extremely poisonous for *Daphnia Magna* (48h-EC50=4ppm).

From these results, it is clear that AMX is more effectively removed by traditional processes (photo-Fenton) rather than photocatalysis, though the latter can operate without addition of the oxidant (H<sub>2</sub>O<sub>2</sub>).

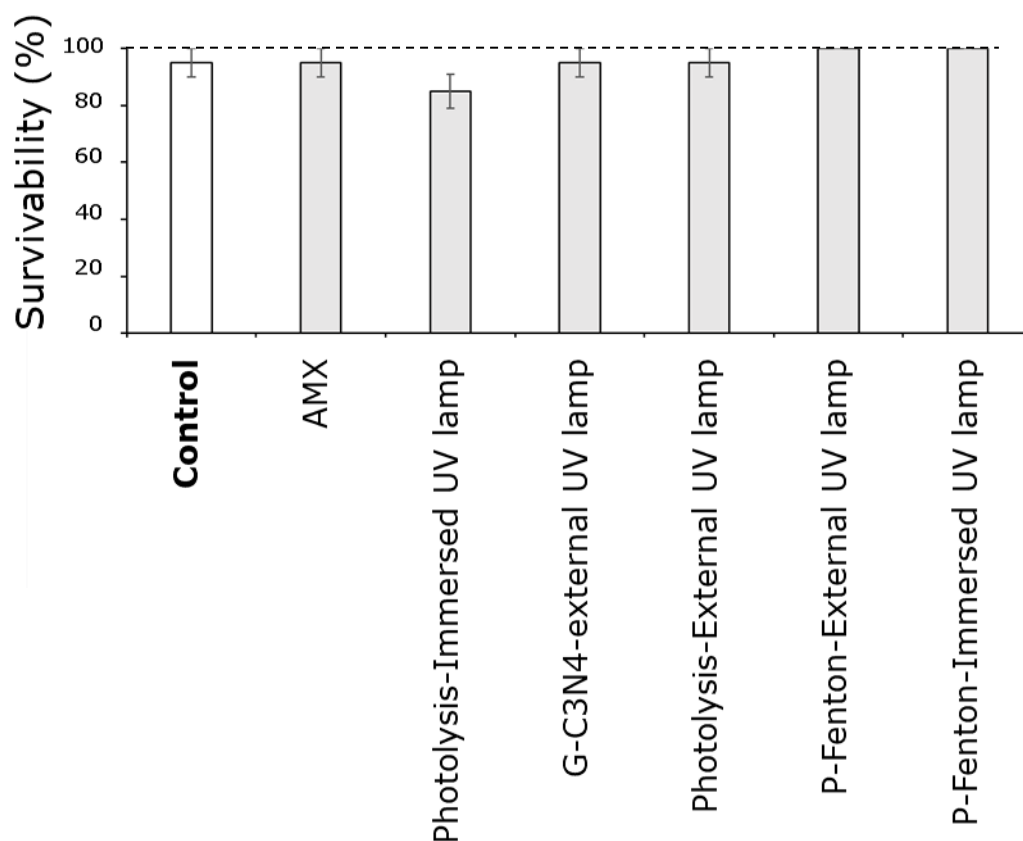


**Figure 6.19.** Results of acute toxicity test expressed as percentage of daphnids that survived after 48h of exposure to the solution



**Table 6.1.** TOC results of selected samples treated with UV light, photocatalysis and Photo-Fenton processes. TC (Total Carbon) = TIC (Total Inorganic Carbon) + TOC (Total organic Carbon)

Test	Lamp	[g-C <sub>3</sub> N <sub>4</sub> ] or [FeSO <sub>4</sub> ] (ppm)	TC (ppm)	TIC (ppm)	TOC (ppm)	Mineralization (%)
AMX untreated	Dark	/	110.0	16.35	93.65	0.0
Photolysis	UV-imm	/	105.5	14.65	90.85	2.99
Photolysis	UV-ext	/	100.1	10.70	89.40	4.54
Photocatalysis	UV-imm	120	105.4	16.24	89.16	4.79
Photocatalysis	UV-ext	120	100.3	10.48	89.82	4.09
Photo Fenton	UV-ext	20	87.24	8.178	79.06	15.58

### 6.3. Conclusions

Several setups, advanced oxidation processes and photocatalysts were tested and the results compared, as well as many pollutants were degraded through these methods, focusing on i) drugs or dyes as models for sanitary or industrial wastewater treatments; ii) single or mixed pollutants in either demineralized or tap water.

Regarding Diclofenac, the setup that adopts an irradiation from inside the solution (*e.g.* immersed UV lamp) is clearly superior to other arrangements of the lamp, since in the selected conditions and using P25 it is possible to degrade the Diclofenac up to 80% in less than 3h. Similar results were achieved using traditional photo-Fenton process, where the irradiation under visible light is as effective as ultraviolet, though it requires more time to reach the same level of conversion.

Using the external lamp, the differences between the bare P25 and surface-modified photocatalysts were highlighted. All the modified photocatalysts (Au, Pd and Ag) performed worse than the benchmark P25, likely due to the preparation technique adopted and that leads to a morphology not suitable for performing photodegradation. The

addition of an external oxidant ( $\text{H}_2\text{O}_2$ ) was found to improve moderately the results and align the activity of 0.1% Au, 0.1% Pd and 1% Ag with that of bare titania P25.

The same setup was successfully applied in the photodegradation of erythromycin, which was effectively degraded under UV and with Au/TiO<sub>2</sub> photocatalyst.

Toxicity tests using *Daphnia magna* as model species unveiled that both photo-Fenton and heterogeneous treatment with 0.1% Au/TiO<sub>2</sub> (P25) performed under UV light were effective to eliminate the DCF from the solution and to reduce its toxicity, as no or limited mortality occurred at the end of the toxicity test. In contrast, when P25 was used alone or photo-Fenton was performed under visible light, 30% to 80% mortality occurred, respectively, probably as a consequence of residual TiO<sub>2</sub> (P25) or undecomposed  $\text{H}_2\text{O}_2$ . Although the presence of by-products in tested solutions was not investigated in the present work, our results demonstrated a notable reduction of the DCF toxicity, suggesting the effectiveness of some photocatalytic treatments.

Speaking of the other pollutants, it was found that AO7, BPB and AMX can be photooxidated under conventional UV lamps as well as by using innovative LEDs arrays that emits in the UVA region and consume way less power (*ca.* 36W). The novel catalyst g-C<sub>3</sub>N<sub>4</sub>, resulted to be more effective than TiO<sub>2</sub> P25 in the photodegradation of AO7 under UV light, however, despite the band gap lower than 2.8 eV, it was not possible to perform the same treatment under visible light (430 nm). Furthermore, simultaneous mineralization of AO7 and BPB and mineralization in a more complex matrix (*i.e.* tap water) was achieved via photocatalysis. Lastly, AO7 is quickly degraded by Photo-Fenton treatment under UV light, which in that case outperform the photocatalytic one.

The effectiveness of the setup applied to the degradation of a problematic pollutant as amoxicillin was assessed via *in vitro* toxicity tests and TOC analysis. At the selected

concentration it was observed that Photo-Fenton treatment is the only one able to reduce the mortality of the daphnids used for the tests, while photocatalytic test with C3N4 achieved the same mortality of the control group.

## References

1. Rockström, J.; Steffen, W.; Noone, K.; Persson, Å.; Chapin, F.S.; Lambin, E.F.; Lenton, T.M.; Scheffer, M.; Folke, C.; Schellnhuber, H.J.; et al. A safe operating space for humanity. *Nature* **2009**, *461*, 472–475, doi:10.1038/461472a.
2. Naidu, R.; Biswas, B.; Willett, I.R.; Cribb, J.; Kumar Singh, B.; Paul Nathanail, C.; Coulon, F.; Semple, K.T.; Jones, K.C.; Barclay, A.; et al. Chemical pollution: A growing peril and potential catastrophic risk to humanity. *Environ. Int.* **2021**, *156*, 106616, doi:10.1016/j.envint.2021.106616.
3. Cribb, J. *Surviving the 21st century: Humanity's ten great challenges and how we can overcome them*; Springer International Publishing: Cham, 2016; ISBN 9783319412702.
4. Kanan, S.; Samara, F. Dioxins and furans: A review from chemical and environmental perspectives. *Trends Environ. Anal. Chem.* **2018**, *17*, 1–13, doi:10.1016/j.teac.2017.12.001.
5. Safe, E.S.; Hutzinger, O. *Polychlorinated dibenzo-p-dioxms and -furans (PCDDs/PCDFs): sources and environmental impact, epidemiology, mechanisms of action, health risks*; Safe, S., Hutzinger, O., Hill, T.A., Eds.; Springer Berlin Heidelberg: Berlin, Heidelberg, 1990; Vol. 3; ISBN 9783642705588.
6. DDT and Related Compounds. In *Handbook of Pollution Prevention and Cleaner Production: Best Practices in the Agrochemical Industry*; Elsevier, 2011; pp.

247–259.

7. Atiwesh, G.; Mikhael, A.; Parrish, C.C.; Banoub, J.; Le, T.A.T. Environmental impact of bioplastic use: A review. *Heliyon* **2021**, *7*, e07918, doi:10.1016/j.heliyon.2021.e07918.
8. Dulio, V.; van Bavel, B.; Brorström-Lundén, E.; Harmsen, J.; Hollender, J.; Schlabach, M.; Slobodnik, J.; Thomas, K.; Koschorreck, J. Emerging pollutants in the EU: 10 years of NORMAN in support of environmental policies and regulations. *Environ. Sci. Eur.* **2018**, *30*, 5, doi:10.1186/s12302-018-0135-3.
9. Von Sperling, M. Wastewater Characteristics, Treatment and Disposal. *Water Intell. Online* **2015**, *6*, 9781780402086–9781780402086, doi:10.2166/9781780402086.
10. Zupanc, M.; Kosjek, T.; Petkovšek, M.; Dular, M.; Kompare, B.; Širok, B.; Blažeka, Ž.; Heath, E. Removal of pharmaceuticals from wastewater by biological processes, hydrodynamic cavitation and UV treatment. *Ultrason. Sonochem.* **2013**, *20*, 1104–1112, doi:10.1016/j.ultsonch.2012.12.003.
11. Ghime, D.; Ghosh, P. Advanced Oxidation Processes: A Powerful Treatment Option for the Removal of Recalcitrant Organic Compounds. In *Advanced Oxidation Processes - Applications, Trends, and Prospects*; IntechOpen, 2020.
12. Kim, S.M.; Vogelpohl, A. Degradation of Organic Pollutants by the Photo-Fenton-Process. *Chem. Eng. Technol.* **1998**, *21*, 187–191, doi:10.1002/(SICI)1521-4125(199802)21:2<187::AID-CEAT187>3.0.CO;2-H.
13. Oumabady, S.; Selvaraj, P.S.; Periasamy, K.; Veeraswamy, D.; Ramesh, P.T.; Palanisami, T.; Ramasamy, S.P. Kinetic and isotherm insights of Diclofenac removal by sludge derived hydrochar. *Sci. Rep.* **2022**, *12*, 2184,

doi:10.1038/s41598-022-05943-z.

14. Fu, Q.; Fedrizzi, D.; Kosfeld, V.; Schlechtriem, C.; Ganz, V.; Derrer, S.; Rentsch, D.; Hollender, J. Biotransformation Changes Bioaccumulation and Toxicity of Diclofenac in Aquatic Organisms. *Environ. Sci. Technol.* **2020**, *54*, 4400–4408, doi:10.1021/acs.est.9b07127.
15. Lonappan, L.; Brar, S.K.; Das, R.K.; Verma, M.; Surampalli, R.Y. Diclofenac and its transformation products: Environmental occurrence and toxicity - A review. *Environ. Int.* **2016**, *96*, 127–138, doi:10.1016/j.envint.2016.09.014.
16. Mestre, A.S.; Carvalho, A.P. Photocatalytic degradation of pharmaceuticals carbamazepine, diclofenac, and sulfamethoxazole by semiconductor and carbon materials: A review. *Molecules* **2019**, *24*, 3702, doi:10.3390/molecules24203702.
17. Fischer, K.; Sydow, S.; Griebel, J.; Naumov, S.; Elsner, C.; Thomas, I.; Latif, A.A.; Schulze, A. Enhanced removal and toxicity decline of diclofenac by combining uva treatment and adsorption of photoproducts to polyvinylidene difluoride. *Polymers (Basel)*. **2020**, *12*, 1–15, doi:10.3390/polym12102340.
18. Baralla, E.; Demontis, M.P.; Dessì, F.; Varoni, M. V. An overview of antibiotics as emerging contaminants: Occurrence in bivalves as biomonitoring organisms. *Animals* **2021**, *11*, 3239, doi:10.3390/ani11113239.
19. Schafhauser, B.H.; Kristofco, L.A.; de Oliveira, C.M.R.; Brooks, B.W. Global review and analysis of erythromycin in the environment: Occurrence, bioaccumulation and antibiotic resistance hazards. *Environ. Pollut.* **2018**, *238*, 440–451, doi:10.1016/j.envpol.2018.03.052.
20. Pereira, J.H.O.S.; Reis, A.C.; Homem, V.; Silva, J.A.; Alves, A.; Borges, M.T.; Boaventura, R.A.R.; Vilar, V.J.P.; Nunes, O.C. Solar photocatalytic oxidation of

- recalcitrant natural metabolic by-products of amoxicillin biodegradation. *Water Res.* **2014**, *65*, 307–320, doi:10.1016/j.watres.2014.07.037.
21. Thirunavukkarasu, A.; Nithya, R. Adsorption of acid orange 7 using green synthesized CaO/CeO<sub>2</sub> composite: An insight into kinetics, equilibrium, thermodynamics, mass transfer and statistical models. *J. Taiwan Inst. Chem. Eng.* **2020**, *111*, 44–62, doi:10.1016/j.jtice.2020.04.007.
  22. Kant, R. Textile dyeing industry an environmental hazard. *Nat. Sci.* **2012**, *04*, 22–26, doi:10.4236/ns.2012.41004.
  23. Hooshmand, S.; Kargozar, S.; Ghorbani, A.; Darroudi, M.; Keshavarz, M.; Bairo, F.; Kim, H.W. Biomedical waste management by using nanophotocatalysts: The need for new options. *Materials (Basel)*. **2020**, *13*, 3511, doi:10.3390/MA13163511.
  24. Krakowiak, R.; Musial, J.; Bakun, P.; Sychała, M.; Czarczynska-Goslinska, B.; Mlynarczyk, D.T.; Koczorowski, T.; Sobotta, L.; Stanis, B.; Goslinski, T. Titanium dioxide-based photocatalysts for degradation of emerging contaminants including pharmaceutical pollutants. *Appl. Sci.* **2021**, *11*, 8674, doi:10.3390/app11188674.
  25. Gupta, K.; Singh, R.P.; Pandey, A.; Pandey, A. Photocatalytic antibacterial performance of TiO<sub>2</sub> and Ag-doped TiO<sub>2</sub> against *S. Aureus*, *P. Aeruginosa* and *E. Coli*. *Beilstein J. Nanotechnol.* **2013**, *4*, 345–351, doi:10.3762/bjnano.4.40.
  26. Pazoki, M.; Parsa, M.; Farhadpour, R. Removal of the hormones dexamethasone (DXM) by Ag doped on TiO<sub>2</sub> photocatalysis. *J. Environ. Chem. Eng.* **2016**, *4*, 4426–4434, doi:10.1016/j.jece.2016.09.034.
  27. Gomes, J.F.; Leal, I.; Bednarczyk, K.; Gmurek, M.; Stelmachowski, M.; Zaleska-

- Medynska, A.; Quinta-Ferreira, M.E.; Costa, R.; Quinta-Ferreira, R.M.; Martins, R.C. Detoxification of parabens using UV-A enhanced by noble metals - TiO<sub>2</sub> supported catalysts. *J. Environ. Chem. Eng.* **2017**, *5*, 3065–3074, doi:10.1016/j.jece.2017.06.010.
28. Mei, P.; Wang, H.; Guo, H.; Zhang, N.; Ji, S.; Ma, Y.; Xu, J.; Li, Y.; Alsulami, H.; Alhodaly, M.S.; et al. The enhanced photodegradation of bisphenol A by TiO<sub>2</sub>/C<sub>3</sub>N<sub>4</sub> composites. *Environ. Res.* **2020**, *182*, 109090, doi:10.1016/j.envres.2019.109090.
29. Yan, S.C.; Li, Z.S.; Zou, Z.G. Photodegradation performance of g-C<sub>3</sub>N<sub>4</sub> fabricated by directly heating melamine. *Langmuir* **2009**, *25*, 10397–10401, doi:10.1021/la900923z.
30. Calza, P.; Sakkas, V.A.; Medana, C.; Baiocchi, C.; Dimou, A.; Pelizzetti, E.; Albanis, T. Photocatalytic degradation study of diclofenac over aqueous TiO<sub>2</sub> suspensions. *Appl. Catal. B Environ.* **2006**, *67*, 197–205, doi:10.1016/j.apcatb.2006.04.021.
31. Mohammadi, R.; Massoumi, B.; Rabani, M. Photocatalytic decomposition of amoxicillin trihydrate antibiotic in aqueous solutions under UV irradiation using Sn/TiO<sub>2</sub> Nanoparticles. *Int. J. Photoenergy* **2012**, *2012*, 1–11, doi:10.1155/2012/514856.
32. Ramis, G.; Conte, F.; Calloni, C.; Tripodi, A.; Parolini, M.; De Felice, B.; Rossetti, I. Development and comparison of advanced oxidation processes (aops) for the mineralization of azo-dyes from wastewaters. *Chem. Eng. Trans.* **2021**, *86*, 601–606, doi:10.3303/CET2186101.
33. Kovacic, M.; Juretic Perisic, D.; Biosic, M.; Kusic, H.; Babic, S.; Loncaric Bozic,

- A. UV photolysis of diclofenac in water; kinetics, degradation pathway and environmental aspects. *Environ. Sci. Pollut. Res.* **2016**, *23*, 14908–14917, doi:10.1007/s11356-016-6580-x.
34. Lara-Pérez, C.; Leyva, E.; Zermeño, B.; Osorio, I.; Montalvo, C.; Moctezuma, E. Photocatalytic degradation of diclofenac sodium salt: adsorption and reaction kinetic studies. *Environ. Earth Sci.* **2020**, *79*, 277, doi:10.1007/s12665-020-09017-z.
  35. Iovino, P.; Chianese, S.; Canzano, S.; Prisciandaro, M.; Musmarra, D. Photodegradation of diclofenac in wastewaters. *Desalin. Water Treat.* **2017**, *61*, 293–297, doi:10.5004/dwt.2016.11063.
  36. Pérez-Estrada, L.A.; Malato, S.; Gernjak, W.; Agüera, A.; Thurman, E.M.; Ferrer, I.; Fernández-Alba, A.R. Photo-fenton degradation of diclofenac: Identification of main intermediates and degradation pathway. *Environ. Sci. Technol.* **2005**, *39*, 8300–8306, doi:10.1021/es050794n.
  37. Hansson, H.; Kaczala, F.; Marques, M.; Hogland, W. Photo-Fenton and Fenton oxidation of recalcitrant industrial wastewater using nanoscale zero-valent iron. *Int. J. Photoenergy* **2012**, *2012*, 1–11, doi:10.1155/2012/531076.
  38. Vogna, D.; Marotta, R.; Napolitano, A.; Andreozzi, R.; D’Ischia, M. Advanced oxidation of the pharmaceutical drug diclofenac with UV/H<sub>2</sub>O<sub>2</sub> and ozone. *Water Res.* **2004**, *38*, 414–422, doi:10.1016/j.watres.2003.09.028.
  39. Zhang, N.; Li, J.M.; Liu, G.G.; Chen, X.L.; Jiang, K. Photodegradation of diclofenac in aqueous solution by simulated sunlight irradiation: Kinetics, thermodynamics and pathways. *Water Sci. Technol.* **2017**, *75*, 2163–2170, doi:10.2166/wst.2017.075.



40. Kim, J.; Monllor-Satoca, D.; Choi, W. Simultaneous production of hydrogen with the degradation of organic pollutants using TiO<sub>2</sub> photocatalyst modified with dual surface components. *Energy Environ. Sci.* **2012**, *5*, 7647–7656, doi:10.1039/c2ee21310a.
41. Espino-Estévez, M.R.; Fernández-Rodríguez, C.; González-Díaz, O.M.; Araña, J.; Espinós, J.P.; Ortega-Méndez, J.A.; Doña-Rodríguez, J.M. Effect of TiO<sub>2</sub>-Pd and TiO<sub>2</sub>-Ag on the photocatalytic oxidation of diclofenac, isoproturon and phenol. *Chem. Eng. J.* **2016**, *298*, 82–95, doi:10.1016/j.cej.2016.04.016.
42. Conte, F.; Rossetti, I.; Ramis, G.; Vaulot, C.; Hajjar-garreau, S.; Bennici, S. Low Metal Loading (Au, Ag, Pt, Pd) Photo-Catalysts Supported on TiO<sub>2</sub> for Renewable Processes. *Materials (Basel)*. **2022**, *15*, 2915, doi:10.3390/ma15082915.
43. Cornish, B.J.P.A.; Lawton, L.A.; Robertson, P.K.J. Hydrogen peroxide enhanced photocatalytic oxidation of microcystin-LR using titanium dioxide. *Appl. Catal. B Environ.* **2000**, *25*, 59–67, doi:10.1016/S0926-3373(99)00121-6.
44. Ferrari, P.F.; Gallese, V.; Rizzolatti, G.; Fogassi, L. Mirror neurons responding to the observation of ingestive and communicative mouth actions in the monkey ventral premotor cortex. *Eur. J. Neurosci.* **2003**, *17*, 1703–1714, doi:10.1046/j.1460-9568.2003.02601.x.
45. Cleuvers, M. Mixture toxicity of the anti-inflammatory drugs diclofenac, ibuprofen, naproxen, and acetylsalicylic acid. *Ecotoxicol. Environ. Saf.* **2004**, *59*, 309–315, doi:10.1016/S0147-6513(03)00141-6.
46. Haap, T.; Triebskorn, R.; Köhler, H.R. Acute effects of diclofenac and DMSO to *Daphnia magna*: Immobilisation and hsp70-induction. *Chemosphere* **2008**, *73*,

- 353–359, doi:10.1016/j.chemosphere.2008.05.062.
47. Yang, D.; Zhao, X.; Chen, Y.; Wang, W.; Zhou, Z.; Zhao, Z.; Jiang, Z. Synthesis of g-C<sub>3</sub>N<sub>4</sub> Nanosheet/TiO<sub>2</sub> Heterojunctions Inspired by Bioadhesion and Biomineralization Mechanism. *Ind. Eng. Chem. Res.* **2019**, *58*, 5516–5525, doi:10.1021/acs.iecr.9b00184.
  48. Liu, M.; Feng Tian, X.; Long Chang, Y. Preparation and Kinetics of g-C<sub>3</sub>N<sub>4</sub>/TiO<sub>2</sub> Nanomaterials for the Photodegradation of Pyridine Under Solar-Light Irradiation. *ChemistrySelect* **2020**, *5*, 6389–6402, doi:10.1002/slct.202001488.
  49. Sturini, M.; Speltini, A.; Maraschi, F.; Vinci, G.; Profumo, A.; Pretali, L.; Albini, A.; Malavasi, L. g-C<sub>3</sub>N<sub>4</sub>-promoted degradation of ofloxacin antibiotic in natural waters under simulated sunlight. *Environ. Sci. Pollut. Res.* **2017**, *24*, 4153–4161, doi:10.1007/s11356-016-8156-1.
  50. Kang, S.; Qin, H.; Zhang, L.; Huang, Y.; Bai, X.; Li, X.; Sun, D.; Wang, Y.; Cui, L. Efficient Photocatalytic Bilirubin Removal over the Biocompatible Core/Shell P25/g-C<sub>3</sub>N<sub>4</sub> Heterojunctions with Metal-free Exposed Surfaces under Moderate Green Light Irradiation. *Sci. Rep.* **2017**, *7*, 44338, doi:10.1038/srep44338.
  51. Shu, H.Y.; Chang, M.C. Pilot scale annular plug flow photoreactor by UV/H<sub>2</sub>O<sub>2</sub> for the decolorization of azo dye wastewater. *J. Hazard. Mater.* **2005**, *125*, 244–251, doi:10.1016/j.jhazmat.2005.05.038.
  52. Chiou, C.H.; Wu, C.Y.; Juang, R.S. Influence of operating parameters on photocatalytic degradation of phenol in UV/TiO<sub>2</sub> process. *Chem. Eng. J.* **2008**, *139*, 322–329, doi:10.1016/j.cej.2007.08.002.
  53. Zhang, W.; Bian, Z.; Xin, X.; Wang, L.; Geng, X.; Wang, H. Comparison of

visible light driven H<sub>2</sub>O<sub>2</sub> and peroxymonosulfate degradation of norfloxacin  
 using Co/g-C<sub>3</sub>N<sub>4</sub>. *Chemosphere* **2021**, 262, 127955,  
 doi:10.1016/j.chemosphere.2020.127955.

## Appendix C

Pollutant	Conc. (ppm)	Catalyst	Conc. (ppm)	Light	pH	H <sub>2</sub> O <sub>2</sub> (mL)	Volume (mL)	Conversion (UV-Vis or TOC)
DCF	100	/	/	UV immersed	6.5	0.8	300	-25%; 120 min
DCF	100	/	/	Dark	6.5	0.8	1000	0%; 120 min
DCF	100	/	/	LED spotlight	6.5	0.8	1000	0%; 120 min
DCF	100	/	/	UV immersed	6.5	0.8	300	89%; 120 min
DCF	100	/	/	UV spotlight	6.5	0.8	1000	0%; 120 min
DCF	12	FeSO <sub>4</sub>	54	LED spotlight	6.5	0.8	1000	23%; 330 min
DCF	25	FeSO <sub>4</sub>	54	LED spotlight	6.5	0.8	1000	36%; 300 min
DCF	50	FeSO <sub>4</sub>	54	LED spotlight	6.5	0.8	1000	88%; 330 min
DCF	100	FeSO <sub>4</sub>	54	LED spotlight	6.5	0.8	1000	75%; 330 min
DCF	100	FeSO <sub>4</sub>	54	LED spotlight	3	0.8	1000	88%; 330 min
DCF	100	FeSO <sub>4</sub>	54	LED spotlight	12	0.8	1000	20%; 240 min
DCF	100	FeSO <sub>4</sub>	54	Dark	6.5	0.8	300	57%; 300 min
DCF	100	FeSO <sub>4</sub>	54	UV immersed	6.5	0.8	300	82%; 300 min
DCF	100	FeSO <sub>4</sub>	54	UV spotlight	6.5	0.8	1000	78%; 120 min
DCF	100	FeSO <sub>4</sub>	54	Sunlight	6.5	0.8	1000	88%; 240 min

Pollutant	Conc. (ppm)	Catalyst	Conc. (ppm)	Light	pH	H <sub>2</sub> O <sub>2</sub> (mL)	Volume (mL)	Conversion (UV-Vis or TOC)
DCF	100	P25	200	UV	6.5	/	1000	74%; 300 min
				spotlight				
DCF	100	0.1%Pd/P25	200	UV	6.5	/	1000	10%; 300 min
				spotlight				
DCF	100	0.1% Au/P25	200	UV	6.5	/	1000	47%; 300 min
				spotlight				
DCF	100	1%Ag/P25	200	UV	6.5	/	1000	11%; 120 min
				spotlight				
DCF	100	P25	200	UV	6.5	0.8	1000	44%; 190 min
				spotlight				
DCF	100	0.1%Pd/P25	200	UV	6.5	0.8	1000	35%; 300 min
				spotlight				
DCF	100	0.1% Au/P25	200	UV	6.5	0.8	1000	92%; 360 min
				spotlight				
DCF	100	1%Ag/P25	200	UV	6.5	0.8	1000	86%; 360 min
				spotlight				
ERY	100	0.1% Au/P25	200	UV	6.5	/	1000	70%; 240 min
				spotlight				
ERY	50	FeSO <sub>4</sub>	28	UV	6.5	0.8	1000	86%; 200 min
				spotlight				
DCF	200	/	/	Dark	6.5	/	1000	24h
DCF	200	/	/	UV	6.5	1.6	1000	24h
				spotlight				
DCF	200	P25	200	UV	6.5	1.6	1000	24h
				spotlight				
DCF	200	FeSO <sub>4</sub>	54	LED	6.5	1.6	1000	24h
				spotlight				
DCF	200	0.1% Au/P25	200	UV	6.5	1.6	1000	24h
				spotlight				
DCF	200	FeSO <sub>4</sub>	54	UV	6.5	1.6	1000	24h
				spotlight				
AO7	50	/	/	LED-UV	6.5	/	300	7.6%; 165 min
				365nm				
AO7	50	P25	125	LED-UV	6.5	/	300	40%; 330 min

365nm								
Pollutant	Conc. (ppm)	Catalyst	Conc. (ppm)	Light	pH	H <sub>2</sub> O <sub>2</sub> (mL)	Volume (mL)	Conversion (UV-Vis or TOC)
AO7	50	C <sub>3</sub> N <sub>4</sub> -550-120W	125	LED 365nm	6.5	/	300	77%; 360 min
AO7	50	C <sub>3</sub> N <sub>4</sub> -550-120W	125	LED 430nm	6.5	/	300	0%; 165 min
AO7	50	/	/	LED-UV 365nm	6.5	0.3	300	25%; 345 min
AO7	50	P25	125	LED-UV 365nm	6.5	0.3	300	100%; 255 min
AO7	50	C <sub>3</sub> N <sub>4</sub> -550-120W	125	LED 365nm	6.5	0.3	300	78%; 255 min
AO7	50	P25	125	UV spotlight	6.5	/	1000	71%; 240 min
AO7	15	C <sub>3</sub> N <sub>4</sub> -550-120W	125	LED 365nm	6.5	/	300	100%; 110 min
AO7	25	C <sub>3</sub> N <sub>4</sub> -550-120W	125	LED 365nm	6.5	/	300	98%; 240 min
AO7	40	C <sub>3</sub> N <sub>4</sub> -550-120W	125	LED 365nm	6.5	/	300	54%; 180 min
AO7+BPB	15(AO7) 25(BPB)	C <sub>3</sub> N <sub>4</sub> -550-120W	125	LED 365nm	6.5	/	300	77%; 260 min 45%; 290 min
AO7	15	C <sub>3</sub> N <sub>4</sub> -550-0W	125	LED 365nm	6.5	/	300	88%; 160 min
AO7	15	C <sub>3</sub> N <sub>4</sub> -550-30W	125	LED 365nm	6.5	/	300	92%; 215 min
AO7	15	C <sub>3</sub> N <sub>4</sub> -600-0W	125	LED 365nm	6.5	/	300	98%; 210 min
AO7	15	C <sub>3</sub> N <sub>4</sub> -550-120W	50	LED 365nm	6.5	/	300	83%; 125 min
AO7	15	C <sub>3</sub> N <sub>4</sub> -550-120W	80	LED 365nm	6.5	/	300	90%; 260 min
AO7	15	C <sub>3</sub> N <sub>4</sub> -550-120W	125	LED 365nm	6.5	/	300-Tap water	89%; 285 min
AO7	50	FeSO <sub>4</sub>	20	LED 365nm	6.5	/	300	22%; 90 min
AO7	50	FeSO <sub>4</sub>	20	LED	3	/	300	95%; 120 min

AO7	50	FeSO <sub>4</sub>	30	365nm LED	3	/	300	95%; 40 min
AO7	15	FeSO <sub>4</sub>	20	365nm LED	3	/	300	100%; 45 min
AO7	25	FeSO <sub>4</sub>	20	365nm LED	3	/	300	95%; 25 min
Pollutant	Conc. (ppm)	Catalyst	Conc. (ppm)	Light	pH	H <sub>2</sub> O <sub>2</sub> (mL)	Volume (mL)	Conversion (UV-Vis or TOC)
AMX	200	/	/	Dark	6.5	/	300	0%; 24h
AMX	200	/	/	LED	6.5	/	300	2.99%; 24h
AMX	200	/	/	365nm UV	6.5	/	1000	4.54%; 24h
AMX	200	C <sub>3</sub> N <sub>4</sub> -550- 120W	125	spotlight LED	6.5	/	300	4.79%; 24h
AMX	200	C <sub>3</sub> N <sub>4</sub> -550- 120W	125	365nm UV	6.5	/	1000	4.09%; 24h
AMX	200	FeSO <sub>4</sub>	20	spotlight LED	6.5	1 eq.	300	20.60%; 24h
AMX	200	FeSO <sub>4</sub>	20	365nm UV	6.5	1 eq.	1000	15.58%; 24h
				spotlight				

## 7. Photocatalysts deposition

### 7.1. Introduction

Among the drawbacks of photocatalysis there is the fact that it typically uses nanosized photocatalysts in form of powder. The main advantage of the suspended photocatalyst testing mode is that it generally leads to high photocatalytic efficiency since high surface area is available and the maximum exposure to the light can be achieved, provided the amount of powder is optimized to prevent a shading effect. On the other hand, depending on the kind of NPs and the type of process that is carried out, it may be challenging to recover or separate such small photocatalyst particles at the end of the process, which in turn results in increased cost and longer processing time [1].

An immobilized photocatalyst is also required for all those processes that involve the treatment of a gaseous phase, for instance CO<sub>2</sub> and NO<sub>x</sub> conversion, VOCs abatement and so on [2,3]. Overall, working with immobilized photocatalysts is required if one is planning to recycle the photocatalyst after a batch treatment or to setup a continuous operation. Generally speaking, several techniques can be exploited to obtain the immobilization of the photo-active phase, from the well-established sol-gel synthesis and solvent deposition to the more exotic ones like chemical and physical vapor deposition [2]. Other deposition methods involve the insertion or anchorage of the photocatalyst NPs to a polymeric membrane [1].

All the techniques aforementioned have been successfully applied to the deposition of titanium dioxide, and, in this work, we present the results achieved by coating titania P25 through a very simple and scalable dip coating technique. This photocatalyst was selected as it is available on the market while being inexpensive and with consistent properties between different production batches. C<sub>3</sub>N<sub>4</sub> would have been interesting to immobilize,

however, the large amount of raw material that was required for the optimization of the coating procedure suggested to use a commercial material to have a large batch of powder with reproducible properties.

Dip coating (also known as solvent deposition) is a simple method to deposit particles over a solid support, for instance glass, metals or ceramics, by dipping the material into the suspension of NPs and slowly removing it, then, the solvent is evaporated. Pre-treatments, post-treatments and the use of binders or other chemicals are all factors that influence the adhesion of the deposited layer over the support. Thus, dip coating is a quite simple and inexpensive technique which can be adapted to several combinations of photocatalysts and supports.

## **7.2. Results and discussion**

### **7.2.1. Optimization of the deposition process**

The supports employed in this work were glass tiles used in microscopy, whose size was 26x76x1 mm<sup>3</sup>, since it is inexpensive and easy to obtain on the market. As already described in Chapter 2, the deposition was performed thanks a home-made dip coating apparatus and a suspension of P25 in distilled water was used as base for the impregnation.

The first coatings were applied to the untreated tiles through several following cycles, as reported in Table 7.1. As expected, the glasses dipped into distilled water and dried at 500°C under air did not show any weight loss or gain. On the other hand, after the first cycle of impregnation with P25/water suspension 5% w/w, an average deposition of 0.7 mg per tile was obtained with a  $\pm 0.1$  mg oscillation after tens of repetitions. This P25 solution was selected as it is fairly stable once the mechanical stirring is stopped and



allows to carry out the dipping while avoiding a massive precipitation of the titania, which could impact on the reliability of the deposition itself. The tiles were clamped on the top, so the powder was distributed over roughly 80% of the surface. Two cycles only led to a slight increase of the deposited P25, up to 1.2 mg with a mean value of 0.9 mg, thus, the deposition after each cycle was ca. 0.5 mg. It is noteworthy to say that the deposited layer was not good-looking and much less homogeneous than expected. A closer analysis with an optic microscope (up to x400 magnification power) unveiled that the surface of the glasses was unfinished, and many microscopic debris prevented a homogeneous deposition of P25 nanoparticles (Figure 7.1.b). To overcome this problem, all the glass tiles were pretreated and washed with piranha solution (3:1  $\text{H}_2\text{SO}_4/\text{H}_2\text{O}_2$  30% w/w), which proved to be effective in cleaning and activating the surface, since after two cycles of deposition the total P25 loaded over the glass was on average 2.3 mg and also the distribution observed with naked eye improved (Figure 7.1.a). From this point, we started to clean in that way all the glasses used for the deposition.

**Table 7.1.** Photocatalyst loading over glass tile after different pretreatments. Dipping in 5%w/w P25 suspension in distilled water, room temperature. Post-treatment was performed in a furnace at 500°C for 1h

Recipe #	Treatment	N° cycle	Av. loading (mg)	Min (mg)	Max (mg)	Loading/Cycle
1	unwhased	1	0.0	/	/	0.00
	unwhased	1	0.7	0.6	0.8	0.70
	unwhased	2	0.9	0.5	1.2	0.45
2	piranha sol.	1	0.1	/	/	0.10
	piranha sol.	2	4.8	4.2	5.4	2.40
	piranha sol.	3	2.2	0.9	4.1	0.70
	piranha sol.	6	5.5	1.1	14.4	0.92
4	piranha sol.*	3	3.4	2.7	4.1	1.13
5	brush	1	6.3	4.0	8.6	6.30

\*rinsed with sodium carbonate

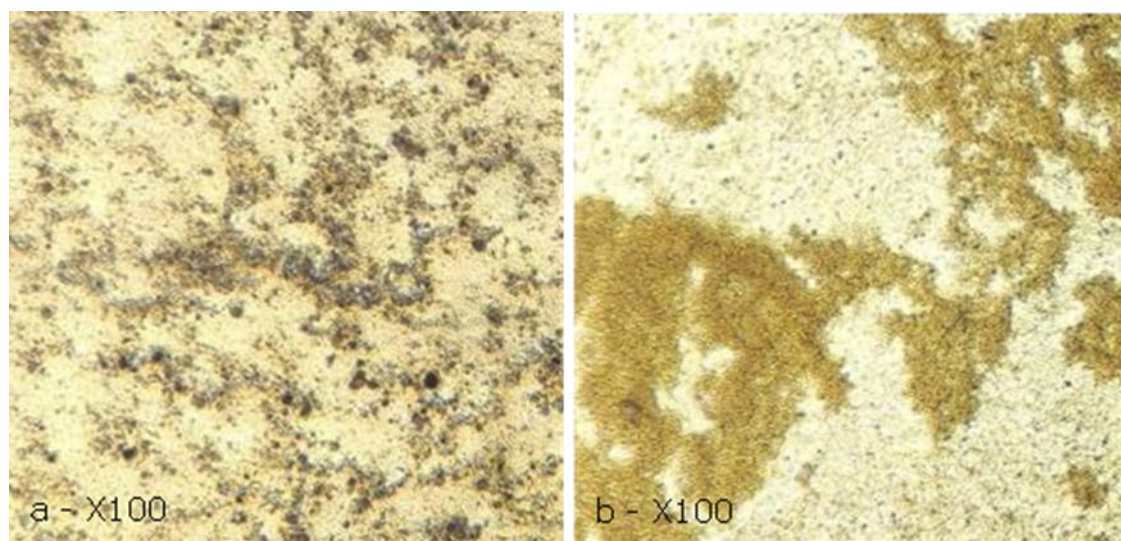


**Figure 7.1.** P25 deposited after two cycles over glass slide (a) washed with piranha solution and (b) untreated surface. Observed through an optic microscope at 100 magnification power

Interestingly, the first deposition did not deposit an appreciable amount of titania, barely 0.1 mg, which is probably due to the leftover traces of piranha solution on the surface. After three deposition cycles, the average photocatalyst layer weight was lower than the same layer after two cycles, that is 1.8 mg, and we interpreted that result with the fact that some titania was detached again during the subsequent dipping. Anyway, at the end of the 6<sup>th</sup> cycle the average layers weighted 5.5 mg, with a peak of 14.4 mg and a minimum of 1.1 mg. To confirm the hypothesis that traces of piranha solution were disturbing the deposition process, the tiles were rinsed with sodium carbonate solution (1 M) and then dipped into the P25/water suspension. After three cycles, the average deposition was 3.4 mg, almost 50% higher than the amount that was previously obtained (2.2 mg). Although satisfied with the results obtained so far, the dip coating was always performed on one tile at a time, thus it is a time-consuming process. Other researchers reported a simpler technique that involves a brush rather than a dip coating apparatus, so that route was explored as well [4]. Unfortunately, despite a mean deposition weight of 6.3 mg after just one cycle, this technique was not reliable, and the layer of titania was less uniform with respect to untreated tiles processed via dip coating.

In light of that results, more tests were developed to assess the robustness of the double washing (piranha and rinsing) procedure. According to Table 7.2, an average of 0.7 mg was added after each cycle and this was pretty consistent among the series of four glasses and six cycles allowed to obtain 4.2 mg of P25 deposited over the surface of the tiles, which is in line with our requirements as the photocatalytic reduction of CO<sub>2</sub> is currently carried out using 38 mg of photocatalyst. Not only the deposited layer looked very homogeneous, but it is also very resistant from a physical point of view. This point was firstly demonstrated by immersion of a glass tile in a beaker containing water and kept

under stirring for 3h. After that amount of time, the glass tile was dried at 105°C and weighted again, which confirmed that no appreciable amount of coating was lost during the tests (reproducibility was ensured by many repetitions, at least 2). In addition, an abrasion test was carried out by using a home-made apparatus constituted of a 500 mm long-plane inclined at 45° and covered with sandpaper (P200). With that setup, each tile was pulled down the plane by its own weight and as a result, roughly the same force was applied during the tests. Then, the tiles were weighted and observed at the microscope. Even after multiple scratch cycles, none of the glasses lost more than 0.1 mg of coating and the surface resulted substantially unaffected. Given the robustness of the deposition technique, it was decided to further optimize the parameters to obtain a higher loading of TiO<sub>2</sub>.

**Table 7.2.** Photocatalyst loading over glasses obtained after several cycles. Dipping in 5%w/w P25 suspension in distilled water, room temperature. Post-treatment was performed in a furnace at 500°C for 1h

Recipe #	N° cycle	Glass #1	Glass #2	Glass #3	Glass #4	Av. loading (mg)
4	1	0.7	0.6	1.2	0.4	0.7
	2	0.3	1.2	1.0	0.5	0.8
	3	0.4	0.7	0.7	0.5	0.6
	4	0.5	0.6	0.3	0.6	0.5
	5	1.3	1.8	1.2	0.6	1.2
	6	0.4	0.2	0.8	0.2	0.4

All the following tests have been performed using two deposition cycles. Table 7.3 summarizes all the results, which show that there is an effect of the solution temperature on the deposition of P25. For instance, the weight of the deposited layer increased by 20%

when the temperature rose to 30°C and by an incredible 87% with a further increase to 50°C. Both the minimum and the maximum weight among the series (usually composed of twelve samples) increased as well. Therefore, we decided to keep working with that temperature while tuning the second parameter, which is the pH. In that regard, the pH was lowered either by addition of HCl or HNO<sub>3</sub>, which are both strong acids and widely used to activate the glass, with the former that is in general more volatile [5]. It was found that a lower pH also advantaged the deposition process, with a mean weight of 3.6 mg (+29% vs 50°C@pH7) in case of HCl and 4.0 mg (+43% vs 50°C@pH7) for the HNO<sub>3</sub>. However, this second set of samples showed a rough surface and lumpy areas, so for a 10% increase of weight with respect the case with HCl used as acid is not probably worth losing the homogeneity of the surface. Conversely, the deposition carried out at pH 12 by addition of ammonia led to a modest increase of the deposited layer, equal to +11% or 3.1 mg in total. In addition, the surface was even less homogeneous and so far, the best option was represented by the addition of HCl and the dip coating performed at 50°C. As expected, many subsequent cycles of deposition lead to a remarkable increase in the weight of the titania layer, up to 10.7 mg after six treatments (Table 7.4).

**Table 7.3.** Photocatalyst loading over glassed obtained with different temperatures and pH. Dipping in 5% w/w P25 suspension in distilled water, two cycles. Post-treatment was performed in a furnace at 500°C for 1h

Recipe #	Temp (°C)	Acid/Base	pH	Av. loading (mg)	Min (mg)	Max (mg)
6	20	/	7	1.5	0.9	2.2
7	30	/	7	1.8	0.9	3.7
8	50	/	7	2.8	1.6	4.1
9	50	HCl	3	3.6	2.7	4.9
10	50	HNO <sub>3</sub>	3	4.0	2.8	5.3
11	50	NH <sub>3</sub>	12	3.1	1.4	10.7

**Table 7.4.** Photocatalyst loading over glasses obtained with different cycles of dip coating in 5% w/w P25 suspension in distilled water at pH 3 (HCl). Post-treatment was performed in a furnace at 500°C for 1h

Recipe #	N° cycle	Av. loading (mg)	Min (mg)	Max (mg)
9	2	3.6	2.7	4.9
	3	4.8	2.6	6.4
	4	8.2	7.5	9.3
	5	9.9	9.1	10.7
	6	10.7	9.9	11.5

Since it was not possible to further increase the deposition with that setup, we instead focused our attention on how to increase concentration of titania in the liquid phase. So far, 5% w/w represented a physical limit without incurring in a massive precipitation of titania in absence of stirring, thus, it was adopted a different approach that consists in the addition of an industrial emulsifying agent for paints based on titanium dioxide and

named Disperbyk-190<sup>®</sup>. It is an organic-based compound which stabilizes the water suspension of titanium dioxide when added up to 3% w/w<sub>TiO<sub>2</sub></sub>. By using Disperbyk-190<sup>®</sup>, it was possible to obtain a concentration up to 25% w/w of titania in the dipping mother suspension. Table 7.5 summarizes the results achieved by using a water mixture of P25 in the range 5-25% w/w. At ambient temperature and after two deposition cycles, the average weight of the deposited layer was higher than our benchmark at 5% w/w, almost 30% higher, and still 1.5-times lower than the weight obtained by using HCl at 50°C. However, thanks to the additive it was possible to match the performance of the latter setup simply by increasing the weight the amount of titania added to the water to 10% w/w. In addition, when this ratio was set to 15.5% the average weight of P25 deposited over the glasses increased by three-fold (12.6 mg vs 4.3 mg). Lastly, by pushing the system to the limit with a 25% solution of P25 in water, it was possible to obtain a very thick deposited layer equal to 100 mg per tile, that, although very homogeneous, was quite fluffy and easy to peel off if accidentally touched. In light of these impressive results, we decided to keep it simple and perform just one impregnation with suspensions not more concentrated than 15% (w/w) to ensure the right adhesion over the glass surface.

**Table 7.5.** Photocatalyst loading over glasses obtained via dip coating in 5-25% w/w P25 and Disperbik-190<sup>®</sup> suspension in distilled water. Post-treatment was performed in a furnace at 500°C for 1h

Recipe #	%w/w	N° cycle	Av. loading (mg)	Min (mg)	Max (mg)
12	5.1	2	2	1.0	3.1
13	10.0	2	4.3	3.4	5.2
14	15.5	2	12.6	6	22.9
15	25.3	2	100.6	89.1	112.8
16	13.7	1	4.0	3.2	4.7

### 7.2.2. Supported photocatalysts functionalization

P25 is poorly active as a photocatalyst and not active at all under visible radiation, therefore, it was modified by metallization and wetness impregnation, in a similar way that we used to with titania P25 in form of powder. The first impregnation experiment was carried out by dip coating of glass tiles in a 13.7% (recipe #16) suspension of titania in water (with Disperbik-190<sup>®</sup> used as additive) followed by a second cycle of impregnation, after treatment in the muffle at 500°C, with a 0.07M water solution of silver nitrate. The slides were then dried for 1h at 105°C and placed in a tubular oven to perform the reduction under hydrogen atmosphere (5°C/min ramp, 150°C, 30 mL/min H<sub>2</sub>). At the end, the slides were carefully scratched in order to recover the catalyst and the powder was analyzed by means of XRD and DRS techniques.

As already discussed, the deposition of silver is clearly evident from the XRD diffractogram, since several peaks can be associated with the Ag phase (JCPDS card #004-0783). In addition, the color of the powder turned from white to black after the treatment, indicating the formation of silver nanoparticles. Also, DRS analysis confirmed the presence of a plasmonic band associated with the formation of Ag<sup>0</sup> clusters. A second



batch of twelve coated and impregnated slides was then prepared by using a 0.01M solution of  $\text{AgNO}_3$  and tested in the pilot photoreactor.

To better understand the correlation between the concentration of the precursor used during the impregnation, we prepared several copper sulfate solutions at selected concentration (0.001M - 0.05M) and they were analyzed by means of a UV-Visible spectrophotometer prior to and after the impregnation of a batch of 34 deposited slides. That precursor was chosen since it has a strong blue color and it is perfectly soluble in water. Starting from the most concentrated solution (*i.e.* 0.05M  $\text{CuSO}_4$ ) we observed a decrease of 2% of the absorbance after the impregnation, meaning that the copper sulfate was effectively adsorbed over titania, and upon calibration it was estimated an average loading of 5.8 mg of copper per glass, comparable with the weight of the deposited titania (5 mg). That value dropped to 1.9 mg per tile (5.5 mg of P25) when halving the concentration of the precursor (0.025M) and was as low as 0.1 mg (4.8 mg of titania) when impregnating with 0.01M copper-containing solution. Again, the coated glasses were reduced in the tubular oven (5°C/min ramp, 500°C, 30 mL/min  $\text{H}_2$ ), and it was observed that the color final aspect of the deposited powder reflects the deposited amount, which means that the highest concentration led to a greenish color that fade away with the dilution of the precursor.

Unfortunately, the XRD analysis did not show any difference between the sample and there were no traces of the  $\text{Cu}^0$  phase, which could also be due to the high dispersion of the copper nanoparticles.

### 7.2.3. Design of reactor supports

The very first test with the coated glasses was performed in a traditional quartz reactor whose capacity is 3L, as will be discussed in the following paragraph. However, our initial idea was to employ the glasses in combination with the pilot photoreactor (see Chapter 2) that was used for all the tests concerning CO<sub>2</sub> photoreduction and carbohydrate photoreforming. Briefly, the reactor has a cylindrical shape, therefore, we decided to design a circular support via 3D-modeling software (SketchUp) in order to fit it around the quartz sleeve that contains the lamp. Firstly, the internal volume of the photoreactor was simulated and it was found that the maximum amounts of glasses that fits the internal volume without touching the lamp, the reactor cap or the magnetic stir bar is 24, disposed on 4 levels (Figure 7.2a). However, this number is impractical for many reasons, for instance, it could lead to a significantly decrease of the internal volume available for the solution and, also, only a half of the glasses would face directly the lamp bulbs, which are two, leaving the other slides to be significantly less active in the photocatalytic process. By keeping in mind these constraints, we realized the first conceptual design of a sample holder that could mount up to twelve glasses, which is illustrated in Figure 7.2b. That solution allowed to insert the glasses from the longer side, but it was still far from the optimal, since the volume of the cage is too big if compared with the 1.3L of the photoreactor. Given the overly complexity of this design, the shape was simplified to include only two rings, each one with six housings for the slides. The key idea was to insert in the photoreactor both the support before closing it with the cap, and by keeping them at the right height by means of three metallic shafts that would be inserted on the rings (the three pins reported in Figure 7.3). From here, the design was further simplified and modified to exploit the two shafts that surround the quartz sleeve and the cage that

protects the end of the sleeve (*i.e.* where the lamp is inserted from the reactor cap), therefore, the support that goes in the upper part of the photoreactor was redesigned as an open ring to better fit between the shafts, while to the support for the lower part were added three stabilizing pins whose purpose was to keep the support anchored to the metallic cage (Figure 7.4). We will refer to this design as the #3, being the first one that was 3D-printed and successfully tested in the photoreactor for the photoabatement of Acid Orange 7 and photoreforming of glucose. Since the upper part was held in place by a metallic wire tied up to the shaft, the fourth version of the support included a small clip that allowed to attach it directly (design #4). Once tested its stability, we decided to adjust the size to print just one kind of support for the low and the upper part of the photoreactor, which is illustrated in Figure 7.5 (design #5).

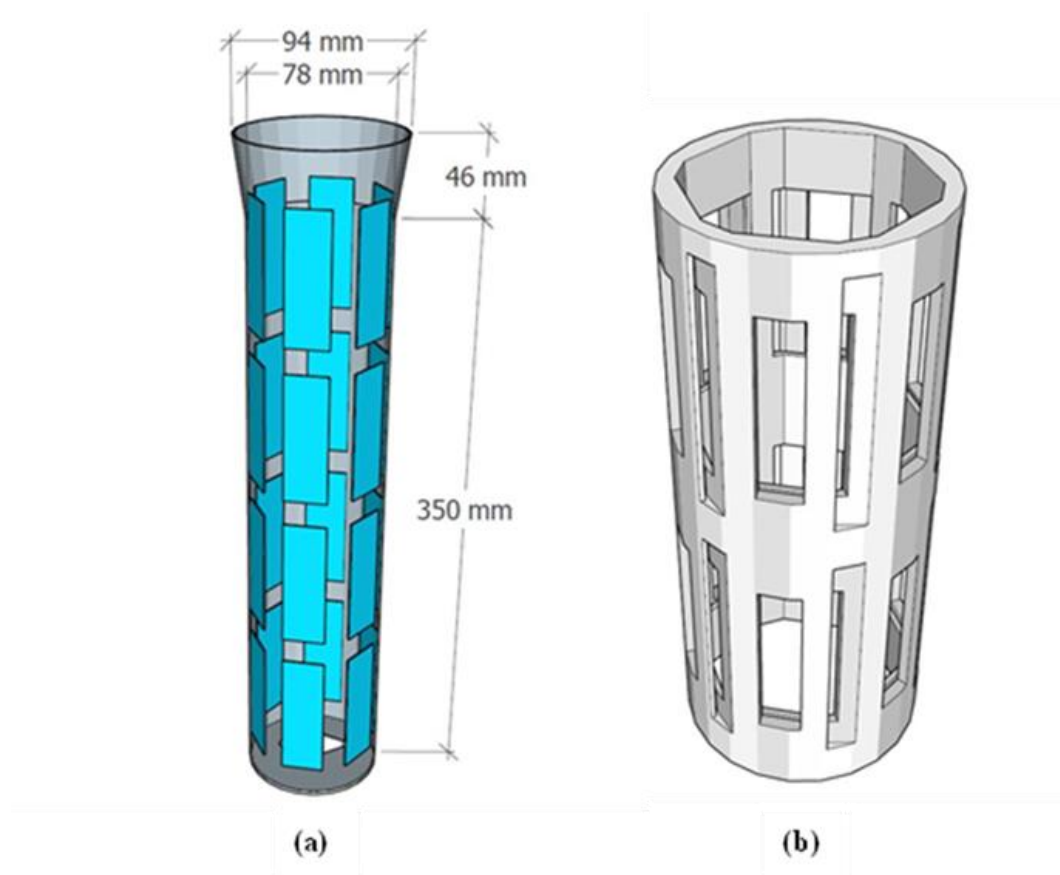


**Figure 7.2.** (a) scheme of the internal volume of the photoreactor and ideal disposition of the glasses and (b) first proposed design of the glass holder. Design #1

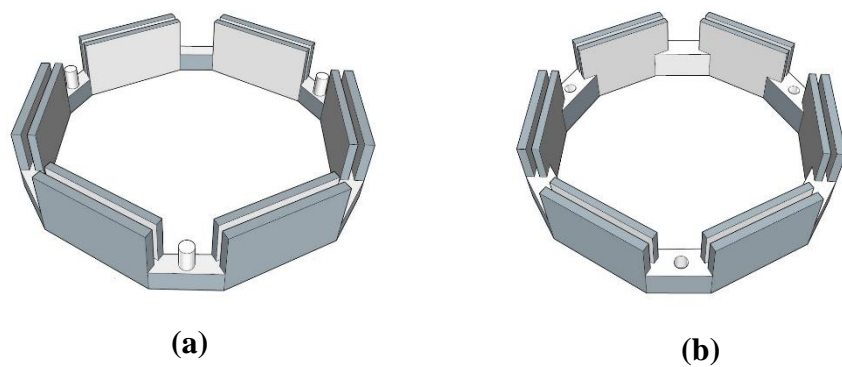


**Figure 7.3.** Second design of the glasses holder. (a) lower part (b) upper part

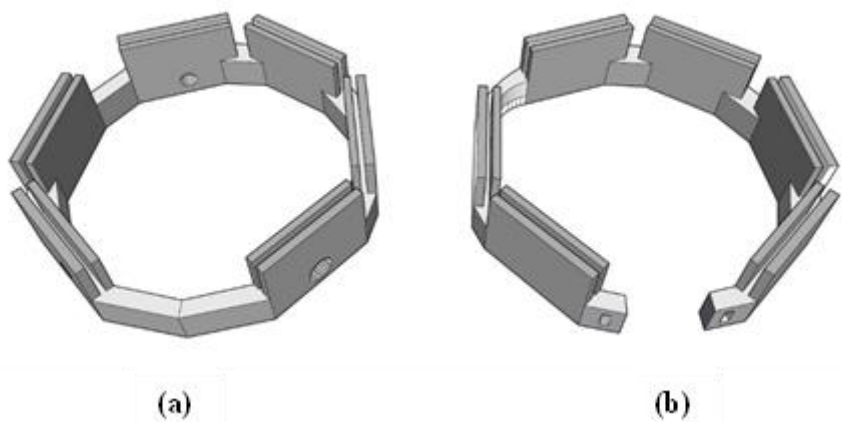


**Figure 7.4.** Third design of the glasses holder. (a) lower part (b) upper part

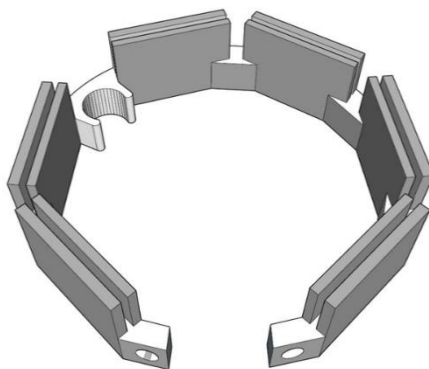


**Figure 7.5.** Fifth and final design of the glasses holder. (a) lower part (b) upper part

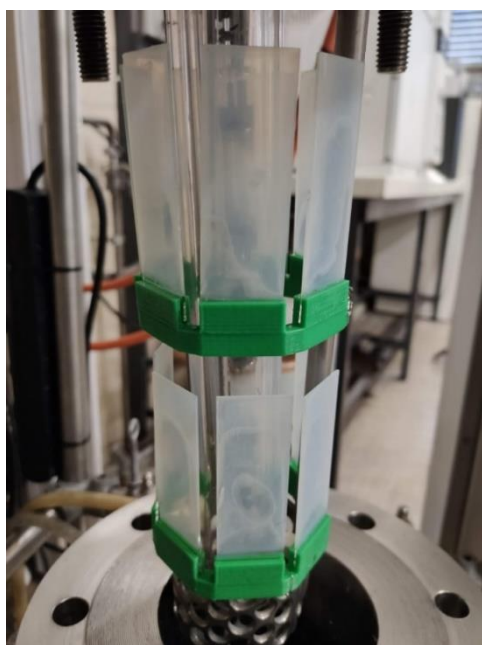
In order to test the proposed design, we took advantage of 3D-printing technique, which is inexpensive and fast, considering the small size of the tools that we needed. Figure 7.6 illustrates all the printings that were tested. The samples labeled as A and B represent the same design (#3) printed with two different filaments, that are A, polylactic acid (PLA)

and B, acrylonitrile-butadiene-styrene (ABS). PLA was problematic due to its relatively low glass temperature ( $T_g$ ), around  $65^{\circ}\text{C}$ , so after one test at that temperature, we verified that the support was deformed and we switched to a PET filament, which is more resistant at the usual temperature adopted during the tests ( $80^{\circ}\text{C}$ ). Unfortunately, its main limitation was the kind of colorant added to the filament, since its green color tend to degrade after two experiments. Sample “D” was obtained with the same filament and the design #5, while sample “C” was made by combining design #5 with a polypropylene (PP) filament reinforced with glass fibers. So far, the latter was the best combination, as the clip added to the ring does not require other solutions to keep the support connected to the lamp shaft and polypropylene is able to resist the aggressive conditions adopted during the photoreduction of  $\text{CO}_2$  (*e.g.*  $80^{\circ}\text{C}$ , UV, pH14). Sample “E” (design #5) was obtained via 3D-printing with a stainless-steel filament (AISI 630) and, despite being resistant to corrosion, it was too rigid and that caused the breakup of some glasses during the insertion into the photoreactor.

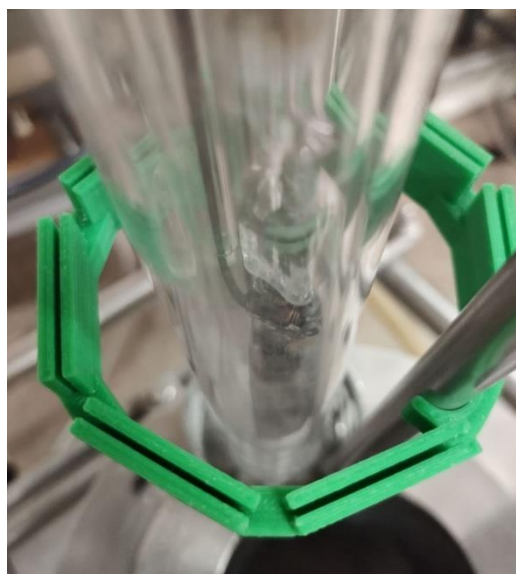
An example of the complete setup is reported in Figure 7.7a. The glasses are inserted through the uncoated area and placed right in front of the bulb. In addition, Figure 7.7b illustrates the connection on the shaft through the clip on the ring.



**Figure 7.6.** Collection of glasses holders 3D-printed with different filaments. (a) PLA, (b)(d) ABS, (c) PP+glass fibers, (e) stainless steel



(a)



(b)

**Figure 7.7.** Picture of the sample mounted on the photoreactor with twelve coated glass slides. (a) ABS with design #3, (b) ABS with design #5

One of the problems of using coated glass slides into this setup is that both the faces of the glass are covered with titania (supposedly equally dispersed). Therefore, the face in front of the bulb receives most of the light, while the rear one is irradiated with the radiation reflected by the wall of the photoreactor or that passed through the glass. To evaluate which portion immobilized catalyst contributes to the photocatalyzed reaction, we built a home-made apparatus to measure the portion of the light absorbed by P25 on the rear face of the glass. The setup was constituted of a box containing the UV light source (*i.e.* UV-LED lamp, Suntech ltd., 48W, 365 nm) connected to a cylinder pipe through a hole, while on the other end of the pipe it was placed the probe of a photoradiometer (Figure 7.8). A 10 mm cut in the middle of the pipe allowed to insert the glass slides in its housing, in a way that left no gap and forced the light from the lamp to pass through the coated glasses. First of all, the background irradiance was collected and an uncoated glass slide was inserted into the apparatus. Then, a batch of 15 glasses coated in the same session (recipe #9) was analyzed with that setup by placing it in the housing, first with one face exposed to the lamp and then with the other one. Five of these glasses were carefully cleaned on one side, to estimate the impact of just one layer on the attenuation of the radiation. Table 7.6 reports the results in light of the weight of the deposited layer, assuming that it is perfectly distributed over the two faces. It was found that the glass itself absorbed about 11.6% of the incident radiation, while the one-layer tiles absorbed on average 76.8% of the light that passed through, with a minimum of 73.4% and a maximum of 79.5%, upon subtraction of the attenuation due to the glass itself. As expected, the adsorption increases when both sides are coated, with an average loss of irradiance of 84.7% (MIN 83.0%, MAX 86.3%). That means that on average the rear face of the coated slide absorbs roughly an 8% of the incident radiation. On one side

there is a waste of material that contributes a fraction to the overall photocatalytic activity, on the other, this dip coating technique is very simple and titania P25 is inexpensive, thus it is likely that it is still favorable trade-off between the simplicity of the deposition technique and the poor usage of half of the photocatalyst.

**Table 7.6.** Attenuation measurement obtained after testing both single-side coated and full-coated glass slides

Slide #	Side coated	Loading (mg)	Mean Irradiance (mW/m <sup>2</sup> )	Transmission (%)
none	/	/	825	100
uncoated	0	0	729	11.6
1.3	1	3.6	85.7	10.4
2.3	1	2.9	79.9	9.7
3.3	1	3.3	73.8	9.0
4.3	1	2.0	124	15.0
5.3	1	2.6	116	14.0
1.1	2	14.4	24.5	3.0
1.2	2	7.0	40.7	4.9
2.1	2	8.4	35.9	4.3
2.2	2	6.4	17.3	2.1
3.1	2	6.5	17.3	2.1
3.2	2	4.3	32.8	4.0
4.1	2	5.7	18.5	2.2
4.2	2	4.2	44.3	5.4
5.1	2	5.0	27.4	3.3
5.2	2	3.7	43.8	5.3



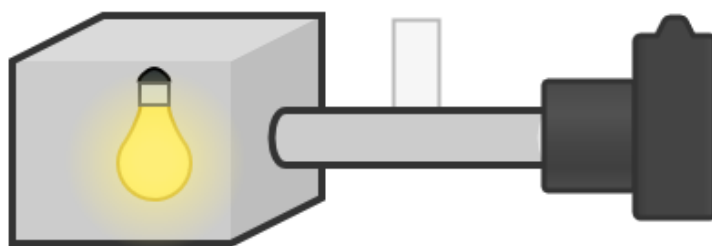


**Figure 7.8.** Simplified drawing of the setup used to measure the amount of light that pass through the coated glasses

#### **7.1.1. Photocatalytic tests using the deposited glasses**

The first test was carried out by using the 3L quartz reactor and the UV spotlight (Figure 7.9). Ten coated glass slides were placed vertically on the reactor wall, slightly tilted towards the lamp, whose bulb was fixed 150 mm from the top of the solution. The latter was a 20-ppm solution of Acid Orange 7, a dye quite easy to degrade which was used as a benchmark to assess the photocatalytic activity of the immobilized P25. Overall, 30 mg of titania P25 were deposited on the slides (recipe #2) and, after 1h of immersion, no appreciable variation of the absorbance of the solution was observed, thus, the adsorption of the dye over titania is negligible. It was found that the photooxidation of the dye is way faster when the photocatalyst is added to the solution, lowering the time required to reach the 50% conversion from 6h to 3h. In addition, no weight loss occurred during the test. After optimization of the support design, we proceeded with further tests in the pilot photoreactor and the same AO7 solution was treated with the PLA support (design #3) and twelve coated slides (recipe #9) loaded with *ca.* 35 mg of P25. Unfortunately, it was found that the UV lamp employed is too powerful and the degradation of the dye occurs

mainly by direct photolysis and even faster without the glasses, since they absorb part of the radiation.

In a third test, twelve coated slides prepared according to recipe #9 (38 mg of P25 in total) were mounted on the support with design #3 (PLA) and 1.14 L of glucose solution (5g/L) were added to the photoreactor. The volume was reduced from the usual 1.20 L given that the extra volume added by the support and the slides is roughly 0.06 L, and, as already explained, the temperature was also reduced to 65°C since PLA cannot sustain higher ones. Figure 7.10 illustrates the results of the test. As expected, the bare glass does not have any photocatalytic activity and titania is required to observe the production of organics or gaseous species and the glucose conversion (0.1%) occurred mainly via photolysis (Table 7.7). On the other hand, it was observed that P25 retained its activity after the deposition process, although the productivity of H<sub>2</sub> decreased by roughly 60% (from 2.46 to 0.99 mol/kg<sub>cat</sub> h) while the amount of CO detected was higher (from 0.86 to 1.46 mol/kg<sub>cat</sub> h). According to the XRD analysis, the deposited titania showed a slightly higher percentage of anatase phase (90%) with respect to untreated P25 (78%), while the crystallite size was comparable, therefore, this difference in the product distribution is not easily explainable. On the other hand, the lower glucose conversion and productivity of the immobilized photocatalyst were probably due to the geometry of the system, as the powder can collect a higher amount of energy from the incident light and the immobilized catalyst had both a fixed and a lower exposed surface. In addition, the dip coating technique causes the deposition of the photocatalyst on both the front and rear side of the glasses (assuming that the amount on the edges is negligible), thus, the portion of the catalyst that faced the wall of the photoreactor was less active since it received the light filtrated through the glass or reflected by the walls.

Then, thanks to the advances of the support design (PP+glass and design #5), it was set up a CO<sub>2</sub> photoreduction experiment in the typical conditions (see Chapter 2 for more details) and by employing the immobilized titania modified via surface metallization with silver NPs (recipe #16, 0.01M AgNO<sub>3</sub>). The graph of Figure 7.11 illustrates the absolute amount of the products detected from the analysis of the liquid and gaseous phase, which is necessary since we are comparing two tests performed with different amount of photocatalyst (Table 7.7). In both cases, the HS conversion was over 95%, anyway, it is clearly visible from the graph that the activity of the photocatalyst is greatly enhanced by the metallization process, as the amount of HCOOH produced increased from 4.62 mmol to 27 mmol, almost six times higher. In addition, the amount of hydrogen produced was three times lower with respect to the bare P25, but traces of methane and CO were detected. After the test, the slides were collected, washed with distilled water and dried overnight at 105°C, then weighted to verify any loss of catalyst during the test, which was negligible. The effects of silver deposition on titanium dioxide are well known, for instance, this metal presents LSPR band that impacts positively on the BG of the material and, also, it improves the separation of the photogenerated charges by acting as electron sink [6]. Many authors reported an increase in the photocatalytic activity after the functionalization [7–9], however, being able to directly modify the immobilized titania through a simple dipping process and to perform the CO<sub>2</sub> photoreduction with such a system represents a great advancement for the technique. Indeed, the literature about titanium dioxide deposition is rich, but few cases of immobilization of modified nanocatalysts or surface modification are reported, and they may not be as scalable or flexible as the synthesis discussed here [10–12]. In addition, the recipes here proposed

allow to obtain anchorage that last even in demanding environment, such as high temperature, extreme pH variation and liquid phase.

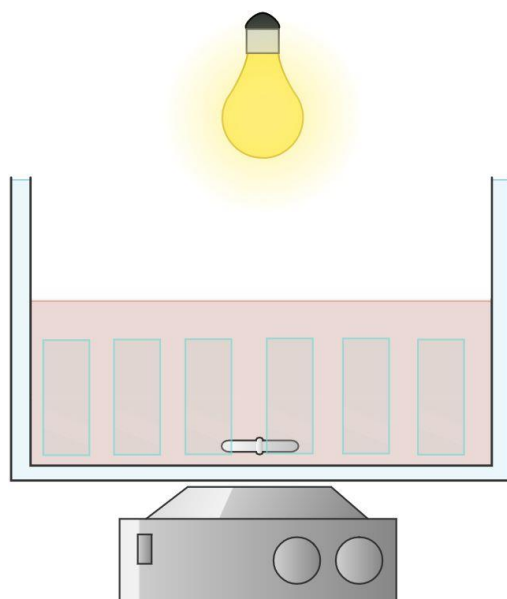


**Figure 7.9.** Schematic representation of the setup used to check the activity of immobilized P25 in case of AO7 photooxidation

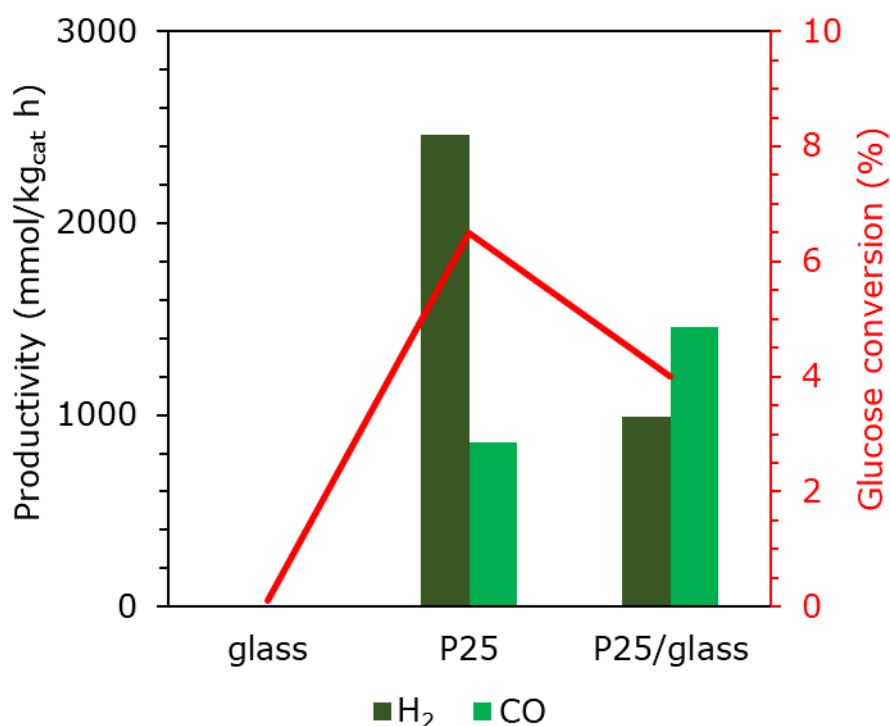


**Figure 7.10.** Glucose photoreforming carried out with P25 in form of powder and the same catalyst immobilized. 65°C, 1.14 L, 5h, 5 bar N<sub>2</sub>, 31 mg/L P25

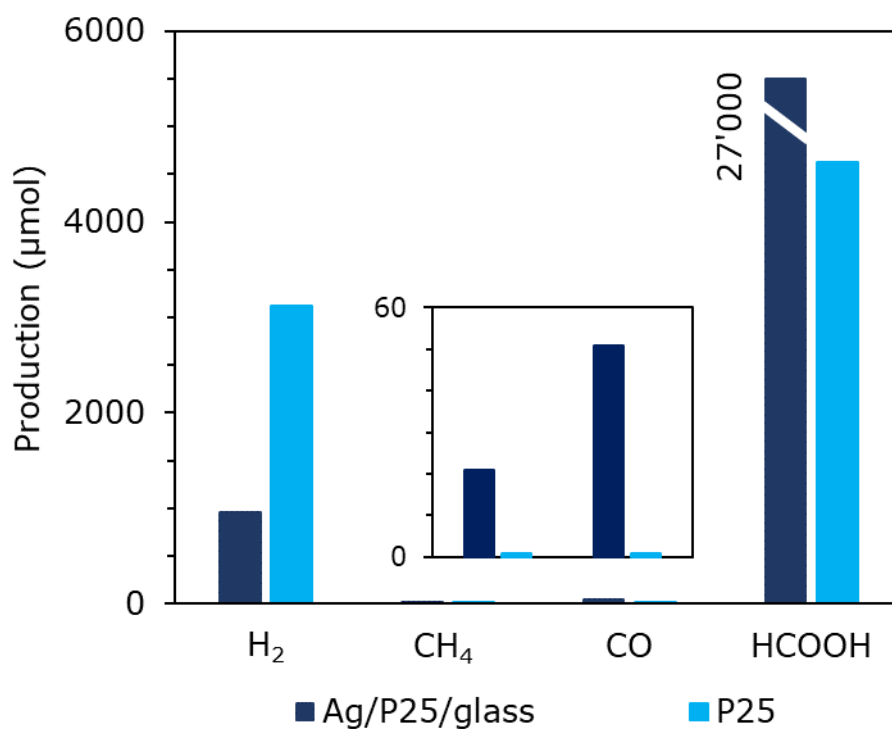


**Figure 7.11.** CO<sub>2</sub> photoreduction carried out with P25 in form of powder and Ag/P25 immobilized. 80°C, 1.14 L, 24h, 8 bar CO<sub>2</sub>, 1.67 g/L Na<sub>2</sub>SO<sub>3</sub>, 38 mg P25 or 50 mg Ag/P25

**Table 7.7** Summary of conditions used during the tests and results obtained in case of glucose photoreforming and CO<sub>2</sub> photoreduction

Photocatalyst	Time (h)	N <sub>2</sub> pressure (bar)	Glucose conc. (g/L)	HS conversion (%)	Other conditions	Productivity mol/kg <sub>cat</sub> ·h
glass	5	5	5 g/L	0.1	65°C; pH6.5	H <sub>2</sub> -0
					31 mg/L cat.	CO-0
P25	5	5	5 g/L	6.5	65°C; pH6.5	H <sub>2</sub> -2.46
					31 mg/L cat	CO-0.86
P25/glass	5	5	5 g/L	4.0	65°C; pH6.5	H <sub>2</sub> -0.99
					31 mg/L cat	CO-1.46

Photocatalyst	Time (h)	CO <sub>2</sub> pressure (bar)	Na <sub>2</sub> SO <sub>3</sub> conc. (g/L)	HS conversion (%)	Other conditions	Productivity mol/kg <sub>cat</sub> ·h
glass	24	18	1.67g/L	<5%	80°C; pH14 31 mg/L cat	HCOOH-0 H <sub>2</sub> -0.02
P25	24	18	1.67g/L	>95	80°C; pH14 31 mg/L cat	HCOOH-6.21 H <sub>2</sub> -4.20 HCOOH-19.8
Ag/P25/glass	24	18	1.67g/L	>95	80°C; pH14 50 mg/L cat	H <sub>2</sub> -0.70 CO-0.05 CH <sub>4</sub> -0.02

### 7.3. Conclusions

Through the simple dip coating technique, we demonstrated that it is possible to immobilized titanium dioxide nanoparticles, in particular TiO<sub>2</sub> P25, over commercial glass. The optimization of the process parameters, including a washing pre-treatment, heating post-treatment, the temperature and the pH of the titania dispersion, allowed to obtain coatings on commercial microscope slides up to several milligrams of titania per dipping cycle, which can be increased up to 100 mg by addition of an organic emulsifier that stabilizes the dispersion of titania in water. The deposited layer was tough enough to be used for photocatalytic application in the liquid phase and at high temperature without incurring in the detachment of the photocatalyst from the glass.

In that way, it was possible to assess that the photocatalytic properties of titania are almost unaltered after the immobilization, and that this material can be further modified by subsequent dipping cycle in order to further enhance its activity.

## References

1. Zakria, H.S.; Othman, M.H.D.; Kamaludin, R.; Sheikh Abdul Kadir, S.H.; Kurniawan, T.A.; Jilani, A. Immobilization techniques of a photocatalyst into and onto a polymer membrane for photocatalytic activity. *RSC Adv.* **2021**, *11*, 6985–7014, doi:10.1039/d0ra10964a.
2. Wood, D.; Shaw, S.; Cawte, T.; Shanen, E.; Van Heyst, B. An overview of photocatalyst immobilization methods for air pollution remediation. *Chem. Eng. J.* **2020**, *391*, 123490, doi:10.1016/j.cej.2019.123490.
3. Forghieri, G.; Ghedini, E.; Menegazzo, F.; Di Michele, A.; Signoretto, M. An investigation on the photo-catalytic oxidation of air pollutants via SiO<sub>2</sub>-supported TiO<sub>2</sub>. *Appl. Catal. A Gen.* **2022**, *644*, 118813, doi:10.1016/j.apcata.2022.118813.
4. Jang, J.I.; Jeong, H.C. Shear induced TiO<sub>2</sub> nano structure using brush-coating for liquid crystal alignment. *Crystals* **2020**, *10*, 1–7, doi:10.3390/cryst10100860.
5. Marques, M.E.; Mansur, A.A.P.; Mansur, H.S. Chemical functionalization of surfaces for building three-dimensional engineered biosensors. *Appl. Surf. Sci.* **2013**, *275*, 347–360, doi:10.1016/j.apsusc.2012.12.099.
6. Zielińska-Jurek, A. Progress, challenge, and perspective of bimetallic TiO<sub>2</sub>-based photocatalysts. *J. Nanomater.* **2014**, *2014*, 1–17, doi:10.1155/2014/208920.
7. Yu, B.; Zhou, Y.; Li, P.; Tu, W.; Li, P.; Tang, L.; Ye, J.; Zou, Z. Photocatalytic reduction of CO<sub>2</sub> over Ag/TiO<sub>2</sub> nanocomposites prepared with a simple and rapid silver mirror method. *Nanoscale* **2016**, *8*, 11870–11874, doi:10.1039/c6nr02547a.

8. Liu, E.; Hu, Y.; Li, H.; Tang, C.; Hu, X.; Fan, J.; Chen, Y.; Bian, J.  
Photoconversion of CO<sub>2</sub> to methanol over plasmonic Ag/TiO<sub>2</sub> nano-wire films enhanced by overlapped visible-light-harvesting nanostructures. *Ceram. Int.* **2015**, *41*, 1049–1057, doi:10.1016/j.ceramint.2014.09.027.
9. Kočí, K.; Matějů, K.; Obalová, L.; Krejčíková, S.; Lacný, Z.; Plachá, D.; Čapek, L.; Hospodková, A.; Šolcová, O. Effect of silver doping on the TiO<sub>2</sub> for photocatalytic reduction of CO<sub>2</sub>. *Appl. Catal. B Environ.* **2010**, *96*, 239–244, doi:10.1016/j.apcatb.2010.02.030.
10. Lopes, F.C.S.M.R.; da Rocha, M. da G.C.; Bargiela, P.; Sousa Ferreira, H.; Pires, C.A. de M. Ag/TiO<sub>2</sub> photocatalyst immobilized onto modified natural fibers for photodegradation of anthracene. *Chem. Eng. Sci.* **2020**, *227*, 115939, doi:10.1016/j.ces.2020.115939.
11. van Grieken, R.; Marugán, J.; Sordo, C.; Martínez, P.; Pablos, C. Photocatalytic inactivation of bacteria in water using suspended and immobilized silver-TiO<sub>2</sub>. *Appl. Catal. B Environ.* **2009**, *93*, 112–118, doi:10.1016/j.apcatb.2009.09.019.
12. Lu, N.; Wang, Y.; Ning, S.; Zhao, W.; Qian, M.; Ma, Y.; Wang, J.; Fan, L.; Guan, J.; Yuan, X. Design of plasmonic Ag-TiO<sub>2</sub>/H<sub>3</sub>PW<sub>12</sub>O<sub>40</sub> composite film with enhanced sunlight photocatalytic activity towards o-chlorophenol degradation. *Sci. Rep.* **2017**, *7*, 17298, doi:10.1038/s41598-017-17221-4.



## 8. Final conclusion and future developments

This thesis showed how versatile and powerful is the photocatalysis, which can be applied successfully to a wide range of different processes, from the valorization of wastes to decontamination of water. The efficiency of these treatments, though, is still orders of magnitudes lower than what is needed for a worldwide application. Therefore, in the near future it will be crucial to improve every aspect of the photocatalytic process, from the light harvesting to the photo charges generation and surface reactions, which can be reached through the engineering of more suitable photoreactors and development of new materials with a band gap suitable for the selected application.

In addition, despite all the efforts from the scientific community, there is still a lack of uniformity in this field, meaning that it is not trivial to compare results obtained with different setups and currently it may be pointless to make evaluations based on activities and efficiencies.

On last point to be addressed is that the photocatalyst here reported, or most of the ones published in literature, work optimally when a sacrificial electron donor is added to the system (in general alcohols and amines), and this should be avoided considering the green chemistry principles. At very least, it would be ideal to exploit bio-based hole scavenger that comes, for instance, from biomass, which however comes with several limitations, being source with a not so well-defined composition and properties that are unstable over time. On the other hand, it would be possible to integrate different processes to exploit the photo oxidation of a species (such as a pollutant from wastewater) to promote the photoreduction of another, and something similar has been already carried out by our research group in case of simultaneous abatement of nitrate and ammonia from contaminated water.



## Appendix D

During my PhD project I was co-author of the following papers and congress memories.

### Publications

1. *Carbon Nitride-Based Catalysts for High Pressure CO<sub>2</sub> Photoreduction*, Conte, F., García-López, E., Marcì G., Bianchi, C., Ramis, G., Rossetti, I., 2022, *Catalysts*, 12(12), 1628
2. *Low Metal Loading (Au, Ag, Pt, Pd) Photo-Catalysts Supported on TiO<sub>2</sub> for Renewable Processes*, Conte, F., Rossetti, I., Ramis, G., (...), Hajja-Garreau, S., Bennici, S., 2022, *Materials* 15(8),2915
3. *Effect of Metal Cocatalysts and Operating Conditions on the Product Distribution and the Productivity of the CO<sub>2</sub> Photoreduction*, Conte, F., Villa, A., Prati, L., (...), Ramis, G., Rossetti, I., 2022, *Industrial and Engineering Chemistry Research* 61(8), pp. 2963-2972
4. *Photocatalytic Reduction of Nitrates and Combined Photodegradation with Ammonium*, Conte, F., Pellegatta, V., Di Michele, A., Ramis, G., Rossetti, I., 2022, *Catalysts* 12(3),321
5. *Photoreforming of model carbohydrate mixtures from pulping industry wastewaters*, Conte, F., Casalini, G., Prati, L., Ramis, G., Rossetti, I., 2022, *International Journal of Hydrogen Energy*, in press.
6. *Photo-oxidation of ammonia to molecular nitrogen in water under uv, vis and sunlight irradiation*, Conte, F., Pellegatta, V., Tripodi, A., Ramis, G., Rossetti, I., 2021, *Catalysts* 11(8),975

7. *Feasibility study of the solar-promoted photoreduction of CO<sub>2</sub> to liquid fuels with direct or indirect use of renewable energy sources*, Conte, F., Tripodi, A., Rossetti, I., Ramis, G., 2021, *Energies* 14(10),2804
8. A review of advances in multifunctional XTiO<sub>3</sub> perovskite-type oxides as piezo-photocatalysts for environmental remediation and energy production, Djellabi, R., Ordóñez, M.F., Conte, F., (...), Bianchi, C.L., Rossetti, I., 2022, *Journal of Hazardous Materials* 421,126792
9. *Photocatalytic selective oxidation of ammonia in a semi-batch reactor: Unravelling the effect of reaction conditions and metal co-catalysts*, Bahadori, E., Conte, F., Tripodi, A., Ramis, G., Rossetti, I., 2021, *Catalysts*, 11(2),209, pp. 1-15
10. *Development and comparison of advanced oxidation processes (AOPs) for the mineralization of azo-dyes from wastewaters*, Ramis, G., Conte, F., Calloni, C., (...), De Felice, B., Rossetti, L., 2021, *Chemical Engineering Transactions* 86, pp. 601-606
11. *Ethylene from renewable ethanol: Process optimization and economic feasibility assessment*, Frosi, M., Tripodi, A., Conte, F., (...), Mahinpey, N., Rossetti, I., 2021, *Journal of Industrial and Engineering Chemistry*, 104, p. 272-285
12. *Solid-Liquid-Liquid Equilibria of the System Water, Acetonitrile, and Ammonium Bicarbonate in Multiphase Reacting Systems*, Tripodi, A., Conte, F., Robbiano, A., Ramis, G., Rossetti, I., 2021, *Industrial and Engineering Chemistry Research*, 60(46), pp. 16791-16804
13. *Feasibility study and process design of a direct route from bioethanol to ethylene oxide*, Ripamonti, D., Tripodi, A., Conte, F., (...), Ramis, G., Rossetti, I., 2021, *Journal of Environmental Chemical Engineering*, 9(5),105969

14. *Flame pyrolysis synthesis of mixed oxides for glycerol steam reforming*, Conte, F., Esposito, S., Dal Santo, V., (...), Ramis, G., Rossetti, I., 2021, *Materials*, 14(3), 652, pp. 1-19
15. *Process Intensification for Ammonia Synthesis in Multibed Reactors with Fe-Wustite and Ru/C Catalysts*, Tripodi, A., Conte, F., Rossetti, I., 2021, *Industrial and Engineering Chemistry Research*, 60(2), pp. 908-915
16. *Conceptual design of the gasification of plastic waste for the production of syngas or naphtha: A circular approach from plastic waste to renewed polymers*, Rossetti, I., Megna, F., Tripodi, A., Conte, F., Ramis, G., 2021, *DGMK Tagungsbericht*, 2021-October, pp. 47-57
17. *Design of a process for the one-pot bio-ethylene oxide production*, Rossetti, I., Ripamonti, D., Tripodi, A., Conte, F., Ramis, G., 2021, *Chemical Engineering Transactions*, 86, pp. 1447-1452
18. *Carbon Dioxide Methanation: Design of a Fully Integrated Plant*, Tripodi, A., Conte, F., Rossetti, I., 2020, *Energy and Fuels*, 34(6), pp. 7242-7256
19. *Evolutionary optimization strategies for Liquid-liquid interaction parameters* Robbiano, A., Tripodi, A., Conte, F., Ramis, G., Rossetti, I., 2023, *Fluid Phase Equilibria*, 564, 113599

**Attended Schools, Congresses and Seminars:**

- Sychem, PhD school, 4–6 February 2020, Bologna
- Enerchem-2, Congress, 12–14 February 2020, Padova (Poster)
- GRICU, PhD School, 11-19 March 2021
- CAMURE11-ISMIR10, Congress, 21-24 March 2021 (Oral presentation)
- ICheaP 15, Congress, 23-26 May 2021 (Poster)
- MIPOL2021, Congress, 6-8 July 2021 (Oral presentation)
- Innovative experimental Physico-Chemical approach to contribute to post-combustion CO<sub>2</sub> Capture, Virtual DCMIC Seminar, 4 Jun 2021
- Hackathon PInK: Lubrican't organized by Stevanato group and Università Ca' Foscari Venezia, 21-25 Sep 2021 (3-day project)

**Period in other universities or research centers:**

- 09-12/2021, Internship at Institut de Science des Matériaux de Mulhouse (IS2M, 15 Rue Jean Starcky, 68057 Mulhouse, France, [www.is2m.uha.fr](http://www.is2m.uha.fr)), tutor Dr. Bennici S. ([simona.bennici@uha.fr](mailto:simona.bennici@uha.fr))